Catalytic synthesis of alcoholic fuels for transportation from syngas

Wu, Qiongxiao

Publication date:
2013

Document Version
Publisher's PDF, also known as Version of record

Catalytic synthesis of alcoholic fuels for transportation from syngas

December 21st 2012

Ph.D. Thesis

Qiongxiao Wu

CHEC Research Center
Department of Chemical and Biochemical Engineering
Technical University of Denmark

Abstract

This work has investigated the catalytic conversion of syngas into methanol and higher alcohols. Based on input from computational catalyst screening, an experimental investigation of promising catalyst candidates for methanol synthesis from syngas has been carried out. Cu-Ni alloys of different composition have been identified as potential candidates for methanol synthesis. These Cu-Ni alloy catalysts have been synthesized and tested in a fixed-bed continuous-flow reactor for CO hydrogenation. The metal area based activity for a Cu-Ni/SiO_2 catalyst is at the same level as a Cu/ZnO/Al_2O_3 model catalyst. The high activity and selectivity of silica supported Cu-Ni alloy catalysts agrees with the fact that the DFT calculations identified Cu-Ni alloys as highly active and selective catalysts for the hydrogenation of CO to form methanol.

This work has also provided a systematic study of Cu-Ni catalysts for methanol synthesis from syngas. The following observations have been made (1) Cu-Ni catalysts (Cu/Ni molar ratio equal to 1) supported on SiO_2, ZrO_2, γ-Al_2O_3, and carbon nanotubes exhibit very different selectivities during CO hydrogenation. However, the metal area based CO conversion rates of all supported Cu-Ni catalysts are at the same level. Carbon nanotubes and SiO_2 supported Cu-Ni catalysts show high activity and selectivity for methanol synthesis. The γ-Al_2O_3 supported Cu-Ni catalyst has a significant amount of acid sites and produces predominantly dimethyl ether. The Cu-Ni/ZrO_2 catalyst exhibits high methanol selectivity at lower temperatures (250 °C), but the selectivity shifts to hydrocarbons and dimethyl ether at higher temperatures (> 275 °C). It seems likely that the Cu-Ni alloys always produce methanol, but that some supports further convert methanol to different products. A combination of in situ XAS, XRD and TEM studies on supported Cu-Ni catalysts shows that the support influences the reduction processes and consequently the formation of Cu-Ni alloys and their CO hydrogenation properties. (2) Cu-Ni/SiO_2 catalysts have been prepared with different calcination and reduction procedures and tested in the synthesis of methanol from H_2/CO. The calcination of the impregnated catalysts (with/without calcination step) and different reduction procedures with varying hydrogen concentration have significant influence on Cu-Ni alloy formation and the alloy particle size and consequently on the catalytic activity. (3) Addition of 3 mol % CO_2 to the H_2/CO feed stream leads to a significant loss of activity for the Cu-Ni/SiO_2 catalyst contrary to the case for the Cu/ZnO/Al_2O_3 catalyst. DFT calculations show in accordance with previous surface science studies that oxygen on the surface (one of the intermediates from water gas shift reaction) could lead to an enrichment of the Ni-content in the surface. Co-fed CO_2 in the syngas should result in an increased oxidative potential of the feed, and this could cause a change of the surface composition and hence the catalytic performance. (4) Silica supported bimetallic Cu-Ni catalysts with different ratios of Cu to Ni have been prepared by impregnation. In situ reduction of Cu-Ni alloys with combined synchrotron XRD and XAS reveal a strong interaction between Cu and Ni, resulting in improved reducibility of Ni as compared to monometallic Ni. At high nickel concentrations silica supported Cu-Ni alloys form a homogeneous solid solution of Cu and Ni, whereas at lower nickel contents, copper and nickel are separately aggregated and form metallic Cu and Cu-Ni alloy phases. At the same reduction conditions, the particle sizes of reduced Cu-Ni alloys decrease with increasing in Ni content. The activity tests of Cu-Ni alloys show that all Cu-Ni alloys produce mainly methanol during CO hydrogenation regardless of the Cu/Ni ratio. The Cu-Ni alloy catalysts show similarities in the selectivity, which is mainly towards methanol (~99 mol %), while exhibiting differences in methanol productivity. The methanol productivity reaches a maximum in the molar ratio of around 1. One possibility is that the active surface structure is similar for all Cu-Ni alloys, but the number of active sites varies with respect to the ratio of Cu to Ni. (5) The effect of catalyst preparation methods has been evaluated. Silica supported Cu-Ni catalysts have been prepared via impregnation, co-precipitation, and

deposition-co-precipitation and tested for methanol synthesis. It is found that co-precipitation and deposition-co-precipitation methods are more efficient than the impregnation method for preparation of small and homogeneous Cu-Ni alloy nanoparticles. The selectivity towards methanol is always higher than 99 mol %, and the metal area based methanol formation rate over these catalysts is at the same level regardless of the preparation method. The methanol productivity increases in the order of impregnation < co-precipitation < deposition-co-precipitation. The increase in activity is predominantly caused by a decrease in particle size of the active metal alloy particles. A maximum methanol productivity of 0.66 kg kg_{cat}^{-1} h^{-1} with methanol selectivity up to 99.2 mol % has been achieved for a Cu-Ni/SiO_2 catalyst prepared by the deposition-co-precipitation method. (6) There is no apparent catalyst deactivation observed during the tested time on stream (40-100 h), contrary to the observation for the industrial Cu/ZnO/Al_2O_3 catalyst.

For higher alcohol synthesis, the main work has been performed on CO hydrogenation over supported Mo_2C. Mo_2C supported on active carbon, carbon nanotubes, and titanium dioxide, and promoted by K_2CO_3, has been prepared and tested for higher alcohol synthesis from syngas. At optimal conditions, the activity and selectivity to alcohols (methanol and higher alcohols) over supported Mo_2C are significantly higher compared to bulk Mo_2C. The CO conversion reaches a maximum, when about 20 wt % Mo_2C is loaded on active carbon. The selectivity to higher alcohols increases with increasing Mo_2C loading on active carbon and reaches a maximum over bulk Mo_2C, while the selectivity to methanol follows the opposite trend. The effect of Mo_2C loading on the alcohol selectivity at a fixed K/Mo molar ratio of 0.14 could be related to the amount of K_2CO_3 actually on the active Mo_2C phase and the size, structure, and composition of the supported carbide clusters. Unpromoted, active carbon supported Mo_2C exhibits a high activity in CO hydrogenation with hydrocarbons as the dominant products. The K_2CO_3 promoter plays an essential role in directing the selectivity to alcohols rather than to hydrocarbons. The optimum selectivity towards higher alcohols and alcohols in general is obtained at a K/Mo molar ratio of 0.21 over the active carbon supported Mo_2C (20 wt %).

Combined in situ XAS and XRD have been used to follow directly the carburization process and formation of bulk and supported molybdenum carbides (20 wt % and 40 wt % Mo_2C on active carbon). The bulk Mo_2C prepared by temperature programmed carburization in flow of 20 mol % CH_4 in H_2 most likely adopts an orthorhombic structure (α-Mo_2C). A two-step mechanism is discovered during the in situ carburization process, composed of the initial reduction of Mo(VI) oxide to Mo(IV) oxide followed by a succeeding conversion to carbide. The necessary carburization temperature is to a significant extent determined by the crystal sizes. A decrease on particle size can initiate the onset of carburization at a lower temperature.

Dansk Resume (Summary in Danish)

I dette arbejde er den katalytiske omdannelse af syntesegas til methanol og højere alkoholer blevet undersøgt. På baggrund af input fra computerbaseret katalysatorscreening er der gennemført en eksperimentel undersøgelse af lovende katalysatorkandidater til syntese af methanol fra syntesegas. Cu-Ni legeringer med forskellige sammensætninger er blevet identificeret som potentielle methanolsyntese-katalysatorer. Disse Cu-Ni legeringskatalysatorer er blevet syntetiseret og testet i CO hydrogenering i en fixed-bed flowreaktor. Aktiviteten i forhold til metalarealet for en Cu-Ni/SiO_2 katalysatorer er på samme niveau som aktiviteten for en Cu/ZnO/Al_2O_3 modelkatalysator. Den høje aktivitet og selektivitet af siliciumdioxid-bårne Cu-Ni legeringskatalysatorer stemmer overens med det faktum, at DFT-beregninger identificerede Cu-Ni legeringskatalysatorer som højst aktive og selektive katalysatorer til hydrogeneringen af CO til methanol.

Dette arbejde har også bibragt en systematisk undersøgelse af Cu-Ni katalysatorer til methanolsyntese fra syntesegas. Dette arbejde har ledt til følgende observationer: (1) Cu-Ni katalysatorer (med et Cu/Ni molforhold på 1) på bærermaterialerne SiO_2, ZrO_2, γ-Al_2O_3 og kulstof nanorør udviser meget forskellige selektiviteter i CO hydrogenering. Aktiviteten i forhold til metalarealet er imidlertid på samme niveau for alle de bårne Cu-Ni katalysatorer. Cu-Ni katalysatorer på SiO_2 eller kulstof nanorør udviser høj aktivitet og selektivitet i methanolsyntese. Cu-Ni katalysatoren på en γ-Al_2O_3 bærer har en betragtelig mægnde sure sites og producerer primært dimethylether. Cu-Ni/ZrO_2 katalysatoren udviser høj methanolselektivitet ved lavere temperaturer (250 °C), men selektiviteten skifter til kulbrinter og dimethylether ved højere temperaturer (>275 °C). Det er mest sandsynligt, at Cu-Ni legeringer altid producerer methanol, men at nogle bærermaterialer katalyserer en videre omdannelse af methanol til forskellige produkter. En kombination af in-situ XAS, XRD og TEM studier af bårne Cu-Ni katalysatorer viser at bærermaterialet påvirker reduktionsprocessen og følgelig også dannelsen af Cu-Ni legeringer og deres egenskaber i CO hydrogenering. (2) Cu-Ni/SiO_2 katalysatorer er blevet fremstillet med forskellige kalcinerings- og reduktionsbetingelser og testet i syntesen af methanol fra H_2/CO. Kalcineringen af de impregnerede katalysatorer (med/uden et kalcineringstrin) og reduktionsproceduren (ved forskellige brintkoncentrationer) har en anselig indflydelse på Cu-Ni legeringsdannelsen og på størrelsen af de legerede partikler og dermed også en effekt på den katalytiske aktivitet. (3) Tilsætning af 3 mol % CO_2 til H_2/CO-fødestrømmen fører, i modsætning til situationen for Cu/ZnO/Al_2O_3 katalysatorer, til et markant fald i aktivitet for Cu-Ni/SiO_2 katalysatorerne. I overensstemmelse med tidligere studier af overfladefænomener viser nye DFT-beregninger, at ilt på overfladen (et af mellemprodukterne i water-gas shift reaktionen) kunne fremkalde en berigelse i Ni-indholdet i overfladen. Tilstedeværelsen af CO_2 i fødestrømmen kunne lede til en forøgelse af gassens oxidative potentiale, og dette kunne medføre ændringer i overfladens sammensætning og dermed de katalytiske egenskaber. (4) Siliciumdioxid-bårne bimetalliske Cu-Ni katalysatorer med forskellige forhold mellem Cu og Ni er blevet fremstillet ved impregnering. In-situ reduktion af Cu-Ni legeringer kombineret med samtidig synchrotron XRD og XAS afslører en stærk interaktion mellem Cu og Ni, som leder til en øget reducerbarhed af Ni i forhold til isoleret Ni. Ved høje nikkelindhold danner Cu-Ni legeringer på siliciumdioxid en homogen fast opløsning af Cu og Ni, hvorimod kobber og nikkel ved lavere nikkelindhold samles separat og danner faser af både Cu-Ni legeringer og isoleret Cu. Ved fastholdte reduktionsbetingelser mindskes partikelstørrelsen af reducerede Cu-Ni legeringer med stigende Ni-indhold. Aktivitetstests af Cu-Ni legeringer viser, at alle Cu-Ni legeringer hovedsageligt producerer methanol i CO hydrogenering uafhængigt af Cu/Ni forholdet. Cu-Ni legeringskatalysatorerne udviser ligheder i selektiviteten, som hovedsageligt er til methanol (~99 mol %), men forskelle i methanolproduktiviteten. Methanolproduktiviteten når et maksimum ved et Cu/Ni molforhold på ca. 1. En mulig forklaring

er, at den afgørende overfladestruktur er ensartet for alle Cu-Ni legeringer, mens antallet af aktive sites varierer med Cu/Ni forholdet. (5) Fremstillingsmetodens indflydelse er også blevet evalueret for katalysatoren. Siliciumdioxid-bårne Cu-Ni katalysatorer er blevet fremstillet ved impregnering, samfældning, og samfældning-afsætning og testet i methanolsyntese. Det er observeret, at samfældning og samfældning-afsætning er mere effektive end impregnering i forhold til at opnå små og homogene, legerede Cu-Ni nanopartikler. Selektiviteten til methanol er altid højere end 99 mol %, og aktiviteten i forhold til metalarealet er på samme niveau uanset fremstillingsmetoden. Methanolproduktiviteten stiger i rækkefølgen impregnering < samfældning < samfældning-afsætning. Stigningen i produktiviteten skyldes primært en mindskelse af partikelstørrelsen af de aktive nanopartikler af metallegeringen. Der blev opnået en maksimal methanolproduktivitet på 0.66 $g_{MeOH}\ g_{cat}^{-1}\ h^{-1}$ og en selektivitet op til 99.2 mol % med en Cu-Ni/SiO_2 katalysator fremstillet ved samfældning-afsætning. Der er ingen observerbar katalysatordeaktivering i den undersøgte reaktionstid (40-100 timer) i modsætningen til observationerne for den industrielle Cu/ZnO/Al_2O_3 katalysator.

Med hensyn til syntesen af højere alkholer er der primært blevet arbejdet med CO hydrogenering over båret Mo_2C. Mo_2C båret på aktivt kul, kulstof nanorør og titandioxid og promoveret med K_2CO_3 er blevet fremstillet og testet i syntesen af højere alkoholer fra syntesegas. Ved optimale betingelser er aktiviteten og selektiviteten til alkoholer (methanol og højere alkoholer) for Mo_2C på en bærer markant højre end aktivitet og selektivitet for ikke-båret Mo_2C. CO omdannelsen når et maksimum, når 20 vægt % Mo_2C deponeres på aktivt kul. Selektiviteten til højere alkoholer øges med en stigende mængde af Mo_2C deponeret på aktivt kul og når et maksimum for ikke-båret Mo_2C, hvorimod methanolselektiviteten følgder den modsatte tendens. Effekten af Mo_2C-mængden på aktivt kul ved et fastholdt K/Mo molforhold på 0.14 kunne være relateret til mængden af K_2CO_3 i kontakt med den aktive Mo_2C-fase og til størrelse, struktur og sammensætning af karbidpartiklerne på bærermaterialet. Ikke-promoveret Mo_2C på aktivt kul udviser høj aktivitet i CO hydrogenering med kulbrinter som de dominerende produkter. K_2CO_3-promotoren spiller en afgørende rolle i forhold til at dirigere selektiviteten mod alkoholer i stedet for kulbrinter. For 20 vægt% Mo_2C på aktivt kul opnås den optimale selektivitet til højere alkoholer og til alkoholer i almindelighed ved et K/Mo molforhold på 0.21.

Kombineret in-situ XAS og XRD er blevet anvendt til direkte at følge karbidiseringsprocessen og dannelsen af bårne og ikke-bårne molybdænkarbider (20 vægt % og 40 vægt % Mo_2C på aktivt kul). Det er mest sandsynligt, at den ikke-bårne Mo_2C fremstillet ved temperatur-programmeret karbidisering i en strøm af 20 mol % CH_4 i H_2 antager en orthorombisk struktur (α-Mo_2C). En to-trins mekanisme er observeret under karbidiseringsprocessen. Mekanismen er sammensat af en indledende reduktion af Mo(VI) oxid til Mo(IV) oxid efterfulgt af en omdannelse til karbidet. Den nødvendige karbidiseringstemperatur er i vid udstrækning bestemt af krystalstørrelsen. En mindskelse af partikelstørrelsen kan fremkalde karbidisering ved en lavere temperatur.

Preface

This thesis is written in partial fulfillment of the requirements to obtain the Doctor of Philosophy degree at the Technical University of Denmark (DTU). This work has been carried out at the CHEC research centre at the Department of Chemical and Biochemical Engineering under the supervision of Professor Anker Degn Jensen (DTU), Professor Jan-Dierk Grunwaldt (Karlsruhe Institute of Technology, KIT), Dr. Burcin Temel (Haldor Topsøe A/S) and Dr. Jakob Munkholt Christensen (DTU).

This work has been financed by the Danish Ministry for Science, Technology and Development under the "Catalysis for Sustainable Energy" (CASE) initiative, the Technical University of Denmark, Haldor Topsøe A/S, Danscatt and X-ray absorption spectroscopy has been performed at HASYLAB at DESY, Hamburg, at ANKA at KIT, Karlsruhe, and at SNBL at ESRF, Grenoble. The corresponding synchrotron radiation sources are acknowledged for providing beamtimes and the EU for financial support of several beamtimes (Contract RII13-CT-2004-506008).

Many people have in various ways contributed to this project, and their help is gratefully acknowledged. First and foremost I would like to thank my advisors Anker Degn Jensen, Jan-Dierk Grunwaldt, Burcin Temel, and Jakob Munkholt Christensen for advice and support during this research project.

From the technical staff at the CHEC research group I thank Anders Tiedje, Mette Larsen, Lilian Beenfeldt Holgersen and Emine Yüksel Coskun for aid in the execution of the experimental work. Furthermore, I thank Trine Arndal (B.Sc.-project), Lars Lyskov Jensen (B.Sc.-project), and Winnie Eriksen (M.Sc.-project), whose projects under the supervision of Anker Degn Jensen, and/or Jakob Munkholt Christensen and myself resulted in a part of the experimental results found in this thesis.

The collaboration within the CASE Alcohol Synthesis subgroup is acknowledged. I would especially like to acknowledge the collaboration with Linus Duchstein (DTU-CEN) and Jakob B. Wagner (DTU-CEN), who performed the TEM investigations presented in this thesis, Christian Danvad Damsgaard (DTU-CEN/Physics), Christian Elkjær (DTU-Physics), Søren Dahl (DTU-Physics) and Helge Kildahl Rasmussen (DTU-Physics) for aid in XRD measurements, Gian Luca Chiarello (KIT) and Alexey Boubnov (KIT) for the setup of the in situ EXAFS/XRD experiments aid in the obtainment and analysis of the X-ray absorption spectroscopy results, and Felix Studt (SLAC and Stanford University), Frank Abild-Pedersen (SLAC and Stanford University) and Jens K. Nørskov (SLAC and Stanford University) for performance of Density Functional Theory (DFT) calculations.

I also thank the people at Haldor Topsøe A/S, who have contributed to this work, particularly Niels Christian Schiødt and Michael Brorson for fruitful discussions. Thank to Birgitte Jespersen and everyone at the synthesis lab of at Haldor Topsøe A/S for helping with experimental work. Furthermore, Haldor Topsøe A/S is gratefully acknowledged for aid in the ICP-OES elemental and sulfur capacity analyses and for providing lab facilities for part of the catalyst synthesis work.

Finally, I would like to thank my family and friends for their support during my PhD studies.

I Table of Contents

II Symbols

M_{MeOH}	Molar mass of methanol
F_{MeOH}	Molar flow rate of methanol out of the reactor.
P	Pressure
R	Gas constant
S_{Al}	Alcohol selectivity
T	Temperature
T	Time
v_0	Linear gas velocity
V_0	Volumetric flow rate
V	Volume
V_m	Molar volume
w	Weight fraction
X_{CO}	CO conversion
X_{CO_2}	CO_2 conversion
x_i	Liquid phase molar fraction of component *i*
Y_i	Yield of product *i*
y_i	Gas phase molar fraction of component *i*

III Abbreviations

BFM	Bubble flow meter
C_n-products	Products with *n* carbon atoms
DFT	Density functional theory
DME	Dimethyl ether
DEE	Diethyl ether
EDX	Energy dispersive X-ray analysis
EXAFS	Extended X-ray absorption fine structure
FID	Flame ionisation detector
FT	Fischer Tropsch (process)
FTIR	Fourier transform infrared spectroscopy
GC	Gas Chromatograph
HAS	Higher Alcohol Synthesis
ICP-OES	Inductively Coupled Plasma - Optical Emission Spectroscopy
MF(P)C	Mass flow (pressure) controller
MS	Mass spectrometry
NL	Normal litre i.e. the volume of 1 L at 273.15 K and 1 atm
STP	Standard temperature and pressure i.e. 298.15 K and 1 atm
STY	Space time yield i.e. mass of product per mass of catalyst and per time
TCD	Thermal conductivity detector
TEM	Transmission electron microscopy
TOS	Time on stream
TPR	Temperature programmed reduction
WGS	Water gas shift
XANES	X-ray absorption near edge structure
XAS	X-ray absorption spectroscopy
XPS	X-ray photoelectron spectroscopy
XRD	X-ray diffraction

IV Incorporated publications

Publication in journal with peer review (1)

F. Studt, F. Abild-Pedersen, **Q. Wu,** A. D. Jensen, B. Temel, J. D. Grunwaldt, J. K. Nørskov. *CO hydrogenation to methanol on Cu-Ni Catalysts: Theory and Experiment, J. Catal.* 293, 2012, 51.

Manuscript has been submitted to peer reviewed journals (1)

Q. Wu, J. M. Christensen, G. L. Chiarello, L. D. L. Duchstein, J. B. Wagner, B. Temel, J. D. Grunwaldt, A. D. Jensen, *Supported molybdenum carbides for higher alcohol synthesis from syngas, submitted to Catal. Today 2012.*

Manuscripts nearly ready for submission to peer reviewed journals (5)

Q. Wu, G. L. Chiarello, L. D. L. Duchstein, J. M. Christensen, J. B. Wagner, B. Temel, J. D. Grunwaldt, A. D. Jensen, *CO hydrogenation on Cu-Ni catalyst: Effect of support and XAS investigations*, to be submitted soon.

Q. Wu, G. L. Chiarello, J. M. Christensen, B. Temel, A. D. Jensen, J. D. Grunwaldt, *Simultaneous in situ XRD and XAS on the formation of bulk and supported molybdenum carbides*, to be submitted soon.

Q. Wu, Winnie L. Eriksen, J. M. Christensen, Christian D. Damsgaard, B. Temel, J. D. Grunwaldt, A. D. Jensen, *CO hydrogenation to methanol on Cu-Ni catalyst: Effect of catalyst preparation methods*, to be submitted soon.

Q. Wu, F. Studt, L. D. L. Duchstein, G. L. Chiarello, J. M. Christensen, C. F. Elkjær, C. D. Damsgaard, J. B. Wagner, S. Dahl, B. Temel, J. D. Grunwaldt, A. D. Jensen, *CO hydrogenation on Cu-Ni catalysts: Influence of catalyst pretreatment and feed composition,* to be submitted soon.

Q. Wu, L. D. L. Duchstein, Winnie L. Eriksen, J. M. Christensen, G. L. Chiarello, Christian D. Damsgaard, J. B. Wagner, B. Temel, J. D. Grunwaldt, A. D. Jensen, *In situ observation of Cu-Ni alloy nanoparticle formation via XAS, XRD, and TEM: Effect of Cu/Ni ratio and their catalytic properties,* to be submitted soon.

Participation in international conferences and schools (6)

1. Abstract 1: '*Novel highly active and selective Cu-Ni based methanol synthesis catalyst*' Abstract 2: '*Higher alcohols synthesis from syngas over carbon-nanotube supported iron-chromium catalysts*'; The 15th International Congress on Catalysis (ICC), 01.07.2012-06.07.2012, Munich, Germany (Poster presentation).
2. Abstract 3: '*Active carbon supported molybdenum carbides for higher alcohols synthesis from syngas*'; SynFuel 2012, 29.06.2012-30.06.2012, Munich, Germany (Poster presentation).
3. Abstract 4: '*Supported molybdenum carbides for higher alcohols synthesis from syngas*'; The 242nd ACS National Meeting: Chemistry of Air, Space, and Water, 28.8.2011-2.9.2011, Denver, USA (Oral presentation).
4. Abstract 5: '*Supported Cu/Group VIII metal alloys for synthesis of alcoholic fuels from syngas*'; The 22nd North American Catalysis Society Meeting (NAM), 5.6.2011-10.5.2011, Detroit, USA (Oral presentation).
5. The International SPECTROCAT-2010 Summer School, 19.7.2010-23.7.2010, Caen, France.
6. European Graduate School on Sustainable Energy - The Molecular Approach, 7.4.2010-9.4.2010, Freising, Germany.

1 Introduction

1.1 Initiative: Catalysis for sustainable energy

The rapid global development over the last century is based on easy-access to inexpensive fossil fuels, and this era will eventually come to an end [1]. The demand for energy around the world is growing rapidly [2]; meanwhile, it is obvious that the emission of CO_2 that follows the use of fossil fuels is threatening the climate of the earth [3, 4]. Arguably this makes the development of sustainable energy solutions the most scientific and technical challenge of our time. The former Danish Minister of Science Helge Sander has granted DKK 120 million to scientists at the Technical University of Denmark. The funding is used to support development of novel methods for converting sustainable energy from the sun, biomass and wind into fuel under the "Catalysis for Sustainable Energy (CASE)" initiative [5]. This Ph.D. project is among one of the sustainable approaches – 'Fuel synthesis from biomass-derived syngas'. The present project is built on the following two aspects:

i. Combination of experimental and computational catalyst screening.

Suitable reference systems have been prepared and tested for benchmarking in syngas conversion. Meanwhile, a rational design of possible catalysts has been performed by computational methods and has been directly linked with the synthesis of the proposed catalyst candidates. Then it has been followed by catalyst testing, and use of the resulting experimental data as input to more detailed calculations, i.e. development of an integrated experimental and computational catalyst discovery process [5]. This approach is illustrated schematically in Fig. 1-1.

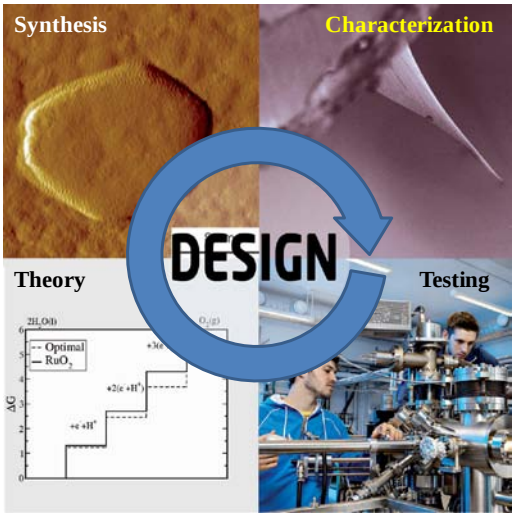

Fig. 1-1 Illustration of the approach to catalyst development applied in the CASE initiative [5].

ii. Structure-activity relationship by electron microscopy, in situ diffraction and spectroscopy.

Clearly, state-of-the-art electron microscopy, diffraction and spectroscopic methods play a significant role in the establishment of structure-activity relationships for reaction at catalytic surfaces [5]. Therefore, comprehensive characterization techniques such as X-ray diffraction (XRD) and X-ray absorption spectroscopy (XAS) have been applied for catalyst structure determination under simulated reaction conditions. This information is then fed back into catalyst synthesis and theoretical understanding.

1.2 Focus of project

In this project, focus has been on the production of methanol and to a lesser extent higher alcohols from synthesis gas or syngas, a mixture of CO and H_2, sometimes with a small amount of CO_2. Theoretic (density functional theory, DFT) and experimental screening (catalyst synthesis, testing and characterization) have been combined for developing catalysts for methanol and higher alcohol syntheses.

For methanol thesis, the focus has been on Cu/Ni-based catalysts. Studt and coworkers [6, 7] at Stanford University have performed DFT calculations for CO hydrogenation on different transition metal surfaces. Based on the calculations, trends have been established over the different surfaces and scaling relations of adsorbates and transition states that link their energies to only two descriptors, the carbon and oxygen binding energies, have been constructed. A microkinetic model of CO hydrogenation has been solved as a function of the values of the two descriptors and a volcano shaped relation for methanol synthesis is obtained. A large number of bimetallic alloys have been screened with respect to the two descriptors and Cu/Ni alloys have been identified as potential candidates for methanol synthesis. Cu/Ni alloys have been prepared and tested. The following systematic studies on the Cu/Ni catalyst system have been carried out with this project:

i. DFT calculations and experimental activity investigation;

ii. Effect of supports: carbon nanotubes (CNT), ZrO_2, SiO_2 and Al_2O_3;

iii. Effect of Cu/Ni ratio;

iv. Effect of pretreatment of catalysts such as calcination and reduction;

v. Effect of operating conditions: temperature and CO_2-cofeeding;

vi. Effect of preparation method: incipient wetness impregnation, co-precipitation and deposition-co-precipitation.

In addition, in situ XAS, XRD, transmission electron microscopy (TEM) and Fourier transform infrared spectroscopy (FTIR) as well as DFT calculations have been combined for establishing the structure-performance relationship for Cu/Ni catalysts.

For higher alcohol synthesis (HAS), the focus has been on molybdenum carbide based catalysts and CNT supported Fe-Cr catalysts. The study of supported molybdenum carbide based catalyst was based on the work previously done by Christensen et al. from our group on higher alcohol synthesis over bulk molybdenum carbide [8]. Molybdenum carbide on different supports such as active carbon, TiO_2 and CNT have been prepared and tested for improving the activity of the carbide catalysts. Combined in situ XAS with XRD have been used to follow directly the carburization process and the formation of bulk and active carbon supported molybdenum carbide. The aim of these studies was to determine the carburization mechanism, the temperature, as well as the differences in structure and catalytic properties between bulk and supported molybdenum carbides. Regarding Fe-Cr/CNT catalyst, the main work has been done within a bachelor project by Trine Arndal and Lars Lyskov Jensen, under the supervision of Anker Degn Jensen and myself. The preliminary results have been presented at the 15th International Congress on Catalysis in Munich, 2012. The abstract entitled *'Higher alcohols synthesis from syngas over carbon-nanotube supported iron-chromium catalysts'* can be found in the Appendix H of this thesis. The detailed information can be obtained from the bachelor thesis entitled '*Synthesis of higher alcohols from syngas using carbon nanotube supported catalysts*' by Arndal and Jensen (June, 2011, DTU) [9].

1.3 Structure of thesis

The thesis is predominantly a compilation of the papers and manuscripts presented in section IV. Below the main contents in each chapter in this thesis is summarized:

Chapter 1 "Introduction" presents the initiative and focus of this Ph.D. project, as well as the structure of thesis, and offers a general background of this project.

Chapter 2 "The catalytic conversion of syngas into methanol and higher alcohols" provides a general background for syngas production and conversion, methanol synthesis and higher alcohol synthesis. There are many reviews in the fields of syngas production and conversion, methanol synthesis and higher alcohol synthesis, and hence this part is kept relatively brief.

Chapter 3 "Experimental work" provides mainly a general description of the high pressure reactor used for the catalyst testing work in this project and a brief introduction of catalyst preparation, characterization, and testing. The details of catalyst preparation, characterization, and testing can be found in the subsequent chapters.

Chapter 4 is the main body of the paper "*CO hydrogenation to methanol over Cu/Ni catalysts: Theory and experiments*" published in Journal of Catalysis (2012).

Chapter 5 is the main body of the manuscript "*CO hydrogenation over Cu/Ni catalysts: Influence of support*", which is about to be submitted.

Chapter 6 is the main body of the manuscript "*CO hydrogenation on Cu/Ni catalysts: Influence of catalyst pretreatment and feed composition*", which is about to be submitted.

Chapter 7 is the main body of the manuscript "*CO hydrogenation on Cu/Ni catalysts: Influence of preparation methods*", which is about to be submitted.

Chapter 8 is the main body of the manuscript "*In situ observation of Cu/Ni alloy nanoparticle formation by XRD, XAS, and TEM: Influence of Cu/Ni ratio and their catalytic properties*", which is about to be submitted.

Chapter 9 is the main body of the manuscript "*Supported molybdenum carbides for higher alcohol synthesis from syngas*", which has been submitted to Catalysis Today (2012).

Chapter 10 is the main body of the manuscript "*Simultaneous in situ XANES and XRD on formation of bulk and supported molybdenum carbides*", which is about to be submitted.

Chapter 11 provides a general conclusion for this Ph.D. project.

Chapter 12 presents suggestions for further work that might be helpful for improving the studied Cu-Ni and molybdenum carbide systems for alcohol synthesis.

In addition, there are appendixes, which are supporting information for corresponding papers or manuscripts and the abstracts that have been presented in international conferences during my Ph.D. study (listed in section IV).

2 The catalytic conversion of syngas into methanol and higher alcohols

This section will provide background information for the present study, including a brief introduction to syngas production and conversion, and to methanol and higher alcohol syntheses. A significant number of general review articles and book chapters are available for syngas production and conversion [10-17], as well as for methanol and higher alcohol syntheses [17-34]. Here a summary of the catalyst systems that have been reported in the literature for methanol synthesis and higher alcohol synthesis, and their performances and other issues are given. In addition, this thesis has mainly focused on Cu/Ni based catalysts for syngas conversion. Hence, a literature review of the use of Cu/Ni catalysts for CO/CO_2 hydrogenation forms an individual section in this chapter. Regarding the detailed information of the catalyst systems for methanol and higher alcohol syntheses the reader is referred to the above mentioned reviews and books.

2.1 Syngas production and conversion

Syngas may be obtained from renewable sources such as biomass and organic waste via gasification [35-41], although syngas is presently produced predominantly via steam reforming of natural gas [13, 14, 17] and partly from coal gasification [42-45]. The syngas production refers to a series of processes, including gasification/reforming, gas cleaning, and gas conditioning (Fig. 2-1).

Syngas can be converted to H_2 by the water-gas shift (WGS) reaction for ammonia synthesis and can also be directly converted to liquid fuels such as methanol, DME, FT diesel/gasoline, and mixed long chain alcohols, as depicted in Fig. 2-1. An alternative to gasoline is alcohols such as methanol, ethanol, propanol and butanol, either alone or as gasoline additives [21, 24, 27, 28, 46, 47]. Diesel may be substituted by ethers derived from the alcohols, such as dimethyl ether (DME) and diethyl ether (DEE) [48, 49]. Here, focus is only on methanol and higher alcohol syntheses, which will be described in detail in the next two sections.

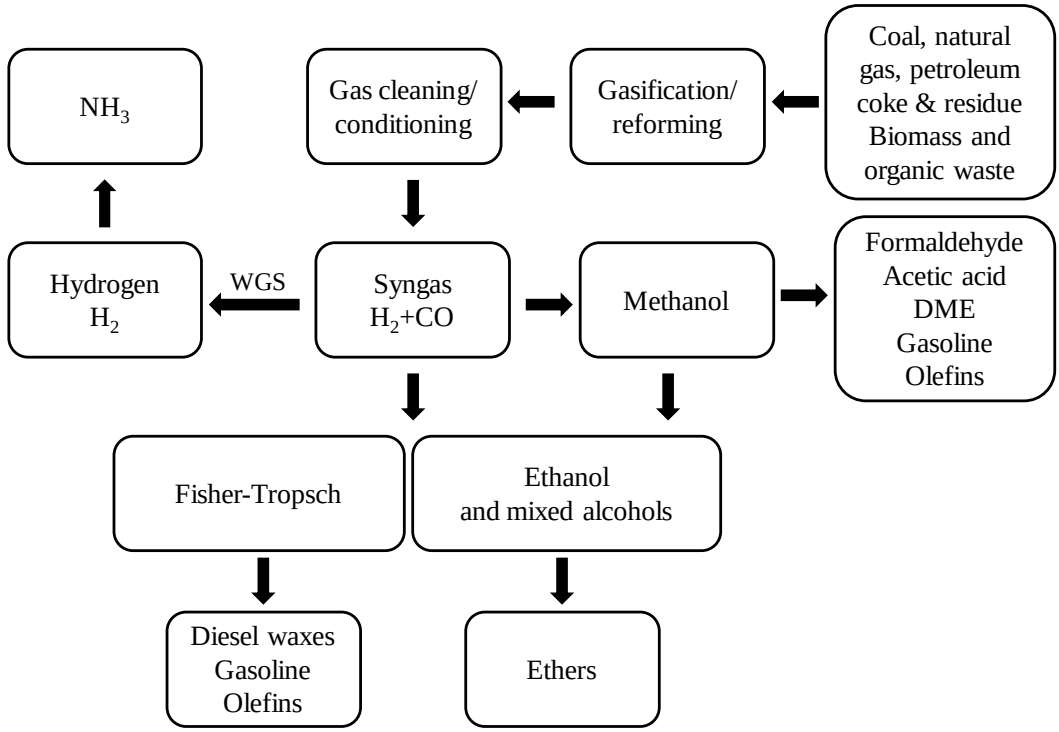

Fig. 2-1 Syngas production and conversion derived from references [14, 16, 17, 36]

2.2 Methanol synthesis

Methanol is one of global top ten petrochemicals, with a worldwide demand about 50 million tons per year, and experiences a strong annual growth in production [17, 24]. The main use of methanol is in the production of chemicals such as formaldehyde and acidic acid as well as in the production of various olefins for the polymer industry [49]. In addition, methanol is an excellent fuel in an internal combustion engine and it can also be blended with gasoline as an octane booster [50, 51]. It can be used in the direct methanol fuel cell (DMFC), where methanol can be converted to carbon dioxide and water to produce electricity [52-54]. Methanol can also be converted to gasoline via a methanol-to-gasoline process with acidic zeolite catalysts [55, 56]. Methanol has therefore been suggested as a main energy carrier for the future [47, 50, 57]. Despite the very high current level of methanol production, the replacement of gasoline would require more than a hundredfold increase in methanol production [50].

Methanol synthesis was commercialized by BASF in the 1920's [58]. It was carried out as a high temperature (400 °C) and high pressure (100-200 bar) process over ZnO/Cr_2O_3 catalysts. Although copper-based catalysts have been found to be highly active and selective catalysts during the 1920-1930's [59, 60], the ZnO/Cr_2O_3 catalysts remained the choice as industrial catalysts due to their better stability against poisons such as chlorine, sulfur and Fe and Ni carbonyls, which could not practically be removed to a suitable low level at that time [61]. In 1960's, improvement of syngas cleaning process renewed the attention to copper-based catalysts for methanol synthesis [18]. A low temperature (220-300 °C) and moderate pressure (50-100 bar) process over $Cu/ZnO/M_2O_3$ (M=Al or Cr) catalysts has been developed by industry, principally by Imperial Chemical Industries, Ltd. (ICI) [62, 63]. These catalysts are more active and can be operated at less demanding conditions. The space time yield (STY) or productivity of methanol is about 1 kg L^{-1} h^{-1}, which has been claimed to be the required productivity for commercial methanol synthesis [25].

Although the commercial Cu/ZnO-based catalysts are rather long lived, 3 years or more, they do deactivate via poisoning or sintering processes and deactivation thus poses one of the biggest challenges for the copper-based catalysts [18]. More than one-third of the activity is lost after the first 1000 h of operation for this catalytic system [18, 24, 64-66]. Development of alternative methanol synthesis catalysts with better stability and activity has been of great interest, and a number of elements such as Cs [67], Th [68], Zr [69, 70], Ce [71], Mn [72], Ga [73], and Pd [73, 74] have been investigated as possible replacements or additives to enhance the catalytic performance of Cu/ZnO-based methanol synthesis catalysts. Several catalyst systems have been investigated for their potential in converting syngas to methanol, such as:

i. Th/Cu-based catalysts [18, 68, 75];

ii. Ce/Cu-based catalysts [71, 76];

iii. Zr/Cu-based catalysts [18, 69, 70, 77];

iv. Alkali(K, Rb, Cs)/Pd/support catalysts [74, 78-82];

v. Mo_2S-based catalysts [83-87];

vi. Homogenous catalysts for methanol synthesis in the liquid phase [88-93].

Table 2-1 presents operating conditions and performances of selected methanol synthesis catalysts reported in the literatures.

Th/Cu-based catalysts with different Cu/Th molar ratio (2/1, 1/2, 1/3.6, and 1/6) have been developed for methanol synthesis in 1980s [18, 68, 75]. The active component is suggested to be

Cu_2O on thorium oxide [75]. $ThCu_6$ was the most active catalysts for methanol synthesis from CO_2-free syngas. This catalyst was more active than the commercial Cu/ZnO catalyst under the same reaction conditions [18]. The productivity of methanol over the $ThCu_6$ catalyst can reach 3.55 kg L^{-1} h^{-1} with 44.5% CO conversion at H_2/CO=2.4, 61 bar, 250 °C, and GHSV=22000 h^{-1}. The selectivity to methanol reaches up to 82 mol % with equal amount of methane and CO_2 as by-products [18]. It should be stated that thorium is a radioactive component, which is not desirable in catalysts for a chemical plant.

Ce/Cu-based catalysts have been developed by ICI for CO hydrogenation [76]. The composition was varied between $CeCu_{1.3}$ and $CeCu_{3.2}$, and the principle product was methanol (76-98 mol % selectivity to methanol) at the operating conditions of H_2/CO=1, 10 bar, 125-240 °C and GHSV=6000h^{-1}. The STY of methanol over $CeCu_2$ reached up to 1.52 kg kg^{-1} h^{-1} at H_2/CO=1, 50 bar, 240 °C and GHSV=72000 h^{-1} [76]. However, Ce/Cu catalysts had poor high temperature stability and deactivated in the presence of CO_2. In addition, rare earth metals like La, Pr, Nd, Gd, and Dy have been used to replace Ce, all these catalysts showed activity for methanol synthesis, but less activity than the Ce/Cu catalysts. It was also found that 1-2 vol % CO_2 in syngas over Ce/Cu catalysts caused deactivation of the catalysts, which appeared to be irreversible [76]. This discovery is quite different from the conventional Cu/ZnO/Al_2O_3 methanol synthesis catalyst, where CO_2 can promote the reaction rate significantly [76].

Zr/Cu-based catalysts prepared by co-precipitation method have been tested for methanol synthesis at H_2/CO=4, 50 bar, 160-330 °C and GHSV=17100 h^{-1} [18]. CuO and ZrO_2 prepared by co-precipitation exhibit no activity for CO conversion after reduction [18]. The CO conversion was a function of the copper content in ZrO_2, and a maximum CO conversion at about 6% was observed for 40-70 wt % CuO for a carbonate precipitated catalysts and at about 8% for 20-40 wt % CuO for a urea precipitated catalysts. It was found in other studies that amorphous precursors of Cu-rich Cu/Zr mixtures yielded better catalyst than the one from crystalline precursors. Crystalline Cu_2Zr [76] and Cu_7Zr_3 [70] were poor catalysts, but amorphous Cu_7Zr_3 yielded a catalyst that showed appreciable activity for methanol synthesis. Loading 5 wt % CuO on ZrO_2, and pretreating in O_2 for 2 h at 300 °C, yielded a catalyst with a methanol productivity up to 0.4 kg kg^{-1} h^{-1} at H_2/CO=0.1, 32 bar, 300 °C and GHSV=30000 h^{-1}. Adding 5 wt % ZnO into the 5 wt % CuO/ZrO_2 catalyst slightly increased the methanol productivity to 0.43 kg kg^{-1} h^{-1} [77].

Alkali promoted Pd/support catalysts have been tested for CO hydrogenation and methanol was observed to be the main product [74, 80]. It has been found that the specific activity of methanol increases in the order of Pd/SiO_2 = Pd/Al_2O_3 < Pd/TiO_2 < Pd/MgO = Pd/ZnO < Pd/ZrO_2< Pd/La_2O_3 [18]. The alkali promotion effect on activity is observed to be Li > Na >> unpromoted > K = Rb = Cs, with little methanol produced over the (K, Rb, Cs)/Pd/support catalysts [82, 94]. Productivities of methanol have been reported in the range of 0.06-0.16 kg L^{-1} h^{-1}, i.e. much lower than the industrial catalysts.

Unpromoted Mo_2S catalysts mainly produced methane and long chain hydrocarbons [18, 95], whereas the sulfide produced mainly methanol, when it is promoted by a proper amount of alkali such as K. The methanol selectivity was typically in the range of 30-60 mol % [83-87]. Christensen et al. [96] found that both methanol selectivity and productivity increased with increased H_2 concentration in the feed gas over an active carbon supported K_2CO_3/Co/MoS_2 catalyst. The methanol productivity reached up to 0.19 kg kg^{-1} h^{-1} with a methanol selectivity of 66.4 mol % at H_2/CO=5.83, 100 bar, 326 °C, and GHSV=2600 h^{-1}.

Table 2-1 Operating conditions and performances of selected methanol synthesis catalysts reported in the literature.

Catalysts	T [°C]	P [bar]	H_2/CO [mol/mol]	Feed CO_2 [mol %]	GHSV [h^{-1}]	CO conv. [%]	MeOH selectivity [mol %]	STY_{MeOH} [kg $L^{-1}(kg^{-1})$ h^{-1}]	Refs
$Cu/ZnO/Al_2O_3$	230	21	8	10	3600	-	100	0.85	[97]
$Cu/ZnO/Al_2O_3$	250	100	1	no	16000	7.2	99.0	0.84	[6]
$Cu/ZnO/Al_2O_3$	250	65	2	3	32000	11.5	99.7	1.71	[98]
$Cu/Mn/ZnO/Al_2O_3$	230	21	8	10	3600	-	100	0.97	[97]
$Cs/Mn/ZnO/Cr_2O_3$	400	104	1	no	-	15	87	0.15	[99]
Th/Cu_6	180-250	61	2.4	-	22000	13-44.5	up to 82	1.04-3.55	[18]
$K/Co/Mo_2S/C$	326	100	5.83	-	2600	44.8	66.4	0.19	[96]
$5\%CuO/ZrO_2$	300	32	0.1	no	30000	-	-	0.4	[77]
Ce/Cu	240	50	1	no	72000	-	-	0.36-1.52	[76]
Pd/SiO_2	260-350	5-110	1-3	no	-	-	up to 98	0.06-0.16	[82, 94]

Homogenous liquid phase catalysts based on Cu, Ni, Ru, Co, Rh complex etc. have been developed for methanol synthesis [88-93]. For example, Li and Jiang developed the $Ni(CO)_4$/KOMe catalytic system, and the methanol productivity reached to 0.13 kg L^{-1} h^{-1} at 18 bar, and 125 °C.

It seems that all these developed methanol synthesis catalysts are not sufficiently selective and/or active compared to the commercial Cu/ZnO catalysts. In this Ph.D. project, the focus has been on methanol synthesis over Cu/Ni-based catalysts and the conventional $Cu/ZnO/Al_2O_3$ methanol synthesis catalysts have been used for comparison. Hence, the composition, reaction mechanism, industrial application and catalyst deactivation of the conventional $Cu/ZnO/Al_2O_3$ methanol synthesis catalyst is briefly discussed in the following sections.

2.2.1 Cu/ZnO-based methanol synthesis catalyst

Methanol synthesis is a well-established process with $Cu/ZnO/Al_2O_3$ catalysts over the last 50 years [32]. Metallic copper itself is often reported to exhibit a relatively low activity for methanol synthesis [18]. ZnO also exhibits low activity for methanol synthesis [59, 60, 100, 101]. Frolich et al. [59, 60] found that Cu/ZnO binary mixtures were much more active than both Cu and ZnO. It seems that there is strong synergetic effect between Cu and ZnO. This effect has been suggested, for example, through the formation of a Cu-Zn surface alloy or ZnO species on the Cu surface [102-106], stabilization of meta-stable copper metal particle structure by ZnO [107] and metallic copper particles with morphology dynamically controlled by the ZnO [108-110], oxidized copper stabilized by ZnO [18, 111], and electronic junction effects at the Cu/ZnO interface [112]. An addition of component such as Cr_2O_3 and Al_2O_3 has been used to improve the activity and stability for the Cu/ZnO catalysts [113-117]. It was also reported that the presence of oxide can increase the copper surface area [117]. Moreover, it was found that a small amount of CO_2 can improve the stability, activity and selectivity of the Cu/Zn-based catalysts for methanol synthesis [18, 118, 119]**.** Therefore, the binary Cu/ZnO (> 50 mol % Cu) system serves as a model system for industrially applied catalysts, which usually contain 5-10 mol % Al_2O_3 [102, 115]. The operating conditions for $Cu/ZnO/Al_2O_3$ catalysts are at 220-300 °C, 50-100 bar, with a H_2/CO ratio of 2 or even higher, together with a small amount of CO_2 [32, 120].

2.2.2 Reaction and mechanism

For the commercial $Cu/ZnO/Al_2O_3$ catalyst, a small amount of CO_2 is generally co-fed for improving both activity and selectivity to methanol [118, 119]. It was found that the presence of CO_2 can significantly increase the durability of the catalyst, and in the absence of CO_2 the catalysts have lower initial activity and deactivate at a rather rapid rate [18].

On the basis of kinetic investigations and ^{14}C-labelling experiments Kagan et al. [121-124] determined that CO_2 is the dominant source of carbon in methanol formed over a commercial copper catalyst. Using ^{14}C-labelling experiments Chinchen et al. [118, 125] arrived at the same conclusion. Moreover, DFT calculations by Grabow and Mavrikakis [126] recently suggested that CO_2 hydrogenation is responsible for ca. 2/3 of the methanol synthesis at typical industrial methanol synthesis conditions, and therefore suggested that methanol synthesis involves two processes: hydrogenation of CO (R1) and hydrogenation of CO_2 (R2):

$$CO + 2H_2 \rightleftarrows CH_3OH \qquad \text{(R1)}$$

$$CO_2 + 3H_2 \rightleftarrows CH_3OH + H_2O \qquad \text{(R2)}$$

The WGS reaction (R3) should be considered as well.

$$CO + H_2O \rightleftarrows CO_2 + H_2 \qquad \text{(R3)}$$

For CO_2 hydrogenation Rasmussen et al. [127, 128] suggested following reaction mechanism, R4-R16:

$$H_2O_{(g)} + * \rightleftharpoons H_2O* \quad \text{(R4)}$$

$$H_2O* + * \rightleftharpoons OH* + H* \quad \text{(R5)}$$

$$2OH* \rightleftharpoons H_2O* + O* \quad \text{(R6)}$$

$$OH* + * \rightleftharpoons O* + H* \quad \text{(R7)}$$

$$2H* \rightleftharpoons H_{2(g)} + 2* \quad \text{(R8)}$$

$$CO_{(g)} + * \rightleftharpoons CO* \quad \text{(R9)}$$

$$CO* + O* \rightleftharpoons CO_2* + * \quad \text{(R10)}$$

$$CO_2* \rightleftharpoons CO_{2(g)} + * \quad \text{(R11)}$$

$$CO_2* + H* \rightleftharpoons HCOO* + * \quad \text{(R12)}$$

$$H* + HCOO* \rightleftharpoons H_2COO* + * \quad \text{(R13)}$$

$$H_2COO* + H* \rightleftharpoons H_3CO* + O* \quad \text{(R14)}$$

$$H_3CO* + H* \rightleftharpoons CH_3OH* + * \quad \text{(R15)}$$

$$CH_3OH* \rightleftharpoons CH_3OH_{(g)} + * \quad \text{(R16)}$$

Where, an asterisk (*) denotes a free site on the surface of the catalyst and X* denotes species X adsorbed on the surface of the catalyst. Reactions R4 to R11 describe the mechanism for the WGS reaction [129], while the reactions R12 to R16 account for hydrogenation of CO_2 to methanol [127, 128]. Kinetic modelling studies indicate that the hydrogenation of dioxymethylene (R14) is probably the rate determining step for CO_2 hydrogenation, while CO oxidation (R10) is the rate limitation step for WGS reaction [127, 128]. On the basis of the above kinetic model, with steps R10 and R14 as rate limiting steps, and with the remaining steps in dynamic equilibrium, Askegaard et al. [30] have derived the rate expression:

$$r = k\ p_{CO_2} p_{H_2}^{3/2} \left(1 - \frac{1}{K_{eq}} \frac{p_{CH_3OH} p_{H_2O}}{p_{CO_2} p_{H_2}^{3}}\right) \theta_*^{2}$$

Where k is a constant composed of equilibrium and rate constants for the elementary reactions above, K_{eq} is the overall equilibrium constant for reaction R2, and $\theta*$ is the fraction of free sites on the surface.

2.2.3 Industrial application

In 1963, ICI developed the low pressure methanol synthesis technology (Cu/ZnO) [32] instead of the high pressure methanol synthesis technology (ZnO/Cr_2O_3), developed by BASF in 1923. The new catalyst and process become very popular and has been very popular and has been adopted by a number of industries over the last 50 years.

A typical methanol synthesis process technology from natural gas involves several common steps, they are: (1) feed purification, (2) steam reforming, (3) syngas compressing, (6) catalytic synthesis, (5) crude methanol distillation, and (5) recycle and recovery [24, 32]. The process design varies depending on the availability of types of feedstock, local energy economy, and process energy efficiency [32]. A number of methanol synthesis processes have been developed by industries such as ICI, Haldor Topsøe A/S, and Lurgi Öl-Gas-Chemie GmbH. The details of these processes can be found in ref [120].

2.2.4 Catalyst deactivation

Although the commercial $Cu/ZnO/Al_2O_3$ catalysts are rather long lived, e.g. 3 years or more, they do deactivate via poisoning or sintering processes and deactivation poses one of the biggest problems [18, 24, 64]. More than one-third of the activity is lost after the first 1000 h of operation [18, 24, 130]. During the industrial methanol production process a high methanol yield is maintained by gradually increasing the reactor temperature as the catalyst ages and loses its activity [18]. However, there is a limit to how high the temperature can be raised because the sintering rate of the metallic Cu component increases with temperature as well. Furthermore, the yield of by-products increases as well, when temperature is increased. The increased sintering rate and the increased by-products formation are undesired effects.

One of the predominant paths to catalyst deactivation is the sintering of metallic Cu, which reduces the area of the active copper surface [66, 131-133]. In CO_2-free H_2/CO syngas, the $Cu/ZnO/Al_2O_3$ catalyst undergoes rapid deactivation. This is probably due to the formation of brass in the highly reducing H_2/CO gas atmosphere. The brass formation has been related to a decreasing of WGS activity [134].

Sulfur, chlorine, and carbonyls of iron and nickel have been reported as poisons to the Cu/ZnO-based methanol synthesis catalysts [18]. The poisoning effect of sulfur is attributed to the blocking of active sites [64, 135]. Wood et al. [136] poisoned the catalysts by sulfur in the form of H_2S and COS and found that H_2S poison the catalysts significantly while COS has no effect on the catalysts. Klier and Herman [137] even observed that COS has a promoting effect at a low level. The presence of chlorine such as HCl accelerates the sintering of copper due to a high mobility of CuCl species [116]. Furthermore, ZnO is converted into $ZnCl_2$, which has a lower melting point and hence cause faster sintering of the catalyst. Carbonyls of iron and nickel form, from the reaction of CO and steel tubes at low temperature, and may deposit metals on the surface of the catalyst [64, 65, 138]. It is known that Fe and Ni are efficient catalysts for FT synthesis [139-141] leading to a decrease of methanol selectivity, and the formation of long chain wax and paraffin products that could block the pore structure of the methanol synthesis catalyst. Additionally, catalyst fouling by carbon deposition also deactivates the catalysts gradually [135, 142]. In conclusion, methanol synthesis catalysts with greater stability are thus highly desired.

2.3 Higher alcohol synthesis

The synthesis of higher alcohols is particularly attractive because these compounds can be used directly as fuels without additional processing. Higher alcohols are more attractive than methanol because they have a lower vapor pressure, higher tolerance of water, better solubility with hydrocarbons, higher overall heating value, and higher commercial value [46].

Currently, higher alcohols like ethanol are mainly produced by two processes. Firstly, fermentation of sugars that derive from sugarcane or corn/maize [143-145]; secondly, hydration of ethylene produced from petroleum [146]. Fermentation can interfere with the food suppliers such as

corn/maize and sugarcane. Additionally, Crutzen et al. [147] found that the corn-ethanol production process could emit nitrous oxide that contributes to global warming as well. Ethylene hydrogenation is a proven industrial process, but still relies on petroleum-derived ethylene. There is therefore a drive for developing new methods to meet the increasing fuel demand in the future. One alternative approach is to convert carbon-feedstock such as biomass or organic waste to syngas, which may then be further converted to higher alcohols.

In 1913, BASF acquired the first patent for higher alcohol synthesis (HAS) from syngas [17]. Later in 1923, Fischer and Tropsch found that alkali promoted Fe catalysts can produce alcohols [46]. Then it was recognized that higher alcohols were by-products of both processes of Fischer-Tropsch (FT) and methanol synthesis when catalysts or conditions were not optimal [46]. HAS can be improved by adding alkali metals and increasing operating temperature and pressure over these catalysts. From 1927 to 1945, plants were in operation for HAS in the US and Germany [30]. However, these plants were shut down due to the increasing petroleum production and the desire for neat alcohols for manufacturing chemicals [30]. The HAS received renewed attention in the 1970s, due to the oil crisis. Therefore, some industrial pilot plants were built for HAS in the 1980's such as Enichem-Snamprogetti-Haldor Topsøe (ESHT), which could produce 15000 ton/year of higher alcohols from syngas. Table 2-2 lists the scale of development for various HAS processes. Institut Francais Du Petrole (IFP) has a number of patents [148-154] for HAS using Cu/Co catalysts promoted by many transition metals including Cr, Zn, Mn, Fe, etc. together with alkali and alkaline earth metals such as Li, Na, K, Cs, and Ca. The process with Cu/Co-based catalysts produced C_1-C_7 linear mixed alcohols, and the higher alcohol selectivity is in the range of 20 and 70 wt %. The IFP process reached a level of 7000 bbl/y in a pilot plant in Chiba, Japan [16]. IFP also tested Cu/Ni based catalysts (promoted by K with additives such as Zn, Mn, and Ti) for higher alcohol synthesis at moderate operating temperature (310-315 °C) and pressure (60-80 bar). The Cu/Ni based catalysts yielded good and stable performance over a period of 400 h. For the Cu/Ni based catalysts a slight increase of higher alcohol content was observed when operating pressure was increased [155]. The HAS lost its attraction again in the late 1980s because of the decreasing oil prices [27]. Dramatically, history has repeated that of 1980s, HAS is becoming attractive again today because of high oil prices, more stringent environmental requirements and politic climates. Recently, the Institute of Coal Chemistry, Chinese Academy of Sciences [156] developed a novel technology that uses a new copper and iron based catalyst at a temperature of 200-260 °C, pressure of 40-60 bar. CO conversion rate reached up to 80%, with 50% higher alcohol selectivity, and a space time yield of alcohols more than 0.23 kg $kg^{-1}(L^{-1})$ h^{-1}. However, no details have been reported in the literature. Most recently, a patent from Haldor Topsøe A/S [157] has been issued regarding a new process for HAS over alkali modified Cu/ZnO-based methanol synthesis catalyst. In this process, adding an amount of methanol and higher alcohols to the syngas feed the yield of higher alcohols can to some extent be increased. Until now, none of the HAS catalysts have been sufficiently active and/or selective to meet the requirements of industry and currently there are therefore no commercial plants that produce higher alcohols from syngas [34].

Herein, short literatures review of the catalysts for HAS from hydrogenation of CO or CO_2 will be presented. The catalysts can broadly be grouped into four categories [18, 19, 21, 27-29]:

i. Modified methanol synthesis catalysts: alkali-doped ZnO/Cr_2O_3 catalysts [99, 158-167] and alkali-doped Cu/ZnO and $Cu/Zn/Al_2O_3$ catalysts [19, 168-173];

ii. Alkali modified FT catalysts: alkali-doped Cu/Co-based [153, 154, 174-189] and Cu/Fe-based catalysts [190-195];

iii. Modified Mo-based catalysts: carbides, sulfides and phosphide [29, 96, 196-206];

iv. Noble metal catalysts, Rh, Pd, Pt, Re, and Ir [207-215] and homogeneous noble metal complexes [216, 217].

Copper-based methanol catalysts give the highest selectivity and activity for alcohols in terms of CO conversion; however, methanol is the predominant alcohol product [20, 21, 30]. The selectivity to higher alcohols is limited by the kinetics of chain growth. The C_1 (methanol) to C_2 (ethanol) step is the rate determining step for HAS, while the higher alcohol formation via ethanol is a faster chain growth mechanism (aldol condensation) [20, 21]. Copper-modified F-T synthesis catalysts show moderate alcohol selectivity and activity, but methane and methanol are still the dominant products [21, 33]. Modified Mo-based catalysts, both carbide and phosphide show low activity for alcohol synthesis [29], while alkali promoted MoS_2-based catalysts exhibit reasonably good activity and selectivity to higher alcohols [96, 196, 197]. However, traces of organic sulfur components also form during the process [96], which is undesirable, especially when the alcohol product is intended for fuel applications. Noble metals usually exhibit low activity in term of CO conversion, although Rh-based catalysts give the best ethanol selectivity [21]. Homogeneous metal complexes based on noble metals may not be desirable due to the high cost of the noble metals and the difficulties in catalyst recovery and reuse [27].

For HAS, the main problem lies in that the catalyst needs to be on one hand efficient in breaking the C-O bond to produce long chain intermediates of hydrocarbons, but retain a large coverage of intact CO molecules to form long chain intermediates of oxygenates, and on the other hand be efficient in hydrogenating long chain oxygenates intermediates into alcohols, but not too efficient, as high hydrogenation activity leads to termination as hydrocarbons. Co and Fe are good at C-O bond breaking, but not good for CO adsorption and CO insertion. Therefore, it seems that is important to optimize the amounts of surface species of associated CO and dissociated CO by adding some components that are good for CO adsorption but not influence the properties of Co and Fe significantly.

In our group, we have worked on HAS with a few bachelor, master and Ph.D. projects. The main work has been done with a Ph.D. project by Jakob M. Christensen, who has focused on Mo_2S-based catalysts and bulk molybdenum carbide. Alkali promoted MoS_2-based catalysts exhibit reasonably good activity and selectivity to higher alcohols [96, 196, 197]. Interestingly, it was found that bulk Mo_2C shows good selectivity to ethanol (up to 34.1 mol %) [8]. However, the bulk Mo_2C exhibits relatively low alcohol yields during CO hydrogenation, which is mainly due to a low specific surface area caused by the high carburization temperature (up to 750 °C) and high loading of promoters (up to 10 wt % K_2CO_3, molar ratio of K/Mo=0.14) [8, 199]. Therefore, in this project, an effort has been made to increase the activity and selectivity of alcohols over molybdenum carbide by supporting the carbide on high surface area support. In addition, in situ characterization work on the formation of bulk and supported molybdenum carbide has been conducted for determination of the carburization mechanism and temperature, as well as for determining the differences in structure and catalytic properties between bulk and supported molybdenum carbides.

Table 2-2 Research and development status of HAS from syngas [27, 46, 156, 157, 218].

Company	The catalysts			Operating conditions					State of development[a)]
	Key elements	Promoters	Others	GHSV [h^{-1}]	T [°C]	P [bar]	H_2/CO [vol/vol]	CO_2 removal	
Enichem-Snamprogetti -Haldor Topsøe	Zn,Cr,Cu	K, Na	Mn, Al, Mo,Ti, La, V, Ce	3000 -15000	350-420	120-160	0.5-3.0	No	Industrial plant, 15000 t/year, Italy)
Lurgi	Cu, Al, Zn	K, others	No	2000 -4000	270-300	70-100	1-1.2	Yes (1% loop)	Bench scale, 2 ton/day
IFP and Idemitsu Kosan	Cu, Co Cu, Ni	Na K K	Al, Cr, Zn, et al. Ti, Mn,Zn	3000 -6000	260-320	60-100	1-2	Yes (0.5-3% loop)	Demonstration unit (20 bbl/day) STY of 0.1-0.15, 70-80% alcohol selectivity
Dow Chemicals (Union Carbide)	Mo,Co,S	K	H_2S	5000 -7000	290-310	120-140	1.1-1.2	Yes	Bench scale, STY of 0.2, 80-85% alcohol selectivity
C1 Chemistry Group (Japan)	Rh, Mn Cu, Zn	Li	No	30000 -45000	260-280	50	1.4	No	Lab scale, STY of 0.2 80-85% alcohol selectivity
PEFI-Ecalene	Mo, S	K	-	-	200-300	35-207			1.5 ton/day (slurry reactor)
Institute of Coal Chemistry, Chinese Academy of Sciences	Cu, Fe	-	-	-	200-260	40-60	-	-	Bench scale,1200 h test, with 50% higher alcohol selectivity, STY of 0.23.
Haldor Topsøe A/S	Cu, Zn	K	Al	2000 -15000	280-320	80-100	0.5-1.1	Yes	Lab scale, STY of ~ 0.35

[a)] All these pilot plants have been closed down.

2.4 Cu/Ni-based catalysts for syngas conversion

As stated above, on the basis of DFT calculations Cu/Ni catalysts have been suggested to be active catalysts for methanol synthesis from syngas [6]. The work presented in this thesis has mainly focused on Cu/Ni based catalysts for syngas conversion. It is therefore important to review what has been investigated over Cu/Ni based catalysts for CO/CO_2 hydrogenation.

Cratty et al. [219] have investigated CO_2 hydrogenation over Cu/Ni alloys with the focus on the production of methane and CO. It has been found that alloying 11% or less copper with Ni produced mainly methane. For alloys that contain more than 50% Cu no methane was produced. Nerlov et al. [220-222] have investigated methanol synthesis on single crystal Cu(100) planes promoted with Ni. Ni was observed to improve the turnover frequency (TOF) of methanol about 3.5 times compared to single crystal Cu(100) with $H_2/CO/CO_2$ gas feed, while there was no difference with CO_2/H_2 feed [221]. It was stated that the addition of CO to the synthesis gas creates segregation of Ni to the surface, whereas this was not the case for a reaction involving CO_2 and H_2 [221]. These experiments were conducted at low pressure (1-1.5 bar).

High pressure CO hydrogenation over Cu/Ni-based catalyst has been studied in some previous work as well. Uchiyama et al. [223, 224] (Table 2-3) found that a co-precipitated bulk Cu/Ni (molar ratio 1:1) catalyst showed 48 mol % alcohol selectivity with 13 wt % of alcohols in the forms of higher alcohols at 60 bar and 320 °C. The proportion of higher alcohols was improved to 36 wt % by impregnating this catalyst with sodium. A co-precipitated Cu/Ni catalyst supported on TiO_2 and promoted by sodium showed 65 mol % alcohol selectivity with 49 wt % of the alcohol product being higher alcohols. However, there are no more details on the productivity of alcohols.

Pereira and Martin [225] found that $Cu/Ni/SiO_2$ catalysts showed lower methanol selectivity than that of Cu/SiO_2 catalysts for CO hydrogenation at 50 bar, 240 °C, $H_2/CO=2$. Higher reduction temperature of $Cu/Ni/SiO_2$ catalysts resulted in higher methanol selectivity (Table 2-3). Sermon et al. [226] found that 2 wt % Ni to Cu/ZnO catalysts suppressed the rate for CO hydrogenation by 85% and the methanol selectivity by 11%. Llorca et al. [227] investigated the influence of Cu promotion on Ni/SiO_2 catalysts in the reaction of CO hydrogenation. Lower CO conversion, but higher selectivity towards methanol was obtained in comparison to the standard Ni/SiO_2 catalyst.

Fraga and Jordao [228] have investigated bulk $Cu/Ni/Al_2O_3$ catalysts that showed to have a methanol selectivity of more than 96 mol %. Fraga and Jordao [228] have found that the selectivity to methanol increased with time on stream, while selectivity to higher alcohols decreased correspondingly. Hence, they presumed that the reaction was affected by the thermodynamic instability of the alloy. Wang et al. [229] reported that pure Cu was more active (in terms of CO conversion) than pure Ni on a ZnO support, whereas the reverse was valid for a SiO_2 support (at 20 bar and 250 °C). They also found that the activity of Cu/ZnO catalyst for CO hydrogenation was dramatically decreased by adding the same amount of Ni, while an opposite trend was observed for Cu/SiO_2 catalysts, where the activity increased 2 times. The selectivity towards methanol on a ZnO

supported catalyst was significantly higher than the corresponding selectivity towards methanol on a SiO_2 supported catalyst (78 mol % and 22 mol %, respectively). Cu_1Ni_1/SiO_2 produced mainly alkanes with a selectivity around 78 mol % [229]. Cu_1Ni_1/ZnO produced about 78 mol % methanol with 20 mol % alkanes as by-product [229]. The observation made by Wang et al. [229] was presumed an indication of metal-support interactions.

In summary, the Cu/Ni catalysts for CO hydrogenation reported in the literature were found to be either active for higher alcohol synthesis [223, 230], hydrocarbon synthesis [231], or methanol synthesis [6, 225]. It seems there are still ambiguities with Cu/Ni catalysts for CO hydrogenation. This ambiguity could be caused by carriers and also potentially by the degree of alloying, i.e. the Cu/Ni composition in the alloys. These effects have been studied in this project as well.

Table 2-3 Selected data of Cu/Ni-based catalysts in the literature.

Catalysts	Contents	Operation conditions					S_{MeOH} [b]	$S_{alcohol}$ [c]	Refs
		T	P	GHSV	H_2/CO	X_{CO} [a]			
		[°C]	[bar]	[h^{-1}]	[vol/vol]	[%]	[mol %]	[mol %]	
Cu/Ni	1/1 (molar ratio)	320	60	4000	2	20	-	48	[223]
Cu/Ni/Na	1/1/0.48 (molar ratio)	325	60	4000	2	21	-	48	
Cu/Ni/Ti	1/1/1 (molar ratio)	315	60	4000	2	18		20	
Cu/Ni/Ti/Na	1/1/1/0.32 (molar ratio)	300	60	4000	2	21		49	
Cu/ZnO	8/92 (wt %)	250	20.3	-	1/3	-	95		[226]
Cu/Ni/ZnO	8/2/92 (wt %)	250	20.3	-	1/3	-	84.4		
$Cu/Ni/Al_2O_3$	16.49/15.46/27.12 (wt %)	250	50	-	2	4.89	97.4	-	[228]
$Cu/Ni/Al_2O_3$	16.49/15.46/27.12 (wt %)	250	50	-	2	8.55	96	-	
$Cu/Ni/Al_2O_3$	16.49/15.46/27.12 (wt %)	250	50	-	2	6.79	96.4	-	
Ni/SiO_2 [d]	15/85 (wt %)	240	50	-	2	1.27	1.5	1.5	[225]
$Cu/Ni/SiO_2$ [d]	3.87/12.7/83.4 (wt %)	240	50	-	2	1.11	15.5	15.5	
$Cu/Ni/SiO_2$ [e]	3.87/12.7/83.4 (wt %)	240	50	-	2	0.1	77.1	78.8	
$Cu/Ni/SiO_2$ [d]	7.44/8.06/84.5 (wt %)	240	50	-	2	0.49	50.7	50.7	
$Cu/Ni/SiO_2$ [e]	7.44/8.06/84.5 (wt %)	240	50	-	2	0.52	92.1	92.1	
Cu/SiO_2 [d]	8/92 (wt %)	240	50	-	2	0.2	98.2	98.2	
$Li/Cu/Ni/SiO_2$ [d]	0.8/7.44/8.06/83.7 (wt %)	240	50	-	2	0.9	79.8	85.9	

[a] CO conversion. [b] Selectivity to methanol. [c] Selectivity to alcohol in general. [d] Catalysts were reduced at 400 °C. [e] Catalysts were reduced at 800 °C.

3 Experimental work

This project has focused on experimental investigations of catalytic CO hydrogenation. The detailed procedures for catalyst preparation, characterization, and testing are varies from catalyst to catalyst. Therefore, these details are included in the later individual chapters. This chapter provides a general description of the high pressure reactor, and the experimental work with catalyst preparation, characterization, and testing.

3.1 High pressure setup

The performance of catalysts for CO hydrogenation has been performed in a high pressure fixed-bed flow reactor setup, which is illustrated in the diagram in Fig. 3-1. The high pressure fixed-bed flow reactor setup has previously been used for both investigations of homogeneous gas phase [232-234] and heterogeneous catalytic reactions [96, 197]. Two manuals regarding a general description of setup and specific details regarding heterogeneous reaction are available from the CHEC research group at DTU Chemical Engineering [235, 236].

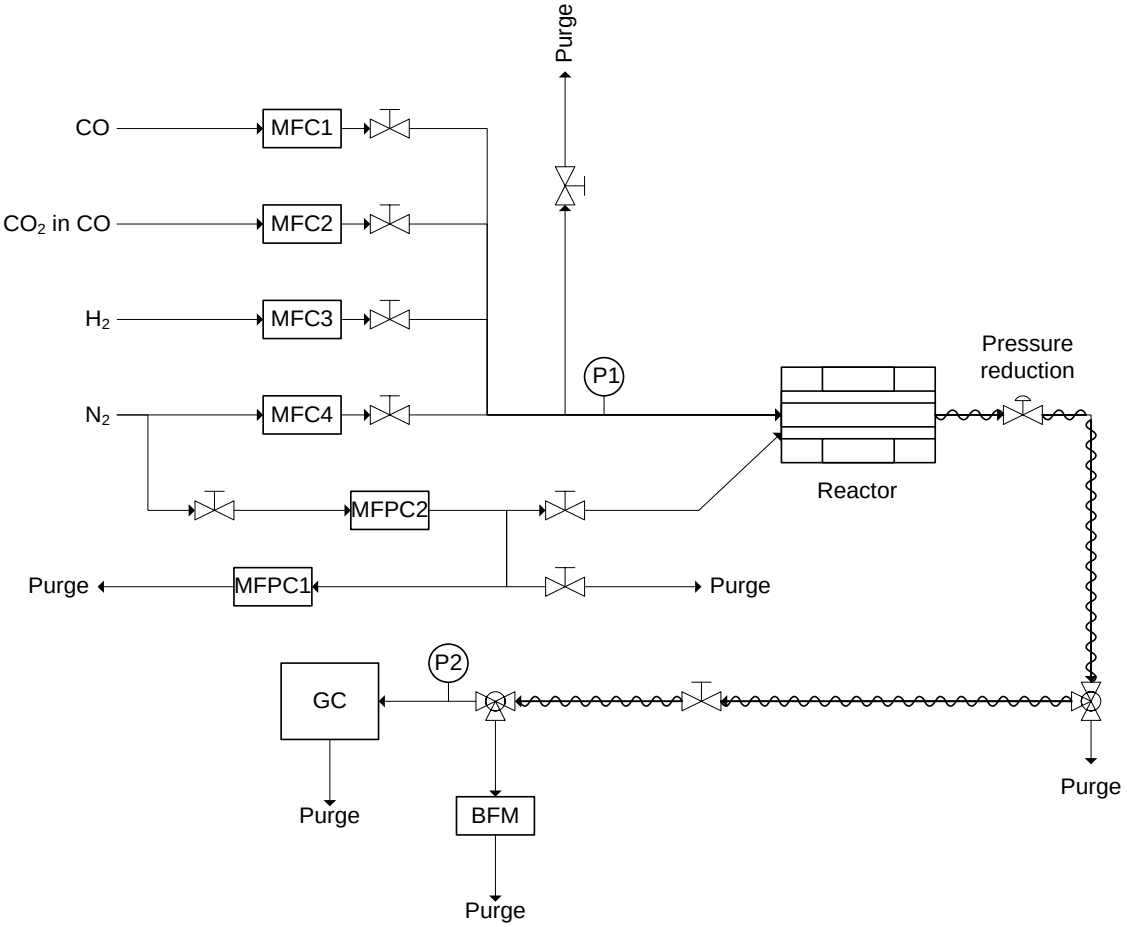

Fig. 3-1 Simplified diagram illustrating the high pressure fixed-bed flow reactor setup. BFM: Bubble Flow Meter; GC: Gas Chromatograph; MF(P)C: Mass Flow (Pressure) Controller; P: Manometer. Heat traced tubing is indicated by sinusoidal curves.

As it can be seen in Fig. 3-1, the high pressure setup consists of three main sections, upstream of the reactor, reactor and oven, and the downstream of reactor. The downstream section includes a GC-FID/TCD detection system for gas composition analysis and a soap film bubble flow meter for gas velocity measurements.

3.1.1 Upstream of reactor

The feed gases used for catalyst activity tests are supplied to the reactor from pressurized cylinders via Brooks 5850S mass flow controllers. Table 3-1 summarizes the applied gasses measurements present experimental work. All gas cylinders are supplied by AGA A/S.

Table 3-1 Gasses used in the catalyst activity tests.

Gas	Purity	Supplier
CO	≥ 99.97 %	AGA A/S
H_2	≥ 99.999 %	AGA A/S
N_2	≥ 99.97 %	AGA A/S
8.6 mol % CO_2 in CO	Composition ± 2 %	AGA A/S
0.6 mol % O_2 in N_2	Composition ± 2 %	AGA A/S

The feed stream ($CO+H_2$, sometimes with a few percent of CO_2) used in a given catalytic test was always pre-calibrated at the reaction pressure with an empty reactor tube, and flow (measured by BFM) and composition (measured by GC) measurements were used to adjust the feed to the desired composition and flow rate.

N_2 is typically used for pressurization of the reactor. The gas 0.6 mol % O_2/N_2 gas mixture in table 3-1 has only been used for passivation of the catalyst samples before they are removed from the reactor.

3.1.2 Reactor and oven

The reactor consists of a 1545 mm long quartz tube (i.d. 8 mm; o.d. 10 mm), which contains the bed of catalysts. The quartz tube is placed inside a TP347 stainless steel pressure shell, as shown in Fig. 3-2. The reactor (quartz tube) is pressurized with N_2. Meanwhile, nitrogen is closed to pressurize the pressure shell with two Brooks 5866 mass flow pressure controllers. Hence, there is no significant pressure gradient across the quartz tube wall. The ensemble of reactor tube and pressure shell is located inside an Entech tube oven with three individually controlled electrical heating elements. Fig. 3-3 shows a schematic overview of the reactor and oven setup.

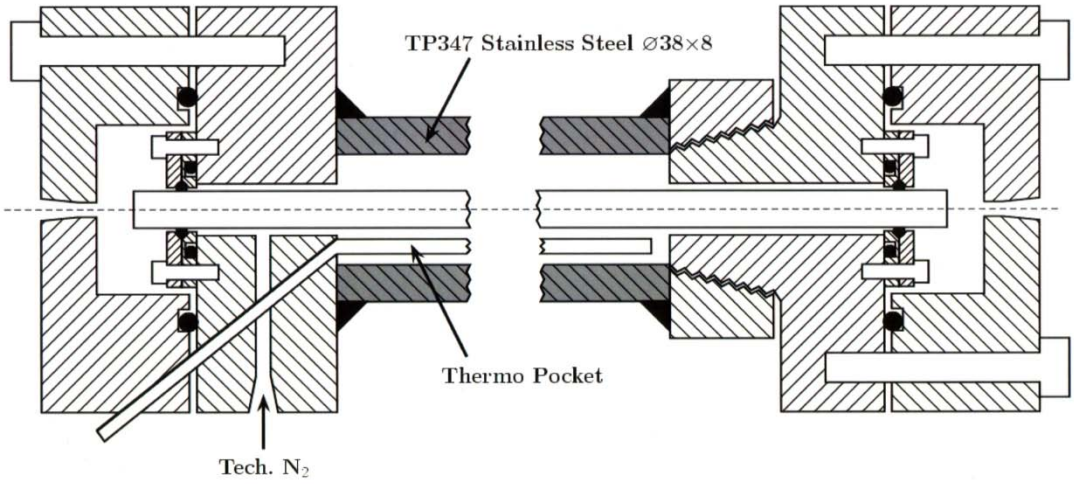

Fig. 3-2 A cross-sectional sketch of steel flanges of the pressure shell utilized in the high pressure fixed-bed reactor. White hatched parts represent AISI 316 stainless steel flanges. Grey hatched parts indicate the TP 347 stainless steel pressure shell. Black circles indicate Viton O-rings. Black triangles represent welded connections. Each flange is fixed by four bolts, with the position of the bolts illustrated by white silhouettes [236].

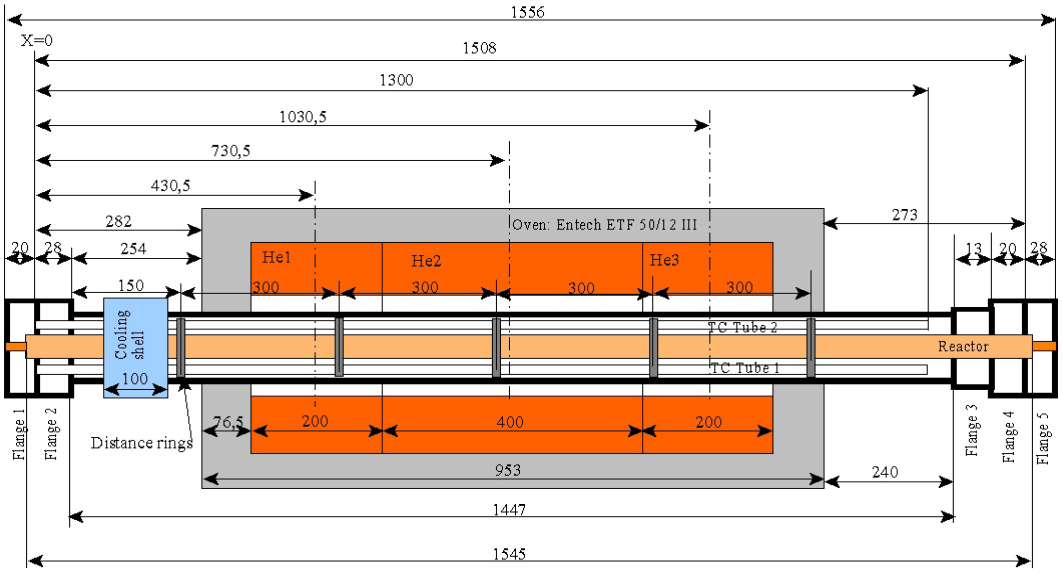

Fig. 3-3 Schematic overview of the reactor and over setup. All measurements are in mm [236].

The three heating elements in the oven offer an isothermal zone in a length of 25 cm in the center part of the oven. The heating elementals are controlled by three Eurotherm 2208e temperature controllers, donated as T1, T2, and T3 and the reactor temperature is monitored by type K (± 2.2 K or 0.75%) thermoelements positioned inside two steel thermo pockets placed in the void between the quartz tube and the pressure shell. The bed of catalyst is contained within the isothermal zone (± 1.0 K) in the oven. Fig. 3-4 shows a series of representative temperature profiles, which have been measured by Christensen

[237]. As it can be seen in Fig. 3-4 the desired isothermal zone is located between 65 and 99 cm from the entrance of the quartz tube. The catalyst is therefore located within this range for all catalyst tests.

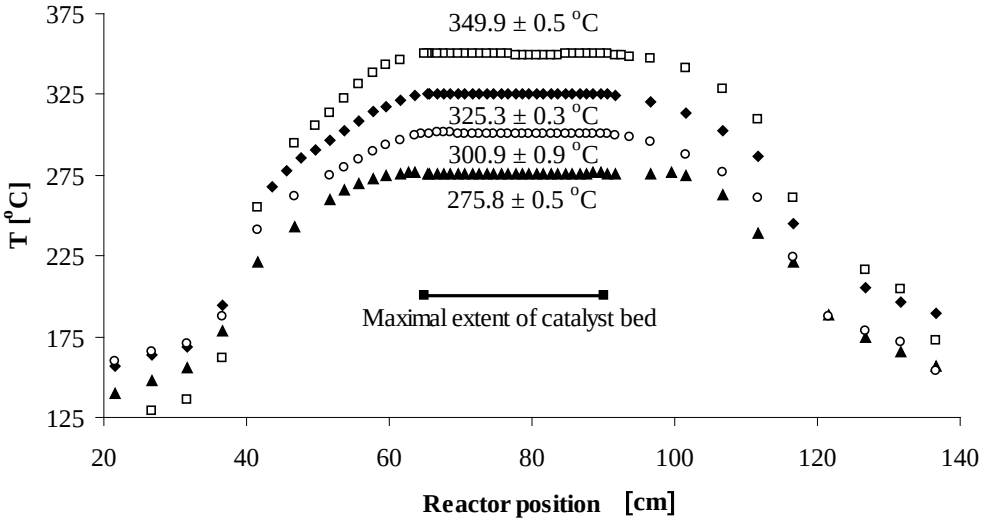

Fig. 3-4 Representative temperature profiles measured in the thermo pocket, which have been measured by Christensen [237].

3.1.3 Downstream of reactor

After the reactor the pressure is reduced, and the gas enters the downstream section, where it is possible to condense the liquid products or analyze the gas composition with a GC-FID/TCD (6890N, Agilent Technologies) detection system. Alcohols and esters are separated using a DB1 column (50 m, 100% Dimethyl polysiloxane). Hydrocarbons, CO, CO_2, H_2, and N_2 are separated using a dual column system, where a Porapak N column (3.05 m, bonded divinyl-benzene/ethylene glycol dimethacrylate) is followed by a 13×Molsieve column (1.2 m, 5 Å molecular sieve zeolite).

The two classes of gas phase constituents (alcohols and hydrocarbons/simple gasses) are quantified in two separate analysis runs, and both these two runs employ both the TCD and the FID detector. Helium is used as the carrier gas in the gas chromatograph. The identification and quantification of peaks in the GC spectra rely on prior calibration against gas mixtures with known compositions.

A soap film bubble flow meter to measure the actual flow rate of the product stream.

3.2 Catalyst preparation

Supported Cu/Ni catalysts were prepared via three different methods, namely incipient wetness impregnation, co-precipitation, and deposition-co-precipitation. Supported molybdenum carbide based catalysts were prepared via temperature programmed carburization/reduction. The preparation procedures of all catalysts will be described in details in the appropriate chapters.

3.3 Catalyst characterization

In present project, in situ or ex situ XAS, XRD, TEM, FTIR, sulfur chemisorption, BET-surface area measurement, inductively coupled plasma optical emission spectroscopy (ICP-OES) analysis, thermogravimetric analysis (TGA) of reduction and calcination and temperature-programmed desorption of ammonia (NH_3-TPD) have been used to identify the structure of selected catalysts. The details will be stated in the appropriate chapters.

3.4 Catalyst testing

Performances of catalysts for CO hydrogenation have been tested in a fixed-bed continuous-flow reactor with an online gas chromatograph equipped with flame ionization and thermal conductivity detectors (6890N GC-FID/TCD from Agilent Technologies). The details of catalyst testing will be stated in the appropriate chapters.

4 CO hydrogenation to methanol on Cu-Ni based catalysts: Theory and Experiments

4.1 Abstract

We present density functional theory calculations for CO hydrogenation on different transition metal surfaces. Based on the calculations, trends are established over the different monometallic surfaces, and scaling relations of adsorbates and transition states that link their energies to only two descriptors, the carbon oxygen binding energies, are constructed. A micro-kinetic model of CO hydrogenation is developed and a volcano-shaped relation based on the two descriptors is obtained for methanol synthesis. A large number of bimetallic alloys with respect to the two descriptors are screened, and Cu-Ni alloys of different surface composition are identified as potential candidates. These alloys, proposed by the theoretical predictions, are prepared using an incipient wetness impregnation method and tested in a high-pressure fixed-bed reactor at 100 bar and 250 -300 °C. The activity based on surface area of the active material is comparable to that of the industrially used $Cu/ZnO/Al_2O_3$ catalyst. We employ a range of characterization tools such as inductively coupled plasma optical emission spectroscopy (ICP-OES) analysis, in situ X-ray diffraction (XRD) and in situ transmission electron (TEM) microscope to identify the structure of the catalysts.

4.2 Introduction

Methanol is among the top ten petrochemicals produced in the world, with its main applications being the production of formaldehyde, acetic acid, and methyl-tertbutyl ether, a gasoline additive to boost the octane number [24]. Apart from its use as a base chemical, methanol has also been suggested as a transportation fuel in an alternative methanol-based economy [57]. A large number of different catalysts have been tested for methanol synthesis, and $Cu/ZnO/Al_2O_3$ catalysts have been established as the catalyst of choice in industry. These catalysts convert synthesis gas, a mixture of CO, CO_2 and H_2, at 230-280 °C and 50-120 bar with high selectivity into methanol. Despite several decades of research there are still a number of open questions regarding the nature of the active site [102, 134] and the reaction mechanism of $Cu/ZnO/Al_2O_3$ catalysts [24]. Deactivation of the catalyst poses one of the biggest problems; more than one-third of the activity is lost after the first 1000 h of operation, and this fact often determines the economic lifetime of the catalyst [130, 238]. Apart from $Cu/ZnO/Al_2O_3$ numerous different catalysts have been studied. While pure Cu is rather inactive for methanol synthesis, promoted and supported Cu catalysts have been tested widely. Apart from the above-mentioned promotion with ZnO, other promoters such as MnO_2 [72, 97], ZrO_2 [239], Ga_2O_3 [240], and B_2O_3 [241], have been tried. Among the noble metals such as Pd, Pt and Ir, Pd stands out in particular with a high activity and selectivity for methanol formation [242], although high selectivities towards methane have been reported for Pd catalysts as well. Potassium-promoted MoS_2 has a significant activity for methanol synthesis, although the selectivity is only about 50% [243]. For the above-mentioned reasons, there are continuous interests in catalysts with improved properties.

Here we present in the following extensive density functional theory (DFT) calculations for the CO hydrogenation on a Cu(211) surface. After the identification of the lowest energy pathway, the study is extended to different transition metal surfaces. We establish scaling relations for adsorbates [244] as well as transition-states [245-250] and use them to reduce the number of independent variables that determine the overall activity to only two. A micro-kinetic model is developed and the theoretical turnover frequency is calculated as a function of the two descriptors resulting in an

activity volcano for this reaction. Based on screening of a large number of bimetallic alloys, CuNi alloys, rich in Cu at steps, are suggested as active and selective methanol synthesis catalysts. The theoretically predicted catalysts have been prepared using an incipient wetness impregnation method and tested in a high pressure fixed bed reactor at 100 bar and 250 to 300 °C. The activity based on surface area of the active material has been shown to be comparable to that of the industrially used $Cu/ZnO/Al_2O_3$ catalyst. Inductively coupled plasma optical emission spectroscopy (ICP-OES) analysis, in-situ X-ray diffraction (XRD), and in-situ transmission electron microscope (TEM) have been used to identify the structure of the catalysts. Preliminary studies of the stability of the Ni-Cu catalyst system have been performed, showing the catalyst to increase its activity with time on stream.

4.3 Results

There are several theoretical studies dealing with CO hydrogenation on Cu surfaces in the literature. However, most of these studies employ the (111) [126] or (100) [251]facets of Cu, or deal with small Cu clusters [252]. We chose the 211 surface for the parent study since it is known that the active site of the industrially used $Cu/ZnO/Al_2O_3$ catalyst has defects such as stacking faults that can be modeled by stepped 211 surfaces [102, 107, 253]. It has also been shown that all intermediates during hydrogenation of CO to methanol bind stronger on the 211 facet of Cu when compared to Cu(100) and (111) [254].

Fig. 4-1 shows the CO hydrogenation pathway over stepped Cu(211) as obtained from DFT calculations. CO hydrogenation occurs via hydrogenation of the carbon end of adsorbed CO; CO gets hydrogenated to HCO, H_2CO and finally to H_3CO. While CO and HCO bind to the surface through the carbon end, H_2CO lies flat and binds through both, its C and O atoms. Methoxy (H_3CO) flips around and binds through the oxygen atom. Hydrogenation of methoxy is the last step in the reaction cascade to yield methanol. In contrast, hydrogenation of the oxygen end involving the intermediates COH, HCOH, and H_2COH is associated with much higher barriers and all intermediates are higher in energy than their carbon hydrogenated counterparts. As can be seen from the lowest energy pathway in Fig. 4-1 (blue line), hydrogenation of CO and H_3CO have the highest barriers of 0.88 and 1.27 eV, respectively.

Having identified the reaction path for the hydrogenation of CO on the copper surface, we will now extend the study to other transition-metal surfaces. This relies on establishing trends in adsorption and transition-state energies from one surface to another and the assumption that the same pathways would be beneficial on the other surfaces. In order to obtain these trends, calculations of H, CO, HCO, H_2CO, and H_3CO adsorption as well as transition states of reactions $CO + H \rightarrow HCO$, $HCO + H \rightarrow H_2CO$, $H_2CO + H \rightarrow H_3CO$, and $H_3CO + H \rightarrow CH_3OH$ have been performed for a number of transition metal surfaces including Ag, Au, Pd, Pt, Rh, Ni, and Ru.

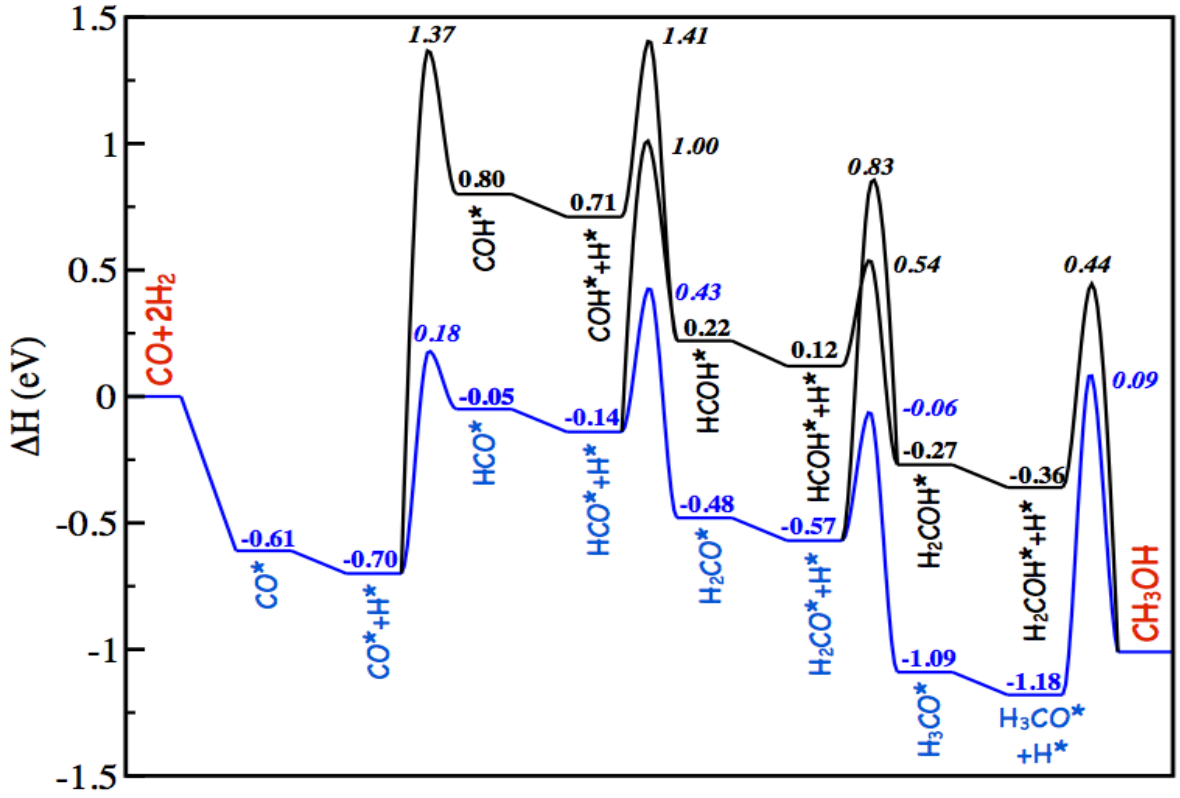

Fig. 4-1 The possible energy pathways for CO hydrogenation on the stepped Cu(211) surface. Intermediates marked with * are adsorbed on the surface. All energies are relative to CO and H_2 in the gas-phase. The lowest energy pathway is depicted in blue. Energies are ZPE corrected.

We will now introduce the concept of scaling and use this concept to reduce the number of independent variables that would otherwise be necessary for a satisfactory description of trends in CO hydrogenation to methanol. We have previously shown that the adsorption energy of an adsorbate AH_x that binds through atom A on a transition-metal surface will scale linearly with the adsorption energy, ΔE_A, of atom A [244]. The slope of this correlation is usually given by simple bond-counting arguments [255]. The intercept of the scaling line with the $\Delta E_A = 0$ axis can be obtained from a single calculation on one transition-metal surface. These scaling relations have been proven useful for the description of complex reaction networks by only few parameters [7, 256-258] and there have already been successful attempts in the discovery of leads for new catalytic materials based on fast screening of these simple parameters [259-261].

Fig. 4-2 shows the scaling relations for intermediates CO, HCO, H_2CO, and H_3CO. Both, CO, and HCO are found to scale relatively well with the chemisorption energy of carbon (ΔE_C). H_2CO binds with both, the carbon and oxygen atom to the surfaces. Simple bond counting arguments for a broken double bond lead to a scaling with ¼ carbons and ½ of oxygens chemisorption energy (ΔE_O), while adsorption is thermoneutral for noble metals [262]. As can be seen from Fig. 4-2, this assumption gives a fairly good scaling description of H_2CO. Finally, H_3CO, which binds through oxygen to the surface, is found to scale with approximately ½ ΔE_O. Hydrogen adsorption is modeled with ΔE_C as reported previously [257].

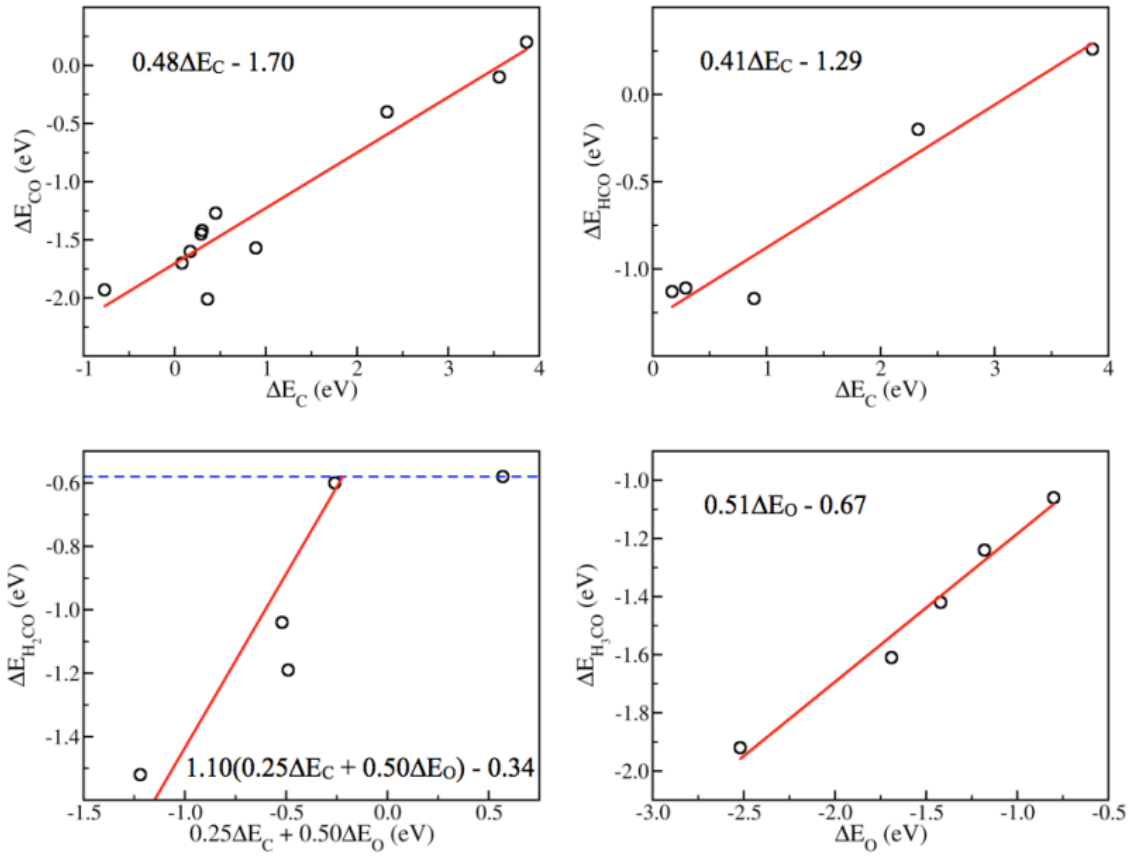

Fig. 4-2 Scaling relations of adsorption energies of the 4 different intermediates of the lowest energy pathway from Fig. 4-1. The adsorption energies are calculated on the stepped (211) surfaces of various transition metals and are taken relative to CO and H_2 in the gas-phase. Zero-point corrections are not included in the adsorption energies. Energies are plotted as a function of ΔE_C for CO, and HCO adsorption, ΔE_O in the case of H_3CO adsorption, and both ΔE_C and ΔE_O in the case of H_2CO adsorption. The red line is obtained by the best fit through data points; the slope and intercept of the fit is given in each figure. The blue line in the figure of H_2CO scaling represents the energy of H_2CO in the gas-phase relative to CO and H_2, a data point on the blue line corresponds to an H_2CO adsorption energy of zero.

For estimating the rates, we will use scaling relations for transition-state energies (Brønsted–Evans–Polanyi (BEP) relations) in a similar way. It has been found that the transition-state energy of simple dehydrogenation reactions correlates with the final-state energy of that reaction [250]. Transition-state scaling relations for the four different hydrogenation reaction steps are shown in Fig. 4-3. There is a fairly good relationship between the transition state energy and the energy of the dehydrogenated state. Note that the correlation is between the transition state and the dehydrogenated state of the molecules. Since we are investigating hydrogenation of CO to methanol, the transition states are correlated with the initial state of the hydrogenation step of the corresponding intermediate. Both adsorbates of the initial step scale with ΔE_C and ΔE_O via the scaling relations described above. The transition state energies are hence described entirely by the carbon and oxygen chemisorption energies, ΔE_C and ΔE_O.

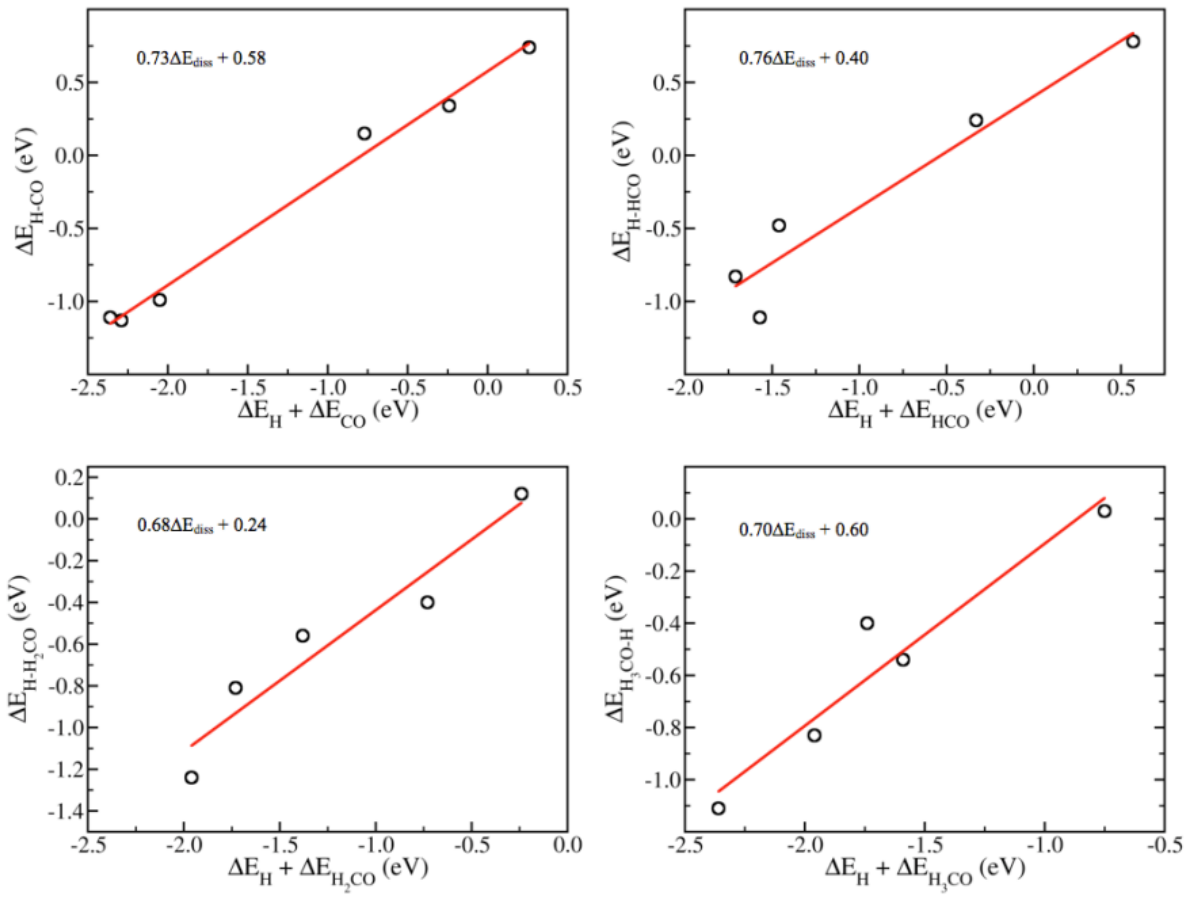

Fig. 4-3 Scaling relations of transition state energies of the 4 different reaction steps of the lowest energy pathway from Fig. 4-1. The transition state energies are calculated on the stepped (211) surfaces of various transition metals and are taken relative to CO and H_2 in the gas-phase. Zero-point corrections are not included. Energies are plotted as a function of the dissociated molecules, ΔE_{diss} (the initial states in the pathway from Fig. 4-1). The red line is obtained by the best fit through data points; the slope and intercept of the fit is given in each figure.

We will now describe the kinetics of methanol synthesis from CO and H_2. The following reaction steps are involved in the hydrogenation of CO:

$CO + * \rightarrow CO*$ (1)

$H_2 + 2* \rightarrow 2H*$ (2)

$CO* + H* \rightarrow HCO* + *$ *Rate determining step* (3)

$HCO* + H* \rightarrow H_2CO* + *$ (4)

$H_2CO* + H* \rightarrow H_3CO* + *$ (5)

$H_3CO* + H* \rightarrow H_3COH + 2*$ *Rate determining step* (6)

where * denotes an empty site on the catalytic surface. Inspection of the pathway on the Cu(211) surface reveals the first hydrogenation of CO to HCO as well as the last hydrogenation of H_3CO to methanol are possible rate determining steps. In the vicinity of Cu in the (ΔE_C, ΔE_O) plane, we will assume this to hold generally. One should be aware of the fact, however, that over the range of transition metal surfaces considered here, alternative pathways and/or different rate determining steps may play a major role.

In order to establish a relationship for the CO hydrogenation activity a micro-kinetic model was developed which is based on the six elementary reaction steps (1)-(6). We solve these reaction rates analytically under the assumption that reactions (3) and (6) are rate determining, while all other reactions are in quasi-equilibrium. For the best catalysts coverages are found to be small and hence we do not include adsorbate-adsorbate interactions in this study. For transition metal surfaces on the strong binding site, coverages close to 1 will lead to adsorbate–adsorbate interactions. While these interactions usually not shift the location of the top of the volcano, they increase the strong binding leg so that the turnover frequency in that region is likely higher than depicted here [263]. Another consequence is that the mean field model is adequate. The overall rate can be written as:

$$R_{tot} = R_3 = k_3 \theta_{CO} \theta_H \left(1 - \gamma_3\right)$$

where

$$\gamma_3 = \frac{\theta_{HCO}\theta_*}{k_3 \theta_{CO} \theta_H}$$

with the rate constant, k_3:

$$k_3 = \frac{k_B T}{h} e^{\frac{-\Delta G^+}{k_B T}} = \frac{k_B T}{h} e^{\frac{-\Delta E^+}{k_B T}} e^{\frac{-\Delta S^+}{k_B}}$$

and the six equilibrium constants, K_i :

$$K_i = e^{\frac{-\Delta G^+}{k_B T}} = e^{\frac{-\Delta E^+}{k_B T}} e^{\frac{-\Delta S^+}{k_B}}$$

where i = 1-6. Both, ΔE^+ and ΔE_i are fully described by the two parameters, ΔE_C and ΔE_O as determined by the scaling relations for adsorbates and transition-states described above (see Fig. 4-2 and Fig. 4-3). Zero-point energy and entropic contributions are calculated in the harmonic approximation. The coverage of free sites, Θ_*, and the approach to equilibrium (backward rate divided by forward rate) for reaction (3), γ_3, are obtained from the self-consistent steady-state solution to the micro-kinetic model. The total rate, R_{tot}, is hence fully described as a function of ΔE_C and ΔE_O.

Fig. 4-4a shows the turnover frequency (TOF) as a function of the two descriptors, ΔE_C and ΔE_O, for a temperature of 523 K and a total pressure of 100 bar. The partial pressures of CO, H_2 and the product methanol are 45, 45, and 10 bar, respectively. Mapping of the TOF as a function of ΔE_C and ΔE_O gives a volcano shaped relation for methanol production. Cu is clearly identified as the only elemental transition metal close to the optimum. All other transition-metal catalysts are on the strong binding (Ni, Rh, Ru, Re, Fe, Pt, Pd) or weak-binding (Au, Ag) side of the reactivity volcano.

Fig. 4-4b shows the selectivity between methanol and methane formation from synthesis gas. The selectivity is defined by the rate of methanol formation divided by the sum of rates of methanol and methane formation. The methane volcano was described in ref [7] and similar reaction conditions have been used for the selectivity plot. Both Cu and Cu_3Zn are found to exhibit high selectivity towards methanol while metals like Ni, Ru, and Co have a high selectivity towards methane formation (Fig. 4-4b). This study does not include the formation of higher hydrocarbons and alcohols. Formation of these products need a more sophisticated kinetic analysis and will be subject of further studies.

In order to identify candidate materials for methanol production, we screened a large number of bimetallic alloys with respect to their stability and activity. The bimetallic alloys were of the A_3B L_12 type and the AB BCC-B_2 type structures. We have calculated the stability of more than 1500 A_3B L_12 and more than 700 AB BCC-B_2 type alloys. Stable alloys (heat of formation negative) have been considered for further screening with respect to ΔE_C and ΔE_O. There are two different steps for the (211) surface of an A_3B L_12 structure, an AB and an AA step (see Fig. 4-5, left), both of which have been included in this study. The corresponding steps of the AB BCC-B_2 structures also have two different step sites: AA and BB (see Fig. 4-5, right). Both types of steps have been considered in the screening procedure. There are a number of different sites on the steps where adsorption of carbon and oxygen can take place. All different adsorption geometries have been calculated, the strongest binding site for each of the surfaces of each alloy is depicted in Fig. 4-4 (blue circles).

While Cu is found to be the transition metal that is closest to the top of the volcano, there are several bimetallic alloys that are within the same region. Industrially, ZnO promotes Cu and we find that alloying of Zn into the Cu step increases its oxygen binding energy and moves Cu closer to the top of the volcano. An interesting alloy found in the screening procedure is Cu_3Ni. The pure Cu step (AA step) of Cu_3Ni is calculated to have a more negative C and O chemisorption energy (stronger bonding) than Cu. Inspection of Fig. 4-4 shows that the activity for the AA step of Cu_3Ni is predicted to be approximately that of pure Cu. Interestingly, the AA step of Cu_3Ni lies within the range for very selective methanol catalysts. The other step and both steps of Ni_3Cu on the other hand are calculated to produce mainly methane. The surface composition of CuNi alloys is hence very sensitive towards the selectivity of different products.

There are several reports on CuNi catalysts for synthesis gas conversion in the literature. Most catalysts produce a mixture of methanol, methane, hydrocarbons and higher alcohols [220-223, 227]. Activity in methane production is not surprising since both the AB step (CuNi step) of $CuNi_3$ and the AA and AB steps of Ni_3Cu are calculated to have ΔE_C and ΔE_O that are within the region exhibiting high selectivity towards methane. The composition of the active site (the step) rather than the bulk composition of the bimetallic alloy will hence determine both the activity and selectivity of CuNi alloys. It has been shown experimentally that for certain preparation methods methanol selectivities up to 92% could be achieved [225].

To test our theoretical predictions we have synthesized and characterized particles with different CuNi compositions and studied their methanol activity. Fig. 4-6 shows the in situ X-ray diffraction (XRD) patterns of a reduced $CuNi/SiO_2$ catalyst, which has been cooled down to room temperature after reduction in hydrogen at 300 °C. The XRD pattern shows only reflections of Cu and CuNi alloys. The ratio of Cu to Ni in the alloys is $Cu_{11}Ni_{14}$ when calculated according to Vegard's law [264]. The particle sizes are 47 and 14 nm for Cu and the $Cu_{11}Ni_{14}$ alloy, respectively, calculated by means of the Sherrer equation. In general, Cu and Ni can form a solid solution [265], however, a separated Cu phase was also formed. This is probably due to the confinement effect of support pores. Cu sinters easily under strongly reducing conditions forming rather large particles (47 nm).

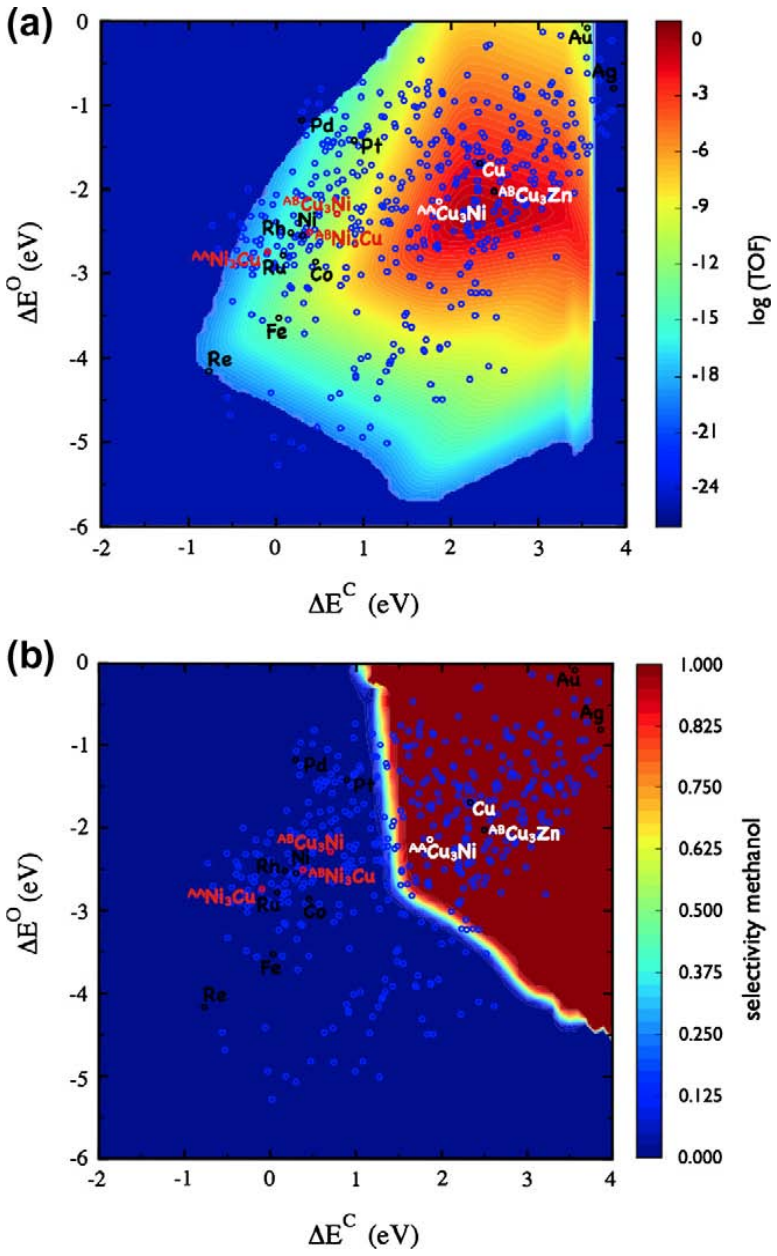

Fig. 4-4 (a) Theoretical activity volcano for the production of methanol from CO and H_2. The turnover frequency is plotted as a function of carbon and oxygen binding energies. The carbon and oxygen binding energies for the stepped surfaces of selected transition metals are depicted. Small circles depict calculated carbon and oxygen binding energies for a range of binary alloys. Two different steps for either of Cu_3Ni and $CuNi_3$ alloys are depicted in red; the Cu step of Cu_3Ni is depicted in white. Cu and the AB step of Cu_3Zn are depicted in black. For the nomenclature of the steps see Fig. 4-5. Reaction conditions are 523 K, 45 bar H_2, 45 bar CO, and 10 bar methanol. (b) Selectivity between methane and methanol formation as function of carbon and oxygen binding energies. The selectivity is defined as the rate towards methanol divided by the total rate of methanol and methane formation. Methane formation is calculated via a similar micro-kinetic model as given in Ref [7] but with slightly different reaction conditions (523 K, 45 bar H_2, 45 bar CO, 5 bar CH_4, and 5 bar H_2O). Labels as in Fig. 4-4a.

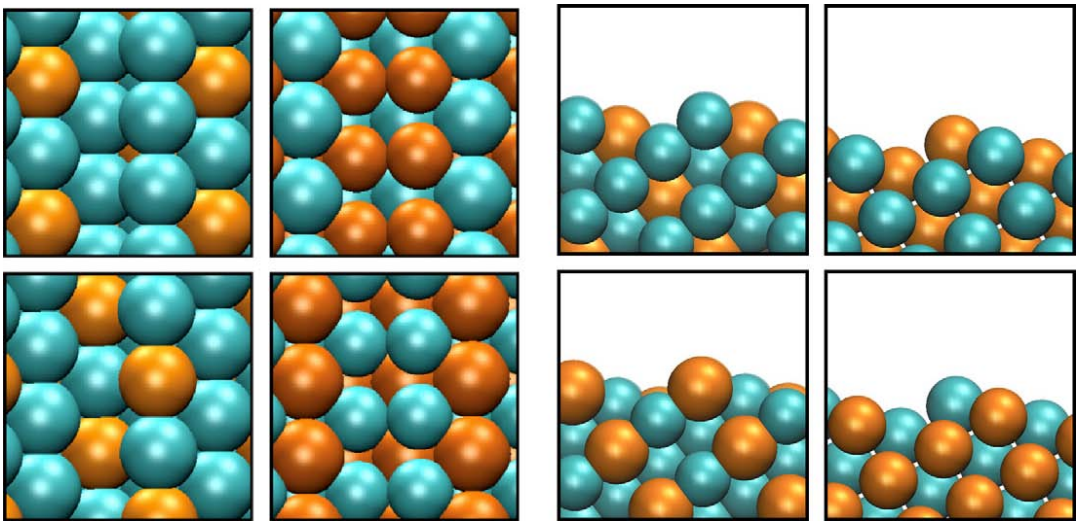

Fig. 4-5 Top left: structure of the 211 step of A_3B alloys (AA step). Bottom left: structure of the 211 step of A_3B alloys (AB step). Top second left: structure of the step of AB alloys (AA step). Bottom second left: structure of the step of AB alloys (BB step). The four pictures on the right side are the corresponding structures depicted from the side.

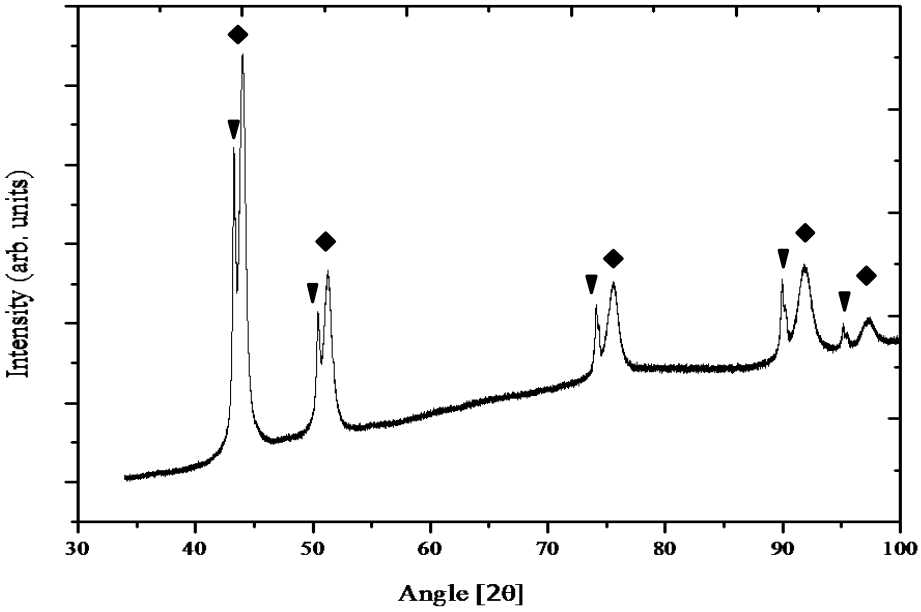

Fig. 4-6 The XRD pattern of reduced $CuNi/SiO_2$ catalyst (cooled down to room temperature after reduction in hydrogen at 300 °C); ▼ - metalic Cu, ◆ - CuNi alloy.

The reduced $Cu/ZnO/Al_2O_3$ catalyst shows distinguished Cu and ZnO peaks with the average particle size of metallic Cu being about 6 nm, and about 3 nm for ZnO.

The inductively coupled plasma optical emission spectroscopy (ICP-OES) elemental analysis results for $CuNi/SiO_2$ and $Cu/ZnO/Al_2O_3$ catalysts are listed in Table 4-1. For $CuNi/SiO_2$ sample, the original sample was designed as 20 wt % CuNi loading on SiO_2, whereas the measured loading was 17.6%. The deviation may be caused by the lost of Cu and Ni salts during preparation procedure. The Cu/Ni and Cu/Zn atomic ratio were close to the expected ratio.

Table 4-1 Elemental analysis results of $CuNi/SiO_2$ and $Cu/ZnO/Al_2O_3$ samples.

Catalysts	Analyzed Loading (wt%)		Cu/Ni or Cu/Zn (atomic ratio)	
	Cu	Ni or Zn	nominal	nominal
$CuNi/SiO_2$	9.23	8.36	1.00	1.02
$CuZnO/Al_2O_3$	44.7	22.0	2.00	2.09

Table 4-2 shows the estimated particle diameters obtained for $CuNi/SiO_2$ and $Cu/ZnO/Al_2O_3$ samples as measured by TEM and XRD. The samples have been reduced in-situ. The weight of the active materials and the active surface area is also shown in Table 4-2.

Table 4-2 Estimated particle diameters, weight of the active material and the active surface area of $CuNi/SiO_2$ and $Cu/ZnO/Al_2O_3$ samples.

Sample	$d_{p,XRD}$ [a] [nm]	$d_{p,TEM}$ [b] [nm]	$m_{active\ materials}$ [c] [g/g_{cat}]	ASA [d] [m^2/g]
$CuNi/SiO_2$	14	10.6	0.176	8.38
$CuZnO/Al_2O_3$	6	-	0.714	79.3

[a] *Average crystal size as determined from peak broadening according to Scherer equation.*
[b] *Average particle size as determined by in-situ TEM.*
[c] *Weight of active material (metallic Cu and Ni for $CuNi/SiO_2$, Cu and ZnO for $Cu/ZnO/Al_2O_3$) per gram of catalyst precursor, which is calculated according to ICP-OAS.*
[d] *Active surface areas (ASA) of catalysts calculated from the particle sizes as determined by in-situ XRD.*

The activity and selectivity of $CuNi/SiO_2$ and $Cu/ZnO/Al_2O_3$ catalysts for CO hydrogenation at various conditions are shown in Table 4-3. The main product that was observed for the $CuNi/SiO_2$ catalyst was methanol at all tested reaction conditions. Trace amounts of C_{2+} oxygenates (including dimethyl ether (DME) and ethanol) and hydrocarbons (HC) (including methane and ethane) have also been detected. The catalysts were first tested at 250 °C. After CO conversion was stabilized, the reactor temperature was increased to 275 °C and finally to 300 °C for continuous testing. The activity increases with an increase in reaction temperature (250-300 °C) while the selectivity towards methanol remains almost constant (99.2 and 99 mol%).

Table 4-3 Behavior of $CuNi/SiO_2$ and $Cu/ZnO/Al_2O_3$ catalysts in CO hydrogenation at steady state at 100 bar, and H_2/CO = 1.0 vol/vol.

Catalysts	T	GHSV	X_{CO}	Carbon based, CO_2-free selectivity [mol %]			STY_{MeOH}	TOF[a]
	[°C]	[h^{-1}]	[%]	MeOH	C_{2+} oxygenates	HC	$g/(kg_{cat}\ h)$	mmol $m^{-2}\ s^{-1}$
$CuNi/SiO_2$	250	2000	5.2	99.2	0.4	0.4	65	$6.7\cdot10^{-5}$
$CuNi/SiO_2$	275	2000	12.1	99	0.4	0.6	167	$1.7\cdot10^{-4}$
$CuNi/SiO_2$	300	4160	11.2	99	0.5	0.5	330	$3.4\cdot10^{-4}$
$Cu/ZnO/Al_2O_3$	250	16000	7.2	99	0.9	0.1	842	$9.2\cdot10^{-5}$
$Cu/ZnO/Al_2O_3$	275	16000	13.5	97.6	2.1	0.3	1315	$1.4\cdot10^{-4}$
$Cu/ZnO/Al_2O_3$	300	32000	12.7	96.3	2.8	0.9	2666	$2.9\cdot10^{-4}$

[a] *Molar amount of methanol based on active surface area of catalysts.*

The in situ XRD patterns show that, the reduced $CuNi/SiO_2$ sample is composed of two phases, Cu particles and the CuNi alloy. There was no trace of elemental Ni that would exhibit methanation activity [266]. The major part of the reduced $CuNi/SiO_2$ catalyst is composed of the CuNi alloy (about 88 mol % according to the alloy molar ratio of Cu:Ni = 11:14, which was synthesized in a molar ratio of 1:1, and 1.02:1 determined by ICP-OES). It is hence reasonable to assume that the

main active phase for methanol synthesis is CuNi. Comparably, $Cu/ZnO/Al_2O_3$ exhibits fairly high activity towards methanol synthesis, it is, however, slightly less selective at higher temperatures.

In order to get a better estimate of the activity of the surface of $CuNi/SiO_2$ in comparison to $Cu/ZnO/Al_2O_3$ the turnover frequency (TOF) based on the active surface area was used instead of the space time yield (STY). As can be seen from Table 3, the TOF of $CuNi/SiO_2$ is within the same order of magnitude as calculated for $Cu/ZnO/Al_2O_3$. While being slightly less active at 250 °C, conversion is slightly higher at 275 and 300 °C. Even though the TOF can be seen as a rough estimate only, it should be mentioned that it agrees reasonably well with the position of $^{AA}Cu_3Ni$ relative to Cu in the methanol volcano (see Fig. 4-4a).

Fig. 4-7 shows the CO conversion and the CO_2-free alcohol selectivity as a function of time on stream for both, $CuNi/SiO_2$ and $Cu/ZnO/Al_2O_3$. For $CuNi/SiO_2$, CO conversion increases from 2.4 to 5.2% while the selectivity to methanol increases from 95 to 99.2 mol % within the first 16 h after which the performance stabilizes. A similar tendency was observed at 275 °C where the CO conversion increased from 9.3 to 12.2% within 12 h.

The conversion and selectivity of the $Cu/ZnO/Al_2O_3$ catalyst as a function of time on stream is shown in Fig. 4-7 (bottom). The CO conversion decreased from 11.3 to 7.2% within the first 14 h of testing. This deactivation phenomenon is a typical problem for commercial methanol synthesis catalysts [130, 238]. The predominant dominant path of deactivation is related to the sintering of the copper particles reducing the active surface area. Another deactivation pathway of the $Cu/ZnO/Al_2O_3$ catalyst is due to brass formation in the highly reducing CO/H_2 gas mixture in the absence of CO_2 [267].

Given the high selectivity that could be obtained with CuNi catalysts, the question arises as to how the step configuration of the Ni-Cu alloy is controlled, since the two elements mix readily at many different concentrations. To a first approximation one would expect Ni to segregate to the step site due its higher binding to CO. This should lead to an increase in methane production due to a shift in carbon and oxygen binding and hence a decrease in methanol selectivity over time. We observed, however, a remarkably high selectivity towards methanol even after 70 hours on stream. This indicates that the CuNi particles are mainly composed of the $^{AA}Cu_3Ni$ step, as this is the only surface composition of CuNi that is predicted to have high activity and selectivity towards methanol. The important question is why this step is stable, particularly at high pressures of CO.

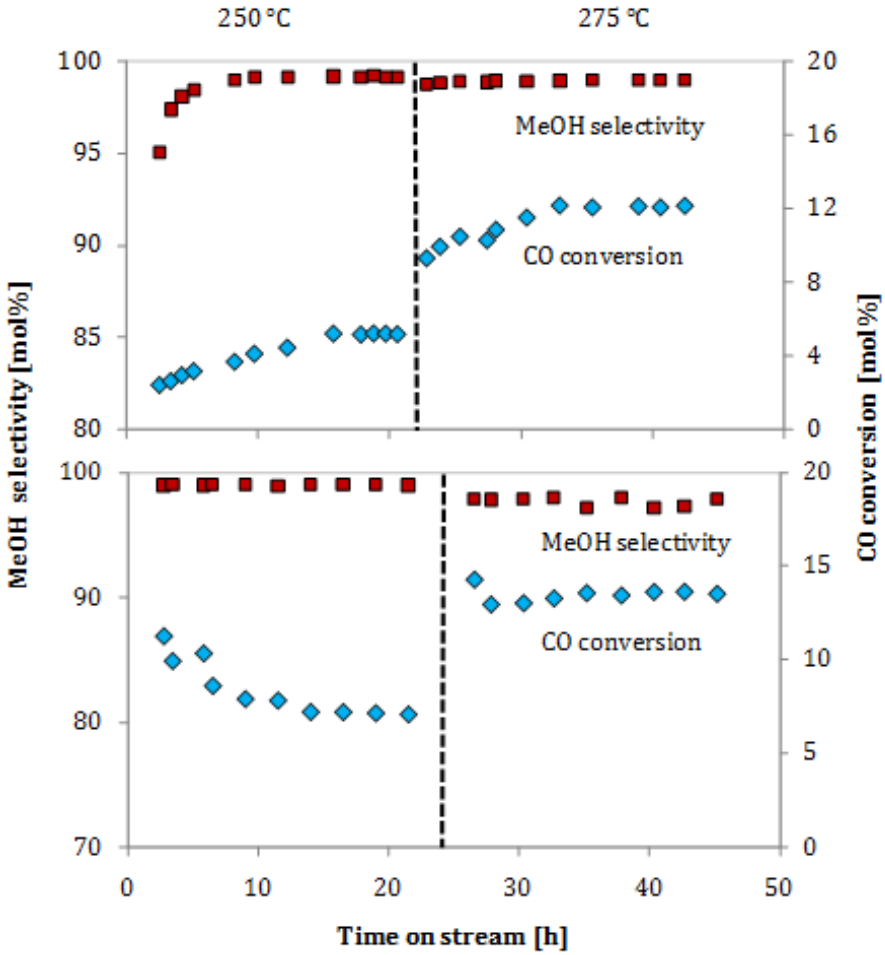

Fig. 4-7 (top). CO conversion (blue diamonds) and methanol selectivity (red squares) as a function of the time on stream for the $CuNi/SiO_2$ catalyst. Reaction conditions are: P = 100 bar, T = 250 and 275 °C, GHSV = 2000 h^{-1}, Feed: H_2/CO =1 (vol/vol). (bottom) CO conversion (blue diamonds) and methanol selectivity (red squares) as a function of the time on stream for the $Cu/ZnO/Al_2O_3$ catalyst. Reaction conditions are: P = 100 bar, T = 250 and 275 °C, GHSV = 16000 h^{-1}, Feed: H_2/CO =1 (vol/vol).

In a related study, it has been shown recently that the less reactive component of CuPt near-surface alloys, Cu segregates to the surface at elevated pressures of CO [268]. Surface segregation of Cu was found to be driven by the formation of a CO/CuPt surface alloy where CO is binding on-top of a Pt atom that is surrounded by 6 Cu atoms. This formation can be explained by the fact that Pt that is surrounded by Cu has a substantially stronger Pt-CO bond as compared to a Pt overlayer due to higher energy d states.

We have investigated the CuNi system theoretically to help establishing the surface structure under reaction conditions that is at high pressures of CO. DFT calculations of a $\sqrt{3}\times\sqrt{3}R30°$ unit cell with different concentrations of Cu and Ni in the first and second layer were used to identify the most stable surface. Due to its lower surface energy, Cu is most stable in the first layer of CuNi when there are no adsorbates present. In the presence of CO, however, Ni segregates to the surface due to its higher bond strength towards CO. Interestingly, the most stable structure in the presence of CO is composed of 1/3 ML of Ni and 2/3 ML of Cu where CO binds on-top of a Ni atom as illustrated in Fig. 4-8. As shown in Table 4-4, the CO binding energy increases from -1.32 eV for a

pure Ni overlayer to -1.92 and -1.52 for $NiCu_2$ overlayer structures. CO induced segregation energies are -0.77 and -0.63 eV for the $NiCu_2$ overlayer structures when compared to a pure Ni overlayer (see Table 4-4).

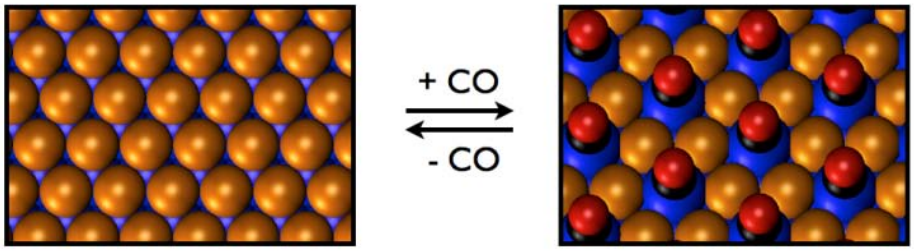

Fig. 4-8 Illustration of CO induced surface segregation of a 1/3 ML Ni to the first layer of an fcc(111) surface composed of Cu and Ni. Left: Cu overlayer on CuNi alloy. Right: CO adsorbed on Ni surrounded by Cu. Blue atoms are Ni; orange atoms are Cu; black atoms are C; red atoms are oxygen. (For interpretation of the references to color in this figure legend, the reader is referred to the web version of this article.)

Table 4-4 Segregation energies for Cu in Ni with and without adsorbed CO on the 111 plane.[a]

Cu content (ML)	Distribution in 1st and 2nd layer (1st:2nd)	ΔE_{seg} in vacuumb	ΔE_{CO}[c]	ΔE_{segCO}[d]
0	Ni	-	-1.32	-
1/3	Ni_2Cu_1:Ni_3Cu_0	-0.64	-1.37	-0.70
	Ni_3Cu_0:Ni_2Cu_1	-	-1.32	-
2/3	Ni_1Cu_2:Ni_3Cu_0	-0.16	-1.92	-0.77
	Ni_2Cu_1:Ni_2Cu_1	-0.24	-1.03	0.04
	Ni_3Cu_0:Ni_1Cu_2	-	-1.31	-
1	Ni_0Cu_3:Ni_3Cu_0	-0.80	-0.41	0.08
	Ni_1Cu_2:Ni_2Cu_1	-0.40	-1.52	-0.63
	Ni_2Cu_1:Ni_1Cu_2	-0.16	-1.35	-0.22
	Ni_3Cu_0:Ni_0Cu_3	-	-1.29	-

[a] *Segregation energies are for a* $\sqrt{3}\times\sqrt{3}R30°$ *four layer slab of Ni where the first two rows are composed according to column 2. All energies are in eV.*
[b] *Segregation energies relative to the state where all Cu atoms are present in the second layer.*
[c] *CO adsorption energies for 1/3 ML of CO.*
[d] *CO induced segregation energy compared to the state where all Cu atoms are present in the second layer.*

Having established the composition of the (111) surface of a CuNi alloy, we will now investigate the stepped (211) surface of Cu_3Ni in order to identify the composition of the active site. The (211) plane of the Cu_3Ni alloy can be cut to produce two different step sites, an AA step that is composed of Cu atoms and an AB step where Cu and Ni atoms alternate (see Fig. 4-5). We calculated both, the CuCu and CuNi step with and without CO adsorbed (see Table 4-5).

Table 4-5 Segregation energies for the CuCu and CuNi step of Cu_3Ni with and without adsorbed CO.[a]

	CuCu step			CuNi step		
	Clean	Ni row	Cu row	Clean	Ni row	Cu row
ΔE_{seg}	-	1.10	-0.07	-	0.54	-0.42
ΔE_{CO}	-1.59	-2.07	-0.71	-1.80	-2.05	-1.63
ΔE_{segCO}	-1.59	-0.96	-0.77	-1.80	-1.51	-2.06

[a] *Segregation energies are for a (211) four layer slab of Cu_3Ni. Energies are for the clean steps, steps with an additional row of Ni atoms and steps with an additional row of Cu atoms. Segregation energies (ΔE_{seg}) are relative to Ni (Cu) in the bulk. CO adsorption energies (ΔE_{CO}) are calculated relative to CO in the gas-phase. CO induced segregation energies (ΔE_{segCO}) are calculated relative to the Ni (Cu) in the bulk and CO in the gas-phase. All energies are in eV.*

CO adsorbs on the Ni atoms behind the CuCu step with -1.59 eV. Adsorption on top of Ni of the CuNi step is larger being -1.80 eV. Segregation of Ni to the CuCu step costs 1.10 eV (per two Ni) when compared to bulk Ni. CO adsorbs with -2.07 eV in the bridge position between two Ni atoms. CO induced segregation, however, amounts only to -0.96 eV since segregation of Ni is uphill in energy. Importantly, this value is smaller than CO adsorption on Ni behind the CuCu step and thus prevents segregation of Ni to the step.

Segregation of Ni to the CuNi step is slightly less costly (0.54 eV per two Ni) and yields approximately the same CO adsorption energy (-2.05 eV) as found for Ni segregated to the CuCu step (the CO sits threefold between the two Ni along the step and one Ni behind the step). CO induced Ni segregation is hence -1.51 eV, being less than CO adsorption on the clean CuNi step. Importantly, Cu segregation to the step is downhill by -0.42 eV (per two Cu atoms). CO adsorption on the Ni atom that now is located behind these Cu atoms is -1.63 eV, similar to the value calculated for CO adsorption ontop Ni behind the CuCu step. CO induced segregation of Cu to the CuNi step amounts hence -2.06 eV, which is more than CO adsorption on the CuNi step. The active site of CuNi will hence have Cu along the step under methanol synthesis reaction conditions (high CO pressure). A picture of the active site is displayed in Fig. 4-9. Importantly, CO adsorbed on Ni is basically a spectator molecule determining the surface structure while methanol synthesis is taking place on the Cu steps.

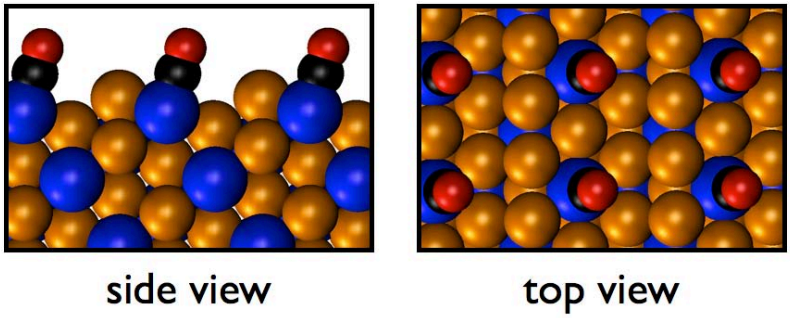

Fig. 4-9 The active site of the Cu_3Ni catalyst under methanol reaction conditions (high CO pressure). CO hydrogenation occurs at the step of the site of the alloy, which is composed out of Cu atoms. CO strongly adsorbed on Ni holds the Cu step in place. Blue atoms are Ni; orange atoms are Cu; black atoms are C; red atoms are oxygen. (For interpretation of the references to color in this figure legend, the reader is referred to the web version of this article.)

4.4 Conclusion

We investigated methanol synthesis from CO and H_2 over transition metal surfaces. Methanol formation was found to proceed via hydrogenation of the carbon end of CO to methoxy, which in turn is hydrogenated to methanol. Hydrogenation of CO and methoxy are the most difficult steps with the highest barriers. We extended the study to other transition metal surfaces and found that all intermediates involved in the reaction scale with the adsorption energy of carbon or oxygen or a combination of both of them. In most cases the scaling was found to follow simple bond counting arguments [244, 255]. Similarly, the transition state energies were found to scale with the dissociated state (BEP relation) and hence with ΔE_C and ΔE_O as well.

We developed an analytical micro kinetic model that assumes hydrogenation of CO and methoxy as being rate determining and constructed a volcano-shaped relationship for methanol synthesis that is based on scaling relations and hence maps out the activity towards methanol as a function of ΔE_C and ΔE_O. A comparison with the rates for methane formation [7] gives a selectivity map between

methane and methanol. We screened a number of binary alloys as leads for methanol synthesis candidates and identified CuNi alloys as being interesting. In particular, the $^{AA}Cu_3Ni$ step was predicted to exhibit high activity and selectivity towards methanol.

We synthesized the calculated candidates, CuNi alloy catalysts, and a model commercial $Cu/ZnO/Al_2O_3$ catalyst and tested them in a fixed-bed continuous-flow reactor for CO hydrogenation. The turnover frequency for a $CuNi/SiO_2$ catalyst indeed was at the same level as the $Cu/ZnO/Al_2O_3$ model catalyst. It even has a slightly higher selectivity to methanol than the model methanol synthesis catalyst. The high activity and selectivity of silica supported CuNi alloy catalyst agreed with the fact that the DFT calculations identified CuNi alloy ($^{AA}Cu_3Ni_1$) catalyst as highly active and selective catalysts for the hydrogenation of CO to form methanol. Additionally, no deactivation took place, but instead an activation process was observed during a total 73 h test of time on stream for the CuNi alloy catalyst. However, long term testing should be carried out as well as optimization of that catalyst composition and preparation procedure.

DFT calculations of CuNi surface structures identified Cu_2Ni as being stable at elevated pressures of CO. Importantly, the step of Cu_3Ni was predicted to be composed of Cu atoms while CO binds to Ni that sits behind the step. This unusual surface structure is believed to be the reason for the high selectivity and also the long-term stability of CuNi catalysts.

In summary, CuNi alloys show some promising first results for the development of durable methanol synthesis catalysts. More studies, however, need to be conducted in the future in order to identify catalysts that would be able to improve or replace commercial $Cu/ZnO/Al_2O_3$ catalysts. In addition, this study needs to be extended to include CO_2 as a possible feed, which calls for the inclusion of the water-gas-shift reaction into the micro kinetic model.

4.5 Experimental details

4.5.1 Density functional theory calculations

Density functional theory calculations were carried out using the Dacapo code [269], which uses a plane wave implementation to describe the valence electrons and Vanderbilt ultrasoft pseudo-potentials [270] to represent the ionic cores. The kinetic energy cutoff was 340 eV with a density cutoff of 500 eV. All calculations were performed using the RPBE [271] functional, which uses a generalized gradient approximation. The self-consistent electron density was determined by iterative diagonalization of the Kohn-Sham Hamiltonian, with the occupation of the Kohn-Sham states being smeared according to a Fermi-Dirac distribution with a smearing factor of $k_bT = 0.1$ eV and Pulay mixing of the resulting electron densities [272]. Spin-polarized calculations have been performed for Fe, Co and Ni.

The stepped surface structures were modeled by 9 layer slabs with (1x3) unit cells. The uppermost close-packed surface layer together with the adsorbates was allowed to relax, whereas the remaining layers have been kept fixed in their RPBE calculated bulk positions. In all cases a sampling of 3x3x1 special k-points of the Monkhorst-Pack type was used to model the 1st Brillouin zone [273]. Increasing the number of *k*-points has shown a negligible effect on adsorption energies. The periodic slab approximation was used and stepped surfaces have been modeled by fcc(211) for (100) symmetry steps and fcc(331) for (111) symmetry steps. The slabs were separated by at least 12 Å of vacuum. Lattice constants of binary alloys were calculated in a periodic cell consisting of 4 atoms with a 8x8x8 *k* point sampling. Slabs of binary alloys were modeled as described above for transition-metal surfaces.

Transition state energies were determined using a fixed bond-length approach in which the

distance between the involved atoms is increased until a saddle-point was reached. The vibrational frequencies that were used to determine the zero-point energy and entropy corrections were calculated in the harmonic normal-mode approximation.

4.5.2 Catalyst preparation

Silica supported CuNi catalyst (20 wt % Cu+Ni loading on silica, molar ratio of Cu:Ni = 1:1) oxide precursors were prepared by the incipient wetness impregnation method. First, an aqueous solution was prepared by dissolving $Cu(NO_3)_2 \cdot 3H_2O$ and $Ni(NO_3)_2 \cdot 6H_2O$ in de-ionized water. Then SiO_2 (with a BET specific surface area of 250 m^2/g) pellets was impregnated by the aqueous solution. After 1 h aging, catalysts were dried at 100 °C in air, and subsequently calcined at 400 °C in air for 4 h with a heating rate of 1.5 °C/min.

A model methanol synthesis $Cu/ZnO/Al_2O_3$ catalyst was prepared by a co-precipitation method similar to that used by Baltes et al. [274]. An aqueous solution of metal nitrates [($Cu(NO_3)_2$ (0.6 mol/L), $Zn(NO_3)_2$ (0.3 mol/L), $Al(NO_3)_3$ (0.1 mol/L))] was coprecipitated by a solution of Na_2CO_3 (1 mol/L) . During the precipitation process, pH was maintained at 7±0.1, temperature was kept at 60 °C, and then aged at 60 °C for 1 h. Afterwards the precipitate was filtered and washed three times with demineralized water followed by drying overnight at 80 °C and calcining at 300 °C under air for 3 h (heating rate 2 °C /min).

All chemicals were supplied by Sigma-Aldrich except SiO_2 that was offered by Saint-Gobain Norpro. All the catalyst precursors have been pressed, crushed and sieved to a size range of 0.6-1.4 mm.

4.5.3 Catalyst characterization

The chemical composition of $CuNi/SiO_2$ and $Cu/ZnO/Al_2O_3$ catalysts were determined by an inductively coupled plasma-optical emission spectrometer (ICP-OES, Perkin–Elmer, model Optima 7300) and using Ar as plasmogene.

In situ XRD was applied with a PANalytical X'Pert PRO diffractometer equipped with an Anton Paar XRK 900 in situ cell (APC), a gas flow control system, a Ni filter and a slit for H_2-TPR. $CuNi/SiO_2$ and $CuZnO/Al_2O_3$ precursors were heated in flowing 20 mol % H_2/He up to 300 °C and 220 °C, respectively. The average particle diameter ($d_{p,XRD}$) of reduced phases (cooling down to room temperature after reduction) were determined by means of the Sherrer equation [275].

In situ TEM was performed using an FEI Titan 80-300kV TEM equipped with an environmental cell and a differential pumping system [276, 277]. This microscope permits the acquisition of TEM images of samples during the exposure to reactive gases (up to ca. 15 mbar) and elevated temperatures. For the present experiments, the specimen was imaged during the exposure to 1.3 mbar H_2. The specimen was heated in the gas environment at a rate of 7 °C/min from room temperature up to 300 °C for $CuNi/SiO_2$ catalyst precursor. The TEM imaging was performed after drift-stabilization of the sample holder.

4.5.4 Catalyst activity testing

The performance of catalysts for CO hydrogenation was evaluated in a fixed-bed continuous-flow reactor (detailed descriptions of the experimental setup and the experimental procedure have been provided elsewhere) [96, 196, 197] with an online GC-FID/TCD detection system (6890N from Agilent Technologies). A bubble flow meter was used for determination of volumetric flow rate of the reactor effluent. Prior to the reaction, all catalysts oxide precursors were pre-reduced in

situ by a 20 vol % H_2/N_2 mixture for $CuNi/SiO_2$ at 300 °C and 1.4 vol % H_2/N_2 at 220 °C $Cu/ZnO/Al_2O_3$ for 12-14 h, with a heat rate of 1 °C/min. The conversion of CO (X_{CO}) is calculated from the molar flow rates of CO into and out of the reactor:

$$X_{CO} = \frac{F_{CO}^{in} - F_{CO}^{out}}{F_{CO}^{in}} \cdot 100\%$$

The CO_2-free selectivity to product is based on the total number of carbon atoms except CO_2 in the products:

$$S_i = (n_i M_i) / (\sum n_i M_i) \cdot 100\%$$

Where n_i ($n_i \geq 1$) is the number of carbon atoms in the product $\boldsymbol{i}$, M_i is the detected percentage of product $\boldsymbol{i}$ in the gas.

The mass balances for carbon generally fulfilled to within 5 mol %.

Appendix A. Supplementary data

Supplementary data associated with this article can be found, in the online version, at http://dx.doi.org/10.1016/j.jcat.2012.06.004.

5 CO hydrogenation on Cu-Ni catalysts: Influence of supports

5.1 Abstract

Copper-nickel catalysts supported on SiO_2, ZrO_2, γ-Al_2O_3, and carbon nanotubes (CNT) exhibit very different selectivities during CO hydrogenation. However, the metal area based activities of all supported Cu-Ni catalysts are at the same level. CNT and SiO_2 supported Cu-Ni catalysts show high activity and selectivity for methanol synthesis. The metal area based activity of both Cu-Ni/CNT and Cu-Ni/SiO_2 catalysts is comparable to a model industrial Cu/ZnO/Al_2O_3 catalyst. The γ-Al_2O_3 supported Cu-Ni catalyst contains a significant amount of acid sites (333 µmol g^{-1}) and produces predominantly dimethyl ether. The Cu-Ni/ZrO_2 catalyst exhibits high methanol selectivity at lower temperatures (250 °C), which shifts to hydrocarbons and dimethyl ether at higher temperatures (> 275 °C). It seems that the Cu-Ni alloy always produce methanol, but that some supports (ZrO_2 and γ-Al_2O_3) further convert methanol to different products (hydrocarbons and dimethyl ether). A combination of in situ XAS, XRD and TEM studies on supported Cu-Ni catalysts shows that the support influences the reduction processes and consequently the formation of Cu-Ni alloys and their CO hydrogenation activity.

5.2 Introduction

Fossil fuel resources are limited, and the demand for energy around the world is growing rapidly [2]. Meanwhile, it is obvious that the emission of CO_2 that follows the use of fossil fuels is threatening the climate of the earth [3, 4]. Liquid fuels from renewable sources such as biomass are clean, sustainable and transportable fuel alternatives or fuel additives [21, 27, 40, 143, 218, 278]. Methanol [6, 102, 279-281], dimethyl ether (DME) [48, 282, 283], mixed long chain alcohols [8, 18, 196, 284, 285], and Fisher-Tropsch (FT) synthetic diesel [139, 141, 286] can be catalytically synthesized from syngas, which can potentially be derived from biomass gasification [13, 14, 37]. These processes are summarized in several reviews [19-21, 27-30]. Methanol, currently produced from syngas over Cu/ZnO-based catalysts, is an efficient fuel in an internal combustion engine or in a fuel cell, and has therefore been suggested as the main energy carrier of the future [47]. Despite the very high current levels of methanol production, the replacement of gasoline would require more than a hundredfold increase in methanol production [50, 57]. In this respect, the deactivation of the commercial Cu/ZnO methanol synthesis catalyst is a major issue [64-66, 130]. More than one third of the activity is typically lost after the first 1000 h of operation, and this determines the economic lifetime of the catalyst [130, 238]. Therefore, methanol synthesis catalysts with greater activity and stability are highly desired.

Based on both density functional theory (DFT) calculations and activity tests for CO hydrogenation we recently identified Cu-Ni alloys supported on SiO_2 as promising methanol synthesis catalysts [6]. There is however significant ambiguity in the literature concerning the properties of Cu-Ni catalysts in syngas conversion. It has been previously reported that Cu-Ni catalysts were active for higher alcohol synthesis on a titanium oxide support [223, 230], hydrocarbon synthesis on a silica support [231], and methanol synthesis on alumina [228], silica [6, 225] or zinc oxide [231] supports. It seems that the support material affects the products formed over Cu-Ni based catalysts. Therefore, it would be valuable to systematically investigate the effect of support on the catalytic properties of Cu-Ni catalysts and determine their structures by in situ techniques such as X-ray diffraction (XRD) and in situ X-ray absorption spectroscopy (XAS), which can clarify the degree of reduction and the extent of alloying in Cu-Ni catalysts.

Here, we present the effect of different supports: SiO_2, ZrO_2, γ-Al_2O_3, and carbon nanotubes (CNT) on the Cu-Ni alloy formation and subsequently on their activity and selectivity in CO hydrogenation. In situ XAS, in situ XRD, in situ transmission electron microscopy (TEM) and temperature-programmed desorption of ammonia (NH_3-TPD) have been used to identify the structure of these catalysts. Additionally, a model industrial $Cu/ZnO/Al_2O_3$ methanol synthesis catalyst is prepared and tested for activity comparison.

5.3 Experimental

5.3.1 Catalyst preparation

Cu-Ni based catalysts were prepared by the incipient wetness impregnation method. First, an aqueous solution was prepared by dissolving $Cu(NO_3)_2 \cdot 3H_2O$ and $Ni(NO_3)_2 \cdot 6H_2O$ (Sigma-Aldrich) in de-ionized water. Then, the pre-made SiO_2, ZrO_2, γ-Al_2O_3 and CNT pellets were impregnated with the aqueous solution. After 1 h aging at room temperature, the catalysts were dried at 100 °C in air, and subsequently calcined at 400 °C in air for 4 h with a heating rate of 1.5 °C min^{-1}. Loading levels were selected based on the following calculation: 20 wt % (Cu + Ni) loading on 80 wt % support with a molar ratio of Cu:Ni = 1:1. Additionally, CNT were purified according to the procedure of Pan et al. [209] by refluxing 5 g commercial CNT (Sigma-Aldrich, 724769) in 500 ml 37 wt % nitric acid at 110 °C for 5 h, followed by filtration, washing, and drying before impregnation. All the catalysts have been crushed and sieved to 0.6-1.4 mm granule size. Table 5-1 shows the physical parameters of all support materials used for preparation of the supported Cu-Ni catalysts. Additionally, commercial CuO and NiO (1:1 weight ratio, 1.08:1 molar ratio) were mechanically mixed as a reference sample for in situ XRD and in situ XAS measurements.

Table 5-1 Support materials used for preparation of Cu-Ni alloy catalysts.

Support	Pore volume mL g^{-1} (water/support)	Surface area m^2 g^{-1}	Supplier
SiO_2	1.28	200	Saint-Gobain Norpro
ZrO_2	0.46	134	Saint-Gobain Norpro
γ-Al_2O_3	0.80	166	Haldor Topsøe A/S
CNT	1.31	328	Sigma-Aldrich

For activity comparison, a model $Cu/ZnO/Al_2O_3$ (molar ratio of Cu/Zn/Al = 6/3/1) methanol synthesis catalyst was prepared by co-precipitation according to the recipe reported by Baltes et al. [274]. During the precipitation, pH was maintained at 7.0 ± 0.1, the temperature was kept at 60 °C, and the precipitate was then aged at 60 °C for 1 h. Afterwards the precipitate was filtered and washed, followed by drying overnight at 80 °C and calcination at 300 °C in air for 3 h (heating rate 2 °C min^{-1}).

5.3.2 Catalyst characterization

In situ XAS studies were performed at the ANKA-XAS beamline using a Si(111) double-crystal monochromator detuned to approximately 60% of the maximum intensity. Incident and transmitted X-ray intensities were measured by ion chambers. A newly fabricated, homemade in situ transmission cell was employed (similar to the one used in Ref. [287]). The cell consisted of a stainless steel cylinder with a central 2x10x2 mm hole closed on both sides with two graphite windows and connected to the in- and outlet gas lines, in which a suitable amount of granulated

catalyst (100-200 μm) was placed. The cell was inserted between two heating blocks for temperature control. Quick extended X-ray absorption fine structure (EXAFS) spectra at the Ni K- (8333 eV) and at the Cu K- (8979 eV) edges were recorded in continuous mode from 8.25 to 9.25 keV with a step size of 1.5 eV. For energy calibration, a Ni foil was used. The in situ XAS experiments during temperature programmed reduction (TPR) were carried out under 5 mol % H_2 in He flow (40 mL min^{-1}) heating up to 410 °C with a heating rate of 5 °C min^{-1} while recording quick EXAFS spectra. Additionally, during the catalytic tests the samples were pre-reduced at 300 °C. Hence, additional in situ XAS investigation were performed on the Cu-Ni/CNT and Cu-Ni/Al_2O_3 samples under dilute syngas at 300 °C, in order to elucidate the reduction state of Cu and Ni under simulated working conditions (1 bar). Here X-ray absorption near edge structure (XANES) spectra were recorded during reduction in 5 mol % H_2/He up to 300 °C followed by a 40 minute isotherm at 300 °C and a succeeding change of the gas mixture to dilute syngas (2.5 mol % H_2 + 2.5 mol % CO/He). The composition of the outlet gas was monitored with a Pfeiffer Quadruple Mass Spectrometer (QMS). The obtained spectra were analyzed and fitted using the Athena and Artemis programs [288]. The fractions of Cu(II) and Ni(II) were determined by linear combination analysis of the XANES spectra recorded at a given temperature by comparing the spectrum to reference CuO (or NiO) and Cu (or Ni) foil.

In situ X-ray diffraction (XRD) measurements on Cu-Ni/CNT, Cu-Ni/Al_2O_3 and a reference bulk CuO and NiO mechanical mixture (1:1 weight ratio) were performed at the ANKA-PDIFF beamline at the synchrotron of Karlsruhe. The X-ray diffraction patterns were recorded using a monochromatic beam at 16 keV (λ = 0.774 Å) by means of a 90° curved Position Sensitive Detector, PSD (Inel CPS590). For a better comparison the 2θ axis of the XRD patterns were converted to the more common laboratory wavelength of the Cu *Kα* radiation (λ = 1.5406 Å) by applying the Bragg equation. The obtained patterns were compared with the Inorganic Crystal Structure Database (ICSD) data for phase identification. The combined TPR-XRD experiments were carried out in flowing 5 mol % H_2/He (20 mL min^{-1}) while heating with a rate of 2.5 °C min^{-1} employing a quartz capillary reactor (diameter of 1 mm) containing the crushed and sieved (100-200 μm) sample. The sample was heated in a controlled way with a hot air blower (Oxford) placed under the capillary, as described in Ref. [289]. In situ XRD measurements on Cu-Ni/ZrO_2, Cu-Ni/SiO_2, and the model Cu/ZnO/Al_2O_3 catalysts were conducted with a PANalytical X'Pert PRO diffractometer equipped with an Anton Paar XRK 900 in situ cell, a gas flow control system and a slit for H_2-TPR. All catalysts were reduced by a flow of 20 mol % H_2/He (100 mL min^{-1}) for 1 h at 300 °C (220 °C for the model Cu/ZnO/Al_2O_3 catalyst).

An environmental transmission electron microscope (ETEM) equipped with a differential pumping system to confine a controlled flow of gas around the specimen was used. This allows observation in a gaseous environment (FEI Titan E-cell, monochromatic, objective lens aberration corrector, Gatan imaging filter) [276, 277, 290]. In combination with a heating holder, this microscope allows studies of catalysts, using a variety of TEM techniques in situ, mimicking the real working conditions. In the present experiments, the specimen was imaged while being exposed to 1.3 mbar H_2. The specimen was heated in the gas environment at a rate of 7 °C min^{-1} from room temperature up to 300 °C for Cu-Ni/SiO_2 and Cu-Ni/CNT catalyst precursors. The TEM imaging was done after drift-stabilization of the sample holder was performed.

NH_3-TPD was performed with a Micromeritics AUTOCHEM II equipped with a TCD detector as follows. First, 115 mg of the sample was loaded into a quartz tube reactor and saturated with ammonia (50 mL min^{-1}, 1 vol % NH_3/N_2) for 1 h at room temperature. Before the NH_3 desorption measurement, the sample was heated to 100 °C in a dry helium flow (50 mL min^{-1}) and held at this

temperature for 2 h to remove physisorbed ammonia. Then the sample was cooled to 50 °C, after which the temperature was raised at a rate of 10 °C min^{-1} up to 500 °C.

5.3.3 Catalyst testing

Performance of catalysts for CO hydrogenation was tested in a fixed-bed continuous-flow reactor with an online gas chromatograph equipped with flame ionization and thermal conductivity detectors (6890N GC-FID/TCD from Agilent Technologies). The amounts of catalysts and the syngas flow rates for the activity tests are listed in Table S1 (in Appendix B, supplementary information). The details of setup are given by Christensen et al. [96, 197]. Methanol, ethanol, 1-propanol, 1-butanol, 2-butanol, and 2-methyl-1-propanol, methane, ethane, ethene, and propane, as well as DME and ethyl acetate were characterized. A bubble flow meter was used for determination of volumetric flow rate of the reactor effluent. Prior to the reaction, the oxide precursors loaded in the reactor were reduced in situ at 1 atm. total pressure by a flow of 20 mol % H_2 in N_2 for 12-14 h at 300 °C which was reached using a heating rate of 1.5 °C min^{-1}. The model $Cu/ZnO/Al_2O_3$ catalyst was reduced by a flow of 1.4 mol % H_2 in N_2 for 12-14 h at 220 °C with a ramping rate of 1.5 °C min^{-1}. The carbon mass balance is generally fulfilled to within 5 mol %.

The conversion of CO (X_{CO}) is calculated from on the molar inlet flow of CO ($n_{CO,in}$) and the outlet molar flow of carbon in the products ($n_{c,products}$):

$$X_{CO} = \frac{\sum n_{c,products}}{n_{CO,in}} \cdot 100\%$$

The CO_2-free selectivity to a given product (S_i) is based on the total number of carbon atoms in the products excluding CO_2:

$$S_i = (n_i y_i) / (\sum n_i y_i) \cdot 100\%$$

where n_i ($n_i \geq 1$) is the number of carbon atoms in component *i*, and y_i is the molar fraction of component *i* in the product.

An additional performance parameter is the space time yield (STY_{MeOH}) of methanol, which is the production rate of methanol per mass of catalyst:

$$STY_{MeOH} = \frac{M_{MeOH} F_{MeOH}}{m_{cat}}$$

where, M_{MeOH} is the molar mass of methanol and F_{MeOH} is the molar flow rate of methanol out of the reactor. Here, we report the space time yield (*STY*) in the units of mass of methanol produced per hour and per mass of catalyst (m_{cat}), which includes both active metals and support.

5.4 Results and discussion

5.4.1 Catalyst structure

5.4.1.1 In situ XAS during reduction and reaction

Fig. 5-1 shows a typical set of XANES spectra at the Ni K- and Cu K-edges for the Cu-Ni/CNT material. Here, a 3D-representation has been chosen. In the electronic support information (Appendix B, Fig. S1) an alternative 2D-projection is depicted. All of the tested materials show a similar development of the in situ XANES spectra at both the Ni K- and Cu K- edges during reduction in 5 mol % H_2/He. The starting material displays an intense whiteline at both edges

indicating the presence of Ni(II) and Cu(II) which stem from the calcination of the corresponding nitrate precursors. By increasing the temperature, the whiteline decreases in intensity, whereas the edge shifts slightly towards lower energy with the appearance of a pre-edge, indicating the reduction of the two elements to their metallic state.

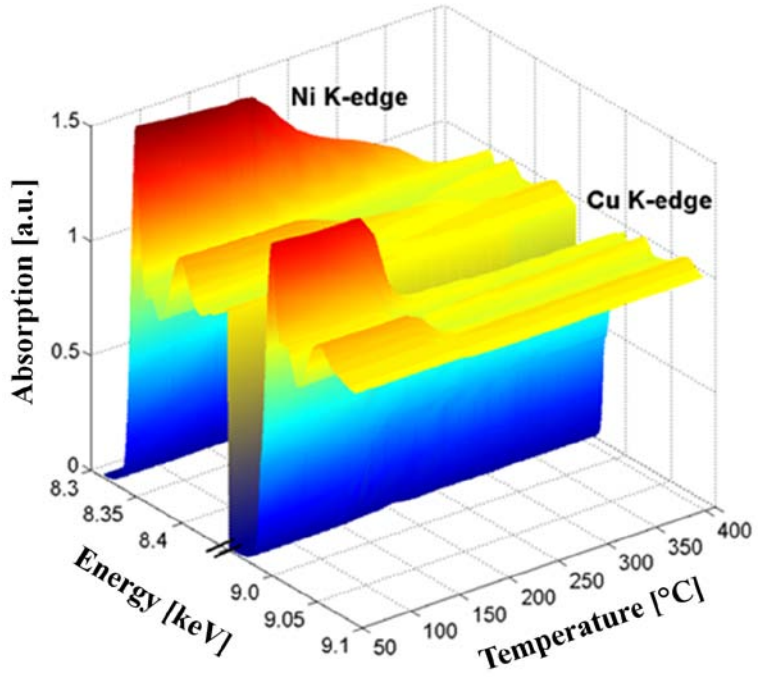

Fig. 5-1 Typical XANES spectra at Ni K- and Cu K- edges recorded at different temperatures (at every 15 °C) during reduction of Cu-Ni/CNT. Experimental conditions: 1 bar; 5 mol % H_2/He (40 mL min^{-1}); temperature increase from 50 to 406 °C using a heating ramp of 5 °C min^{-1}. The whiteline intensity decreases and the edge shifts towards lower energy with increasing temperature (cf. Appendix B, Fig. S1), due to the reduction of Ni(II) and Cu(II).

Linear combination analyses (LCA) of the XANES spectra of all of the studied Cu-Ni samples are shown in Fig. 5-2 together with the corresponding TPR profiles given by the m/z=18 QMS signal intensity (corresponding to H_2O evolution) vs. temperature. The LCA shows the fraction of Cu(II) and Ni(II) as functions of temperature, which is useful for the interpretation of the TPR profile. The investigated samples exhibit significantly different TPR profiles, depending on the type of the support. A closer look at the Cu(II) and Ni(II) reduction vs. temperature trends reveals that Ni is much more influenced by the support type than Cu. In all cases CuO is reduced in a single step between 160 and 200 °C. In general, reduction of NiO begins at a higher temperature on the supported samples compared to the CuO, and except for the SiO_2 supported sample, proceeds in multiple steps. We observe the following:

i) For the reference CuO + NiO mixture sample, the QMS-TPR profile displays two reduction steps, centered at 200 and 240 ºC, respectively. In situ XANES shows that CuO starts to be reduced at around 160 °C, and NiO reduction starts at 210 °C.

ii) A single-broad QMS-TPR peak centered at 240 ºC can be observed for the silica supported sample, and in situ XANES shows that NiO and CuO are reduced simultaneously around 200 ºC. The simultaneous reduction could indicate the formation of alloy, which will be discussed later with the XRD analysis.

iii) The QMS-TPR profile of Cu-Ni/CNT displays a second peak at 340 ºC, which is attributed to the reduction of a small fraction of isolated NiO phase. Similar results were obtained over the ZrO_2

sample, except for a split of the first main peak, suggesting that metallic Cu is first formed, and then promoting the succeeding reduction of Ni.

iv) The γ-Al_2O_3 supported sample shows a significantly different reduction profile. Both NiO and CuO are completely reduced at 375 °C in the other samples, whereas on Al_2O_3 a reduction temperature of 600 °C is required in order to achieve complete reduction of Ni. This suggests the presence of an additional Ni-containing species (possibly $NiAl_2O_4$ spinel), which might have formed during the calcination process [291]. Also for copper a high temperature tail is observed, probably due to reduction of small fractions of $CuAl_2O_4$, as reported in earlier studies for low copper loadings [292].

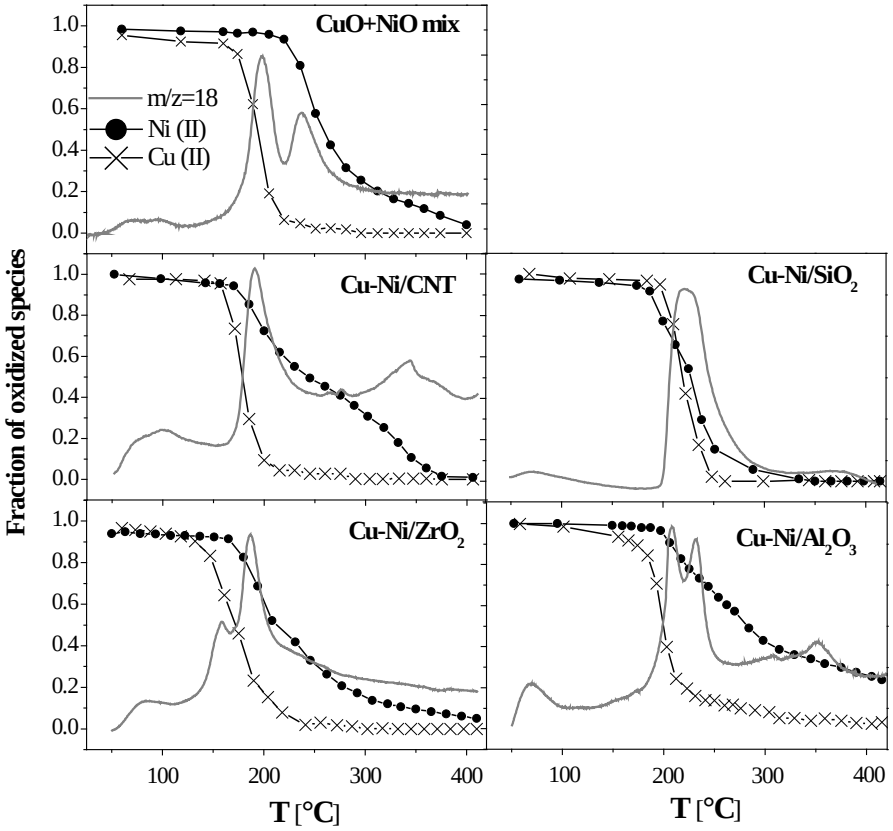

Fig. 5-2 Linear combination analysis of XANES spectra at Ni K-edge and Cu K-edge showing the Cu(II) (×) and Ni(II) (●) fractions vs temperature overlapped with the water signal (m/z=18) during QMS-TPR (solid line) of mechanical CuO + NiO mixture, Cu-Ni/SiO_2, Cu-Ni/CNT, Cu-Ni/Al_2O_3, and Cu-Ni/ZrO_2 during reduction: 1 bar; 5 mol % H_2/He (40 mL min^{-1}); heating ramp 5 °C min^{-1}.

The Cu-Cu shell is very difficult to distinguish from the Cu-Ni shell and vice-versa because Ni and Cu have similar atomic radii and backscattering factors. Thus the EXAFS investigation can give element-specific information on the reduction behavior, but alone it is not enough to confirm the formation of an alloy. We have used the combination of XAS results with in situ XRD, which will be discussed later. Fitting of the Fourier transformed, k^3-weighted EXAFS spectra (Appendix B, Table S2 and Fig. S2 in supplementary information) gives coordination numbers (CN) for the Ni-Ni(Cu) and Cu-Cu(Ni) shells ranging from 9.5 for the Al_2O_3 supported, to 11.2 for the SiO_2 supported catalyst. These high CN typically indicate the presence of relatively large particles [293].

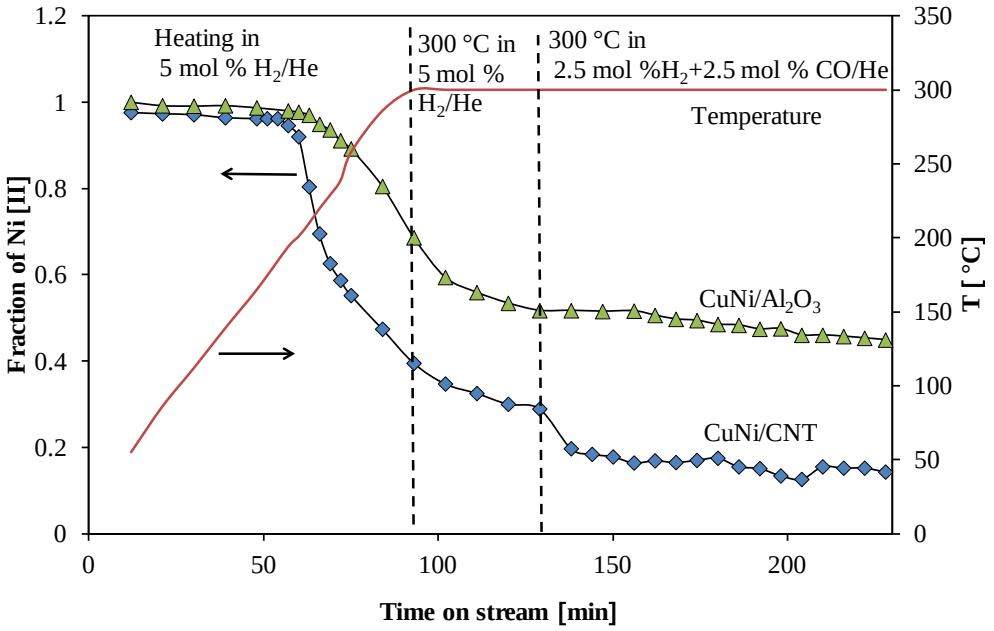

Fig. 5-3 Comparison of fraction of Ni(II) in CuNi on CNT (circles) and on Al_2O_3 (triangles) obtained by linear combination analysis of XANES spectra recorded during reduction in 5 mol % H_2/He up to 300 °C followed by 40 minutes isotherm at 300 °C and succeeding switch of the gas mixture to syngas (2.5 mol % H_2 + 2.5 mol % CO/He) at 1 bar.

Equally important is the clarification of the oxidation state of catalysts under reaction conditions. During the catalytic tests the samples are pre-reduced at 300 °C and 1 atm. total pressure. Hence, additional in situ XAS investigations were performed on the Cu-Ni/CNT and Cu-Ni/Al_2O_3 samples under dilute syngas at 300 °C, in order to elucidate the reduction state of Cu and Ni under simulated working conditions. Copper is fully reduced below 300 °C (not shown, as in agreement with results in Fig. 5-2) and remains reduced also under syngas. However, with respect to the nickel, a significant fraction of oxidized species in both samples is still observed (50% for Cu-Ni/Al_2O_3 and 40% for Cu-Ni/CNT as estimated from LCA; Fig. 5-3), which is further reduced during time on stream (Fig. 5-3, t = 90 to 130 minutes). Strikingly, the nickel is reduced further in the Cu-Ni/CNT when adding carbon monoxide in a 1:1 molar ratio to the hydrogen (up to the 90%), reflecting syngas reaction conditions. Considering the much higher reduction potential of the syngas used in our catalytic tests, due to the higher total pressure and higher mole fraction of reductive species, copper and nickel are probably in their reduced metallic states under reaction conditions. Similar behavior might be expected over the Cu-Ni/ZrO_2 sample, which possesses similar TPR profiles to the Cu-Ni/CNT sample above 300 °C (Fig. 5-2). By contrast, Ni is hardly further reduced in Cu-Ni/Al_2O_3, and at the end of the experiment it is still 45% oxidized (Fig. 5-3); hence here significant amounts of oxidized nickel can be expected on this sample, in the form of incorporated nickel, e.g, as nickel aluminates.

In summary, the in situ XAS study demonstrated that in the fresh catalyst nickel is present in different forms i.e. partially mixed with Cu (possibly in a $Cu_xNi_{1-x}O$ structure), which is reduced at lower temperatures, and as isolated NiO and possibly $NiAl_2O_4$ in the case of the alumina supported sample [291], which are reduced at higher temperatures. These latter species are generated in the catalyst preparation process, during calcination.

5.4.1.2 In situ XRD studies

Typically, high CN indicates the presence of relatively large particles [293] (Appendix B, EXAFS data in Table S2), therefore, XRD can be used to distinguish the Cu-Ni alloy phase from those of the isolated metals. Cu and Ni have two main reflections, belonging to the [111] and the [002] crystal planes, at 43.17° and 50.27° for Cu (ICSD file 53758) and at 44.50° and 51.85° for Ni (ICSD file 52265), respectively. The two pairs of reflections are sufficiently separated to be distinguished and can be seen in the XRD pattern of the CuO+NiO mixture after reduction at 300 °C (Fig. 5-4). In contrast, a Cu-Ni alloy produces a single pair of reflections for the [111] and [002] crystal planes, both located along the 2θ scale at an intermediate position with respect to those of the two pure metals. This position may be closer to Cu or to Ni depending on the Cu:Ni molar ratio of the sample (Appendix B, Table S3 in supplementary information). The in situ XRD results on CuO+NiO mixture, Cu-Ni/CNT and Cu-Ni/Al_2O_3 are shown in Fig. 5-4 and these results are in agreement with the XAS results (see Fig. 1). The color maps, shown under the XRD patterns, illustrate the changes in the XRD reflections through the temperature changes (the chromatic scale is proportional to the counts). All three fresh samples exhibit the characteristic reflections of CuO at 35.56° and 38.75° (ICSD file 16025) and of NiO at 37.24° and 43.28° (ICSD file 92133) initially. The high mutual solubility of Cu and Ni [294] allows formation of different $Cu_xNi_{1-x}O$ species and also X-ray invisible species during the calcination. The XRD patterns of these species are similar to that of pure NiO, except for a slight shift towards lower 2θ angles (e.g. ICSD file from 61545 to 61549). Thus $Cu_xNi_{1-x}O$ mixed oxide species might be present, but they are difficult to identify in the XRD patterns.

Fig. 5-4 shows that for the CuO+NiO sample the XRD pattern of CuO phase disappears around 180 °C with the simultaneous appearance of the two characteristic reflections of metallic Cu. Around 240 °C the second pair of reflections of metallic Ni appears. For the Cu-Ni/CNT sample, only a single diffraction reflection appears during the reduction, confirming the formation of a Cu-Ni alloy. According to the Scherrer equation [295] the particle size is about 6 nm. Moreover, this signal shifts very slightly towards higher 2θ angles over the temperature range of 220-350 °C (Appendix B, Fig. S5, in supplementary information). This could suggest that a fraction of the NiO that is being reduced at a higher temperature is incorporated in the Cu-Ni alloy, increasing the Ni content of the alloy. This is supported by the reduction of several Ni species at higher temperature as found by XAS (Fig. 5-2).

Different reduction stages are observed on the Cu-Ni/Al_2O_3 (Fig. 5-4) and Cu-Ni/SiO_2 (Appendix B, Fig. S6, in supplementary information) samples, where first the formation of copper and then the Cu-Ni alloy formation are seen (reflection centered at 43.16° due to metallic Cu and 43.90° due to Cu-Ni). These two reflections already appear at 150-200 °C in the case of Cu-Ni/SiO_2 (Cu and Ni are simultaneously reduced below 200 °C according to XAS), whereas on Cu-Ni/Al_2O_3 the metallic Cu appears first at 200 °C followed by the growth of the second reflection between 300-600 °C. The XRD pattern of the Cu-Ni/Al_2O_3 sample exhibits a strong reflection at 37.1° together with a weaker reflection located at 45.1° ($NiAl_2O_4$ spinel, ICSD file 247076). This phase is more difficult to reduce than NiO. The presence of $NiAl_2O_4$ phase thus hinders the low temperature formation of a Cu-Ni alloy in consistency with XAS data (Fig. 5-2). The XRD patterns of reduced Cu-Ni/ZrO_2 and a reference model Cu/ZnO/Al_2O_3 catalysts are shown in the supplementary materials. The XRD particle sizes (based on the Scherrer equation [295]) and active surface areas of all reduced samples are calculated and summarized in the Table 5-2. The particle size of Cu-Ni alloys is in the same range for all supported Cu-Ni catalysts, 15±1 nm, except the one supported on CNT that has a particle size of only 6 nm. This is probably related to the initial specific surface area of the CNT support which is about twice as high as the others (in Table 5-1).

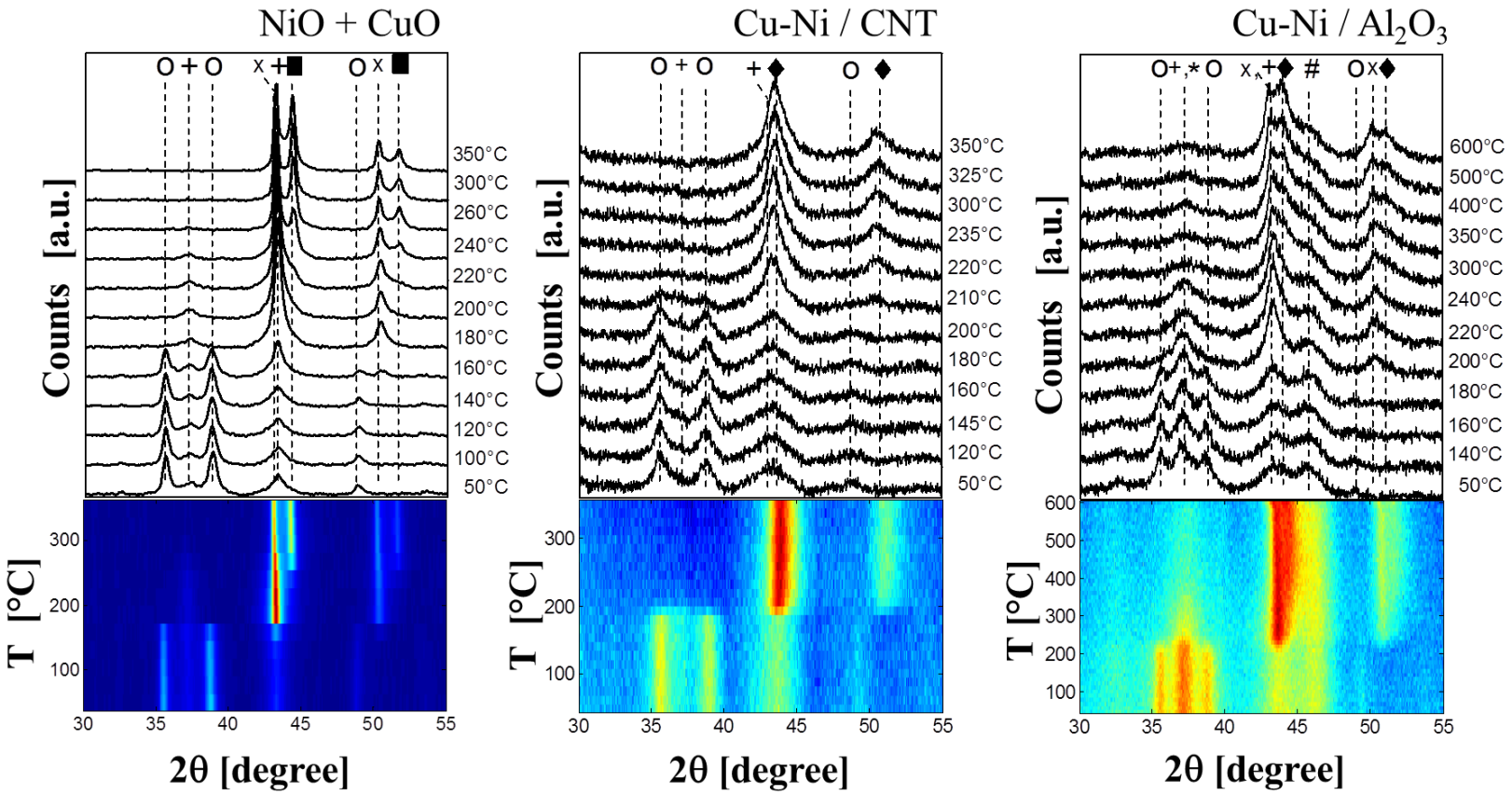

Fig. 5-4 In situ XRD of reference NiO+CuO mixture (left panel), Cu-Ni/CNT (central panel) and Cu-Ni/Al_2O_3 (right panel) during reduction in 5 mol % H_2/He. Selected XRD at the indicated temperatures (top panels) and color map plots (lower panels) with temperature and 2θ on the axis and chromatic scale proportional to the counts. The symbols indicate the main reflections of: (o) CuO; (+) NiO or $Cu_xNi_{1-x}O$; (*) $NiAl_2O_4$; (#) Al_2O_3; (x) metal Cu; (■) metal Ni; (◆) Cu-Ni alloy.

Table 5-2 XRD particle sizes and active surface areas of all reduced supported Cu-Ni and $Cu/ZnO/Al_2O_3$ samples, as well as acidity of all supported Cu-Ni samples.

Catalysts	d_{XRD} [nm]	Calculated weight of active metal [1)] [g g_{cat}^{-1}]	$S_{active\ metal}$ [$m^2\ g^{-1}$]	Acidity [µmol g^{-1}]
$Cu-Ni/SiO_2$	14	0.17	8.2	39
Cu-Ni/CNT	6	0.17	19.0	49
$Cu-Ni/Al_2O_3$	14	0.17	8.2	333
$Cu-Ni/ZrO_2$	16	0.17	7.1	309
$Cu/ZnO/Al_2O_3$	6	0.45	50.3	-

[1)] Active metal for supported Cu-Ni catalysts is metallic Cu+Ni, the weight is estimated according to elemental analysis of $Cu-Ni/SiO_2$ sample; for $Cu/ZnO/Al_2O_3$ catalyst is metallic Cu, which is determined by elemental analysis.

In general, Cu and Ni can easily form a solid solution [265]. However, we only observed the formation of a pure Cu-Ni alloy on Cu-Ni/CNT, whereas on $Cu-Ni/SiO_2$, $Cu-Ni/Al_2O_3$, and $Cu-Ni/ZrO_2$ both the Cu-Ni alloy and metallic copper are formed, which may be attributed to: *i*) the catalyst precursors transform into several metal oxide phases, i.e individual crystallites of CuO and NiO together with crystalline or amorphous $Cu_xNi_{1-x}O$ (and $NiAl_2O_4$ species); and *ii*) the support confinement effect because of the microporous structure morphology, which is dominant in SiO_2, Al_2O_3, and ZrO_2. Indeed, copper sinters easily under strongly reducing conditions (20 mol % H_2/ N_2) and forms rather large particles, which then cannot move and merge with Ni, if they are confined in the micropores. However, for the particular morphology of the CNT that contains only mesopores [296], pore confinement is probably less influential and therefore even though reduction takes place in two steps, the reduction leads to the formation of Cu-Ni alloy particles as evidenced by XAS.

5.4.1.3 In situ TEM studies

Fig. 5-5 shows TEM images of $Cu-Ni/SiO_2$ and Cu-Ni/CNT catalysts in their precursor and reduced (in situ at 300 °C) states as well as the particle size distributions. A statistical analysis of the TEM images for both reduced samples reveal average particles sizes of 10.6 nm (112 particles) and 6.8 nm (55 particles) for $Cu-Ni/SiO_2$ and Cu-Ni/CNT catalysts, respectively. Only 55 particles were counted for the Cu-Ni/CNT catalyst because of strong agglomeration of the CNT, which makes it difficult to visualize single particles on the reduced samples. The particle sizes of Cu-Ni alloys obtained from TEM are close to the ones that are estimated from the line width of the XRD patterns, 14 nm and 6 nm for $Cu-Ni/SiO_2$ and Cu-Ni/CNT catalysts, respectively.

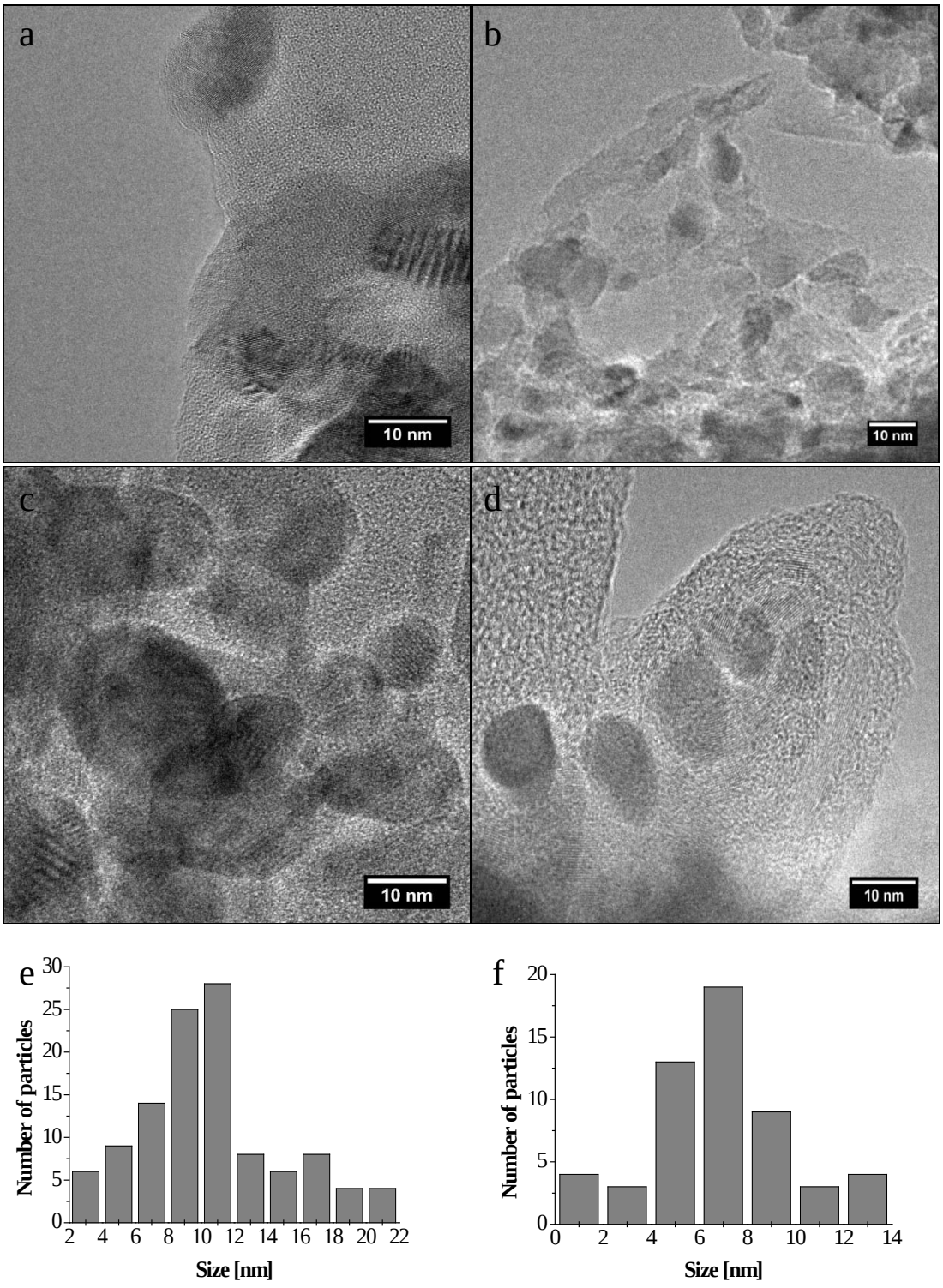

Fig. 5-5 TEM images of selected supported Cu-Ni samples. (a) Cu-Ni/SiO_2 (fresh). (b) Cu-Ni/CNT (fresh). (c) Cu-Ni/ SiO_2 (reduced in situ). (d) Cu-Ni/CNT (reduced in situ). (e) Particle size distribution of reduced Cu-Ni/SiO_2. (f) Particle size distribution of reduced Cu-Ni/CNT.

5.4.1.4 NH_3-TPD measurements

The surface acidity is calculated from the NH_3-TPD measurements as the amount of desorbed ammonia per gram of catalyst at standard conditions. The ammonia concentration in the off gas during desorption as function of temperature can be found in the supplementary materials (Appendix B, Fig. S9). The results obtained for all supported Cu-Ni catalysts are listed in Table 5-2. Cu-Ni/Al_2O_3 and Cu-Ni/ZrO_2 catalysts show much higher acidity (333 µmol g^{-1} and 309 µmol g^{-1}, respectively) than the other catalysts. Typically, acid sites would contribute to dehydrogenation reactions. This will be further discussed in the following section.

5.4.2 Catalyst activity and selectivity

5.4.2.1 Time on stream catalytic behavior

Fig. 5-6 shows the development of CO conversion and methanol selectivity as functions of the time on stream for the Cu-Ni/CNT catalyst. The CO conversion increases from 0.8% to 4.4% during 45 h and then stabilizes. The selectivity to methanol is also improved from 97.6 mol % to a stable level of 98.9 mol %, while the selectivity of hydrocarbons (not shown) declines correspondingly. This could be due to restructuring of the Cu-Ni alloy species including the reduction of remaining oxidized Ni species (Fig. 5-3) in the strongly reducing syngas atmosphere (50 bar CO + 50 bar H_2). The activation process is similar to what we reported for a Cu-Ni/SiO_2 catalyst [6], but a longer induction time (16 h for SiO_2 supported sample at 250 °C) is required for the CNT supported catalyst. During time on stream one would expect surface segregation of the Ni to the surface of Cu-Ni particles according to DFT calculations [6]. The catalyst precursor is reduced in H_2/N_2 (20 mol % H_2) gas flow first, and then exposed to the more reducing CO and H_2 mixture. After reduction, Cu occupies the first surface layer due to its lower surface energy whereas under reaction conditions Ni moves to the surface due to the stronger binding of CO on Ni than on Cu [6, 297, 298]. The phase segregation process could be related to the observed 45 h activation process during testing and once the catalyst forms a stable surface, it reaches a steady state. Additionally, NiO may not be fully reduced during the reduction in 20 mol % H_2/N_2 at 300 °C (for example in cases of Cu-Ni/CNT and Cu-Ni/Al_2O_3 catalysts), and could possibly be further reduced in the higher reduction potential of the synthesis gas (50 bar of CO and 50 bar of H_2). This increases the degree of alloying, which could hence change the activity as well. This may be the reason that the Cu-Ni/CNT catalyst displays a longer activation period (45 h) than the Cu-Ni/SiO_2 catalyst (16 h), since the latter is fully reduced during the reduction period with 20 mol % H_2/N_2 according to the XAS analysis.

The γ-Al_2O_3 supported catalyst (Fig. 5-7) shows an activation process similar to those observed for the silica and CNT supported catalysts, and a shorter activation period, about 15 h at 250 °C. The main product for the γ-Al_2O_3 supported catalyst is DME instead of methanol, with a maximum selectivity to DME of 82 mol % at 250 °C. This is probably due to the large numbers of acid sites (333 µmol g^{-1}) of γ-Al_2O_3 that can dehydrate methanol to DME [283, 299]. Meanwhile, the selectivity to hydrocarbons (HC) is between 10 and 20 mol % at all tested conditions, which could be produced by the metal sites (Cu and Ni) that interact strongly with the support. It was reported both Cu/Al_2O_3 [300] and Ni/Al_2O_3 [266] catalysts form hydrocarbons during CO hydrogenation.

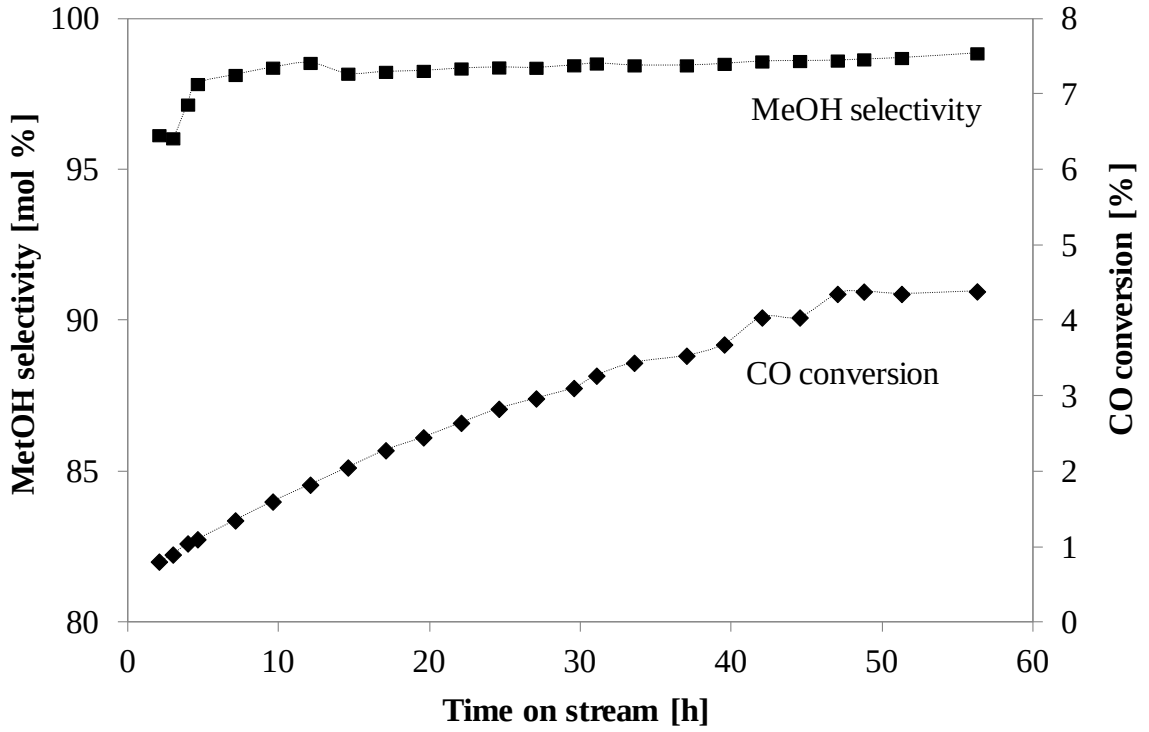

Fig. 5-6 CO conversion and methanol selectivity as functions of the time on stream for the Cu-Ni/CNT catalyst. The operating conditions are: P = 100 bar, T = 250 °C, GHSV = 4200 h^{-1} (based on total bed volume and gas flow referring to 298.15 K and 1 atm), feed: H_2/CO = 1 (vol/vol).

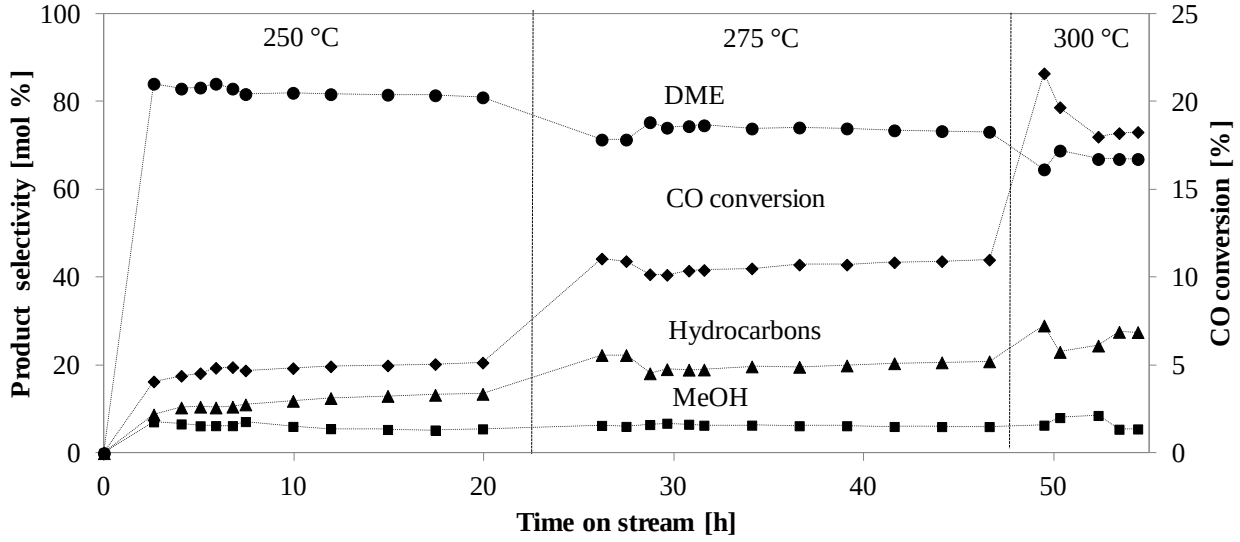

Fig. 5-7 CO conversion and the product selectivity as functions of the time on stream for the Cu-Ni/Al_2O_3 catalyst. The operating conditions are: P = 100 bar, T = 250-300 °C, GHSV = 2000 h^{-1} (based on total bed volume and gas flow referring to 298.15 K and 1 atm), feed: H_2/CO = 1 (vol/vol).

5.4.2.2 Effect of temperature

Table 5-3 shows that the CO conversion increases significantly from 2.6% to 7.4% for the Cu-Ni/CNT catalyst, when the reaction temperature is increased from 250 to 300 °C. In order to compare the area-based activity of CO and to avoid methanol condensation in the system, a higher gas velocity is used for the Cu-Ni/CNT catalyst (GHSV=7500 h^{-1}) as this catalyst is much more active compared to the other catalysts (GHSV=2000 h^{-1}). The methanol selectivity decreases from 98.9 mol % to 97.6 mol %, while the selectivity of C_{2+} oxygenates (including ethanol and DME) increases from 0.6 mol % to 2.1 mol %, and the hydrocarbon selectivity remains at 0.3 - 0.5 mol %. The space time yield (STY) of alcohols, mainly methanol, reaches 0.658 kg kg_{cat}^{-1} h^{-1} (catalyst bed volume based STY is approximately 0.263 kg L_{cat}^{-1} h^{-1}). The commercial methanol synthesis catalysts have a space time yield of about 1 kg L_{cat}^{-1} h^{-1} [18]. Our STY is calculated per gram of catalyst, but about 80 wt % of it is the support, while commercial catalysts usually are composed of approximately 5-15 wt % support [274]. As described above, Cu-Ni alloy is the only component observed in XRD after in situ reduction. The Cu-Ni alloy therefore seems as an attractive catalyst for methanol synthesis by CO hydrogenation.

Table 5-3 Behavior of the Cu-Ni/CNT catalyst during CO hydrogenation at steady state. Experimental conditions: P = 100 bar, T = 250-300 °C, H_2/CO = 1.0 vol/vol, and GHSV = 7500 h^{-1}.

T	X_{CO} [1)]	Carbon based, CO_2-free selectivity [mol %]			STY_{MeOH}
[ºC]	[%]	MeOH	C_{2+}-oxygenates [2)]	Hydrocarbons	kg kg_{cat}^{-1} h^{-1}
250	2.6	98.9	0.6	0.5	0.234
275	6.2	98.7	0.9	0.4	0.558
300	7.4	97.6	2.1	0.3	0.658

[1)] CO conversion. [2)] C_{2+}-oxygenates include both C_{2+}OH and DME.

The CO conversion and product selectivity over Cu-Ni/ZrO_2 catalyst with respect to temperature is shown in Fig. 5-8. The CO conversion is enhanced by increasing temperature, however, the selectivity to methanol decreases by increasing temperature, while the selectivity to DME and hydrocarbons (includes methane, ethane and propane) increases. According to our NH_3-TPD analysis, this catalyst contains a large number of acid sites (309 µmol g^{-1}). It is thus not surprizing that it produces DME as by-product. However, Cu-Ni/ZrO_2 catalyst contains similar amounts of acid sites to that of Al_2O_3 supported catalyst (333 µmol g^{-1}), but Cu-Ni/ZrO_2 catalyst mainly produces hydrocarbons above 275 °C instead of DME (the main product over the Al_2O_3 supported catalyst). The NH_3-TPD generally counts the total amount of Brønsted acid and Lewis acid sites. The ability of solids to facilitate acid-catalyzed reactions depends not only on the amount of acid sites but also on their strength. Alumina is usually a better catalyst than zirconia for DME formation from methanol. It is therefore not supersizing that the γ-Al_2O_3 supported catalyst exhibits much higher DME selectivity than the ZrO_2 supported catalyst. It was reported that zirconium dioxide itself is active and selective to hydrocarbons in CO hydrogenation [301-304], and produces DME and methanol as by-products [303, 304]. This is related to the oxygen vacancy sites in ZrO_2, because the ZrO_2 can be partly reduced in syngas and form oxygen vacancy sites [305], whereas Al_2O_3 does not. Additionally, zirconium dioxide is also able to convert methanol and DME into hydrocarbons [304, 306]. The selectivity to hydrocarbons increases when the reaction temperature is raised [303, 304] in agreement with the present results as seen in Fig. 5-8. It is therefore likely that the support, ZrO_2, could further convert the produced methanol and DME into hydrocarbons

over the Cu-Ni/ZrO_2 catalyst. The shift of product distribution with temperature could be related to both the increase of temperature and CO conversion.

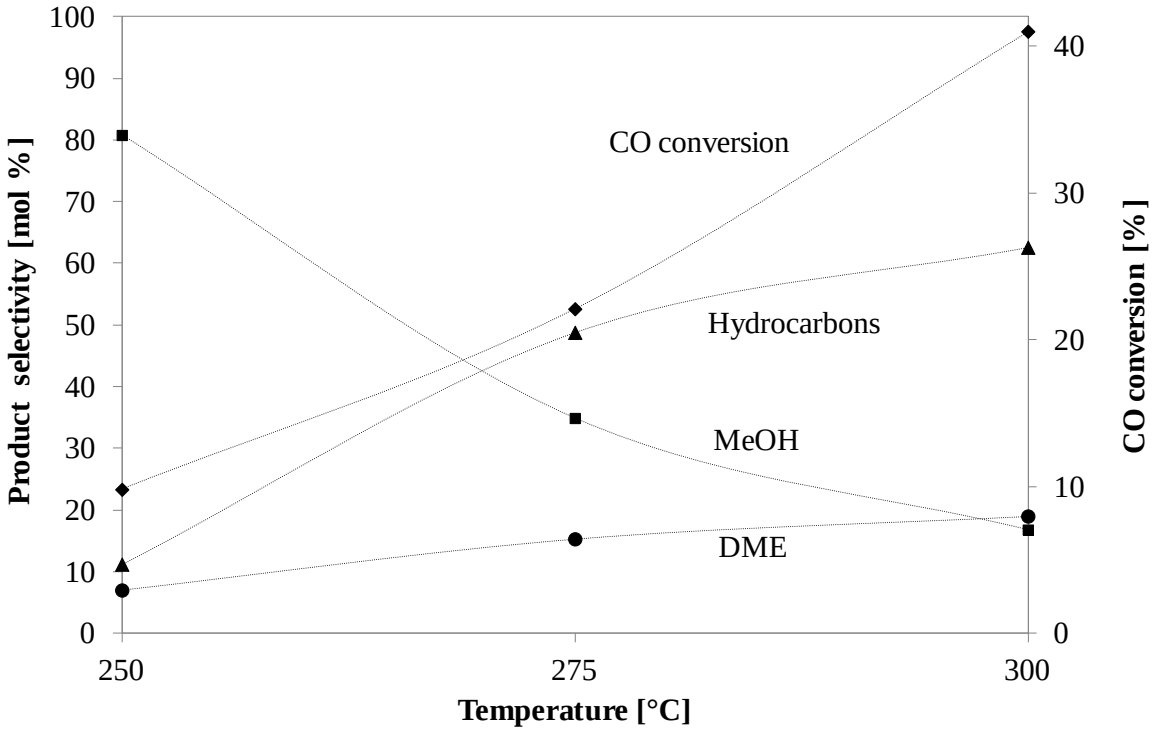

Fig. 5-8 Influence of temperature on CO conversion and the product selectivity over Cu-Ni/ZrO_2 catalyst. The operating conditions are: P = 100 bar, T=250-300 °C, GHSV = 2000 h^{-1} (based on total bed volume and gas flow referring to 298.15 K and 1 atm), feed: H_2/CO=1.

5.4.2.3 Effect of support

Table 5-4 summarizes the results of the activity tests for Cu-Ni catalysts on different supports during CO hydrogenation at 250 °C at steady state. Methanol is the dominant product over Cu-Ni/SiO_2 and Cu-Ni/CNT catalysts. The γ-Al_2O_3 supported catalyst produces mainly DME, probably due to methanol production over the Cu-Ni alloy followed by the dehydration of methanol to DME by acid sites of γ-Al_2O_3. The Cu-Ni/ZrO_2 catalyst produces mainly methanol with hydrocarbons and DME as by-products. The model industrial Cu/ZnO/Al_2O_3 catalyst, as expected, produces mainly methanol with selectivity up to 99 mol %.

The activity of all tested catalysts is normalized by using area-based CO conversion rate based on the active surface area of the catalysts, as shown in Table 5-4. The area-based CO conversions over different supported catalysts are at a same level. The selectivity of the catalysts clearly depend on the type of support. Among the catalysts, which are highly selective to methanol, the area-based activity of CO on the Cu-Ni/CNT ($2.0 \cdot 10^{-7}$ mol m^{-2} s^{-1}) and the Cu-Ni/SiO_2 ($1.3 \cdot 10^{-7}$ mol m^{-2} s^{-1}) catalysts is comparable to the model Cu/ZnO/Al_2O_3 catalyst ($2.7 \cdot 10^{-7}$ mol m^{-2} s^{-1}).

Table 5-4 Behavior of Cu-Ni catalysts over different supports during CO hydrogenation at steady state. Experimental conditions: P = 100 bar, T=250 °C, and H_2/CO = 1.0 vol/vol.

Catalysts	TOS[1)]	GHSV[2)]	X_{CO}[3)]	Carbon based, CO_2-free selectivity [mol %]				STY_{MeOH}	Area-based activity[4)]
	[h]	[h^{-1}]	[%]	MeOH	$C_{2+}OH$	Hydrocarbons	DME	kg kg_{cat}^{-1} h^{-1}	mol m^{-2} s^{-1}
Cu-Ni/SiO_2	20	2000	2.4	99.2	0.4	0.4	0.0	0.065	$1.3 \cdot 10^{-7}$
Cu-Ni/CNT	55	7500	2.6	98.9	0.1	0.5	0.5	0.234	$2.0 \cdot 10^{-7}$
Cu-Ni/Al_2O_3	20	2000	5.0	5.6	0.0	12.5	81.9	0.003	$2.1 \cdot 10^{-7}$
Cu-Ni/ZrO_2	57	2000	9.8	80.8	1.0	11.2	7.0	0.057	$2.0 \cdot 10^{-7}$
Cu/ZnO/Al_2O_3	22	16000	7.2	99	0.4	0.1	0.5	0.842	$2.7 \cdot 10^{-7}$

[1)] TOS: time on stream. [2)] Gas hourly space velocity. [3)]CO conversion. [4)] Area-based activity: CO converted rate based on a unit active surface area of catalysts.

The results presented here indicate both a strong influence of the support on the alloy formation dynamics and a variation of the catalytic activity depending on the underlying support. Specifically, Cu-Ni alloy particles on SiO_2 and CNT produce methanol selectively, acid sites on γ-Al_2O_3 and also partly on ZrO_2 cause dehydration of methanol to DME (and hydrocarbons for the ZrO_2 supported catalyst). The SiO_2 supported catalyst has the highest methanol selectivity of 99.2 mol %. This shows that SiO_2 from a point of selectivity, by being more inert than the other tested supports, is an ideal support, which does not influence the catalytic properties of the supported catalyst system significantly, and does not on its own further transform the product. The CNT supported catalyst is able to produce methanol almost as selectively as the Cu-Ni/SiO_2 catalyst but at a significantly enhanced productivity. This is due to the contribution from a higher active surface area. The γ-Al_2O_3 supported Cu-Ni catalyst contains a significant amount of acid sites (333 µmol g^{-1}) and produces predominantly dimethyl ether. The Cu-Ni/ZrO_2 catalyst exhibits high methanol selectivity at lower temperatures (250 °C), which shifts to hydrocarbons and dimethyl ether at higher temperatures (> 275 °C). It seems that the Cu-Ni alloy always produce methanol, but that some supports (ZrO_2 and γ-Al_2O_3) further convert methanol to different products (hydrocarbons and dimethyl ether).

5.5 Conclusions

CO hydrogenation has been investigated over Cu-Ni supported on different carriers (SiO_2, CNT, ZrO_2 and γ-Al_2O_3) and was shown to display major differences in product selectivity. The metal area based activities of all supported Cu-Ni catalysts are at the same level. CNT and SiO_2 supported Cu-Ni catalysts show high activity and selectivity for methanol synthesis. We found that the SiO_2 and CNT supported catalysts show a very high selectivity to methanol – around 99 mol % and low selectivity to hydrocarbons (< 0.5 mol %) at all temperatures tested. The area-based activity of CO on the Cu-Ni/CNT and the Cu-Ni/SiO_2 catalysts is comparable to the model Cu/ZnO/Al_2O_3 catalyst. The other supports tested, γ-Al_2O_3 and ZrO_2, influenced the Cu-Ni alloy selectivity strongly by making more by-products (hydrocarbons and DME) than methanol. In particular, the γ-Al_2O_3 supported catalyst contains a significant amount of acid sites (333 µmol g^{-1}) and produces predominantly DME, which is probably due to the dehydration of methanol produced initially by the Cu-Ni alloys. The ZrO_2 supported catalyst also contains a high amount of acid sites (309 µmol g^{-1}), however, it produces largely hydrocarbons above 275 °C. The ability of solids to facilitate acid-catalyzed reactions depends not only on the amount of acid sites but also on their strength. Alumina is usually a better catalyst than zirconia for DME formation from methanol. It is therefore not supersizing that the γ-Al_2O_3 supported catalyst exhibits much higher DME selectivity than the ZrO_2 supported catalyst. Moreover, ZrO_2 can further convert the produced methanol and DME into hydrocarbons. Therefore, it seems that the significant ambiguity in the literature concerning the properties of Cu-Ni catalysts in syngas conversion is related to the effect of the support, which on its own may be able to further convert the product.

Appendix B. Supplementary data

6 CO hydrogenation on Cu-Ni catalysts: Influence of catalyst pretreatment and feed composition

6.1 Abstract

$Cu\text{-}Ni/SiO_2$ catalysts in connection with different calcination and reduction procedures are compared with a conventional $Cu/ZnO/Al_2O_3$ catalyst in the synthesis of methanol from synthesis gas (CO/H_2) in the presence and absence of carbon dioxide. In general, the synthesized Cu-Ni alloy catalysts that are prepared by incipient wetness impregnation are very active and highly selective (~99 mol %) for methanol synthesis during CO hydrogenation. In H_2/CO, the metal area based activity of methanol formation on the Cu-Ni catalyst is comparable to a conventional $Cu/ZnO/Al_2O_3$ model catalyst. The Cu-Ni catalyst activity increases initially and in contrast to the performance of a commercial methanol synthesis catalyst no apparent catalyst deactivation during 60 hours on stream is observed. The calcination of the impregnated catalysts (with/without calcination step) and different reduction procedures with varying hydrogen concentration have significant influence on Cu-Ni alloy formation and their particle size and consequently on its activity. Particle size distribution and alloying are estimated by both in situ XRD and in situ TEM combined with electron energy loss spectroscopy (TEM-EELS). Addition of 3 mol % CO_2 to the H_2/CO leads to a significant loss of activity (17% to 48%, depending on temperature). Density functional theory calculations show in accordance with previous surface science studies that oxygen as one of the intermediates from water gas shift reaction could induce segregation of Ni to the first layer by its adsorption on the surface. Hence, this could be one of the reasons of the unusual detrimental influence of CO_2 on the catalytic performance.

6.2 Introduction

Today methanol is one of the ten most produced chemicals in the world with strong annual growth [17, 24]. The main use of methanol is in the production of chemicals such as formaldehyde and acidic acid as well as in the production of various olefins for the polymer industry [49]. Additionally, methanol is an efficient fuel in an internal combustion engine or in a fuel cell, as well as an octane booster for gasoline, and methanol has therefore been suggested as a main energy carrier for the future [50, 57, 307, 308]. Despite the large current methanol production, the replacement of gasoline would require more than a hundredfold increase in methanol production [47]. Almost exclusively commercial methanol is produced utilizing $Cu/ZnO/Al_2O_3$ based catalysts from syngas, a mixture of CO, CO_2 and H_2 [18, 22-24, 309], which is mostly obtained via steam reforming of nature gas currently [102, 115, 310] and can be potentially produced from renewable resources such as biomass [8, 35, 37, 38]. However, deactivation of the commercial $Cu/ZnO/Al_2O_3$ methanol synthesis catalyst is a major problem. More than one third of the activity is lost after the first 1000 h of operation, something that often determines the ultimate catalyst lifetime [24, 64, 66, 130]. It would therefore be of great value, if methanol synthesis catalysts with greater activity and stability are developed.

Whereas metallic copper itself is often reported to exhibit a relatively low activity for methanol synthesis via CO hydrogenation [18], the use of ZnO as support and the addition of CO_2 improve the rates for methanol synthesis significantly [115, 134, 277, 280]. Nickel is known as an active methanation catalyst, which is able to dissociate CO, and subsequently form methane [266, 311-313]. Cu-Ni based catalysts have previously been reported to be active for higher alcohol synthesis [223, 225, 230], hydrocarbon synthesis [266], and methanol synthesis [228] during CO

hydrogenation. The reactivity differences in these studies may originate from support effect. We have recently found that Cu-Ni on supports such as ZrO_2 and γ-Al_2O_3 produce mainly hydrocarbons and dimethyl ether (DME), and this probably due to the support that are able to further convert methanol to hydrocarbons and DME [314]. In addition, based on both density functional theory (DFT) calculations we have also predicted and verified experimentally that Cu-Ni alloys (supported on SiO_2) as alternative to the Cu-Zn systems are active and highly selective to methanol during CO hydrogenation [6].

The Cu-Ni catalysts reported earlier by our group [6, 314] were prepared via simple incipient wetness impregnation as a very general and practically simple method with low waste streams [315]. For this approach several types metal salts are typically used, i.e. nitrate, chloride, acetate, and citrate. Metal nitrates are most convenient due to their high solubility in water and low cost [316]. After impregnation especially the subsequent treatment of catalysts is essential for their final catalytic properties, for example, instead of calcination in air treatment in N_2 or NO/N_2 has a strong influence [316-318]. Alternatively, glow discharge plasma-assisted nitrate decomposition has been used instead of calcination in gas atmosphere [319], and direct reduction of the metal nitrate to the metal [320-322] has been reported to be beneficial because it can prevent agglomeration of particles and yield a higher metal dispersion on the support. Obviously, a more detailed study of the influence of the preparation parameters on the novel Cu-Ni methanol synthesis catalysts may significantly improve their performance.

Hence, we present here a more detailed study of the effect of pretreatment of the impregnated Cu-Ni/SiO_2 catalysts on the activity of methanol synthesis i.e. the structure and activity of Cu-Ni catalysts with/without calcination of the nitrate precursors and the influence of the reduction procedure of catalyst precursors in 2 mol % H_2 or 20 mol % H_2 in N_2. Finally, the effect of CO_2 cofeeding into H_2/CO feed stream has been investigated. The alloy formation of catalysts has been evaluated by in situ X-ray diffraction (XRD), in situ X-ray absorption spectroscopy (XAS), and in situ transmission electron microscopy (TEM) and DFT calculations have been used to substantiate the interpretation of the observations when co-feeding CO_2 over Cu-Ni bimetallic alloys.

6.3 Experimental

6.3.1 Preparation of catalyst

Cu-Ni based catalysts (Cu:Ni molar ratio of 1:1, 20 wt % Cu+Ni on silica) were prepared by the incipient wetness impregnation method. First, an aqueous solution was prepared by dissolving $Cu(NO_3)_2 \cdot 3H_2O$ (Sigma-Aldrich) and $Ni(NO_3)_2 \cdot 6H_2O$ (Sigma-Aldrich) in de-ionized water. Then the aqueous solution was impregnated on SiO_2 (Saint-Gobain Norpro) and the product was aged at room temperature for 1 h, and then dried at 100 °C. This sample is denoted as Cu-Ni/SiO_2-dried. Cu-Ni/SiO_2-calc was formed by calcining the Cu-Ni/SiO_2-dried precursor in air at 400 °C (heating rate 1.5 °C min^{-1}) for 4 h.

For comparison, a model Cu/ZnO/Al_2O_3 (molar ratio of Cu/Zn/Al = 6/3/1) methanol synthesis catalyst was prepared by co-precipitation according to the recipe reported by Baltes et al. [274]. During the precipitation, the pH-value was maintained at 7.0 ± 0.1, the temperature was kept at 60 °C, and the precipitate was then aged at 60 °C for 1 h. Afterwards the precipitate was filtered and washed, followed by drying overnight at 80 °C and calcination at 300 °C in air for 3 h (heating rate 2 °C min^{-1}).

Finally, all the catalyst materials were crushed and sieved to a size range of 0.6-1.4 mm before using them for catalytic activity test.

6.3.2 Characterization of catalyst

The chemical composition of Cu-Ni/SiO_2-calc, Cu-Ni/SiO_2-dried, and Cu/ZnO/Al_2O_3 catalysts were determined by an inductively coupled plasma-optical emission spectrometer (ICP-OES, Perkin–Elmer, model Optima 7300) and using Ar as plasmogene. In a typical analysis, 5 g of $K_2S_2O_7$ was melted together with 0.25 g sample and dissolved in 10 ml HCl in 200 ml water and then analyzed.

In situ XRD was performed with a PANalytical X'Pert PRO diffractometer equipped with an Anton Paar XRK 900 in situ cell and a gas flow control system for H_2-TPR. Cu-Ni/SiO_2-calc and Cu-Ni/SiO_2-dried catalysts were heated in flowing 20 mol % H_2/He up to 300 °C for 1 h. Additionally, in order to understand the effect of reducing gas composition, the Cu-Ni/SiO_2-dried catalyst was reduced in a dilute H_2 gas atmosphere with a 2 mol % H_2/He flow at 300 °C for 1 h. The model Cu/ZnO/Al_2O_3 catalyst was reduced in 2 mol % H_2 in N_2 flow at 220 °C for 1 h. On-line mass spectrometry (MS) allowed recording TPR spectra.

In order to tackle both the amorphous and the crystalline structure of the samples, two complementary in situ techniques have been applied. The combined in situ XAS and XRD measurements were performed at the European Synchrotron Radiation Facility (ESRF, Grenoble) at the Swiss-Norwegian Beamlines (BM01B beamline). The storage ring was operated at electron energy of 6 GeV and injection current of 200 mA. The beamline was designed to rapidly switch between the XAS and XRD modes and hence carry out quasi-simultaneous measurements with the two techniques. The in situ experiments were carried out using the quartz capillary micro-reactor. XAS were acquired at the Cu and Ni K-edge in transmission mode using a continuously scanning Si(111) double-crystal monochromator and a gold-coated mirror for the rejection of higher harmonics. A Cu (Ni) foil was measured at all times as an energy-calibration reference. XRD patterns were collected using a Si(111) channel-cut monochromator set to a wavelength of λ = 0.503 Å. The diffractometer with a high-resolution detector consisting of 6 individual channels equipped with Si(111) analyser crystals was scanned between 2θ values of 23° and 80°. Prior to the experiments, the diffractometer was calibrated using a crystalline powder Si standard.

An environmental transmission electron microscope (ETEM) equipped with a differential pumping system to confine a controlled flow of gases such as H_2 and CO_2 around the specimen, allowed observation of catalysts in a gaseous environment (FEI Titan E-cell, monochromatic, objective lens aberration corrector, Gatan imaging filter) [276, 277, 290]. The microscope is equipped with a heating holder allowing catalyst characterization in situ in a reactive environment mimicking the working conditions of the catalysts. In the present experiments, the specimen was imaged while being exposed to 1.3 mbar H_2. The specimen was heated in the gas environment at a rate of 7 °C min^{-1} from room temperature up to 300 °C for Cu-Ni/SiO_2-calc and Cu-Ni/SiO_2-dried precursors. The TEM imaging was performed after drift-stabilization of the sample holder. The electron energy loss spectroscopy (EELS) of selected particles was performed to determine the contents of reduced catalyst particles after in situ reduction. For this purpose the Cu L_2/L_3 and Ni L_2/L_3 edges were analyzed.

6.3.3 Catalyst testing

The performance of the catalysts for CO hydrogenation was evaluated in a fixed-bed continuous-flow reactor with an online GC-FID/TCD detection system (6890N from Agilent Technologies). Details of the setup are given by Christensen et al. [8, 96]. The feed gases CO, H_2, and 8.6 mol % CO_2 in CO (all from AGA A/S) were supplied to the reactor from pressurized cylinders via Brooks 5850S mass flow controllers, and mixed before entering the reactor. A bubble flow meter was used

for determination of the volumetric flow rate of the reactor effluent. Methanol, ethanol, 1-propanol, 1-butanol, 2-butanol, iso-butanol, methane, ethane, ethane, propane, dimethyl ether (DME), and ethyl acetate were analyzed by GC. The alcohols were separated using a DB1 column whereas CO, H_2, CO_2, N_2 and hydrocarbons were analysed using a Parapak N column and followed by a 13 x Molesieve column [196, 197].

Prior to the reaction, the Cu-Ni/SiO_2-calc and Cu-Ni/SiO_2-dried samples were pre-reduced in situ by a 20 mol % H_2 in N_2 gaseous mixture for 12 h by heating to 300 °C with a heating rate of 1-1.5 °C min^{-1}. These two catalysts were denoted as Cu-Ni/SiO_2-calc-20H2 and Cu-Ni/SiO_2-dried-20H2. The Cu-Ni/SiO_2-dried and the model Cu/ZnO/Al_2O_3 catalysts were reduced in the reactor with a 1.4 mol % H_2 in N_2 flow at 300 °C and 220 °C, respectively, for 12 h with a ramping rate of 1-1.5 °C min^{-1} (this Cu-Ni sample was denoted as Cu-Ni/SiO_2-dried-2H2).

The conversion of CO (X_{CO}) is calculated from the molar flow rates of CO_2 (F_{CO}) into and out of the reactor:

$$X_{CO} = \frac{F_{CO}^{in} - F_{CO}^{out}}{F_{CO}^{in}} \cdot 100\% \ [\%]$$

The conversion of CO_2 (X_{CO_2}) is calculated from the molar flow rates of CO_2 (F_{CO_2}) into and out of the reactor:

$$X_{CO_2} = \frac{F_{CO_2}^{in} - F_{CO_2}^{out}}{F_{CO_2}^{in}} \cdot 100\% \ [\%]$$

The CO_2 free selectivity to a given product (S_i) is based on the total number of carbon atoms in the products except CO_2:

$$S_i = (n_i y_i) / (\sum n_i y_i) \cdot 100\% \ [mol\ \%]$$

Where n_i ($n_i \geq 1$) is the number of carbon atoms in components *i*, and y_i is the fraction of component *i* in the product. The carbon mass balance was generally fulfilled to within 5 mol %.

The space time yield (*STY*) of methanol is the production rate of methanol per mass of catalyst:

$$STY_{MeOH} = \frac{M_{MeOH} F_{MeOH}}{m_{cat}} \ \left[kg\ kg_{cat}^{-1}\ h^{-1} \right]$$

where, M_{MeOH} is the molar mass of methanol and F_{MeOH} is the molar flow rate of methanol out of the reactor. Here, we report the *STY* in the units of mass of methanol produced per hour and per mass of catalyst (m_{cat}), which includes both active metals and support.

The Area based activity of methanol is the production rate of methanol per metal surface area of catalyst:

$$Area\,based\ activity = \frac{STY_{MeOH}}{M_{MeOH} \times S_{active\ metal} \times 3600 \frac{s}{h}} \ \left[mol\ m^{-2}\ s^{-1} \right]$$

where, M_{MeOH} is the molar mass of methanol, $S_{active\ metal}$ is the metal surface area of catalyst determined from the estimated particle size from XRD.

$$S_{active\ metal} = \frac{3 m_{cat}}{\rho r}$$

where, ρ is the density of metals (8.935 g cm^{-3}), and r is the radii of metal particles.

6.3.4 Density functional theory calculations

Density functional theory (DFT) calculations were carried out using the Dacapo code [269], which uses a plane wave implementation to describe valence electrons and Vanderbilt ultrasoft pseudopotentials [270] to represent the ionic cores. All calculations were performed using the generalized gradient approximation (GGA) RPBE functional [271]. The kinetic energy and density cutoffs were 340 and 680 eV, respectively. Slabs consisting of 4 layers separated by approximately 18 Å of vacuum were periodically repeated in a $\sqrt{3} \times \sqrt{3}\,R30°$ unit cell for the (111) surfaces. The top two layers and the adsorbates were allowed to relax until the sum of total forces was less than 0.03 eV $Å^{-1}$. A Monkhorst-Pack 8×8×1 k-point sampling was applied in order to sample the surface Brillouin zone [273]. Spin-polarization was taken into account for all calculations considering Ni atoms. Gas-phase O_2 for which the RPBE functional performs poorly has been corrected as described in Ref [323].

6.4 Results and discussion

6.4.1 Catalyst structure

The elemental analysis results for Cu-Ni/SiO_2-calc, Cu-Ni/SiO_2-dried, and Cu/ZnO/Al_2O_3 catalyst materials are listed in Table 6-1. For Cu-Ni/SiO_2-calc and Cu-Ni/SiO_2-dried samples, the theoretical loading was 20 wt % Cu+Ni on SiO_2, the measured loading was 17.6 wt % and 15.3 wt %, respectively. The deviation is probably due to the fact that nitrates/hydroxynitrates/carbonates will be present in the catalysts that add to the total mass but may also be caused by loss of Cu and Ni salts during the preparation procedure. The Cu/Ni and Cu/Zn atomic ratio are close to the expected ratio.

Table 6-1 Elemental analysis by ICP-OES of CuNi/SiO_2-calc, Cu-Ni/SiO_2-dried, and Cu/ZnO/Al_2O_3 catalyst precursors.

Catalysts	Loading (wt %)		Cu/Ni or Cu/Zn (atomic ratio)	
	Cu	Ni or Zn	nominal	measured
Cu-Ni/SiO_2-calc	9.2	8.4	1.00	1.02
Cu-Ni/SiO_2-dried	8.0	7.3	1.00	1.01
Cu/ZnO/Al_2O_3	44.7	22.0	2.00	2.09

Fig. 6-1 shows the in situ XRD patterns of the Cu-Ni/SiO_2-calc precursors at different temperatures in a flow of 20 mol % H_2/He. No SiO_2 reflections are observed in the XRD pattern due to its amorphous structure. At 25 ºC, the catalyst precursor contains CuO, NiO, and probably $CuNiO_2$ species whose reflections overlap with NiO at 2θ equal to 37.Ᵽ. It seems that the catalyst precursors are not homogeneously distributed after calcination, as the catalyst contains distinct phases of CuO and NiO. The main reduction occurs between 140 and 160 ºC. Above 160 ºC, there are no reflections from either CuO or NiO in the XRD patterns. Additionally, the in situ XRD patterns show that NiO and CuO start to be reduced almost simultaneously. At 300 ºC, the XRD pattern shows two sets of reflections at {43.32°, 50.45°, and 74.12°} and {44.02°, 51.29°, and 75.54°}. According to the Inorganic Crystal Structure Database (ICSD), the first set of reflections corresponds well to the reported [111], the [200], and the [220] crystal planes, at {43.32°, 50.45°, and 74.12°} for Cu (ICSD file 64699). The second set of reflections at {44.02°, 51.29°, and 75.54°} lies in between the reflections of metallic Cu and Ni (ICSD file 52265) at {44.49°, 51.85°, and 76.38} which can be ascribed to alloyed Cu-Ni. According to Vegard's law [264] the composition of Cu-Ni in the alloys can be calculated to be $Cu_1Ni_{1.49}$. Based on ICP-OES analysis the Cu/Ni molar ratio is 1.02/1. Therefore, about 13 mol % metallic Cu phase exist in the reduced

catalysts. According to the Scherrer equation [275, 295] the particle sizes are 47 nm and 14 nm for Cu and Cu-Ni alloys, respectively.

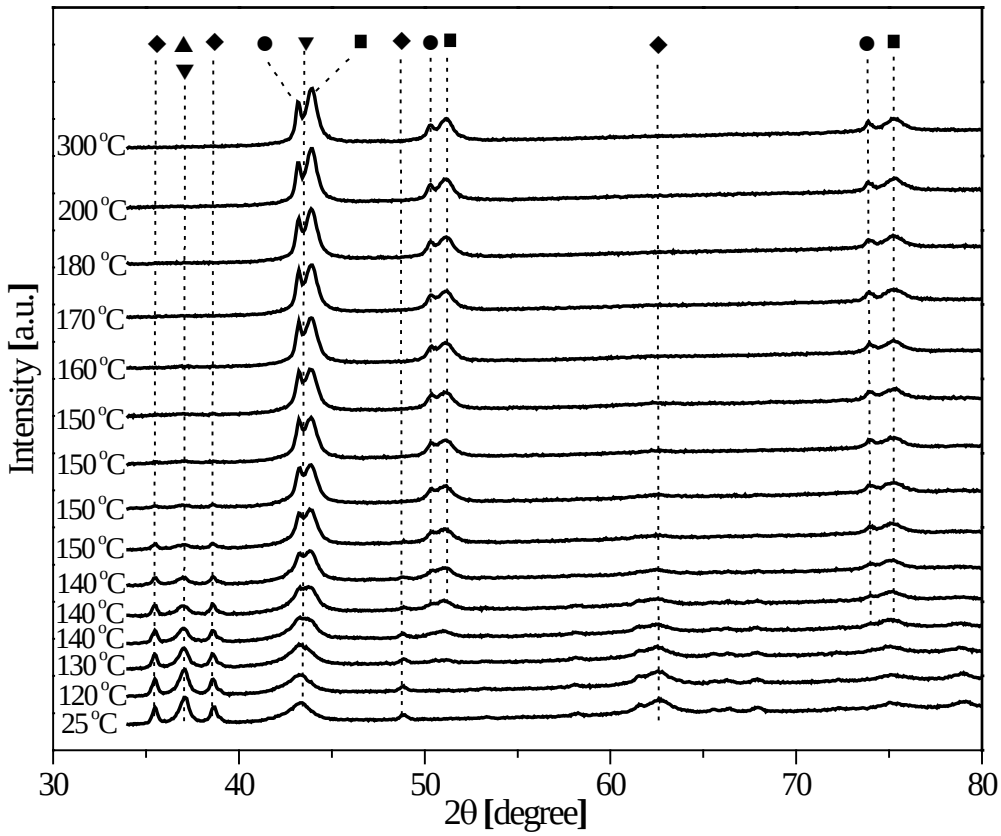

Fig. 6-1 XRD patterns at different temperatures during in situ reduction of the Cu-Ni/SiO_2-calc-20H2 sample in a flow of 20 mol % H_2/N_2 with a flow rate of 100 ml·min^{-1}. ▼ - NiO, ◆ – CuO, ▲- $CuNiO_2$, ● - metallic Cu, ■ - Cu-Ni alloy. (The temperature profile and MS (H_2O evolution) results are shown in the Appendix C, supplementary materials.)

Fig. 6-2 shows the in situ XRD patterns for reduction of the Cu-Ni/SiO_2-dried precursors at different temperatures in the flowing of 20 mol % H_2/He. The catalyst precursor contains Cu/Ni hydroxynitrates that are formed during the drying of impregnated metal nitrate precursors at elevated temperature and upon exposure will also from carnonates [324, 325]. The main reduction occurs between 220 ºC and 240 ºC. There are no observed reflections of either CuO or NiO in the XRD patterns during the reduction process. Only metallic Cu and Cu-Ni alloy reflections are observed after reduction, which is similar to the Cu-Ni/SiO_2-calc catalyst. From the position of the reflections in the same way a composition of $Cu_1Ni_{1.57}$ and a fraction of 15 mol % pure metallic Cu particles can be estimated. The particle size is about 41 nm and 6 nm for Cu and Cu-Ni alloy particles, respectively. Compared to the oxide precursor, the reduction temperature for the nitrate precursor is 100 ºC higher. The temperature range for calcination of Cu and Ni nitrate was reported between 210 and 300 ºC [326-328]. Note that simultaneous on-line gas analysis by the mass spectrometer uncovered that water is not observed until significant NO/NO_2 are released. This indicates that the catalyst is first calcined and reduced afterwards.

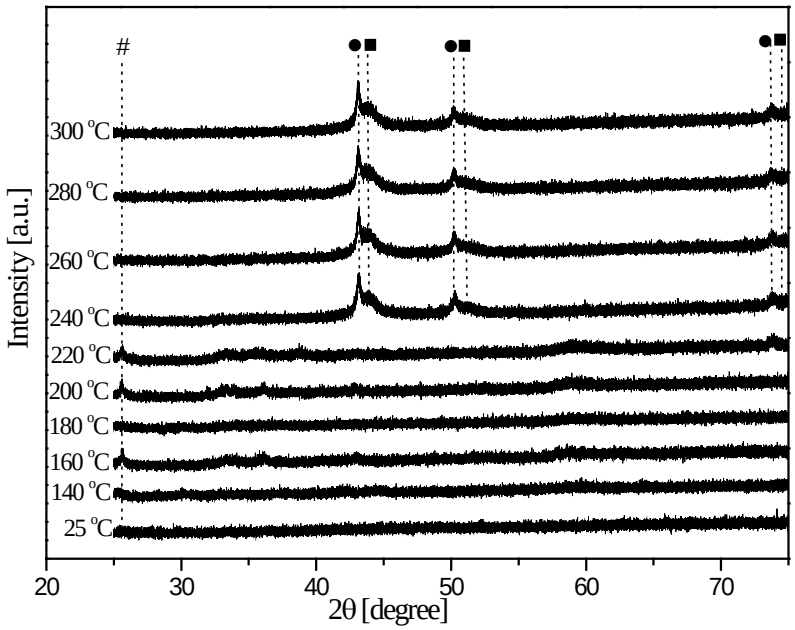

Fig. 6-2 XRD patterns at different temperatures during in situ reduction of the Cu-Ni/SiO_2-dried-20H2 sample in a flow of 20 mol % H_2/N_2 with a flow rate of 100 ml·min^{-1}. # - Cu/Ni nitrate hydroxides, ● - metallic Cu, ■ - Cu-Ni alloy.

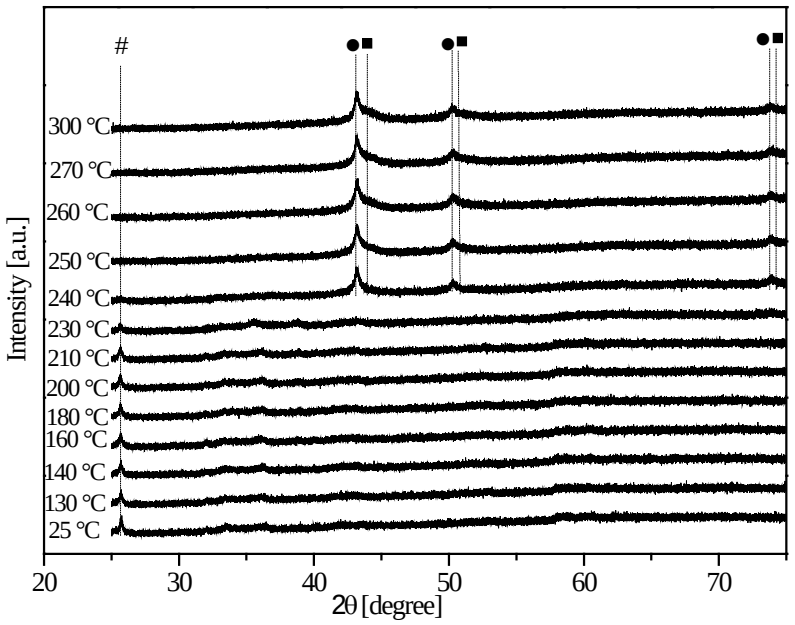

Fig. 6-3 XRD diffractograms at different temperatures during in situ reduction of the Cu-Ni/SiO_2-dried-2H2 sample in a flow of 2 mol % H_2/N_2 with a flow rate of 100 ml min^{-1}. ■ - Cu-Ni alloy.

In order to understand the influence of the H_2 concentration on the catalytic properties, Cu-Ni/SiO_2-dried was additionally reduced in 2 mol % H_2/N_2 instead of 20 mol % H_2/N_2. Fig. 6-3 shows the in situ XRD patterns for reduction of the Cu-Ni/SiO_2-dried precursor, donated as Cu-Ni/SiO_2-dried-2H2. The main reduction occurs in a similar way as for the 20 mol % H_2/N_2 between 230 ºC and 240 ºC. Similarly and despite also in this case Cu and Cu-Ni alloy reflections are observed after reduction the reflections are much broader with only about 10 mol % of the pure metallic phase and the main part being present as $Cu_1Ni_{1.1}$ particles (see above, estimated from Vegard's law [264]). The particle sizes are about 24 nm for the supported copper and 5 nm for the Cu-Ni alloyed particles, respectively.

According to above XRD analyses, all impregnated Cu-Ni/SiO_2 precursors always form separated metallic Cu and Cu-Ni alloy phases after reduction. Pretreatment of impregnated catalyst with calcination process seems has limited influence on the phase segregation of Cu and Ni (13 mol % segregated Cu) compared to the non-calcined catalyst (15 mol % segregated Cu) and lies within the error bar, while the influence on the particle sizes of Cu and Cu-Ni alloy are more obvious. The Cu-Ni/SiO_2-calc catalyst is calcined at 400 °C, which probably causes sintering of the catalytic particles. However, the reduction of the impregnated catalyst with a more dilute H_2 atmosphere (2 mol % H_2/N_2) has a more pronounced influence. It decreases the phase segregation slightly (10 mol % segregated Cu) and, especially, the particle sizes of metallic Cu and Cu-Ni alloy decrease.

The bulk Cu-Ni binary phase diagram shows that Cu and Ni can form a solid solution [265], but this may be significantly different for supported Cu-Ni particles. For Cu-Ni particles (with different composition of Cu and Ni) supported on SiO_2/Al_2O_3 the following trend has been reported [329] - at high nickel concentration, a homogeneous solid solution of Cu-Ni formed, whereas at lower nickel concentrations, Cu and Ni were separated. Lin et. al. [56] and Ungureanu et. al. [57] also found phase segregation of Cu and Ni on supports (CeO_2 or Al_2O_3). The phase segregation of Cu and Ni has been claimed to be due to a strong metal-support interaction and confinement of Cu-Ni particles in the porous structure [330, 331]. Naghash et. al. [332] has also observed that at high copper doping into Ni and at elevated reduction temperatures segregation took place, the binding energies tended to restore to those of nickel due to copper segregation, which reduces the interfacial surface energies.

It is known that XRD could not identify amorphous species or fine crystalline particles. Although silica usually is considered as an inert support, which has less influence on supported metals, there still could unreduced oxide species such as NiO exist in the sample after reduction at 300 °C. In order to tackle both the amorphous and the crystalline structure of the samples, two complementary in situ techniques, XAS and XRD, have been applied. The Cu-Ni/SiO_2-dried sample has been analyzed in situ at ESRF synchrotron. The starting material displays an intense whiteline at both edges indicating the presence of both Ni(II) and Cu(II) in the precursors (Fig. 6-4). Intensity of the whiteline decreases with increase in temperature during reduction, while the edge shifts slightly towards lower energy with the appearance of a pre-edge, indicating the reduction of both Ni(II) and Cu(II) species to their metallic state at around 250 °C, which is similar to what we have observed in the conventional in situ XRD analysis.

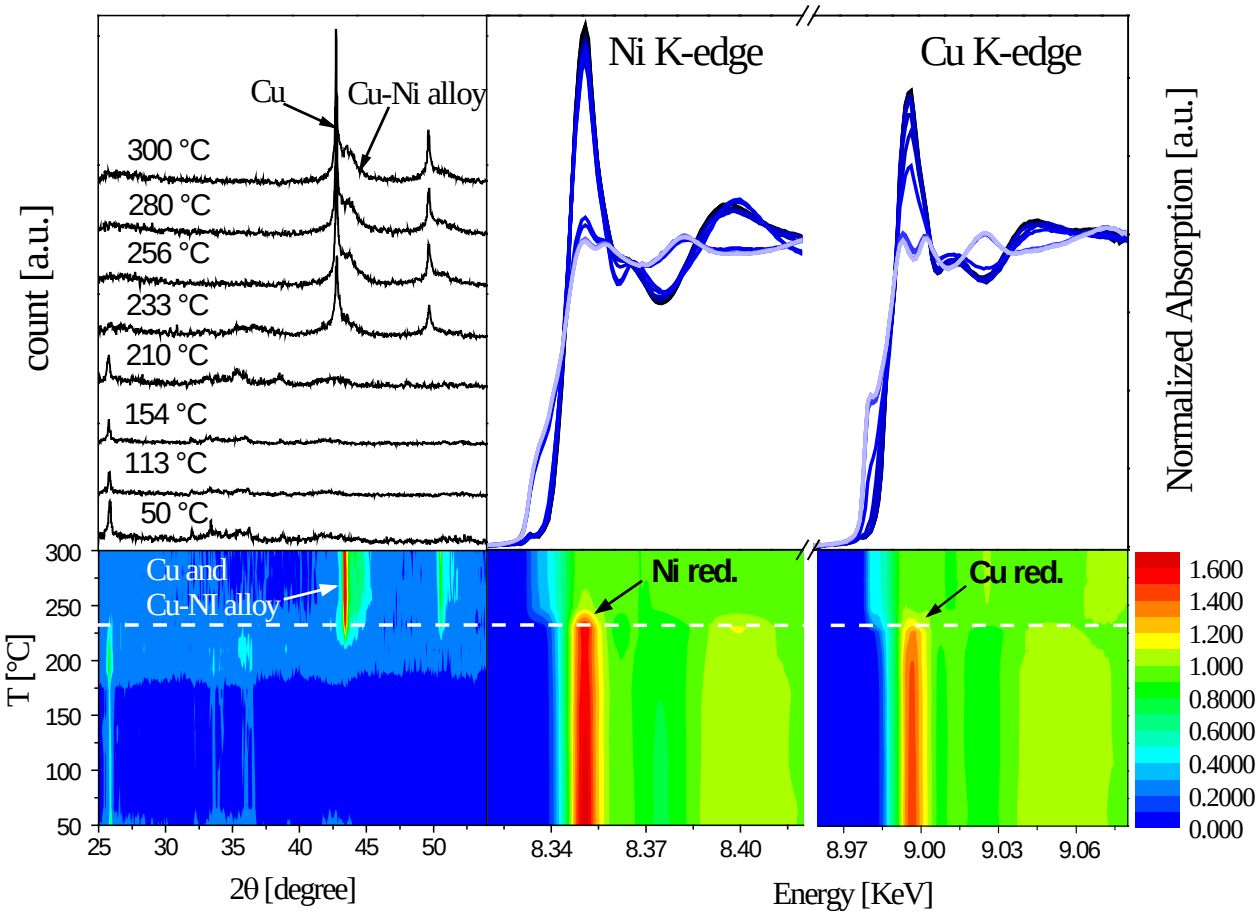

Fig. 6-4 Simultaneous in situ XANES and XRD for reduction of Cu-Ni/SiO_2-dired sample. For XANES: the colors from blue to red are the transition from no absorption to strong absorption; for XRD: the colors from blue to red are the transition from low intensity to high intensity.

In order to further confirm the formation of Cu-Ni alloys, the Cu-Ni/SiO_2-calc and Cu-Ni/SiO_2-dried precursors were reduced in situ in the ETEM. It is very difficult to distinguish the lattice parameters among Cu-Cu, Ni-Ni and Cu-Ni, because Cu and Ni have similar atomic radii of 1.276 Å and 1.244 Å, respectively [333]. However, the EELS spectra could be utilized to determine components in a single particle (Fig. 6-5). For both catalysts, the EELS spectra of selected particles show both Cu and Ni L-edge contributions in all measured particles showing that Cu-Ni alloys are formed. The electron microscopy images further uncovered that the distribution of particles in both samples is rather broad. In accordance with XRD results the Cu-Ni/SiO_2-dried sample shows a narrower particle size distribution than the one of Cu-Ni/SiO_2-calc sample. The broad particle size distribution of Cu-Ni/SiO_2-calc sample probably causes by the calcination step, which could redisperse and increase sintering of Cu and Ni components in the sample. The TEM average particle size is 10.6 nm for the Cu-Ni/SiO_2-calc and 5.9 nm for the Cu-Ni/SiO_2-dried samples, which are similar to what the average particle size obtained from the in situ XRD patterns. Table 6-2 sumarizes the TEM and XRD particle sizes of all samples, and active surface areas (calculated from XRD particle size) of all reduced silica supported Cu-Ni and Cu/ZnO/Al_2O_3 samples.

Table 6-2 Particle sizes derived by TEM and XRD and active surface areas (estimated from XRD particle size) of all reduced silica supported Cu-Ni and $Cu/ZnO/Al_2O_3$ samples.

Catalysts	d_{TEM} [nm]	d_{XRD} (Cu-Ni) [nm]	d_{XRD} (Cu) [nm]	Analyzed weight of active metal [1)] [g g_{cat}^{-1}]	$S_{active\ metal}$ [$m^2\ g^{-1}$]
$Cu-Ni/SiO_2$-calc	10.6	14	48	0.176	8.4
$Cu-Ni/SiO_2$-dried-20H2	-	6	41	0.153	17.0
$Cu-Ni/SiO_2$-dried-2H2	5.9[2)]	5	24	0.153	20.4
$Cu/ZnO/Al_2O_3$	-	-	6	0.714	79.3

[1)] Active metal for supported Cu-Ni catalysts is metallic Cu+Ni, for $Cu/ZnO/Al_2O_3$ catalyst is Cu+ZnO, which are determined by ICP-OES analysis; [2)] Reduced in 1.3 mbar H_2.

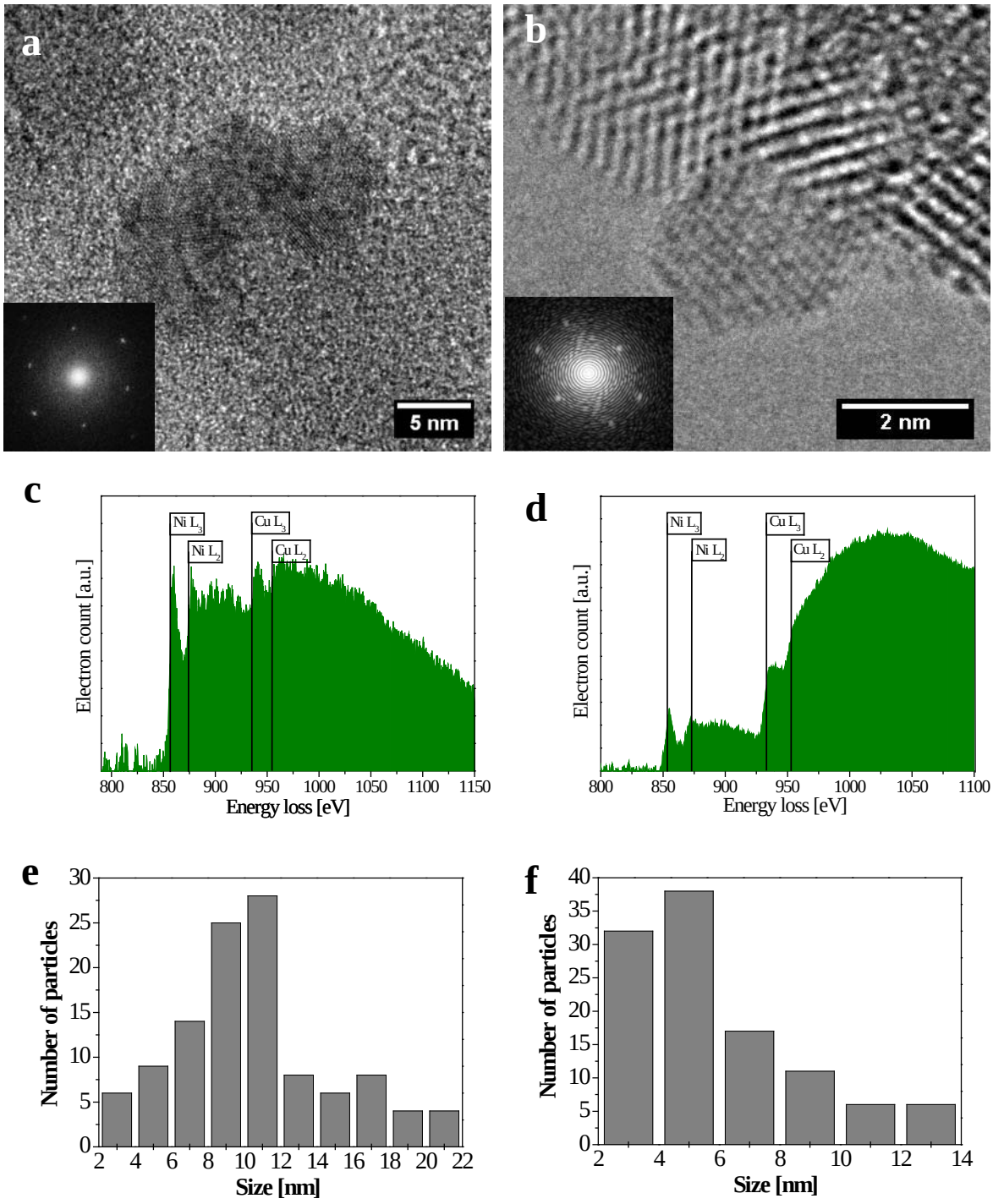

Fig. 6-5 (a) TEM image of Cu-Ni/SiO_2-calc, (b) TEM image of Cu-Ni/SiO_2-dried, (c) EELS spectrum of Cu-Ni/SiO_2-calc, (d) EELS spectrum of Cu-Ni/SiO_2-dried, (e) particle size distribution of Cu-Ni/SiO_2-calc, and (f) particle size distribution of Cu-Ni/SiO_2-dried.

6.4.2 Time on stream

Fig. 6-6 shows the CO conversion and methanol selectivity as functions of time on stream over the Cu-Ni/SiO_2-dried-2H2 catalyst as an example, which is in a similar way also observed for the other Cu-Ni-catalysts. At 250°C the CO conversion increases from 1.2% to 3.1% while the selectivity to methanol increases from 96.5 to 98.2 mol % during the first 22 h after the syngas is introduced into the reactor and a steady state is then reached. Usually, Cu/ZnO-based catalysts deactivate with time on stream, such as observed for the commercial methanol synthesis catalyst [64-66, 130]. The time on stream of our tested Cu/ZnO/Al_2O_3 catalyst also shows this typical deactivation profile with time on stream (cf. Appendix C, supplementary material). However, this is not observed for the Cu-Ni based catalyst, at least within the time frame of the experiment. One feasible explanation for the activation of the Cu-Ni/SiO_2-dried-2H2 catalyst with time on stream is as follows. After its initial reduction in diluted hydrogen, Cu is expected to occupy the first layer of Cu-Ni particles due to its lower surface energy, whereas under reaction conditions Ni moves to the surface due to the stronger binding of CO on Ni than on Cu [6]. The phase segregation process could be related to the observed activation process and once the catalyst form a stable surface, it reaches a steady state.

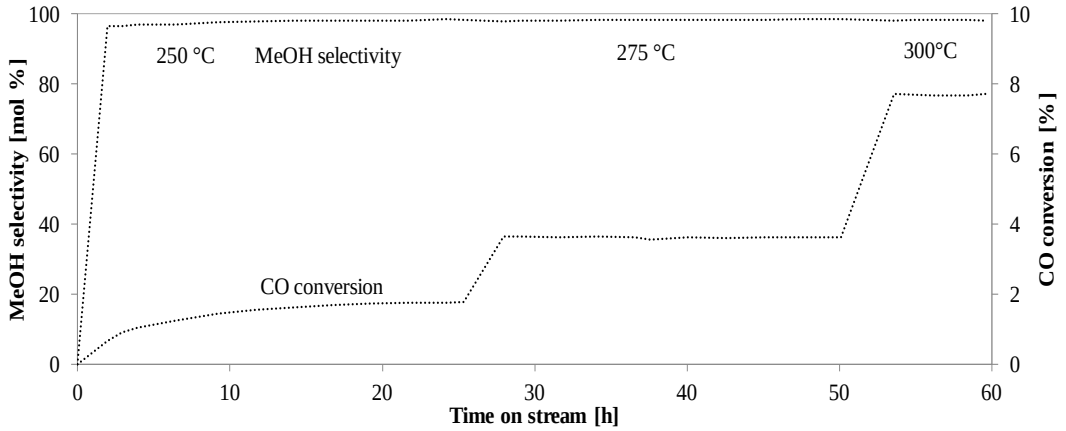

Fig. 6-6 The CO conversion and methanol selectivity as functions of time on stream for the Cu-Ni/SiO_2-dried-2H2 catalyst. The operating conditions: P = 100 bar, T = 250-300 °C, H_2/CO = 1 (vol/vol), gas velocity = 7.8 NL g^{-1} h^{-1} (based on the weight of catalyst and the gas flow referring to 298.15 K and 1 atm).

6.4.3 Effect of calcination

The catalytic performances of the Cu-Ni/SiO_2-dried-20H2 and Cu-Ni/SiO_2-calc-20H2 catalysts are summarized in Table 6-3. Both Cu-Ni/SiO_2-dried-20H2 and Cu-Ni/SiO_2-calc-20H2 catalysts show a high selectivity to methanol in the range of 98.9 to 99.2 mol %. The Cu-Ni/SiO_2-calc-20H2 catalyst shows the same methanol selectivity to Cu-Ni/SiO_2-dried-20H2 catalyst at 250 °C. Moreover, the selectivity to hydrocarbons (mainly methane) is at a low level of 0.1-0.4 mol % for both Cu-Ni/SiO_2-dried-20H2 and Cu-Ni/SiO_2-calc-20H2 catalysts at 250 °C. The Cu-Ni/SiO_2-dried-20H2 catalyst exhibits about 1.6 times higher methanol productivity than the Cu-Ni/SiO_2-calc-20H2 catalyst at 250 °C. This is probably explained by the particle sizes derives from XRD which show that the Cu-Ni alloys are 6 nm and 14 nm for the Cu-Ni/SiO_2-dried-20H2 and Cu-Ni/SiO_2-calc-20H2 catalysts, respectively.

Table 6-3 Behavior of Cu-Ni/SiO_2-calc-20H2 and Cu-Ni/SiO_2-dried-20H2 catalysts in CO hydrogenation at steady state at 100 bar, and H_2/CO = 1.0, vol/vol.

Catalysts	T	Gas velocity	CO conv. [mol %]	Carbon based, CO_2-free selectivity [mol %]			STY_{MeOH}	Area-based activity
	[°C]	[NL g^{-1} h^{-1}]	[%]	MeOH	C_{2+}-Oxygenates[a)]	Hydrocarbons	kg kg_{cat}^{-1} h^{-1}	mol m^{-2} s^{-1}
Cu-Ni/SiO_2-calc-20H2	250	3.9	2.1	99.2	0.4	0.4	0.065	$6.7 \cdot 10^{-8}$
Cu-Ni/SiO_2-calc-20H2	275	3.9	5.1	99.1	0.5	0.4	0.167	$1.7 \cdot 10^{-7}$
Cu-Ni/SiO_2-calc-20H2	300	7.6	6.0	98.9	0.5	0.6	0.33	$3.4 \cdot 10^{-7}$
Cu-Ni/SiO_2-dried-20H2	250	4.1	3.7	99.2	0.7	0.1	0.107	$5.5 \cdot 10^{-8}$

[a)] *C_{2+}-Oxygenates include ethanol and DME.*

Table 6-4 Behavior of Cu-Ni/SiO_2-dried-20H2, Cu-Ni/SiO_2-dried-2H2 and Cu/ZnO/Al_2O_3 catalysts in CO hydrogenation at steady state at 100 bar, and H_2/CO = 1.0.

Catalysts	T	Gas velocity	CO conv. [mol %]	Carbon based, CO_2-free selectivity [mol %]			STY_{MeOH}	Area-based activity
	[ºC]	[NL g^{-1} h^{-1}]	[%]	MeOH	C_{2+}-Oxygenates[a)]	Hydrocarbons	kg kg_{cat}^{-1} h^{-1}	mol m^{-2} s^{-1}
Cu-Ni/SiO_2-dried-20H2	250	3.7	3.7	99.2	0.70	0.10	0.107	$5.5 \cdot 10^{-8}$
Cu-Ni/SiO_2-dried-2H2	250	7.8	1.8	98.3	1.5	0.2	0.136	$5.8 \cdot 10^{-8}$
Cu-Ni/SiO_2-dried-2H2	275	7.8	3.6	98.5	1.1	0.4	0.268	$1.1 \cdot 10^{-7}$
Cu-Ni/SiO_2-dried-2H2	300	7.8	7.7	98.2	1.3	0.5	0.583	$2.5 \cdot 10^{-7}$
Cu/ZnO/Al_2O_3	250	16.8	7.2	99	0.9	0.1	0.842	$9.2 \cdot 10^{-8}$
Cu/ZnO/Al_2O_3	275	16.8	13.6	97.6	2.1	0.3	1.315	$1.4 \cdot 10^{-7}$
Cu/ZnO/Al_2O_3	300	33.6	12.7	96.3	2.8	0.9	2.666	$2.9 \cdot 10^{-7}$

[a)] *C_{2+}-Oxygenates include ethanol and DME.*

In fact, the methanol rate calculated based on the surface area of active metals shows that the area-based activities are similar for both catalysts at the same temperature. Both catalysts contain a small amount of free copper (about 13-15 mol %), which will also contribute but to a significantly smaller amount [18]. The methanol productivity increases with increasing of temperature, the methanol selectivity declines slightly, while the C_{2+}-Oxygenates (ethanol and DME) and hydrocarbons increase slightly.

6.4.4 Effect of reducing gas composition

Table 6-4 summarizes the performance of Cu-Ni/SiO_2-dried-20H2, Cu-Ni/SiO_2-dried-2H2, and Cu/ZnO/Al_2O_3 model catalysts. In order to compare the area-based activity, different gas velocities are used for different catalysts. All tested catalysts show high selectivity to methanol in the range of 96.3 to 99.2 mol %. Note, however, that in the CO/H_2 syngas the methanol selectivity of the Cu/ZnO/Al_2O_3 model industrial catalyst is actually lower than for the Cu-Ni based catalysts. The metal area-based activity for methanol synthesis of both the Cu-Ni/SiO_2-dried-20H2 and the Cu-Ni/SiO_2-dried-2H2 are comparable to the model catalyst at the same temperature (Table 6-4).

The Cu-Ni/SiO_2-dried-20H2 catalyst shows a slightly higher selectivity to methanol than the Cu-Ni/SiO_2-dried-2H2 catalyst at 250 °C. The difference could be attributed to the higher selectivity to dimethyl ether (DME) over the Cu-Ni/SiO_2-dried-2H2 catalyst. The DME is probably formed by dehydration of methanol over acidic sites on the catalysts. At 250 °C, the Cu-Ni/SiO_2-dried-2H2 catalyst shows about 27% higher methanol productivity compared to the Cu-Ni/SiO_2-dried-20H2 catalyst. The in situ XRD show that the Cu-Ni/SiO_2-dried-2H2 has less segregated Cu (alloying as $Cu_1Ni_{1.1}$) with a particle sizes of 5 nm, however, the Cu-Ni/SiO_2-dried-20H2 catalyst has about 6 mol % more Cu separates from Cu-Ni ($Cu_1Ni_{1.57}$) alloy, which influences of Cu-Ni alloying degree and hence potentially affect the activity. The alloy particle size is slightly larger for the Cu-Ni/SiO_2-dried-20H2 catalyst (Table 6-2).

6.4.5 Effect of CO_2 co-feeding and DFT calculations

For the commercial Cu/ZnO/Al_2O_3 catalyst, a small amount of CO_2 is generally co-fed for improving both activity and selectivity to methanol [18]. Most reports in the literature also suggest that CO_2 is the dominant source of carbon for methanol formation over commercial Cu/ZnO catalysts [118, 119]. It is therefore important also to evaluate Cu-Ni in a CO_2 containing syngas. Here both Cu/ZnO/Al_2O_3 and Cu-Ni/SiO_2-calc-20H2 catalysts were tested at commercial-like conditions: 65 bar with 3 mol % CO_2 in syngas (H_2/CO = 2/1, mol/mol). The selectivity of methanol formation over the Cu/ZnO/Al_2O_3 model catalyst reaches up to 99.7 mol % at a rate of $1.9 \cdot 10^{-7}$ mol m^{-2} s^{-1} without any measurable selectivity to hydrocarbons in CO_2 containing syngas (Table 6-5). For the Cu-Ni/SiO2-calc-20H2 catalyst, the methanol productivity decreases by about 17% to 48% (depending on the temperature) compared to the methanol productivity in CO/H_2 (CO_2-free) at the same conditions, while the selectivity for methanol slightly increases. Additionally, net CO_2 conversion is observed over Cu-Ni/SiO_2-calc-20H2 catalyst, which produces water as a byproduct. The deactivation of Cu-Ni based catalyst in CO_2-cofed syngas may be related to the water-gas shift (WGS) reaction and surface restructuring, which will be discussed later together with the results of DFT calculations.

Table 6-5 Behavior of Cu-Ni/SiO2-calc-20H2 and $Cu/ZnO/Al_2O_3$ catalysts in CO_2-cofed syngas conversion at steady state at 65 bar.

Catalysts	T	Gas velocity	$H_2/CO/CO_2$	X_{CO}[a)]	X_{CO2}[b)]	Carbon based, CO_2-free selectivity [mol %]			STY_{MeOH}	Area-based activity
	[ºC]	[NL g^{-1} h^{-1}]		[%]	[%]	Methanol	C_{2+}-Oxygenates[c)]	Hydrocarbons	kg kg_{cat}^{-1} h^{-1}	mol m^{-2} s^{-1}
$CuNi/SiO_2$-calc-20H2	250	4.0	62/38/0	1.8	-	96.7	2.1	1.0	0.037	$1.9 \cdot 10^{-8}$
$CuNi/SiO_2$-calc-20H2	275	4.0	62/38/0	4.5	-	95.6	2.5	1.7	0.095	$4.9 \cdot 10^{-8}$
$CuNi/SiO_2$-calc-20H2	300	4.0	62/38/0	9.2	-	87.9	4.6	7.1	0.181	$9.2 \cdot 10^{-7}$
$CuNi/SiO_2$-calc-20H2	250	3.9	62/35/3	1.0	3.4	97.7	1.2	1.1	0.019	$9.7 \cdot 10^{-9}$
$CuNi/SiO_2$-calc-20H2	275	3.9	62/35/3	3.0	9.5	96.8	1.6	1.6	0.058	$3.0 \cdot 10^{-8}$
$CuNi/SiO_2$-calc-20H2	300	7.7	66/31/3	4.7	4.5	90.3	4.0	5.5	0.151	$7.7 \cdot 10^{-8}$
$Cu/ZnO/Al_2O_3$	250	33	66/31/3	11.5	13.4	99.7	0.2	0	1.706	$1.9 \cdot 10^{-7}$

[a)] CO conversion; [b)] CO_2 conversion; [c)] C_{2+}-Oxygenates include ethanol and DME.

On the basis of kinetic investigations and ^{14}C-labelling experiments Kagan et al. [121-124] determined that CO_2 is the dominant source of carbon in methanol formed over a commercial Cu/ZnO catalyst. Using ^{14}C-labelling experiments Chinchen et al. [118, 125] arrived at the same conclusion. Moreover, DFT calculations by Grabow and Mavrikakis [126] recently suggested that CO_2 hydrogenation is responsible for about 2/3 of the methanol synthesis under a typical industrial methanol synthesis conditions. In our studies, the area-based activity on the $Cu/ZnO/Al_2O_3$ model catalyst is about 19 times higher than for the Cu-Ni catalyst in a CO_2 containing syngas at the same temperature and pressure. As described above, in CO/H_2 the area-based activities for both catalysts are similar at similar conditions. It is clear that CO_2 promotes the $Cu/ZnO/Al_2O_3$ catalyst, whereas to some extent poisons the Cu-Ni catalyst. Wandelt and Brundle [298] found that exposing a Cu-Ni surface to an O_2 containing atmosphere brings more Ni to the surface compared to CO. In the present studies, co-feeding CO_2 in syngas, thereby probably raises the oxidative potential of the feed syngas, is expected to bring more Ni to the surface with CO_2 in the gas. In addition, as the net CO_2 conversion over $Cu-Ni/SiO_2$-calc-20H2 catalyst produces water as a byproduct, which leads to hydroxyl and oxygen species on the surface, in particular, because Cu-Ni based catalysts are efficient catalysts for the WGS reaction [330, 334, 335]. Hence this shows that as soon as carbon dioxide is introduced this will involve free O species as surface species, which will induce more Ni segregating to the surface.

Table 6-6 Segregation energies for Cu in Ni with and without adsorbed oxygen on the 111 plane.[a)]

Cu content (ML)	Distribution in 1st and 2nd layer (1st:2nd)	ΔE_{seg} in vacuum[b)]	ΔE_O[c)]	ΔE_{segO}[d)]
0	Ni	-	-2.25	-
1/3	Ni_2Cu_1:Ni_3Cu_0	-	-1.94	-
	Ni_3Cu_0:Ni_2Cu_1	0.64	-2.60	-0.03
2/3	Ni_1Cu_2:Ni_3Cu_0	-	-2.05	-
	Ni_2Cu_1:Ni_2Cu_1	-0.08	-1.95	0.02
	Ni_3Cu_0:Ni_1Cu_2	0.16	-2.31	-0.10
1	Ni_0Cu_3:Ni_3Cu_0	-	-1.29	-
	Ni_1Cu_2:Ni_2Cu_1	0.40	-1.61	0.08
	Ni_2Cu_1:Ni_1Cu_2	0.64	-1.93	0.00
	Ni_3Cu_0:Ni_0Cu_3	0.80	-2.36	-0.27

[a)] Segregation energies are for a $\sqrt{3} \times \sqrt{3}\,R30°$ four layer slab of Ni where the first two rows are composed according to column 2. All energies are in eV. [b)] Segregation energies relative to the state where all Cu atoms are present in the first layer. [c)] Adsorption energies for 1/3 ML of oxygen relative to ½ O_2 in the gas-phase. [d)] Oxygen induced segregation energies compared to the state where all Cu atoms are in the first layer.

In order to substantiate and estimate the effect DFT calculations were performed. In previous studies we have shown that Cu is most stable in the first layer of Cu-Ni when there are no adsorbates present [6]. In the presence of CO, however, Ni segregates to the surface due to its stronger bond towards CO than that of Cu [6]. The next step is now the influence of carbon dioxide, which is connected to oxygen or hydroxyl species on the surface. Hence, we present here DFT calculations of a $\sqrt{3} \times \sqrt{3}\,R30°$ unit cell for the (111) surfaces with different concentrations of Cu and Ni in the first and second layer to identify the stable surface. As shown in Table 6-6, the oxygen induces segregation energies are -0.10 eV and -0.27 eV for the Ni_3Cu overlayer structures when

compared to a pure Ni overlayer. Cu, however, is segregating to the surface under vacuum conditions, as its surface energy is lower than that of Ni. This is in agreement with the experimental studies by Wandelt and Brundle [298] that oxygen segregates more Ni to the surface compared to CO. It seems that co-feeding CO_2 in syngas will introduce additional oxygen species as surface species, which could change the surface composition by moving more Ni to the first layer. This change in surface composition could hence be one of the reasons of the unusual influence of CO_2 on the catalytic performance.

6.5 Conclusion

We have synthesized silica supported Cu-Ni based alloy catalysts that show high selectivity (~99 mol %) and activity for methanol synthesis from H_2/CO and analysed the alloying both by in situ XRD and in situ TEM combined with EELS. In a H_2/CO synthesis gas in the absence of CO_2, the area-based methanol formation rate on the Cu-Ni catalysts is comparable to a commercial $Cu/ZnO/Al_2O_3$ model catalyst. There is no apparent catalyst deactivation observed during 60 h time on stream, in contrary to the commercial methanol synthesis catalyst.

The pretreatment of dry impregnated catalysts has a significant influence on Cu-Ni particle sizes and the alloy formation itself and consequently on its catalytic activity. Calcination of the impregnated catalyst leads to a broader particle size distribution and bigger particles compared to that of direct reduced impregnated catalyst. By reducing impregnated Cu-Ni catalyst in a more dilute H_2 gas (2 mol % H_2/N_2, compared to the same catalyst reduced at 20 mol % H_2/N_2) the amount of Cu particles that segregate from the Cu-Ni particles could be decreased. In addition the Cu and Cu-Ni particle sizes are smaller. Consequently, this increases the overall productivity of methanol.

Addition of 3 mol % CO_2 in a 2:1 H_2/CO feed (similar to the industrial methanol synthesis conditions) lowers the activity of the catalyst. Density functional theory calculations show that oxygen adsorbed on the surface induces segregation of Ni to the first layer due to stronger oxygen (one of the intermediates for water gas shift reaction) adsorption on Ni. Probably, the co-feeding CO_2 in syngas increases its oxidative potential and therefore changes the surface composition by moving more Ni to the first layer, which is therefore, the reasons of the unusual influence of CO_2 on the catalytic performance. The study shows in general how tuning of the preparation parameters influences the catalytic performance and the in situ techniques such as XRD, XAS and TEM together with DFT-calculations are important to understand the structure-activity relationships in more detail; this will both be beneficial for improving the present but also other bimetallic methanol synthesis catalysts in future.

7 CO hydrogenation on Cu-Ni catalysts: Influence of preparation methods

7.1 Abstract

Silica supported Cu-Ni alloy catalysts are prepared via incipient wetness impregnation, co-precipitation, and deposition-co-precipitation methods and tested for activity in CO hydrogenation to methanol. The formation of bimetallic Cu-Ni alloy nanoparticles has been studied during reduction with in situ X-ray diffraction. It is found that co-precipitation and deposition-co-precipitation methods are more efficient than the impregnation method for preparation of small and homogeneous Cu-Ni alloy nanoparticles. The selectivity towards methanol is always higher than 99 mol %, and the area-based methanol formation rate over these catalysts are at the same level regardless of the preparation method. The methanol productivity increases in the order of impregnation < co-precipitation < deposition-co-precipitation. The space time yield of methanol is about 3 times higher on the deposition-coprecipitated catalyst than the impregnated catalyst. The increase in activity is attained predominantly by a decrease in particle size of the active metal alloy particles. A maximum methanol productivity of 0.66 kg kg_{cat}^{-1} h^{-1} with selectivity up to 99.2 mol % has been achieved for a Cu-Ni/SiO_2 catalyst prepared by the deposition-co-precipitation method.

7.2 Introduction

Methanol is one of the top ten petrochemicals produced in the world, and is mainly used as a starting material for production of chemicals such as acetic acid, formaldehyde, and olefins, and as a solvent for a large variety of syntheses [24, 50, 102]. Additionally, methanol has also been suggested as a transportation fuel [57, 336-338]. Methanol is currently produced over Cu/ZnO/Al_2O_3 catalysts from syngas [115, 134, 279], which can be derived from natural gas reforming [11, 13, 15] or coal [42, 44] and biomass by gasification [8, 35, 37, 41, 96]. The methanol synthesis process can be carried out at a moderate temperature (250-300 °C) and pressure (50-100 bar) [18, 46], and a productivity of about 1 kg of methanol per liter catalyst per hour, which is stated to be the required number for the industrial methanol synthesis at low pressure (<100 bar) [18, 25]. Although the commercial Cu/ZnO/Al_2O_3 catalysts are rather long lived, 3 years or more, they do deactivate via poisoning or sintering processes and thus deactivation poses one of the biggest problems [18]; more than one-third of the activity is lost after the first 1000 h of operation for this catalytic system [18, 24, 64-66]. Development of alternative methanol synthesis catalysts for better stability and activity has been of great interest, and numerous elements such as Cs [67], Th [68], Zr [69, 70], Ce [71], Mn [72], Ga [73], and Pd [73, 74] have been investigated as possible replacements or additives to enhance the catalytic performance of Cu/ZnO-based methanol synthesis catalysts.

Based on both density functional theory (DFT) calculations and activity tests for CO hydrogenation we recently identified Cu-Ni alloys supported on SiO_2 as promising methanol synthesis catalysts [6]. We also found that Cu-Ni catalysts on different supports such as SiO_2, carbon nanotubes, ZrO_2 and γ-Al_2O_3, display significant differences in their catalytic behaviors for CO hydrogenation in terms of product selectivity [314]. Furthermore, we found that the pretreatment steps of Cu-Ni catalysts such as calcination and reduction atmosphere have significant influence on the activity of catalysts [98]. These catalysts were prepared by the incipient wetness impregnation method. However, it has been reported that metal particles prepared from nitrate precursors via impregnation generally are larger, more than 10 nm, than by e.g. co-precipitation which has been ascribed to agglomeration of metal hydroxynitrate during the drying and calcination

steps [322, 339-341]. Cu-based catalysts are often prepared by a co-precipitation approach since high loadings of metals can be achieved in combination with high metal dispersion and better stability [111, 342, 343].

In this work we investigate the effect of preparation methods on the activity of methanol synthesis over the novel Cu-Ni methanol synthesis catalysts. Firstly, we used both a high and a low surface area silica as carriers for impregnation to compare the influence of carrier surface area on catalytic activity and secondly, we prepared silica supported Cu-Ni catalysts via two additional types of preparation methods: co-precipitation, and deposition-co-precipitation and tested the catalysts at the same conditions for CO hydrogenation. Inductively coupled plasma optical emission spectroscopy (ICP-OES) elemental analysis, BET surface area measurements, in situ X-ray diffraction (XRD), thermogravimetric analysis (TGA) and transmission electron microscopy (TEM) have been used to identify the catalyst structure.

7.3 Experimental Section

7.3.1 Preparation of Cu-Ni precursor materials

Silica supported Cu/Ni catalyst precursors (20 wt % Cu+Ni, Cu/Ni=2 molar ratio) were prepared by incipient wetness impregnation, co-precipitation, and deposition-co-precipitation. The specific preparation procedures are described below.

Incipient wetness impregnation: An aqueous solution was prepared by dissolving $Cu(NO_3)_2 \cdot 3H_2O$ and $Ni(NO_3)_2 \cdot 6H_2O$ (Sigma-Aldrich) in de-ionized water. Two types of silica were used for impregnation (a) silica with a BET specific surface area of 207 m^2/g (denoted as SiO_2) supplied by Saint-Gobain Norpro, (b) mesoporous silica MCM-41 (denoted as MCM-41) with a BET surface area of 748 m^2/g supplied by Sigma-Aldrich. Support pellets (600-1400 µm) were impregnated with an amount of the aqueous solution based on the pore volume of support (1.2 mL g^{-1} for SiO_2 and 1.37 g mL^{-1} for MCM-41). After 1 h aging at room temperature, the catalyst precursors were dried at 110 °C in air overnight. These two catalysts were denoted as Cu-Ni/SiO_2-IWI and Cu-Ni/MCM-41-IWI, respectively.

Co-precipitation: An aqueous solution of mixed metal nitrates [($Cu(NO_3)_2 \cdot 3H_2O$ (0.0690 M L^{-1}) and $Ni(NO_3)_2 \cdot 6H_2O$ (0.0345 M L^{-1}), 250 mL] with 37 wt % HNO_3 (25 mL, to increase the acidity of nitrate solution that can neutralize the $Na_2Si_2O_3$ solution, which has a strong basicity), was coprecipitated by a solution of $Na_2Si_2O_3$ (Sigma-Aldrich, 0.213 M L^{-1}, 500 mL) in 500 mL of preheated (60 °C) demineralized water. During the precipitation process, pH was maintained at 7±0.05 by controlling the flow of the nitrate and silicate solutions, and temperature was kept at 60 °C. Then the precipitate was aged at 60 °C for 1 h (with continuous stirring). During this hour the pH value was maintained at 7±0.02 with metal solution and co-precipitation agent solution. Then the precipitate was aged at room temperature overnight. Afterwards the precipitate was filtered and washed three times with demineralized water, followed by drying overnight at 110 °C and calcination at 300 °C in a flow of N_2 for 4 h (ramping rate 2 °C min^{-1}). This sample was denoted as Cu-Ni/SiO_2-Copr.

Deposition-co-precipitation: An aqueous solution of metal nitrates [($Cu(NO_3)_2 \cdot 3H_2O$ (0.0690 M L^{-1}), and $Ni(NO_3)_2 \cdot 6H_2O$ (0.0690 M L^{-1}), 250 mL] was coprecipitated by a solution of Na_2CO_3 (Sigma-Aldrich, 500 mL, 0.103 M L^{-1}) in a 1 L of preheated (about 60 °C) demineralised water containing a suspension of SiO_2 (207 m^2/g, in a size range of 150-300 µm). During the precipitation process, pH was maintained at 7±0.05 by controlling the flow of the nitrate and carbonate solutions, and the temperature was kept at 60 °C. Then the precipitate was aged at 60 °C for 1 h (with continuous stirring). During this hour the pH value was maintained at 7±0.02 with metal solution and co-precipitation agent solution. The precipitate was aged at room temperature overnight.

Afterwards the precipitate was filtered and washed three times with demineralized water, followed by drying overnight at 110 °C and calcination at 300 °C in a flow of N_2 for 4 h (heating rate 2 °C min^{-1}). This sample was denoted as Cu-Ni/SiO_2-Dep-Copr.

7.3.2 Characterization

The chemical composition of all catalysts were determined by an inductively coupled plasma-optical emission spectrometer (ICP-OES, Perkin–Elmer, model Optima 7300) and using Ar as plasmogene. In a typical analysis, 5 g of $K_2S_2O_7$ was melted together with 0.25 g sample and dissolved in 10 ml HCl in 200 ml water and then analyzed.

The BET surface area was determined by N_2-adsorption at 77 K by means of a QuantaChrome Autosorb iQ^2 gas sorption analyzer. The specific surface area was analyzed using a 7-point, linear BET plot in the range of p/p0 = 0.05-0.3. Prior to the BET measurement the sample was dried under nitrogen flow (200 NmL min^{-1}) at 150 °C for 2 h.

In order to understand the reduction or calcination processes of the nitrate catalyst precursors (Cu-Ni/SiO_2-IWI), TGA analysis with different types of gases was carried out with a NETZSCH STA-449-F1 setup. First, 15 mg of the samples was loaded into an alumina sample holder. The sample was then heated to 400 °C in a 120 ml min^{-1} flow of 4.2 vol % H_2/N_2 or pure N_2 with a heating rate of 2 °C min^{-1}.

In situ XRD was performed with a PANalytical X'Pert PRO diffractometer equipped with an Anton Paar XRK 900 in situ cell and a gas flow control system for H_2-TPR. Silica supported Cu-Ni samples were heated in flow of 2 mol % H_2/He up to 300 °C for 1 h. Fig. 7-1 shows a typical temperature-time profile with the plateaus for XRD measurement applied to the reduction of Cu-Ni precursor materials in 2 mol % H_2/N_2 with a flow rate of 100 ml min^{-1}. Each XRD measurement takes 10 minutes, and the temperature was maintained during the XRD measurement. After reduction, the sample was cooled to room temperature, and then a long XRD scan (640 minutes) was performed to determine the particle sizes of Cu-Ni alloys.

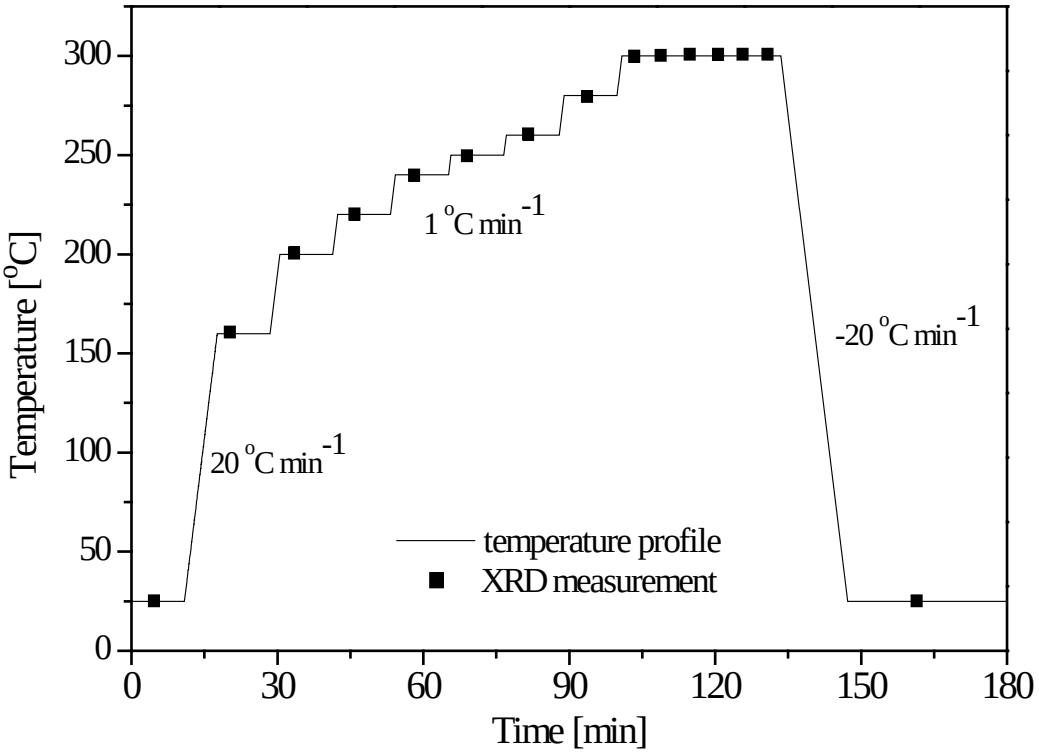

Fig. 7-1 A typical temperature-time profile applied for the reduction of Cu-Ni precursor materials in 2 mol % H_2/N_2 with a flow rate of 100 ml min^{-1}.

TEM images were acquired using an FEI Titan 80–300 aberration corrected microscope operated at 300 kV and an FEI Tecnai T20G2S microscope operated at 200 kV. The catalyst precursors were dispersed in dry form on the TEM grids, which were Au-grids coated with a holey carbon film.

7.3.3 Catalyst testing

CO hydrogenation experiments were performed in a high pressure, fixed-bed flow reactor setup with an online gas chromatograph equipped with flame ionization and thermal conductivity detectors (6890N GC-FID/TCD from Agilent Technologies). Detailed descriptions of the experimental setup and the experimental procedure have been provided in the Refs [196, 197]. Methanol, ethanol, 1-propanol, 1-butanol, 2-butanol, 2-methyl-1-propanol, methane, ethane, ethene, and propane, as well as dimethyl ether (DME) and ethyl acetate were characterized. A bubble flow meter was used for determining the volumetric flow rate of the reactor effluent. Prior to the reaction, all catalytic precursors were reduced in situ by a flow of 1.4 mol % H_2 in N_2 for 12-14 h at 280 °C (which was reached using a heating rate of 1 °C min^{-1}). The carbon mass balance was generally fulfilled to within 5 mol %.

The conversion of CO (X_{CO}) is calculated from the molar flow rates of CO (F_{CO}) into and out of the reactor:

$$X_{CO} = \frac{F_{CO}^{in} - F_{CO}^{out}}{F_{CO}^{in}} \cdot 100\%$$

The selectivity to a given product (S_i) is based on the total number of carbon atoms in the products:

$$S_i = (n_i y_i) / (\sum n_i y_i) \cdot 100\%$$

where n_i ($n_i \geq 1$) is the number of carbon atoms in component *i*, and y_i is the mole fraction of component *i* in the product.

The space time yield (STY_{MeOH}) of methanol is the production rate of methanol per mass of catalyst:

$$STY_{MeOH} = \frac{M_{MeOH} F_{MeOH}}{m_{cat}} \left[kg\ kg_{cat}^{-1}\ h^{-1} \right]$$

where, M_{MeOH} is the molar mass of methanol and F_{MeOH} is the molar flow rate of methanol out of the reactor. Here, we report the *STY* in the units of mass of methanol produced per hour and per mass of catalyst (m_{cat}), which includes both active metals and support.

The metal area-based activity of methanol is the production rate of methanol per metal surface area of catalyst:

$$Area-based\ activity = \frac{STY_{MeOH}}{M_{MeOH} \times S_{metal} \times 3600 \frac{s}{h}} \left[mol\ m^{-2}\ s^{-1} \right]$$

where, M_{MeOH} is the molar mass of methanol, S_{metal} is the metal surface area of catalyst, determined from the XRD particle size of the Cu-Ni alloy particles.

7.4 Results and Discussion

7.4.1 Catalyst structure

7.4.1.1 ICP-OES elemental analyses and BET surface area studies

The ICP-OES elemental analysis results for all catalyst precursors are listed in Table 7-1. The desired composition was 20 wt % Cu+Ni metal loading on silica, and the samples are close to this value. In addition, the Cu/Ni atomic ratios are also close to the expected atomic ratio of 2.

Table 7-1 ICP-OES elemental analysis and BET surface area measurement results of catalyst precursors.

Catalysts	Analyzed Loading (wt %)				Metal loading in reduce catalyst [a)]	Cu/Ni (atomic ratio)		BET surface area
	Cu	Ni	Si	Na	Cu+Ni (wt %)	nominal	measured	$m^2\ g^{-1}$
Cu-Ni/SiO_2-IWI	9.17	4.1	20	-	23.7	2.00	2.07	116
Cu-Ni/MCM-41-IWI	9.00	4.09	23.4	-	20.7	2.00	2.03	291
Cu-Ni/SiO_2-Copr	13.0	5.3	30.4	0.205	20.8	2.00	2.12	322
Cu-Ni/SiO_2-Dep-Copr	12.8	4.87	34.4	0.023	22.0	2.00	2.26	253

The specific surface area of impregnated samples, Cu-Ni/SiO_2-IWI and Cu-Ni/MCM-41-IWI decrease about 44% and 61%, respectively, compared to original SiO_2 (207 $m^2\ g^{-1}$) and MCM-41

(748 m^2 g^{-1}) supports. This is probably due to blocking of the pore structure by the loaded metals. Using the same silica (207 m^2 g^{-1}), the surface area of the deposition-coprecipitated sample, Cu-Ni/SiO_2-Dep-Copr, increases to 253 m^2 g^{-1}. The increase in the surface area can presumably be ascribed to the presence of small precipitate nanoparticles in the sample. The coprecipitated sample, Cu-Ni/SiO_2-Copr, shows the highest specific surface area of 322 m^2 g^{-1}. This novel approach to co-precipitate the SiO_2 from Na_2SiO_3 together with metal precursors seems to be an efficient way to prepare high surface area silica supported catalysts. The surface areas of the three catalysts prepared by different methods are in increasing order: impregnation < deposition-co-precipitation < co-precipitation.

7.4.1.2 In situ XRD and TGA studies

Fig. 7-2 shows the in situ XRD patterns for reduction of the Cu-Ni/SiO_2-IWI precursors at different temperatures in the flowing of 2 mol % H_2/He. The catalyst precursor contains Cu/Ni hydroxynitrate that is formed during the drying of impreganated metal nitrate precursors at elevated temperature, which resulting in agglomeration during hydrogenlysis of metal nitrate hydrate to metal hydroxynitrate [324, 325]. There are no observed reflections of either CuO or NiO in the XRD patterns during the reduction process. The main reduction occurs between 230 ºC and 240 ºC. Metallic Cu and Ni have two main reflections, belonging to the [111] and the [002] crystal planes, at 43.3° and 50.4° for Cu and at 44.5° and 51.8° for Ni (ICSD file 52265), respectively. In Fig. 7-2, the first reflection locates at 43.3° with a small shoulder at 43.7° and the second reflection locates at 50.4° with a shoulder at 50.65°. The reflections at 43.3° ad 50.4° are assigned to metallic Cu phase and shoulders are located in between of metallic phases of Cu and Ni are assigned to Cu-Ni alloys. The Cu-Ni alloy phase composition is calculated by using Vegard's law is Cu/Ni=2.0. Based on ICP-OES analysis the Cu/Ni molar ratio is 2.07. Therefore, a small fraction of metallic Cu (about 4 mol % metallic Cu is estimated by using Vegard's law) in the reduced catalysts. In general, Cu and Ni can form a solid solution [265], in the present case, however, a separate Cu phase is also formed. It was reported that the standard reduction potential for Cu is 0.337 eV, which is higher than that of Ni -0.25 eV [330, 332]. Cu is therefore easier to reduce compared to Ni, whereas reduced Cu can act as catalysts to promote the reduction of Ni and whereby Cu-Ni alloys are formed. The phase Cu-Ni alloys is probably due to the Cu segregation at elevated temperatures, which has also been reported before [329, 332]. According to the Scherrer equation [295] the average particle size is about 11 nm for Cu-Ni alloys.

In order to understand the reduction and calcination processes of nitrate precursors, TGA analyses were performed in an inert gas (N_2) flow and a reducing gas (4.2 vol % H_2/N_2) flow. Fig. 7-3 shows the relative weight loss as a function of temperature in two different gas atmospheres. In the flow of 4.2 vol % H_2/N_2, there are three major peaks, the first one is starting at 210 ºC and centered at 250 ºC, and the second and third peaks centered at around 260 and 265 ºC, respectively. In the flow of N_2, there is one major peak start at 210 ºC and center at 250 ºC as well. The temperatures for calcination of Cu and Ni nitrate are similar to what have been reported in literature, between 210 and 280 ºC [326-328]. Therefore, the first peak centered at 250 ºC probably can be ascribed to mass lost resulting from a calcination process. It seems that the nitrate precursors are first calcined and subsequently reduced. The second peak centered at around 260 ºC in reducing gas flow is probably related to the beginning reduction of Cu, which is easy to reduce, and the reduced Cu then acts as a catalyst and enhances the reduction of Ni, whereby a two-peak structure is seen in the mass loss curve. This might further indicate that initially Cu and Ni are not reduced simultaneously and this causes the phase separation. A similar reduction process is observed for the Cu-Ni/MCM-41-IWI sample via the same in situ studies with XRD. The first reflection located at

43.3° with a small shoulder at 43.7° and the second reflection located at 50.45° with a shoulder at 50.8°. This indicates that both metallic Cu phase and Cu-Ni alloys are exist in the reduced Cu-Ni/MCM-41-IWI sample. The Cu-Ni alloy phase composition is calculated by using Vegard's law is Cu/Ni=1.8. On the basis of ICP-OES analysis the Cu/Ni molar ratio is 2.03. Therefore, about 11mol % metallic Cu exists in the reduced catalysts. Moreover, the particle size is about 5 nm for the Cu-Ni alloys.

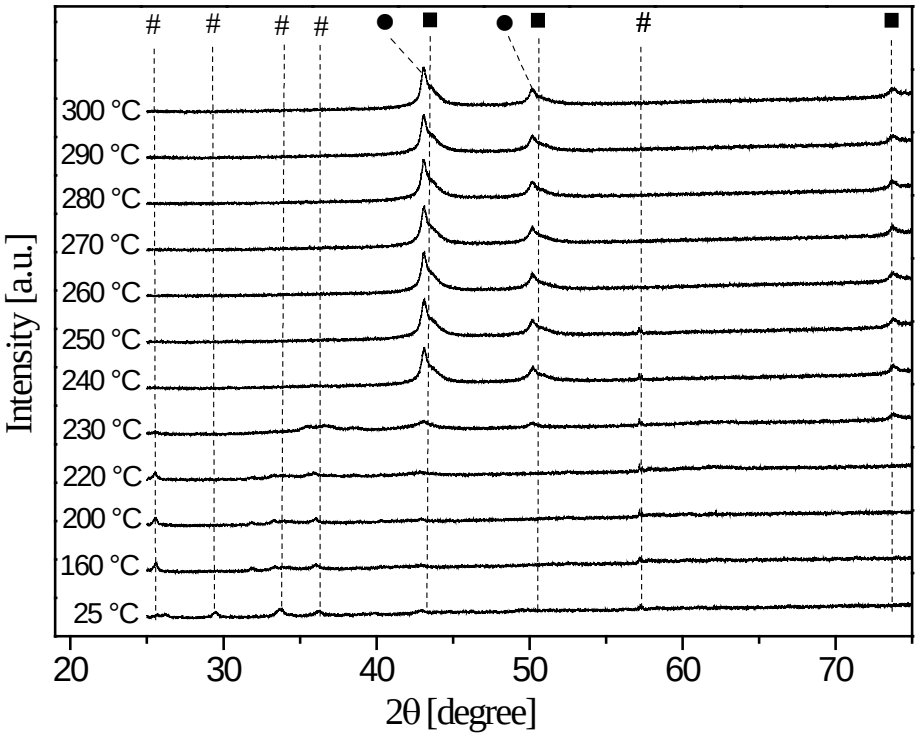

Fig. 7-2 XRD patterns at different temperatures during in situ reduction of the Cu-Ni/SiO_2-IWI sample in a flow of 2 mol % H_2/N_2 with a flow rate of 100 ml min^{-1}. # - Cu/Ni hydroxynitrate, ● - metallic Cu, and ■ - Cu-Ni alloys.

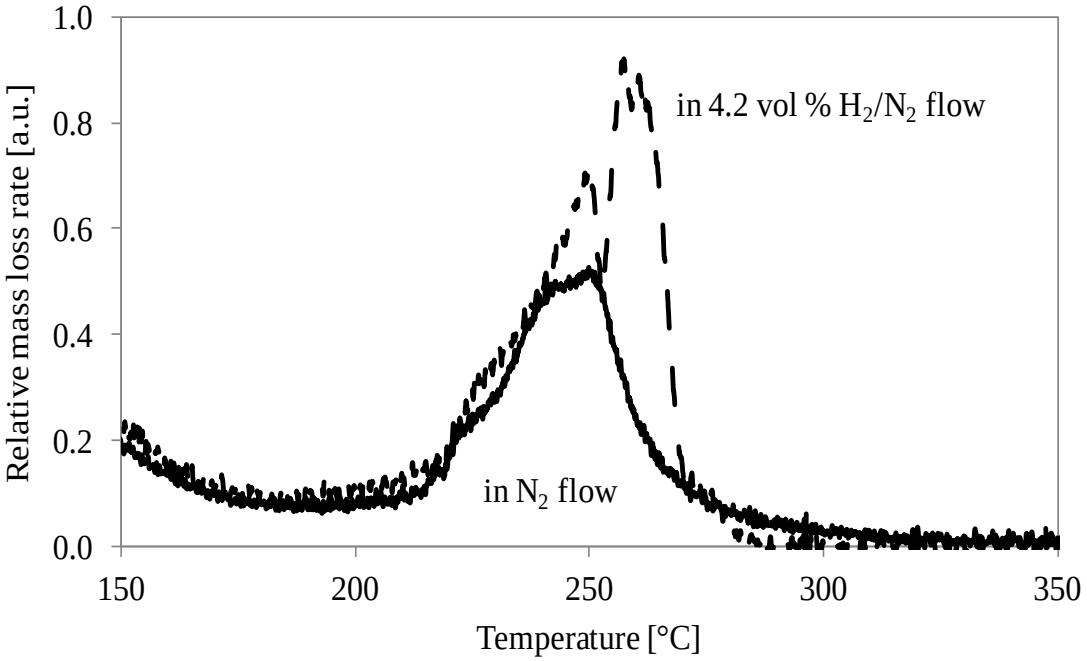

Fig. 7-3 TGA analysis of the Cu-Ni/SiO_2-IWI sample in a flow of N_2 and 4.2 mol % H_2/N_2 with a flow rate of 120 ml min^{-1}.

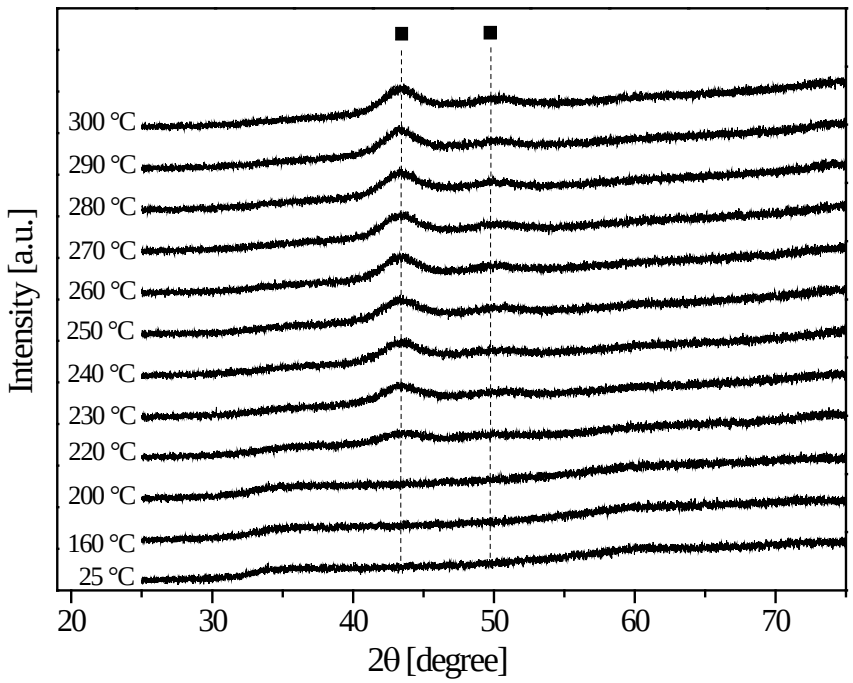

Fig. 7-4 X-ray diffractograms at different temperatures during in situ reduction of the Cu-Ni/SiO_2-Copr sample in a flow of 2 mol % H_2/N_2 with a flow rate of 100 ml min^{-1}. ■ - Cu-Ni alloy.

Fig. 7-4 depicts the in situ XRD scan on Cu-Ni/SiO_2-Copr sample during the reduction process. There are no observed reflections of either CuO or NiO in the XRD patterns in the oxide precursors.

It seems that these species are dispersed finely or in amorphous form in the precursors. The Cu-Ni alloy starts to emerge at 220 ºC, and there is no obvious change after 250 ºC. Two symmetric reflections located at 43.4° and at 50.35° are observed after reduction. It seems that only the Cu-Ni alloys are formed in this case. The Cu-Ni alloys in the impregnated sample (Cu-Ni/SiO_2-IWI) are formed by impregnation and subsequent reduction of separated metal salts on the support. In the coprecipitated sample the Cu-Ni alloys are formed by the reduction of homogeneous oxide solid solution. According to the Scherrer equation [295] the particle size is about 4 nm for Cu-Ni alloys. A very similar reduction process is observed for Cu-Ni/SiO_2-Dep-Copr sample by in situ studies with XRD. Two symmetric reflections located at 43.5° and at 50.6° are observed after reduction, indicating the formation of Cu-Ni alloys. The particle size is 5 nm for the Cu-Ni alloys, as it is shown in Fig. 7-5.

The XRD particle sizes (based on the Scherrer equation [295]) and active surface areas of all reduced samples are calculated and summarized in Table 7-2. The initial support surface area determines the particle size of loaded materials (Cu-Ni alloy) – 11 nm and 5 nm for the 200 m^2 g^{-1} and 750 m^2 g^{-1} silica supported catalysts, respectively. The particle sizes of Cu-Ni alloys are 4 nm and 5 nm for catalysts prepared by co-precipitation and deposition-co-precipitation methods, respectively - significantly smaller than for catalysts prepared via the impregnation method (on SiO_2).

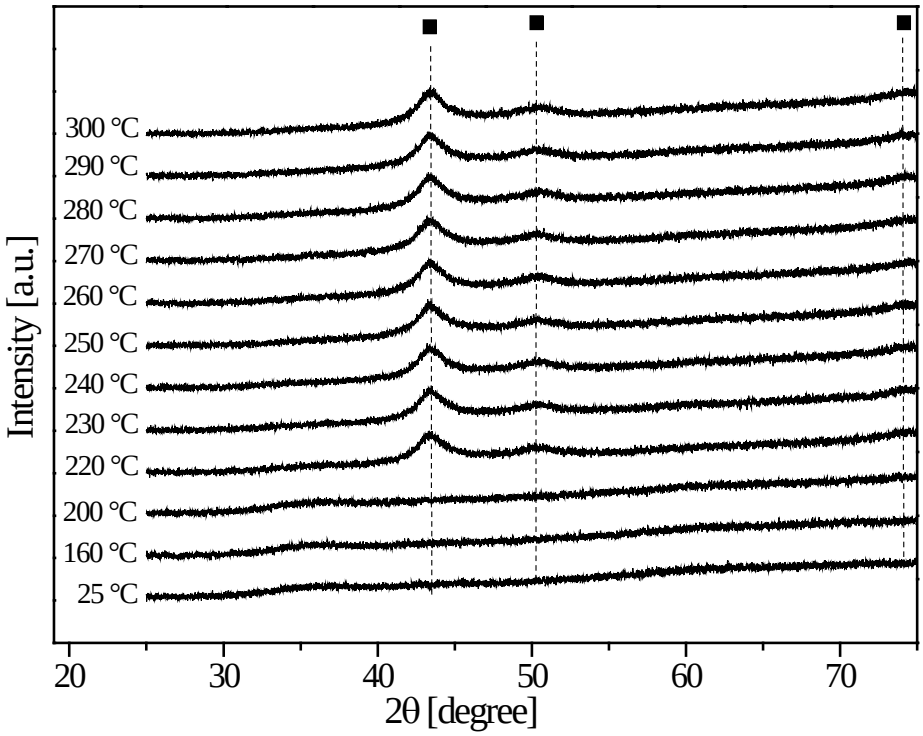

Fig. 7-5 XRD patterns at different temperatures during in situ reduction of the Cu-Ni/SiO_2-DC sample in a flow of 2 mol % H_2/N_2 with a flow rate of 100 ml min^{-1}. ■ - Cu-Ni alloy.

Table 7-2 XRD particle sizes and active surface areas of all reduced supported Cu-Ni samples.

Catalysts	d_{XRD}	Weight of active metal [1)]	S_{metal}
	[nm]	[g]	[m^2 g^{-1}]
CuNi/SiO_2-IWI	11	17.13	10.4
CuNi/MCM-41-IWI	5	13.09	17.4
CuNi/SiO_2-Copr	4	17.67	29.4
CuNi/SiO_2-Dep-Copr	5	18.3	24.4

[1)] *Active metal is metallic Cu+Ni, the weight of metal material per gram of catalyst precursor, which is determined by ICP-OES analysis.*

7.4.1.3 TEM studies

Fig. 7-6 shows TEM images of catalyst nitrate/oxide precursors prepared by three different preparation methods as well as the particle size distributions. A clear difference in structure among these three catalysts can be observed. For the impregnated catalyst (Cu-Ni/SiO_2-IWI), obviously the particle sizes are inhomogeneous, as it can be seen in Fig. 7-6 (a) and corresponding particle size distributions, Fig. 7-6 (b). The distribution of particles is rather broad from a range of 3 to 15 nm. The average particle size is 8.5 nm.

It was reported that for silica-supported metal nitrate that the drying step is of vital importance for the particle size distribution [320]. Drying at elevated temperature resulted in agglomeration of particles of metal hydroxynitrate crystal, which is formed during hydrogenlysis of metal nitrate [320, 325]. Drying at ambient temperatures could prevent the formation of large metal hydroxynitrate crystals, but the subsequent calcination step still result in broad particle size distributions [316]. This could also explain the rather broad particle size distribution observed in the present study.

For both the deposition-co-precipitation prepared catalyst (Cu-Ni/SiO_2-Dep-Copr) and the co-precipitation prepared catalyst precursor (Cu-Ni/SiO_2-Copr), the particle sizes are distributed in a narrow range, and most particles are in the size range between 3 and 5 nm. The average particle size is 4.3 nm and 4.1 nm for Cu-Ni/SiO_2-Dep-Copr and Cu-Ni/SiO_2-Copr catalyst precursors, respectively. The specific surface areas of both deposition-co-precipitation and co-precipitation prepared catalysts are thus 2 to 3 times higher than the surface area of the impregnated catalyst (Cu-Ni/SiO_2-IWI).

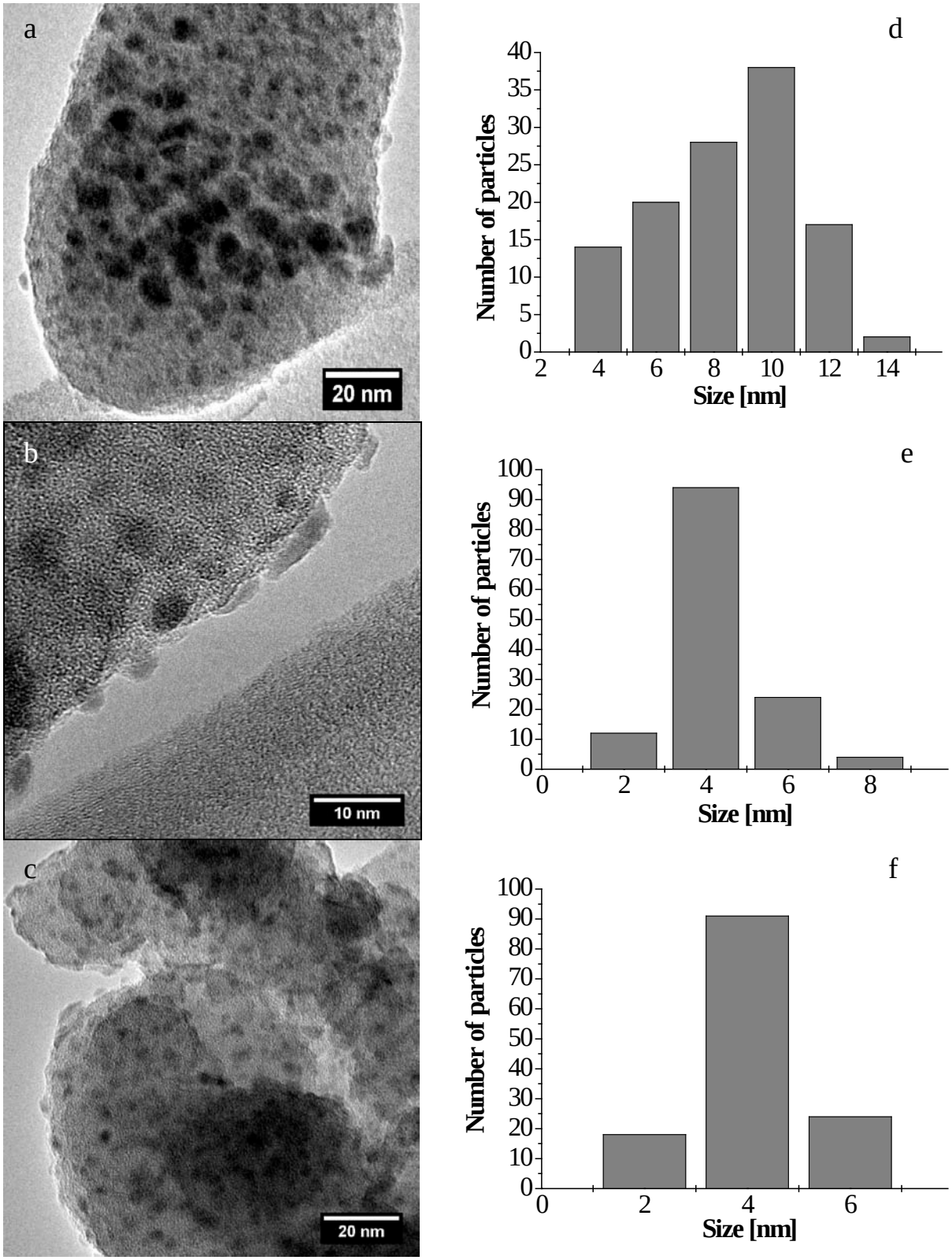

Fig. 7-6 TEM images of (a) Cu-Ni/SiO_2-IMI, (b) Cu-Ni/SiO_2-Dep-Copr, and (c) Cu-Ni/SiO_2-Copr and particle size distributions of (d) Cu-Ni/SiO_2-IMI, (e) Cu-Ni/SiO_2-Dep-Copr, and (f) Cu-Ni/SiO_2-Copr samples.

7.4.2 Catalyst activity and selectivity

7.4.2.1 Time on stream catalytic behavior

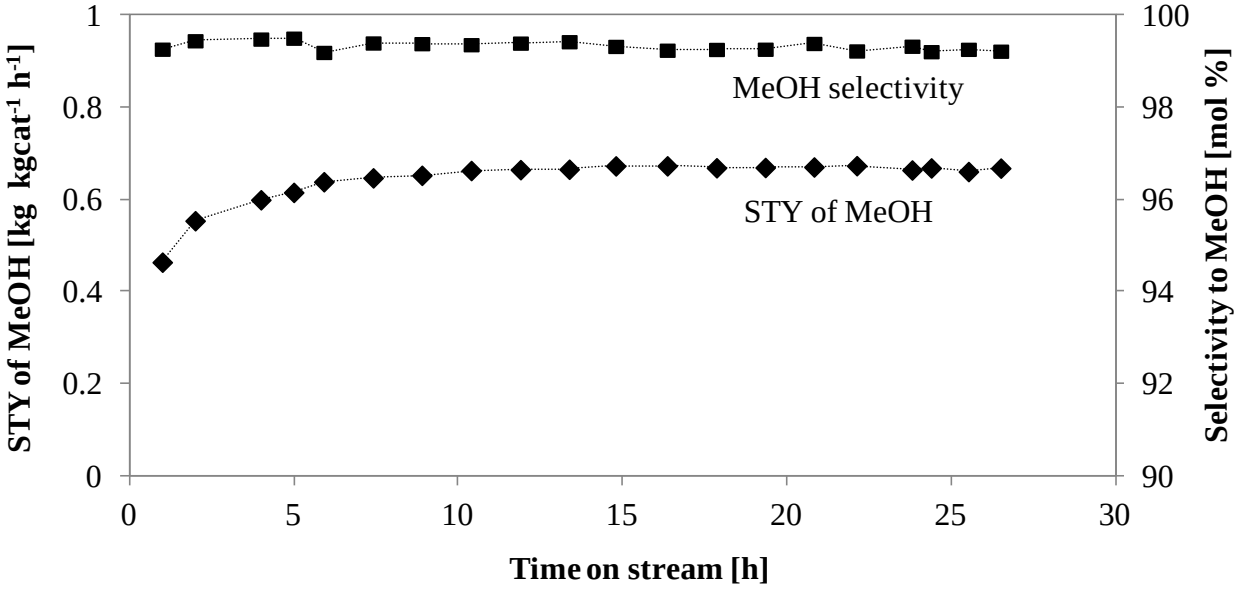

Fig. 7-7 STY and selectivity of methanol as functions of the time on stream for the Cu-Ni/SiO_2-Dep-Copr catalyst. The operating conditions are: P = 100 bar, T = 275 °C, GHSV = 4000 h^{-1} (based on total bed volume and gas flow referring to 298.15 K and 1 atm), feed: $H_2/CO = 2$ (vol/vol).

Fig. 7-7 shows the development of STY and selectivity to methanol as functions of time on stream for the Cu-Ni/SiO_2-Dep-Copr catalyst. The methanol STY increases from 0.46 to 0.66 kg kg_{cat}^{-1} h^{-1} during the first 10 h and then stabilizes. The activation process could be related to surface segregation of Cu-Ni alloys upon syngas introduction. During time on stream one would expect surface segregation of the Ni to the surface of Cu-Ni particles according to both DFT calculations [6] and experiments [297, 298]. The catalyst precursor is reduced in H_2/N_2 (1.4 mol % H_2) gas flow first, and then exposed to the more reducing CO and H_2 mixture. After reduction, Cu occupies the first surface layer due to its lower surface energy, whereas under reaction conditions Ni moves to the surface due to the stronger binding of CO on Ni than on Cu [6, 297, 298]. The selectivity to methanol is maintained at a stable level of 99 mol %. No loss in activity has been observed during the test, which is different than the commercial Cu/ZnO/Al_2O_3 methanol synthesis catalyst for CO hydrogenation, which lost 36% activity within the first 14 h in a test at similar conditions [6]. A similar time on stream behavior is observed for all catalysts that have been tested in this work.

7.4.2.2 Effect of surface area of support

Table 7-3 shows results from the activity tests with both the Cu-Ni/SiO_2-IWI and the Cu-Ni/MCM-41-IWI catalysts at steady state at 275 °C. The Cu-Ni/SiO_2-IWI catalyst produces predominantly methanol with a selectivity of 99.7 mol %, with a small fraction of ethanol and methane. The Cu-Ni catalyst supported on a higher surface area silica (MCM-41, 748 m^2 g^{-1}), which has an ordered mesoporous structure, shows a selectivity to methanol (99.4 mol %) very similar to the Cu-Ni/SiO_2-IWI catalyst, while the activity is about 33% higher than the Cu-Ni/SiO_2-IWI catalyst. As discussed above, the XRD particle sizes of Cu-Ni alloy is 11 and 5 nm for Cu-Ni/SiO_2-IWI and Cu-Ni/MCM-41-IWI catalysts, respectively. The metal areas differ by 1.7 times. Therefore, the methanol production rate based on the metal surface area is calculated and compared

in Table 3. The area-based activities over both catalysts are at the same level. Hence, the impregnated active material on a support with a higher surface area could increase the overall activity to some extent, but not to the extent of the increase in support surface (MCM-41 has 3.6 times higher surface area than the SiO_2). Using the impregnation method, most of support pores are blocked by the loading of metals (as mentioned above that about 44-61% of surface area of support was lost after impregnation), and increasing the surface area of support used for impregnation is thus not a sufficient way to improve the catalytic activity.

Table 7-3 Silica supported Cu-Ni catalysts prepared by different surface areas of supports and different methods during CO hydrogenation at steady state. Experimental conditions: P = 100 bar, T=275 °C, GHSV = 4000 h^{-1} and H_2/CO = 2.0 vol/vol.

Catalysts	TOS[1)]	X_{CO}[2)]	Carbon based selectivity [mol %]				STY_{MeOH}	Activity[3)]
	[h]	[%]	MeOH	Ethanol	Methane	DME	[kg kg_{cat}^{-1} h^{-1}]	[mol m^{-2} s^{-1}]
Cu-Ni/MCM-41-IWI	27	10.3	99.4	0.1	0.4	0.1	0.258	$1.3 \cdot 10^{-7}$
Cu-Ni/SiO_2-IWI	42	8.5	99.7	0.2	0.1	0	0.193	$1.6 \cdot 10^{-7}$
Cu-Ni/SiO_2-Copr	28	14.3	99.1	0.2	0.6	0.1	0.517	$1.5 \cdot 10^{-7}$
Cu-Ni/SiO_2-Dep-Copr	26	16.6	99.2	0.3	0.2	0.1	0.665	$2.4 \cdot 10^{-7}$

[1)] TOS: time on stream. [2)] CO conversion. [3)] Area-based activity.

7.4.2.3 Effect of preparation methods

The performance of silica supported Cu-Ni catalysts prepared by different methods during CO hydrogenation at steady state is shown in Table 7-3. The rest of the product is a small amount of oxygenates (ethanol and/or DME) and methane. With respect to the influence of catalyst preparation method on the productivity of methanol increased in the following order: impregnation < co-precipitation < deposition-co-precipitation. The space time yield of methanol is about 3 times higher on the deposition-coprecipitated catalyst than the impregnated catalyst. The STY of methanol reaches 0.66 kg kg_{cat}^{-1} h^{-1} (the density of catalyst is about 1 kg L^{-1}, and therefore the volume based STY is about 0.66 kg L_{cat}^{-1} h^{-1}) and corresponding selectivity of 99.2 mol % has been achieved for a silica supported Cu-Ni catalyst prepared by deposition-co-precipitation. This is comparable with, although slightly below, the desired industrial productivity of 1 kg L_{cat}^{-1} h^{-1} [18, 25]. Our STY is calculated per gram of catalyst, but more than 80 wt % of the catalyst is support, while the commercial CuZnO/Al_2O_3 methanol synthesis catalyst usually composed of about 85-95 wt % active materials (Cu+ZnO) and 5-15 wt % support (Al_2O_3) [115, 274].

It seems that both catalysts prepared by co-precipitation and deposition-co-precipitation are much more efficient than the impregnated catalyst. Interestingly, the area-based activities for all of these catalysts are at the same level. According to the in situ XRD results, Cu-Ni alloy particle size of the Cu-Ni/SiO_2-Copr catalyst (4 nm) is even smaller than the Cu-Ni/SiO_2-Dep-Copr catalyst (5 nm) and the surface area of the former catalyst is about 1.2 times higher than the surface area of the latter. However, the methanol STY of the Cu-Ni/SiO_2-Copr catalyst is about 22% less than the Cu-Ni/SiO_2-Dep-Copr catalyst. Looking at the results from the ICP-OES elemental analyses, it is found that there is 0.205 wt % Na in the Cu-Ni/SiO_2-Copr catalyst and 0.027 wt % of Na in the Cu-Ni/SiO_2-Dep-Copr catalyst. One could hypothesize that presence of Na might block the surface active sites of Cu-Ni alloys and hence decrease the activity of catalysts. It has been reported that

alkali metals decrease the activity of Cu/Co-based catalysts for CO hydrogenation [175]. Both catalysts are washed in a similar approach, however, the coprecipitated catalysts form nano-scale bulk materials after co-precipitation, which is agglomerated together and hard to redisperse (they formed a dense cake during filtration) in the water during the washing process. This may be less of a problem for the deposition-coprecipitated catalyst, with silica particle sizes of 150-300 µm suspended in the precipitation water medium therefore the bulk materials are supposed to be in micro-scale. This might explain why there is more Na in the co-precipitated catalyst than the deposition-coprecipitated catalyst.

7.5 Conclusion

Silica supported bimetallic Cu-Ni alloy catalysts have been prepared via the incipient wetness impregnation, co-precipitation, and deposition-co-precipitation methods and tested for CO hydrogenation. In addition, the formation of bimetallic Cu-Ni alloy nanoparticles during reduction has been studied with in situ XRD. The results show that co-precipitation and deposition-co-precipitation methods are more efficient than the impregnation method for preparation of small and homogeneous Cu-Ni alloy nanoparticles.

For CO hydrogenation, the selectivity towards methanol is always higher than 99 mol % and the area-based activity to methanol over these Cu-Ni catalysts are at the same level, rather independent on the preparation methods, while the productivity of methanol is significantly influenced by the preparation methods. The STY of methanol increases in the order impregnation < co-precipitation < deposition-co-precipitation. The methanol productivity is about 3 times higher over the deposition-coprecipitated catalyst than the impregnated catalyst. A maximum methanol productivity of 0.66 kg kg_{cat}^{-1} h^{-1} and corresponding selectivity of 99.2 mol % have been achieved for a Cu_2Ni_1/SiO_2 catalyst prepared via the deposition-co-precipitation method. The increase in activity is caused predominantly by a decrease in particle size of the active metal alloy particles in combination with a low content of residual alkali metal (Na) from the co-precipitation agent. Simply increasing the surface area of the support for impregnation is not a very effective way to improve the catalytic activity compared to using a co-precipitation or deposition-co-precipitation methods to prepare the catalysts.

8 In situ observation of Cu-Ni alloy nanoparticle formation by XRD, XAS, and TEM: Influence of Cu/Ni ratio and their catalytic properties

8.1 Abstract

Silica supported, bimetallic Cu-Ni nanoparticles have been prepared with different ratios of Cu to Ni. The Cu-Ni/SiO_2 nanoparticles have been prepared by incipient wetness impregnation without a separate calcination step before reduction. The materials have been characterized by different in situ techniques such as TEM, XAS, FTIR, and XRD. In situ reduction of Cu-Ni alloys studied by combined synchrotron XRD and XAS reveals that a strong interaction between Cu and Ni, results in improved reducibility as compared to monometallic Ni. A high nickel concentration promotes formation of a homogeneous solid solution of Cu and Ni, whereas at lower nickel contents copper and nickel are separately aggregated and form metallic Cu and Cu-Ni alloy phases. At the same reduction conditions, the particle sizes of reduced Cu-Ni alloys decrease with the increase in Ni content. The activity tests of all Cu-Ni alloy based catalysts for CO hydrogenation show that they have similar selectivity, which is mainly towards methanol (~99 mol %), while exhibiting differences in methanol productivity. The methanol productivity reaches a maximum at a molar ratio of around 1. It seems likely that the determining surface structure is the same for all Cu-Ni alloys, but the number of active sites varies with the ratio of Cu to Ni.

8.2 Introduction

Bimetallic alloy nanoparticles have attracted considerable attention in many fields such as catalysis, magnetism, and optics due to their different properties compared to their monometallic constituents [344-349]. For instance, bimetallic alloys of two active metals Fe and Ni (Ni_3Fe) have been proven to be better catalysts for methanation reaction than the monometallic Ni or Fe [7, 260, 350]. Properties of bimetallic alloys may be merely a sum of both metals or may differ completely from the constituent elements because the modification of surface electronic structure in combination with modified surface morphologies.

Mixtures of Cu and Ni are of particular interest in catalysis for a number of reactions, including e.g. the methanation [266], higher alcohol synthesis [155, 223, 230], dehydrogenation of cyclohexane [351, 352], methanol synthesis [6, 225, 228, 231], steam reforming [291, 334, 353, 354], and water gas shift [355, 356]. The structure of Cu-Ni alloys has been the topic of numerous studies. In these cases, Cu-Ni samples were prepared by using different preparation methods such as: impregnation [6, 314, 354], co-precipitation [332], microemulsion [357], and sol-gel [358], and supported on different supports such as SiO_2 [6, 331, 354, 359], Al_2O_3 [332, 360, 361], ZnO [231], TiO_2 [223, 230, 362], ZrO_2 [314, 363, 364], CeO_2 [365], zeolites [360], and carbon nanotubes [314, 366].

It has also been found that upon variation in the Cu/Ni ratio, the selectivity and/or the activity changes significantly for reactions such as hydrogenolysis of ethane [351], dehydrogenation of cyclohexane [351], steam reforming [354], CO_2 hydrogenation [219], and water gas shift [330]. These changes in activity and/or selectivity are related to the structure of the catalysts [219, 330, 351, 352, 354]. It is known that bulk Cu and Ni can form solid solutions [265], and that Cu has a lower binding energy than Ni with adsorbates such as C and O [6, 126, 335, 367]. It would therefore be expected that the bonding properties of the alloy surfaces could be altered, when the Cu/Ni ratio in the alloy is varied. Much of the work regarding different Cu/Ni ratios have been conducted

without in situ studies.

With respect to the alloy formation, the phase diagram of bulk Cu-Ni binary system shows that a solid solution is formed across the composition range [265]. However, it has been reported that for Cu-Ni samples supported on SiO_2/Al_2O_3 prepared by impregnation (with a calcination step), the ex situ X-ray diffraction (XRD) on pre-reduced catalysts showed that at high nickel concentration, a homogeneous solid solution of Cu-Ni formed [329]. At lower nickel concentrations, separated Cu and Ni phases formed [329]. Using a co-precipitation method and XRD and XPS characterizations on pre-reduced $Cu\text{-}Ni/Al_2O_3$ samples, Naghash et al. [332] arrived at the same conclusion. They found that at high copper doping into Ni and at elevated reduction temperatures, the binding energies tended to restore to those of nickel due to copper segregation, and the formation of separate phases of metallic Cu and Cu-Ni alloy [332]. Recently, based on in situ XRD analysis we also found that supported Cu-Ni (molar ratio of Cu/Ni=1) on Al_2O_3 [314] and SiO_2 [6], exhibited a phase separation into Cu and Cu-Ni alloy. Furthermore, on the basis of temperature programmed reduction experiments by using X-ray absorption spectroscopy (XAS), we found that the supports such as SiO_2, ZrO_2, γ-Al_2O_3, and CNT play an important role for the reducibility of Cu-Ni alloy [314]. Silica was found to be more inert than the other support, because Cu and Ni can be reduced almost simultaneously [314].

Interestingly, we have also found that the oxide precursors of $Cu\text{-}Ni/Al_2O_3$ and $Cu\text{-}Ni/SiO_2$ (prepared via incipient wetness impregnation followed by drying at 110 °C and calcination in air at 400 °C) contained several metal oxide phases, i.e. individual crystallites of CuO and NiO together with crystalline $Cu_xNi_{1-x}O$ after calcination [98, 314]. It seems that Cu and Ni were redispersed after calcination of the impregnated Cu-Ni precursors. Therefore, it might be interesting to clarify, if it is possible to prepare uniform alloy phases on silica by avoiding the calcination step. This is obtained by reducing the impregnated Cu-Ni nitrate precursors in reducing gas atmosphere. This pretreatment step was reported to be an efficient way to prepare nanoparticles from nitrate precursors of Cu and Ni [320-322, 368].

It is thus necessary to clarify the nature of synergism on the formation of Cu-Ni alloy nanoparticles with respect to different Cu/Ni ratios. The difficulty of characterization of Cu-Ni alloys lies in the fact that both Cu and Ni crystallize in the FCC structure and the small lattice size difference between Cu and Ni (3.615 Å and 3.524 Å, respectively) [265, 369]. In addition, both crystalline and amorphous species could exist in the samples. It is therefore important to apply complementary characterization techniques such as X-ray absorption spectroscopy (XAS) and in situ XRD for revealing the material structures.

In this work silica supported bimetallic Cu-Ni materials have been prepared with different compositions of Cu and Ni by incipient wetness impregnation and reduced directly without a separate calcination step. Furthermore, we have applied comprehensive in situ characterization using techniques such as transmission electron microscopy (TEM), XAS, and XRD (on both conventional XRD and synchrotron XRD setups). In addition, inductively coupled plasma optical emission spectrometry (ICP-OES) was used for elemental analysis, sulfur chemisorption was used to determine the metal surface area, and Fourier transformed infrared spectroscopy (FTIR) experiments were carried out to identify the surface species on selected samples. Finally, the catalytic performance of the Cu-Ni alloys for CO hydrogenation is reported in order to conclude on structure-performance relationships.

8.3 Experimental Section

8.3.1 Preparation of Cu-Ni precursor materials

Silica supported Cu/Ni samples (20 wt % Cu+Ni, Cu/(Cu+Ni)=0, 10, 25, 50, 66.7, 75, and 100 mol %) precursors were prepared by the incipient wetness impregnation method. First, an aqueous solution of $Cu(NO_3)_2 \cdot 3H_2O$ and $Ni(NO_3)_2 \cdot 6H_2O$ (Sigma-Aldrich) was prepared. Then, the SiO_2 (supplied by Saint-Gobain Norpro, pore volume 1.2 mL g^{-1}) pellets were impregnated with the aqueous solution. After 1 h aging at room temperature, the samples were dried at 110 °C and directly reduced in the XRD and XAS cells and the CO hydrogenation reactor with dilute H_2 in N_2. Details on the reduction process will be stated in later parts.

8.3.2 ICP-OES analysis and sulfur chemisorptions

The chemical compositions of all Cu-Ni samples were analyzed by ICP-OES, Perkin–Elmer, model Optima 7300 and using Ar as plasmogene. In a typical analysis, 5 g of $K_2S_2O_7$ was melted together with 0.25 g sample and dissolved in 10 ml HCl in 200 ml water and then analyzed.

For sulfur chemisorption, all samples were reduced with 1 vol % H_2/N_2 at 300 °C with 1 °C min^{-1} ramping rate and held there for 1 hour using a flow of 1 vol % H_2S/H_2 over the sample until saturation. The sulfur capacity was measured by ICP-OES analysis. The surface areas of samples were calculated according to the methods used by Bernardo et al. [370].

8.3.3 In situ XRD studies

In situ XRD was performed with a PANalytical X'Pert PRO diffractometer equipped with an Anton Paar XRK 900 in situ cell and a gas flow control system for H_2-TPR. Silica supported Cu-Ni nitrate samples were heated in flowing H_2/He (2 mol % H_2, 100 ml min^{-1}) up to 300 °C for 1 h. An exception was the silica supported Ni sample, which was reduced in 5 mol % H_2/He up to 400 °C for 1 h. During reduction, each XRD measurement took about 10 minutes, and the temperature was maintained during the XRD measurement. After reduction, the sample was cooled to room temperature, and then a long XRD scan (640 minutes) was conducted to determine the position of reflections and particle sizes of Cu-Ni alloys. Fig. 8-1 shows a typical temperature-time profile applied in the reduction of Cu-Ni precursor materials. The average particle diameter ($d_{p,XRD}$) of crystal was calculated by means of the Sherrer equation [295]:

$$d_{p,XRD} = \frac{0.9\lambda}{\beta_{½}\cos(\theta)}$$

where, λ is the X-ray wavelength, θ is the Bragg angle, and $\beta_{½}$ is the full width at half maximum of the diffraction peak corrected for K_α-doublet separation and instrumental broadening.

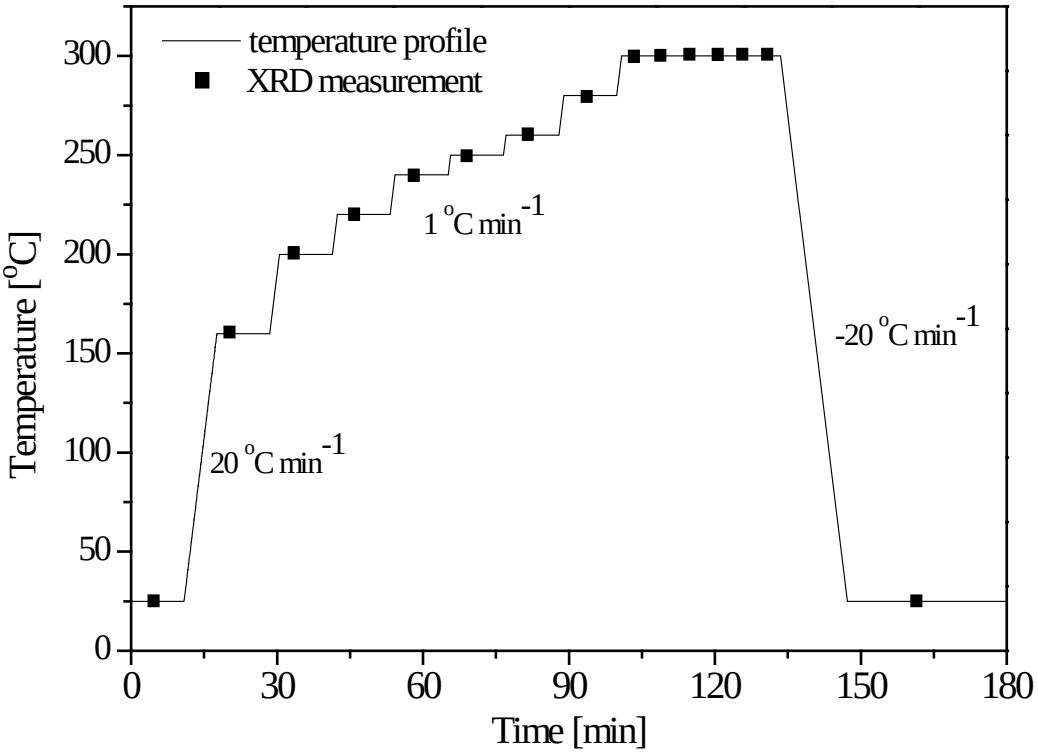

Fig. 8-1 A typical temperature-time profile applied for the reduction of Cu and Cu-Ni precursor materials in 2 mol % H_2/N_2 with a flow rate of 100 ml min^{-1}.

8.3.4 Combined in situ XAS and XRD studies

Typically, XRD can be used to identify the crystalline structure and provide information on the long-range order of the samples. In order to tackle both the amorphous and the crystalline structure of the samples, two complementary in situ techniques have been applied. In situ X-ray absorption near edge spectroscopy (XANES) together with extended X-ray absorption fine structure (EXAFS) spectroscopy is capable of giving information on the amorphous components such as the existence of amorphous NiO in the structure. The combination of XAS and XRD has been useful in a number of previous studies [289, 371-374]. The combined in situ XAS and XRD measurements were performed at the European Synchrotron Radiation Facility (ESRF, Grenoble) at the Swiss-Norwegian Beamlines (BM01B beamline). The storage ring was operated at electron energy of 6 GeV and injection current of 200 mA. The beamline was designed to rapidly switch between the XAS and XRD modes and hence carry out quasi-simultaneous measurements with the two techniques.

The in situ experiments were carried out using the quartz capillary micro-reactor originally developed by Clausen and Topsøe [375] for use with in situ XRD studies of catalysts, extended to combined XAS/XRD studies [376] and further developed by Grunwaldt and co-workers [287, 377] and workers of the Swiss-Norwegian Beamlines [378]. XAS spectra were acquired at the Cu and Ni K-edges in transmission mode using a continuously scanning Si(111) double-crystal monochromator and a gold-coated mirror for the rejection of higher harmonics. A Cu (or Ni) foil was measured at all times as an energy-calibration reference. XRD patterns were collected using an

Si(111) channel-cut monochromator set to a wavelength of λ = 0.503 Å. The diffractometer with a high-resolution detector consisting of 6 individual channels equipped with Si(111) analyser crystals was scanned between 2θ values of 23° and 80°. Prior to the experiments, the diffractometer was calibrated using a crystalline powder Si standard. A procedure repeatedly exchanged the dedicated monochromators after every XAS and XRD acquisition.

XANES data analysis was carried out using Athena and Artemis interfaces of the IFEFFIT software [288]. The spectra were energy-calibrated, normalised and background-subtracted. The k^2-weighted EXAFS spectra were Fourier-transformed in the k-range of 2-14 $Å^{-1}$ and fitted in R-space between 1.0-3.2 Å using single path standards generated by FEFF6 [288, 379].

8.3.5 In situ TEM studies

An environmental TEM (ETEM) equipped with a differential pumping system to confine a controlled flow of gases such as H_2, CO and CO_2 around the specimen, allowed observation of catalysts in a gaseous environment (FEI Titan E-cell, monochromatic, objective lens aberration corrector, Gatan imaging filter) [276, 277, 290]. In combination with a heating holder, this microscope allows samples to be studied using a variety of TEM techniques in situ in a reactive environment approaching the working conditions of the samples. In the present experiments (Fig. 8-2), an aqueous nitrate solution of Cu-Ni (2:1 molar ratio) was prepared and then dropped on a silica grid. The specimen was then exposed in air at 25 °C first and imaged. The specimen was heated in the gas environment (1.3 mbar H_2) at a rate of 7 °C min^{-1} from room temperature up to 300 °C for the Cu_2Ni_1 precursor. The TEM imaging was performed after drift-stabilization of the sample holder. The electron energy loss spectroscopy (EELS) of selected particles was performed to determine the composition of particles during reduction. For this purpose the Cu L_2/L_3 and Ni L_2/L_3 edges were analyzed.

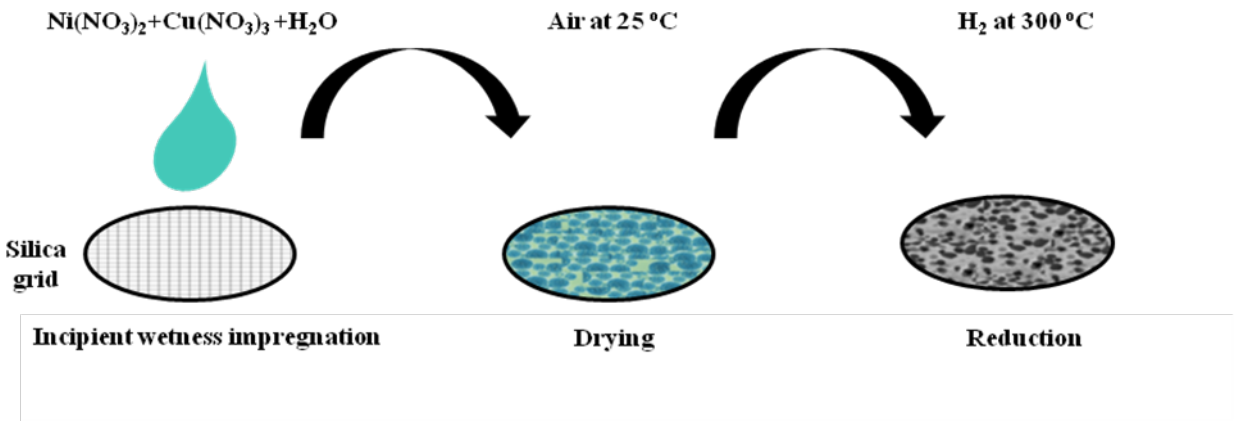

Fig. 8-2 In situ preparation and formation of Cu-Ni alloys on silica grid with ETEM.

8.3.6 FTIR spectroscopy

FTIR experiments were carried out with a Bruker Vertex 70 spectrophotometer. The Cu-Ni sample precursors were reduced in 2 vol % H_2/He at 300 °C with 1 °C min^{-1} ramping and held there for 1 hour. Then 50 vol % CO/He was introduced into the sample with a flow rate of 100 ml min^{-1}

at 300 °C for 30 minutes. The cell was then cooled to room temperature, and after the sample was flushed with a He flow of 100 ml min^{-1} for 30 minutes, a long spectrum was taken by then.

8.3.7 CO hydrogenation

The performances of all Cu-Ni samples for CO hydrogenation were evaluated in a fixed-bed continuous-flow reactor with an online GC-FID/TCD detection system (6890N from Agilent Technologies). Details of the setup are given by Christensen et al. [8, 96] The details regarding catalyst testing and parameters such as CO conversion, selectivity to a given product, productivity of methanol, and the metal area-based activity are given in the supplementary materials (Appendix D).

8.4 Results and Discussion

8.4.1 Elemental analysis and sulfur chemisorption

ICP-OES elemental analysis shows that the Cu/Ni atomic ratios of all fresh catalysts are very close to the expected Cu/Ni ratios, as shown in Table 8-1. The metal surface area also shown in Table 1 is calculated from the sulfur capacities (µg g_{cat}^{-1}). The metal surface area is calculated by assuming the same copper segregation as in the bulk alloy samples [370]. The saturation value for sulfur chemisorption are taken to be 449 µg sulfur/(m^2 Ni) and 384 µg sulfur/(m^2 Cu), which correspond to the mean value for the [100], [110], and [111] surfaces of Ni and Cu, respectively [370, 380].

Table 8-1 ICP-OES elemental analyses, sulfur capacity, and active metal surface areas of all silica supported Cu-Ni samples.

Samples	**Cu/(Cu+Ni), atomic ratio (%)**		**Sulfur capacity**	**As[a)]**
	Nominal	**Analyzed**	**µg g_{cat}^{-1}**	**m^2 g_{cat}^{-1}**
Ni/SiO_2	0	0	5950	13.3
Cu_1Ni_9/SiO_2	10	10.1	6540	16.4
Cu_1Ni_3/SiO_2	25	22.2	7200	18.3
Cu_1Ni_1/SiO_2	50	50.3	7630	19.7
Cu_2Ni_1/SiO_2	66.7	67.4	7420	19.3
Cu_3Ni_1/SiO_2	75	74.9	5270	13.7
Cu/SiO_2	100	100	2720	7.1

[a)] Metal surface area of Cu+Ni, which is calculated from sulfur capacity according to the method of Bernardo et al [370].

8.4.2 Reduction of samples

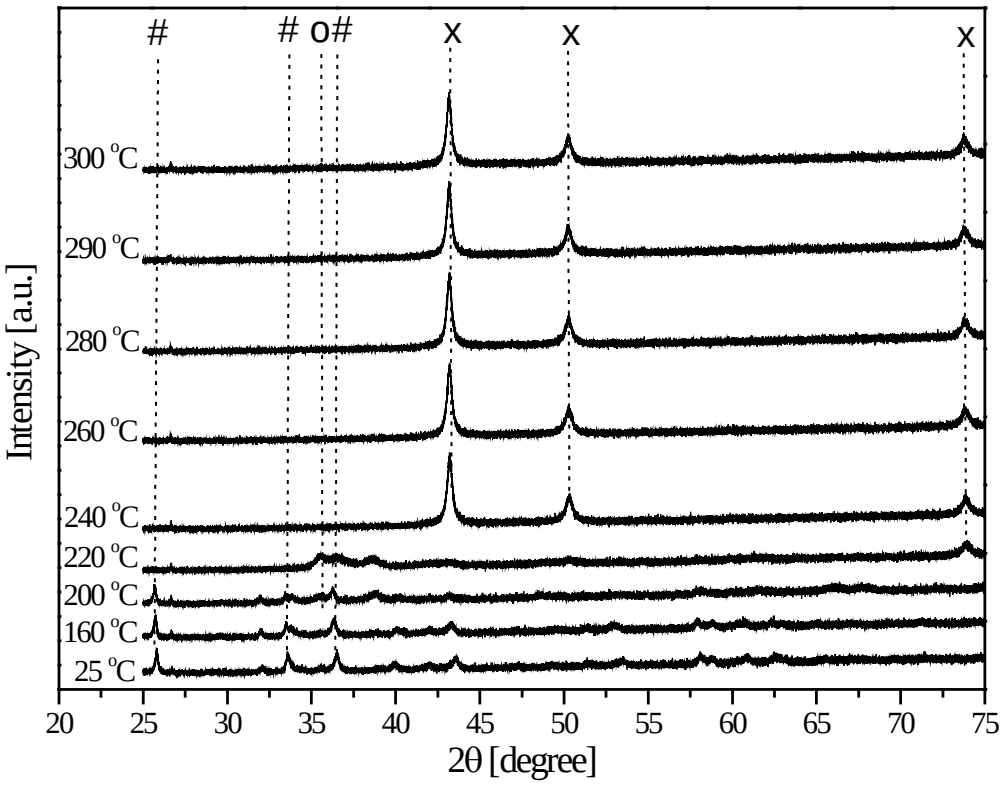

Fig. 8-3 XRD patterns at different temperatures during in situ reduction of the Cu /SiO_2 sample in a flow of 2 mol % H_2/N_2 with a flow rate of 100 ml·min^{-1} at 1 bar. (#) Cu hydroxynitrate, (o) CuO, (x) metallic Cu.

Fig. 8-3 illustrates the XRD patterns for reduction of the Cu/SiO_2 precursor. Only Cu hydroxynitrate is observed before reduction, which disappears at 220 ºC. This is probably due to decomposition of Ni hydroxynitrate, which was reported to occur at about 200 ºC [327, 328]. Cu hydroxynitrate is formed during the drying process of impreganated Cu nitrate precursors at elevated temperature, which resulting in agglomeration during hydrogenlysis of metal nitrate hydrate to metal hydroxynitrate [324, 325]. A CuO reflection (35.51°) starts to emerge at 200 ºC and disappears at 240 ºC in the XRD patterns during the reduction process. The main reduction occurs between 220 ºC and 240 ºC. After reduction, reflections at 43.33°, 50.44°, and 74.13° are observed. According to the Inorganic Crystal Structure Database (ICSD file 41508), metallic Cu has three main reflections, belonging to the [111], the [200] and the [220] crystal planes, at 43.32°, 50.45°, and 74.12°, respectively. It is hence only metallic Cu phase that is observed after reduction.

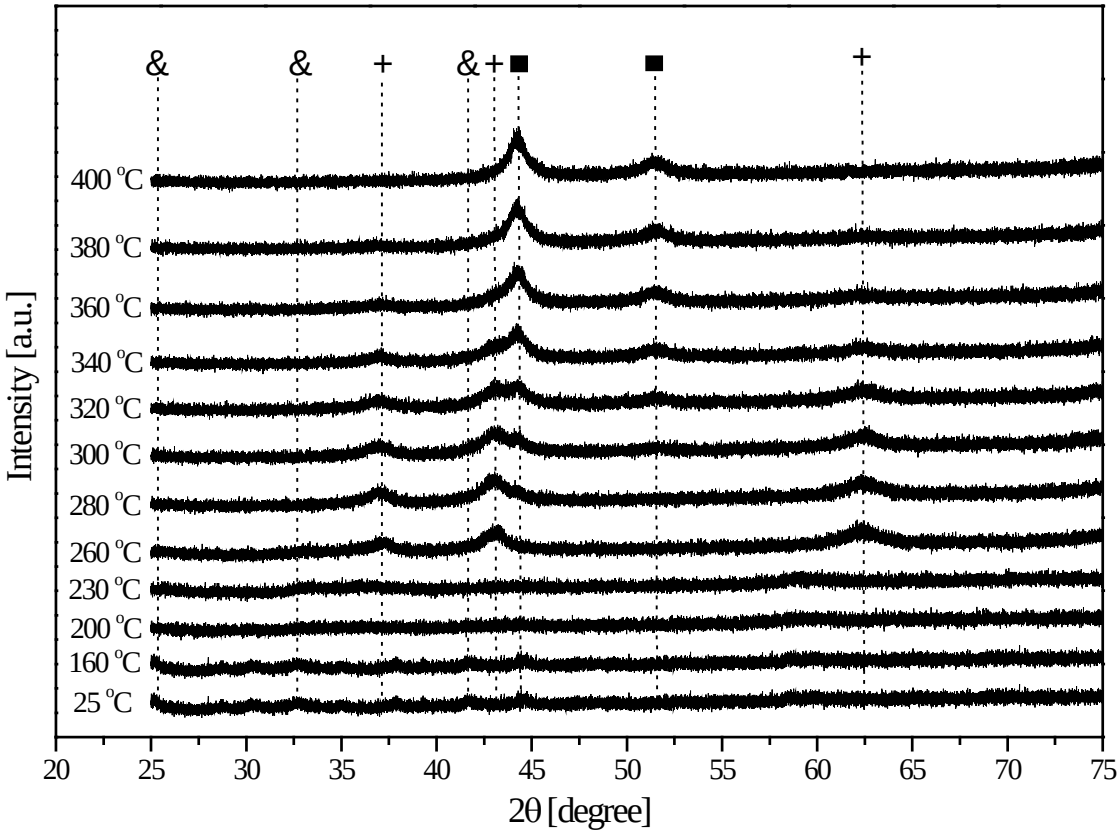

Fig. 8-4 XRD patterns at different temperatures during in situ reduction of the Ni/SiO_2 sample in a flow of 2 mol % H_2/N_2 with a flow rate of 100 $ml \cdot min^{-1}$. (&) Ni hydroxynitrate, (+) NiO, (■) metallic Ni.

Fig. 8-4 shows the XRD patterns for reduction of the Ni/SiO_2 precursor. Only Ni hydroxynitrate is observed before reduction and it disappears at 230 ºC. Decomposition of Ni hydroxynitrate was reported to occur at about 200 ºC [328]. Meanwhile, NiO reflections (37.3° and 43.2°) were observed at 260 ºC and no metallic Ni reflection was observed at this temperature. At 280 ºC, metallic Ni starts to emerge and the intensity of NiO reflection begins to decrease, which indicates that reduction of NiO occurs. NiO reflections disappear at 380 ºC. Finally, reflections at 44.43° and 51.80° are detected after reduction. According to ICSD file 52265, metallic Ni has two main reflections, 44.49° and 51.85° belonging to the [111] and the [200] crystal planes, respectively. The reflections in the reduced Ni/SiO_2 can thus be ascribed to the metallic Ni phase. It seems that Ni is more difficult to reduce compared to Cu. This can be explained by the standard reduction potentials, which were reported to be 0.337 eV for Cu and -0.25 eV for Ni [330, 332].

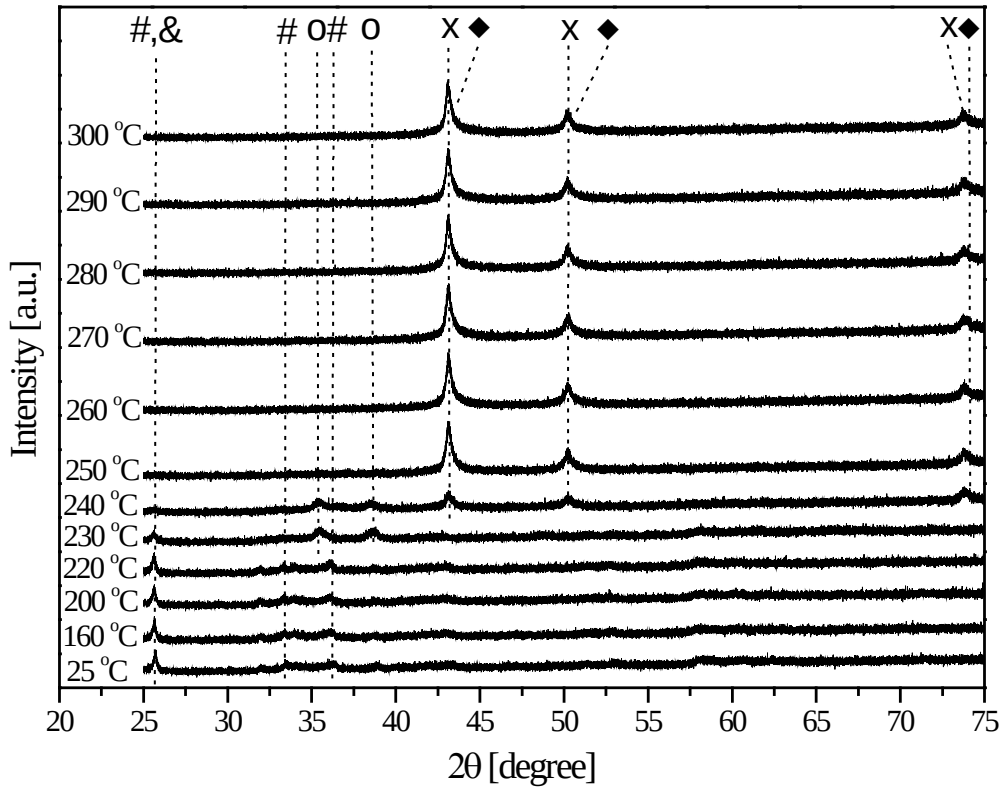

Fig. 8-5 XRD patterns at different temperatures during in situ reduction of the Cu_3Ni_1/SiO_2 sample in a flow of 2 mol % H_2/N_2 with a flow rate of 100 ml·min^{-1}. (#) Cu hydroxynitrate, (&) Ni hydroxynitrate, (o) CuO, (x) metallic Cu, (◆) Cu-Ni alloy.

Fig. 8-5 presents the reduction process for a Cu rich Cu-Ni sample (Cu_3Ni_1/SiO_2). Initially, both Cu hydroxynitrate and Ni hydroxynitrate could exist in the precursor. It is difficult to distinguish between Cu and Ni hydroxynitrates due to the overlap of reflections. During reduction, only CuO is observed at the position of 35.50º and 38.80º between 230 ºC and 240 ºC. There is no obvious change of reflection above 250 ºC. After reduction at 300 ºC, three reflections can be detected. Each reflection shows a shoulder at a slightly higher angle. The reflections at 43.32°, 50.43°, and 74.13° are assigned to metallic Cu. Shoulders are located at 43.63°, 50.71°, and 74.18° in between the reflections of metallic Cu and Ni, and are assigned to Cu-Ni alloys. The Cu-Ni alloy phase composition calculated by using Vegard's law is Cu/Ni=2.65. Based on ICP-OES analysis the Cu/Ni molar ratio is 2.98. Therefore, about 11 mol % isolated metallic Cu is estimated to exist in the reduced catalyst.

Fig. 8-3 and Fig. 8-4 show that Cu can be reduced at lower temperature than Ni. When Cu and Ni coexist in the sample Cu may be reduced first at lower temperature (230 ºC), and reduced Cu can then act as catalyst and promote the reduction of Ni, whereby Cu-Ni alloys are formed. It has also been reported that Cu can promote the reduction of nickel oxide efficiently [381, 382]. This non-simultaneous reduction of Cu and Ni might be part of reason for the phase separation of Cu and Cu-Ni alloys. On the basis of XRD and XPS studies, Naghash et. al. [332] have found that at high copper content and elevated reduction temperature, copper tends to segregate in order to reduce the

interfacial surface energies. Such a phase separation in Cu-Ni samples has been observed in some other studies as well [6, 330, 382].

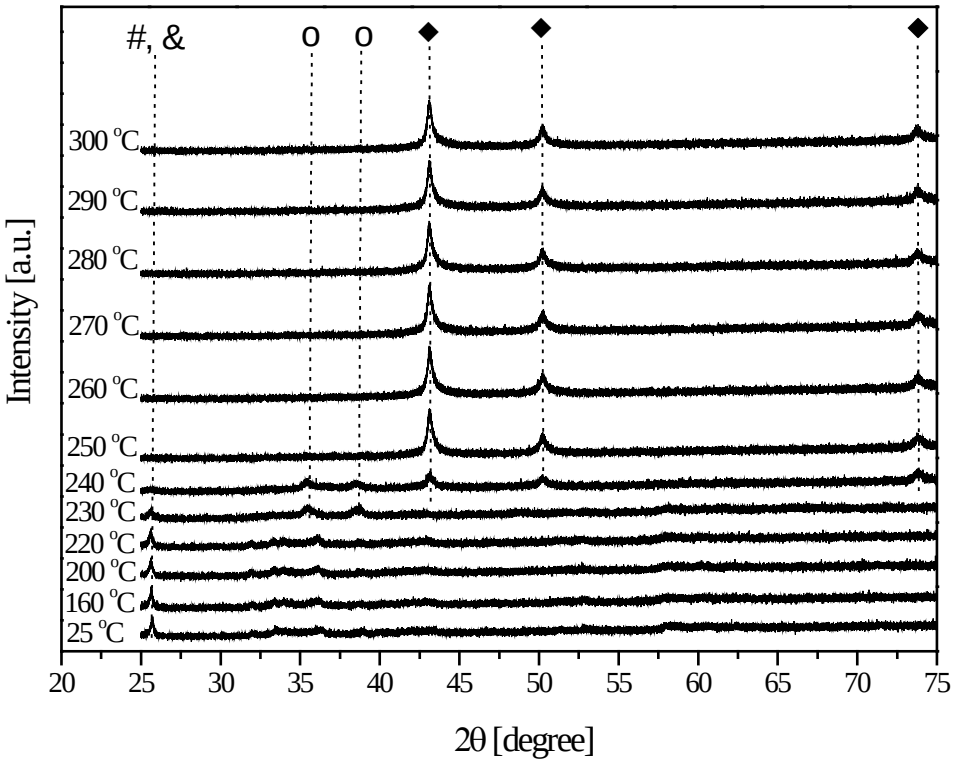

Fig. 8-6 XRD patterns at different temperatures during in situ reduction of the Cu_1Ni_3/SiO_2 sample in a flow of 2 mol % H_2/N_2 with a flow rate of 100 ml·min^{-1}. (#) Cu hydroxynitrate, (&) Ni hydroxynitrate, (o) CuO, (x) metallic Cu, (◆) Cu-Ni alloy.

Fig. 8-6 illustrates the reduction process of a Ni rich Cu-Ni sample (Cu_1Ni_3/SiO_2). Similar to the Cu rich Cu-Ni sample (Cu_3Ni_1/SiO_2), both Cu hydroxynitrate and Ni hydroxynitrate could exist in the precursor. Interestingly, still only CuO reflections are observed at the position of 35.51º and 38.77º between 230 ºC and 240 ºC, even though this sample has about 3 times higher Ni loading. This might due to NiO particles finely dispersed/spread on the support. An alloy phase of Cu-Ni emerges at 240 ºC and no obvious changes are seen above 250 ºC. After reduction, only symmetric reflections can be detected at 44.19°, 51.61°, and 73.80°, which are assigned to metallic Cu-Ni alloys. The Cu-Ni alloy phase composition is calculated by using Vegard's law is Cu/Ni=0.278, which is very similar to the ICP-OES analyzed Cu/Ni molar ratio 0.285. It seems that there is no phase separation between Cu and Ni when the Ni content in the material is high. This is in agreement with earlier studies, which also found that when the material is rich in Ni, Cu and Ni form homogeneous alloys [329, 332].

Similar reduction processes have been observed for the other three Cu-Ni samples (Cu_2Ni_1/SiO_2, Cu_1Ni_1/SiO_2, and Cu_1Ni_9/SiO_2). Fig. 8-7 shows the long scan XRD (640 minutes) patterns at room temperature after reduction for all silica supported Cu, Ni and Cu-Ni samples. It can be clearly seen in Fig. 8-7 that a phase separation of Cu and Cu-Ni alloys are observed for the Cu rich samples

(Cu_3Ni_1/SiO_2, Cu_2Ni_1/SiO_2 and Cu_1Ni_1/SiO_2), while the Ni rich samples (Cu_1Ni_3/SiO_2 and Cu_1Ni_9/SiO_2) form only Cu-Ni alloys. The Cu-Ni alloy compositions in all samples estimated using Vegard's law is listed in Table 8-2. The average particle diameter ($d_{p,XRD}$) of the Cu-Ni alloys was calculated by means of the Sherrer equation [295].

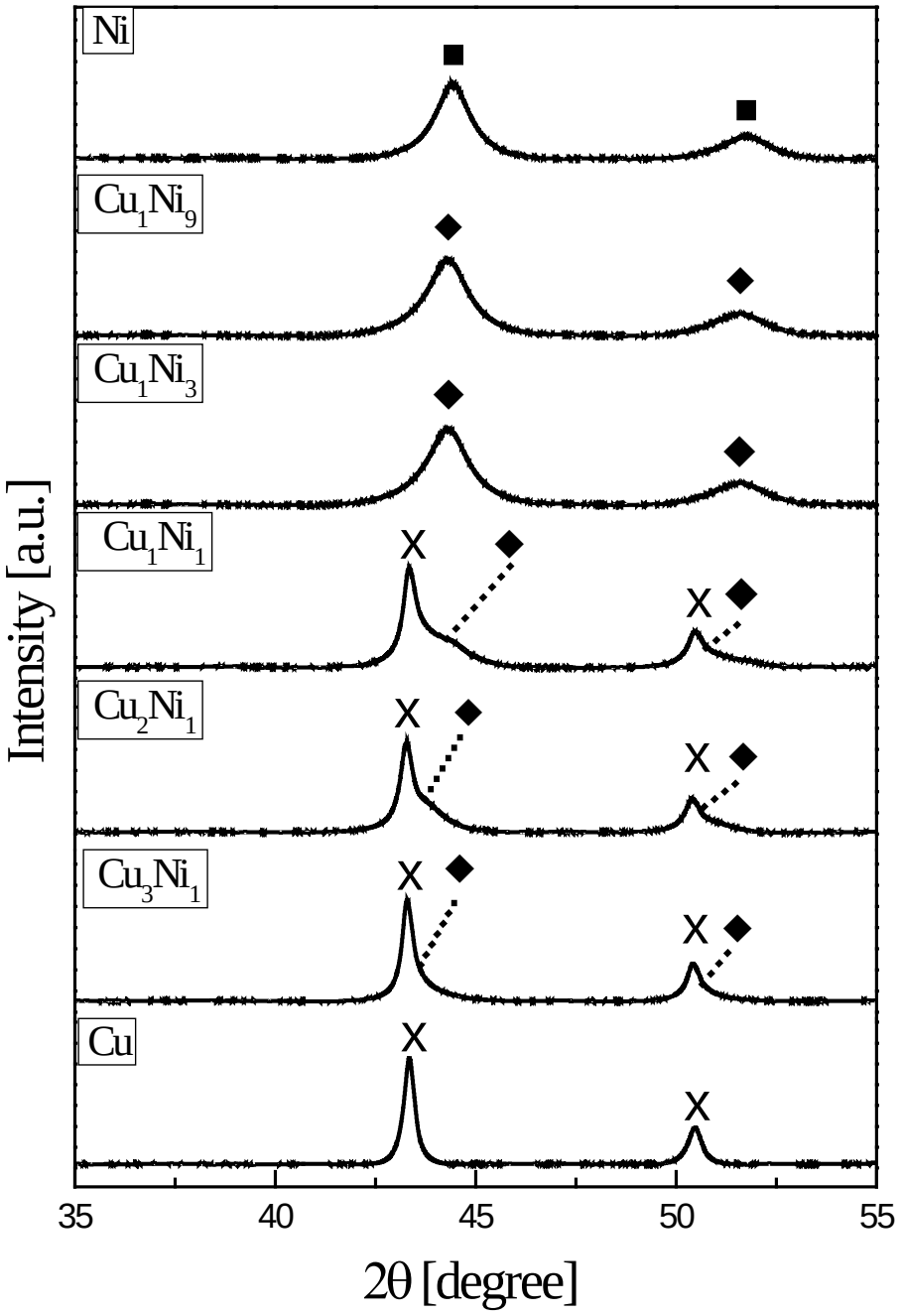

Fig. 8-7 Long scan (640 minutes) XRD patterns at room temperature after reduction of Cu, Ni and Cu-Ni samples.

Table 8-2 Cu/Ni ratios determined by ICP-OES elemental analysis and Vegard's law, Cu-Ni [111] XRD angle, Cu separation percentage and particle sizes of metals in all samples.

Samples	Cu/ Ni atomic ratio		Cu-Ni [111]	Cu separation	$d_{p,XRD}$ (Cu-Ni)
	ICP-OES	Calculated	[degree]	[mol %]	[nm]
Ni/SiO_2	-	-	44.43	no	7[a)]
Cu_1Ni_9/SiO_2	0.112	0.119	44.31	no	6
Cu_1Ni_3/SiO_2	0.285	0.278	44.19	no	6
Cu_1Ni_1/SiO_2	1.012	0.91	43.90	~10	5
Cu_2Ni_1/SiO_2	2.067	1.98	43.70	~4	11
Cu_3Ni_1/SiO_2	2.984	2.65	43.63	~11	15
Cu/SiO_2	-	-	43.33	no	30

[a)] *This sample was reduced at 400 ºC, while all the other samples are reduced at 300 ºC. Therefore, the particle size of Ni/SiO_2 sample should not be compared to the rest samples.*

The results in Table 8-2 show that at the same reduction conditions, the Cu/SiO_2 sample contains the largest metal particle sizes of 30 nm. The particle sizes of reduced metals decreases with increasing Ni content. It seems that Cu-Ni alloys are more thermally stable than pure metallic Cu (Fig. 8-8), and the stability increases with the Ni content. For example, when alloying 50 mol % or more Ni with Cu, the particle size decreases to 5-6 nm. It is also shown in Fig. 8-8 that the lattice parameter of Cu-Ni increases with increasing Cu content. This is a typical tendency for bimetallic alloys, for example the Pt-Fe system, where lattice parameter varies as a function of Fe content in the alloys [383].

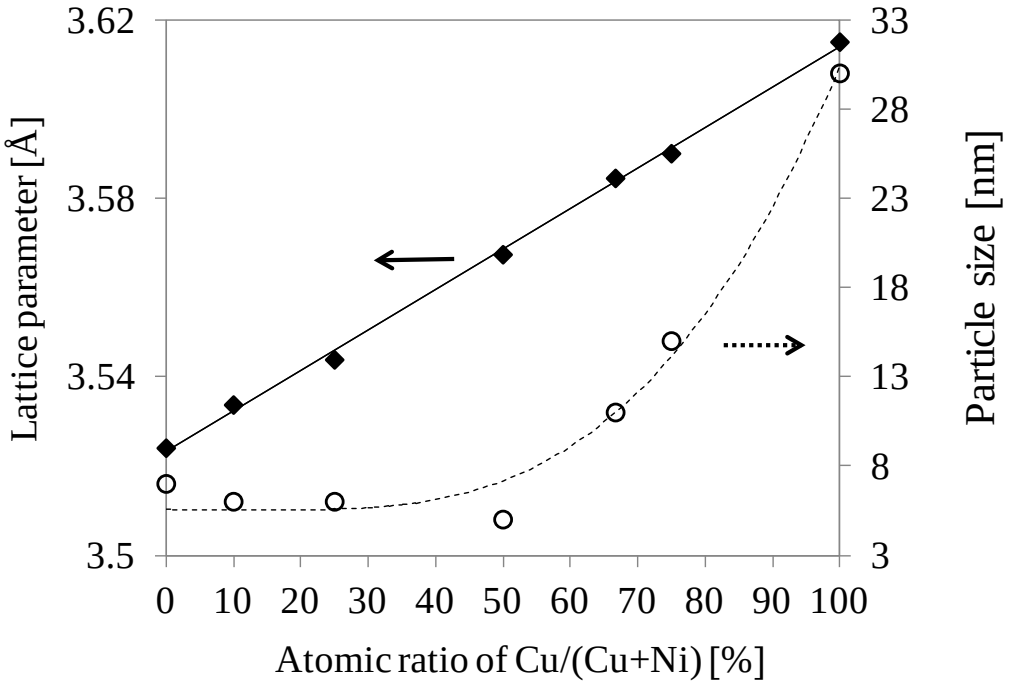

Fig. 8-8 Variation of XRD particle sizes and lattice parameter with amount of Cu in Cu-Ni alloys nanoparticles.

In situ XRD can confirm the reduction process and the alloy formation of Cu-Ni. However, XRD cannot identify amorphous species or fine crystalline particles. Although silica usually is considered as an inert support, which has a limited influence on supported metals, there could still exist unreduced oxide species, such as NiO, in the sample after reduction at 300 °C. It is shown above in

the Ni/SiO_2 sample that NiO reduction is completed at around 360 °C. In order to investigate both the amorphous and the crystalline structure of the samples, two complementary in situ techniques, XAS and XRD, have been applied. Cu rich and Ni rich Cu-Ni samples, Cu_3Ni_1/SiO_2 and Cu_1Ni_3/SiO_2, as well as the Cu_1Ni_1/SiO_2 sample have been analyzed in situ at the ESRF synchrotron. All of these samples show a similar development of the in situ XANES spectra at both Ni K- and Cu K-edges during reduction (Fig. 8-9 and Fig. 8-10). The starting material displays an intense whiteline at both edges indicating the presence of both Ni(II) and Cu(II) in the precursors. The intensity of the whiteline decreases with increasing in temperature in a flow of 5 mol % H_2/He, while the edge shifts slightly towards lower energy with the appearance of a pre-edge, indicating the reduction of both Ni(II) and Cu(II) species to their metallic state at around 250 °C. This observation agrees with the in situ XRD analysis. A similar trend has been observed for the Cu_1Ni_1/SiO_2 sample as well (see Appendix D, supplementary materials).

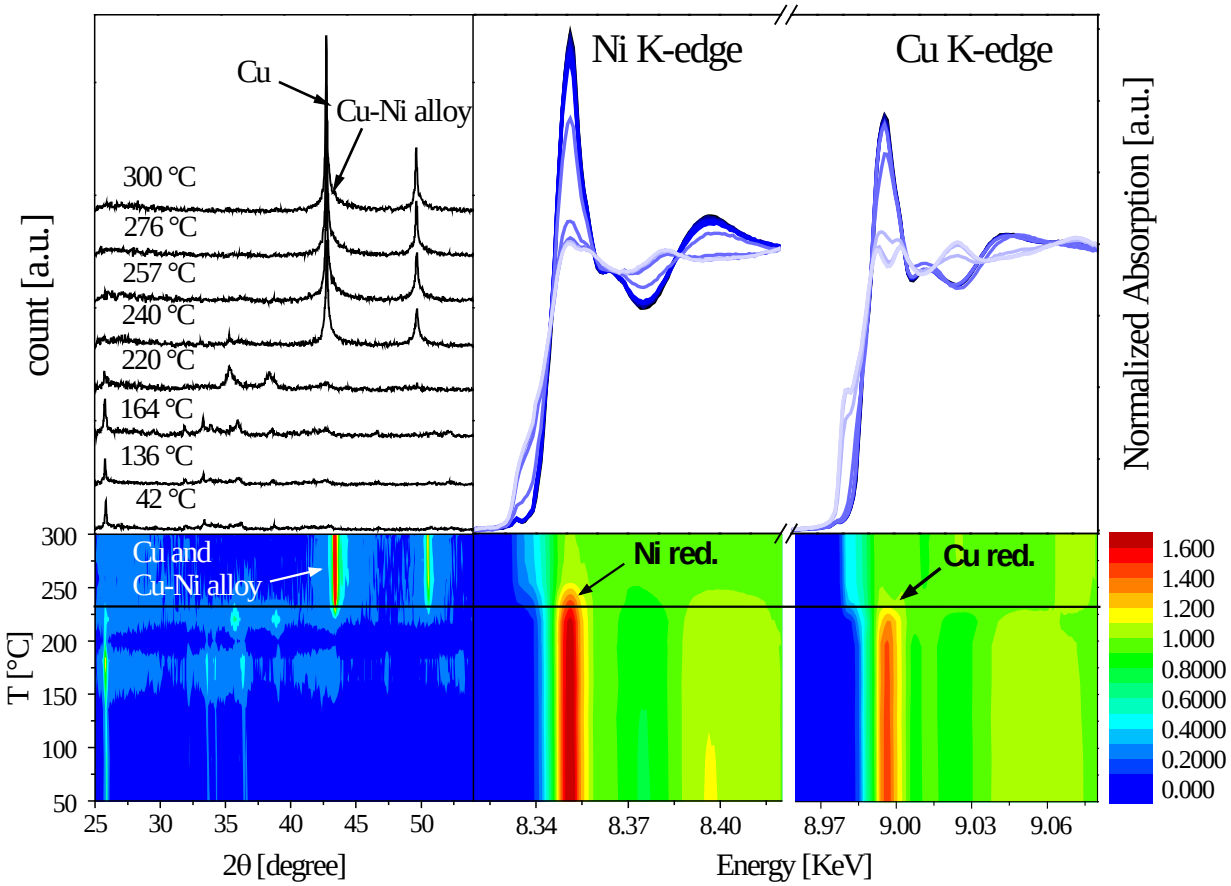

Fig. 8-9 Simultaneous in situ XANES and XRD for reduction of Cu_3Ni_1/SiO_2 sample. For XANES: the colors from blue to red are the transition from no absorption to strong absorption refer to the references; for XRD: the colors from blue to red are the transition from low intensity to high intensity.

It is very difficult to distinguish the Cu-Cu shell from the Cu-Ni shell and vice-versa, because Cu and Ni have similar atomic diameters (2.552 Å and 2.488 Å [333], respectively) and backscattering factors. Thus the EXAFS investigation can give element-specific information on the reduction behavior, but alone it is not enough to confirm the formation of an alloy. Fitting of the Fourier transformed, k^3-weighted EXAFS spectra (Table S1 and Fig.S1 in the Appendix D, supplementary information) gives coordination numbers (CN) for the Ni-Ni(Cu) and Cu-Cu(Ni) shells ranging

from 8.5 for the Cu_1Ni_3/SiO_2 sample, to around 10 for Cu_1Ni_1/SiO_2 and Cu_3Ni_1/SiO_2 samples. Typically high CN indicates the presence of relatively large particles [293]. On the basis of XRD particle sizes, the Cu_1Ni_3/SiO_2 sample has a particle size of 6 nm, which is smaller than the other two samples (11-15 nm). This is in the agreement with the trend in the CNs.

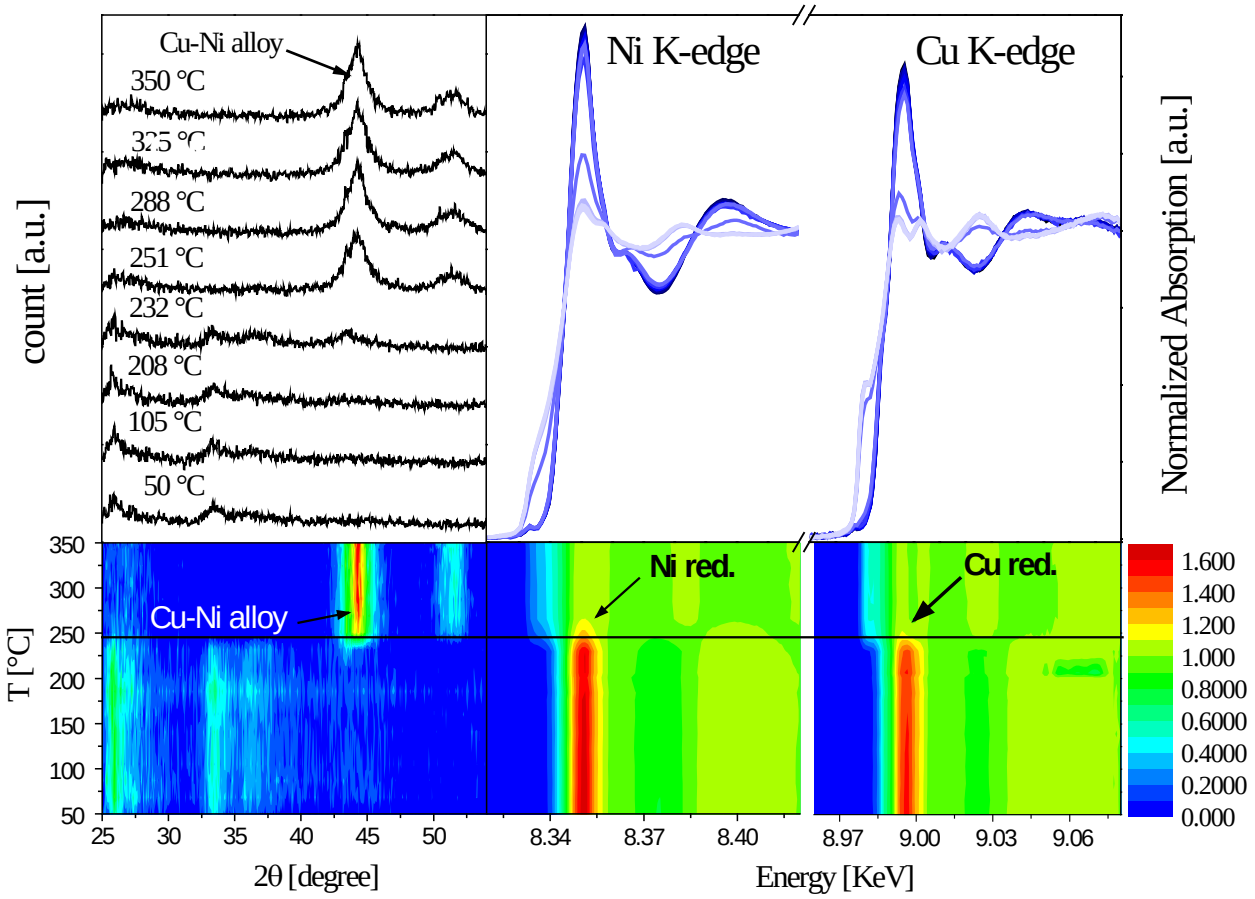

Fig. 8-10 Simultaneous in situ XANES and XRD for reduction of Cu_3Ni_1/SiO_2 sample. For XANES: the colors from blue to red are the transition from no absorption to strong absorption refer to the references; for XRD: the colors from blue to red are the transition from low intensity to high intensity.

8.4.3 In situ TEM

Fig. 8-11 illustrates the capability of ETEM to follow dynamic changes in the sample structure during reduction. An aqueous nitrate solution of Cu-Ni (2:1 molar ratio) was dropped on a silica grid and the specimen was then exposed to air at 25 °C first and imaged (Fig. 8-11a). Diffraction pattern (Fig. 8-11c) shows no crystal forms at this stage. The electron energy loss spectroscopy (EELS) of selected particles shows that both the Cu L_2/L_3 and Ni L_2/L_3 edges are observed (Fig. 8-11e). The specimen is then heated in the gas environment (1.3 mbar H_2) at a rate of 7 °C min^{-1} from room temperature up to 300 °C by which nanoparticles are formed on the grid (Fig. 8-11b). The diffraction pattern supports that crystals are formed after reduction (Fig. 8-11d). The EELS spectra of selected particles show a decrease of the intensity of Cu L_2/L_3 significantly, which indicates the Cu species change its valance states from Cu(II) to its metallic form (Fig. 8-11f). Cu and Ni both exist in the probed particles after reduction, indicating the formation of Cu-Ni alloys.

Similar to EXAFS, it is very difficult to distinguish the lattice parameters among Cu-Cu, Ni-Ni, and Cu-Ni in TEM, because Cu and Ni have similar lattice parameters, and because Cu and Ni have close atomic diameters of 2.552 Å and 2.488 Å, respectively [333]. Fig. 8-12 exhibits the HRTEM image of the synthesized Cu_2Ni_1 alloy at room temperature after reduction at 300 °C. The Cu-Ni [111] surface is observed in the selected particle. The d values for [110] are calculated to be 2.51 Å, 2.58 Å, and 2.58 Å from three different orientations, which correspond to d [111] of 2.05 Å, 2.09 Å, and 2.09 Å, respectively. The d values for Cu[111] is 2.087 Å (ICSD file 41508) and Ni[111]) is 2.034 Å (ICSD file 52265). It is therefore difficult to determine the exact composition of Cu-Ni alloys by lattice distance due to the uncertainty of measurements and the similarity between the lattice parameters of Cu and Ni.

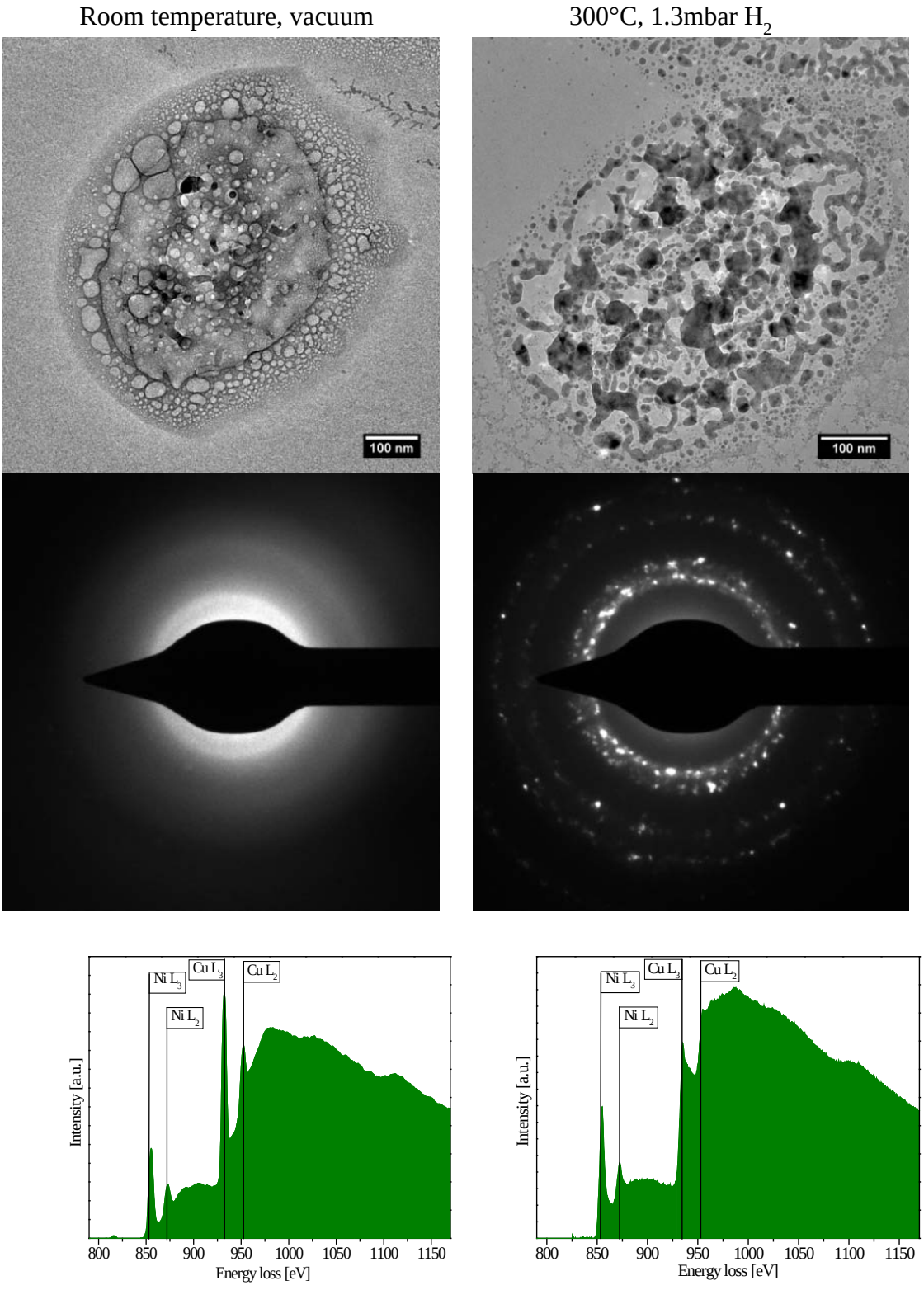

Fig. 8-11 In situ TEM investigation of the synthesis of a Cu_2Ni_1 alloy on a silica grid out of their nitrate salts solution. (a) TEM image at room temperature and (b) TEM image at 300 °C (c) Diffraction pattern at room temperature and (d) Diffraction pattern at 300 °C and (e) EELS spectra at room temperature and (f) EELS spectra at 300 °C.

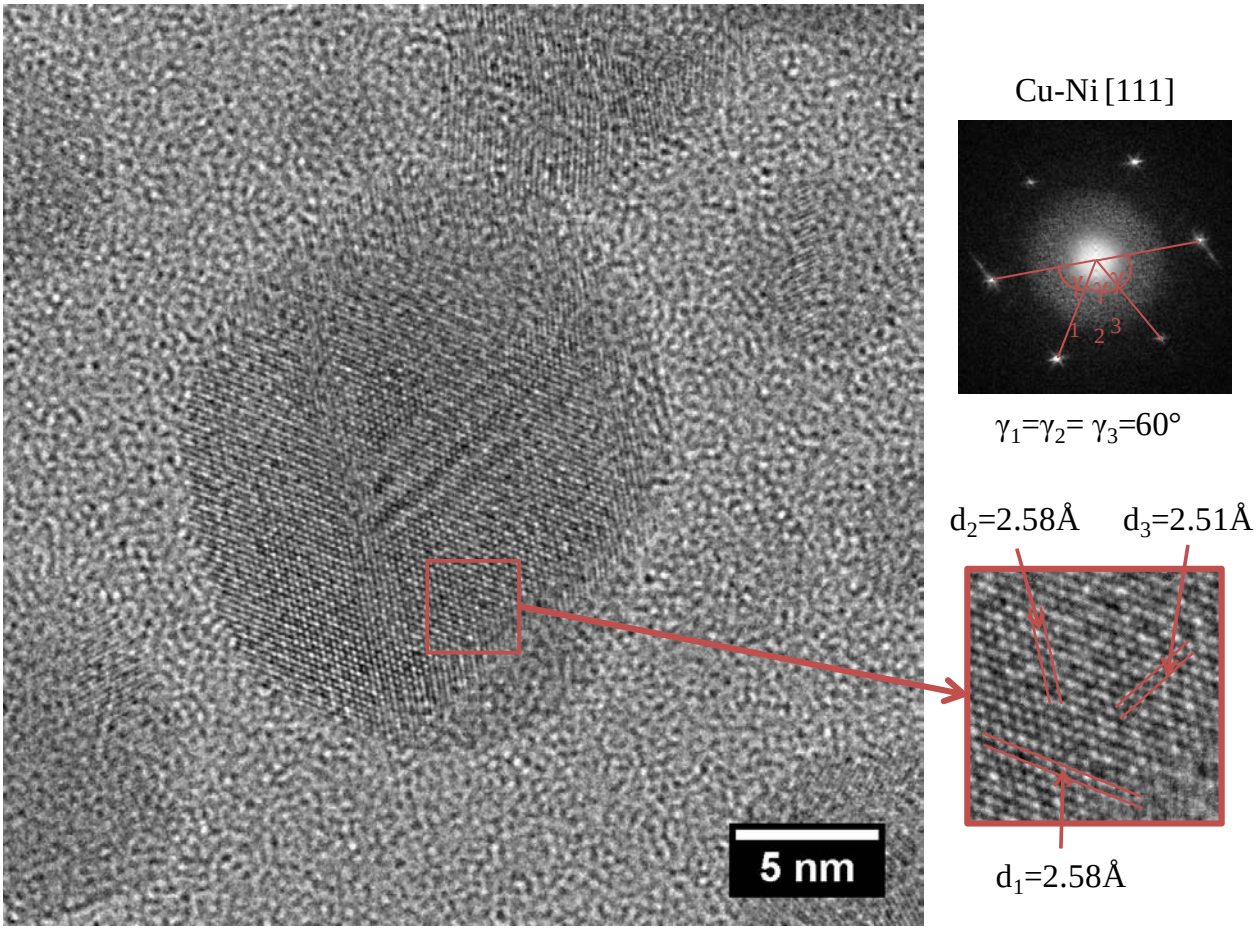

Fig. 8-12 HRTEM image of the synthesis of a Cu_2Ni_1 alloy on a silica grid out of their nitrate salts solution.

8.4.4 Catalytic behaviors for CO hydrogenation

Studt et al. [6] found that Cu-Ni alloys rich in Cu (supported on SiO_2) are active and selective catalysts for methanol synthesis from syngas. It would be valuable to know the effects of Cu-Ni composition on the behavior of CO hydrogenation. Here, we tested all of Cu-Ni alloys for CO hydrogenation in a fixed-bed high-pressure reactor.

Fig. 8-13 shows the steady state productivity of methanol and selectivities to various products over Cu-Ni catalysts with different atomic ratios of Cu/Ni. Metallic copper shows a relatively low activity and selectivity for methanol synthesis compared to Cu-Ni alloys. Initially the pure Ni catalyst produces hydrocarbons, but the activity for CO hydrogenation disappears rapidly. It is known that Ni forms volatile nickel carbonyl ($Ni(CO)_4$) species, when the partial pressure of CO is higher than 0.2 bar and temperature is lower than 425 °C, and at elevated partial pressures of CO ultimately removal of nickel from the catalytic reactor occurs through these volatile species [384]. This is in agreement with earlier studies by Tsu et. al. [385] who reported that Ni catalysts deteriorate due to $Ni(CO)_4$ formation at about 3.8 bar of CO. It is therefore not too surprising that the pure metallic Ni catalyst shows no long term activity at 50 bar of CO at 275 °C due to active metal loss.

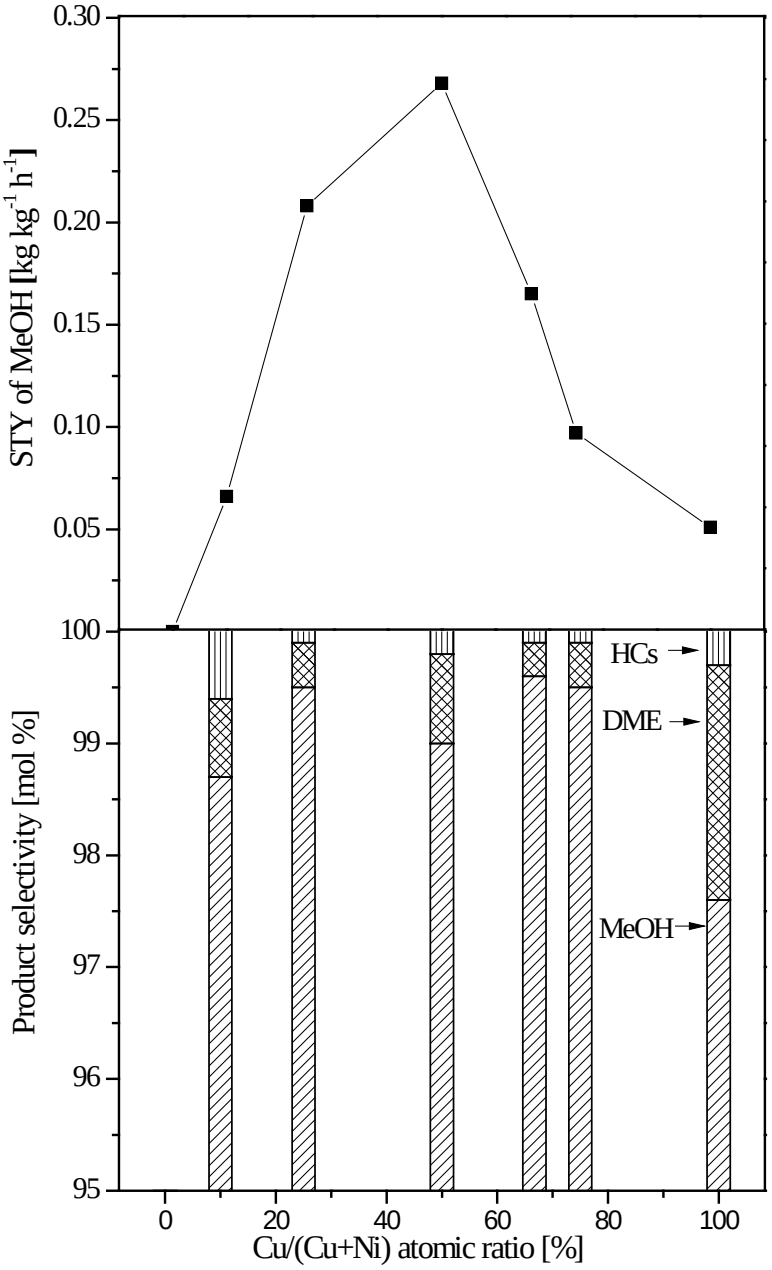

Fig. 8-13 Steady state productivity of methanol (top) and selectivities to various products (bottom) over Cu-Ni catalysts with different Cu/Ni atomic ratios. The operating conditions are: P = 100 bar, T=275 °C, GHSV = 4000 h^{-1}, Feed: H_2/CO=1, vol/vol.

Interestingly, all tested Cu-Ni alloys produce methanol as the dominant product (about 99 mol % selectivity) with a small amount of dimethyl ether (DME) and trace amounts of methane during CO hydrogenation. It seems that Cu dominates the catalytic properties of Cu-Ni alloys and that nickel's methanation activity is suppressed. Cu-Ni alloys usually form Cu-shell/Ni-core structures since Cu has lower surface energy compared to Ni [6, 298]. However, both experiments and DFT calculations show that CO is able to pull Ni out to the surface due to the stronger binding of CO on Ni than on Cu [6, 297, 298]. Here, we also have conducted FTIR of CO adsorption on Cu, Cu_2Ni_1, and Cu_1Ni_3 catalysts (Fig. 8-14). Metallic copper shows a band at 2130 cm^{-1}, which is ascribed to

the linear bond of CO with Cu [386]. With either Cu or Ni rich Cu-Ni alloy catalysts, both a linear Cu-CO band (around 2130 cm^{-1}) [386] and a band assigned to linear subcarbonyl $Ni(CO)_{2-3}$ (2050-2080 cm^{-1}) [387] can be observed in Fig. 8-14. This indicates that both Cu and Ni exist in the surface of these alloy samples (in both Cu or Ni rich Cu-Ni alloys) when they are exposed to CO. Additionally, we observed a slight shift of Cu-CO to a higher vibration frequency (around 2100 cm^{-1}). This shift might originate from the surface alloy, where the properties of Cu are modified by the presence of Ni.

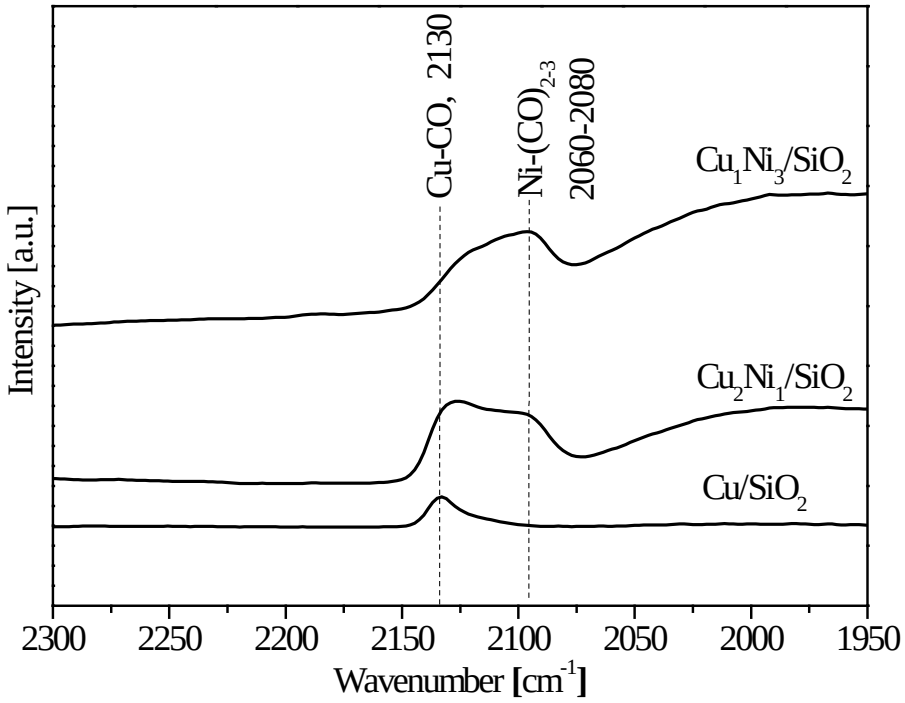

Fig. 8-14 FTIR spectra of CO adsorbed on the surfaces of silica supported Cu, Cu_2Ni_1, and Cu_1Ni_3 catalysts.

The reactivity of catalytic surfaces is often dominated by low-coordinated atoms such as step sites, which usually have higher activity [388-392]. On the basis of both DFT calculations and experiments, it was found that step sites containing Ni are the primary active sites for CO dissociation, while closely packed Ni atoms on the terraces are unable to dissociate CO [312, 393, 394]. Additionally, it was reported that additives like sulfur [394], potassium [394], gold [394], and silver [392] preferentially bind on the step sites of Ni, which block these sites for other reactions. In our case, Ni forms a surface alloy with Cu in CO and H_2 atmosphere, which must be scarce in nickel step sites to explain why only trace amount of methane is observed in the catalytic tests.

The methanol productivity over Cu-Ni alloys reaches a maximum at equal amounts of Cu and Ni based on space time yield of methanol as shown in Fig. 8-13. Based on the XRD analyses it is shown in Fig. 8-8 that the particle size of Cu-Ni alloys decreases with increasing Ni content in the particles. The metal areas are hence different for Cu-Ni samples with the same loading on silica, and this is also expected to influence the activity of catalysts. A more specific measure of activity

can be obtained by calculating the metal surface area based reaction rate. Hereby the ability of Ni to provide smaller particles is removed from the effect of composition on activity. The active surface areas of catalysts are determined by sulfur chemisorption. The relationship of activity with respect to the atomic ratio of Cu/Ni is shown in Fig. 8-15. The area-based activities for all Cu-Ni samples still reaches a maximum at equal amounts of Cu and Ni.

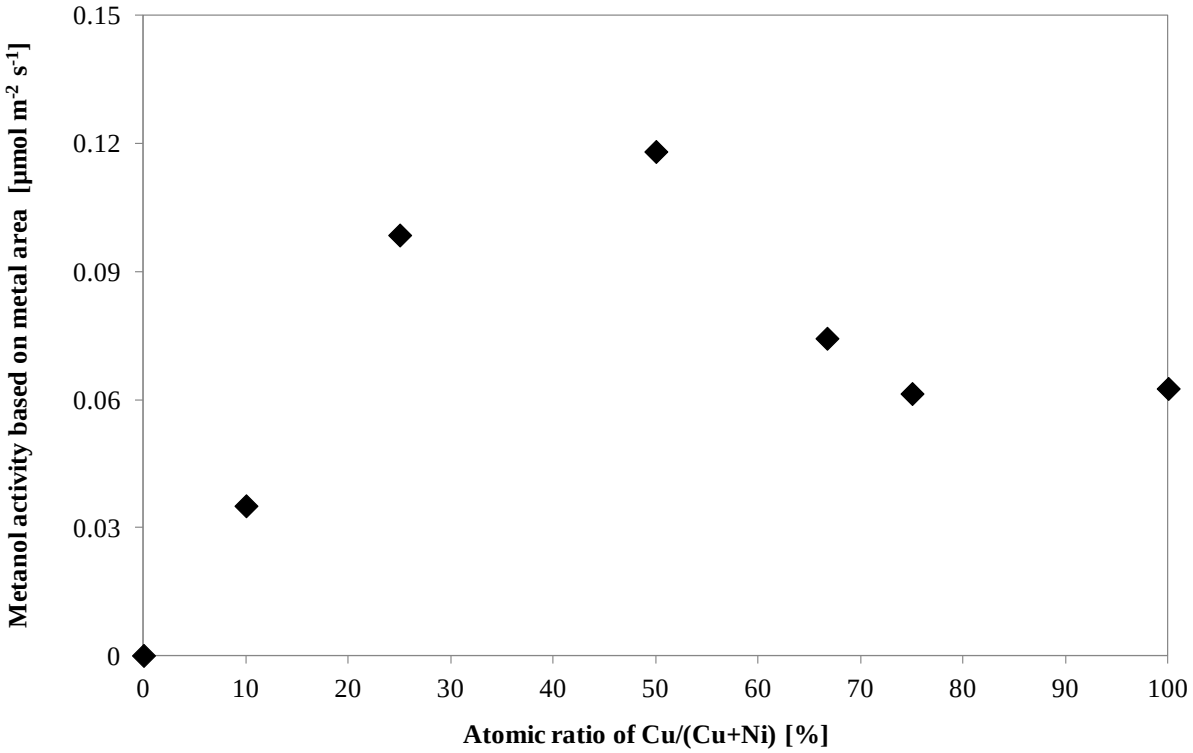

Fig. 8-15 Area formation rate of methanol from CO hydrogenation over Cu-Ni catalysts at steady state. The operating conditions are: P = 100 bar, T=275 °C, GHSV = 4000 h^{-1}, Feed: H_2/CO=1.

It is clear that the difference in mass-based productivity of methanol among the alloys to some extent stems from the metal particle size. This could explain that with increasing nickel content up to 50 mol % (Cu_1Ni_1), the methanol productivity reaches a maximum. However, the productivity of methanol decreases with further increasing the amount of nickel (Cu_1Ni_9<Cu_1Ni_3<Cu_1Ni_1), where the particle sizes of Cu-Ni are similar. This may be related to the bond strength of the CO on the Cu-Ni surfaces. The bonding of CO on the different ratios of Cu-Ni alloys has been studied by thermal desorption spectroscopy [395]. The CO binding energy decreases linearly with increasing surface Cu concentration in Cu-Ni alloys [395]. The 'volcano-type' activity is usually related to the Sabatier Principle – the optimum activity at intermediate binding energy [248, 396]. Another possibility is that the determining surface structure is similar for all Cu-Ni alloys, but the number of active sites varies with the ratio of Cu to Ni.

8.5 Conclusion

Cu-Ni alloy nanoparticles with different Cu to Ni ratios have been prepared and characterized by XRD, XAS, TEM, and FTIR. In situ reduction of Cu-Ni nanoparticles on both XRD and XAS reveal that a strong interaction between Cu and Ni, resulting in improved reducibility as compared to monometallic Ni. In situ XRD shows that silica supported Cu-Ni alloys, at high nickel

concentrations form a homogeneous solid solution of Cu and Ni, whereas at lower nickel contents, copper and nickel are separately aggregated and form metallic Cu and Cu-Ni alloy phases. At the same reduction conditions, the particle sizes of reduced Cu-Ni alloys decrease with the increase in Ni content.

The activity tests of Cu-Ni alloys for CO hydrogenation show that all Cu-Ni alloys produce mainly methanol (~99 mol %) regardless of the Cu/Ni ratio but exhibit differences in methanol productivity. The methanol productivity reaches a maximum in the molar ratio of around 1. It seems likely that the determining surface structure is similar for all Cu-Ni alloys, but the number of active sites varies with the ratio of Cu to Ni.

9 Supported molybdenum carbides for higher alcohol synthesis from syngas

9.1 Abstract

Molybdenum carbide supported on active carbon, carbon nanotubes, and titanium dioxide, and promoted by K_2CO_3, has been prepared and tested for methanol and higher alcohol synthesis from syngas. At optimal conditions, the activity and selectivity to alcohols (methanol and higher alcohols) over supported molybdenum carbide are significantly higher compared to the bulk carbide. The CO conversion reaches a maximum, when about 20 wt % Mo_2C is loaded on active carbon. The selectivity to higher alcohols increases with increasing Mo_2C loading on active carbon and reaches a maximum over bulk molybdenum carbide, while the selectivity to methanol follows the opposite trend. The effect of Mo_2C loading on the alcohol selectivity at a fixed K/Mo molar ratio of 0.14 could be related to the amount of K_2CO_3 actually on the active Mo_2C phase and the size, structure and composition of the supported carbide clusters. Unpromoted, active carbon supported Mo_2C exhibits a high activity for CO conversion with hydrocarbons as the dominant products. The K_2CO_3 promoter plays an essential role in directing the selectivity to alcohols rather than to hydrocarbons. The optimum selectivity towards higher alcohols and total alcohols is obtained at a K/Mo molar ratio of 0.21 over the active carbon supported Mo_2C (20 wt %).

9.2 Introduction

Higher alcohol synthesis from syngas has received renewed attention in the last years for its application in the field of biofuel and fuel additive production [19-21, 27, 28, 397]. Syngas can be obtained by gasification of renewable sources such as biomass [10, 37, 39], organic waste [38] as well as from coal gasification [13, 14, 45, 398] and reforming of natural gas [399]. Several catalytic systems have been investigated for higher alcohol synthesis, such as alkali promoted Cu/ZnO [160, 168, 171-173, 285], Cu/Co-based catalysts [174-176, 183, 184], Rh-based catalysts [207, 208, 400], and alkali/MoS_2-based catalysts [29, 196, 197]. These catalysts show either too low higher alcohol ($C_{2+}OH$) selectivity or too low activity except for alkali promoted MoS_2-based catalysts, which exhibit reasonably good activity and selectivity to higher alcohols [96, 196, 197]. However, traces of organic sulfur components also form during the process [96], which is undesirable, especially when the alcohol product is intended for fuel applications. Previous studies have also reported alkali modified bulk molybdenum carbides as potential catalysts for higher alcohol synthesis [8, 199, 401]. However, bulk Mo_2C suffers from a low specific surface area due to the high carburization temperature (up to 750 °C) and high loading of promoters (up to 10 wt % K_2CO_3, molar ratio of K/Mo=0.14) [8, 199], which result in relatively low alcohol yields during CO hydrogenation [8, 199]. Xiang et al. [203, 204, 402, 403] found that the addition of Ni, Co, and Fe can significantly improve the overall activity of alkali promoted bulk Mo_2C for CO hydrogenation, however, hydrocarbons are still dominant products (up to 55 C-mol %), which is undesired.

Here, we present a prospective approach to increase the activity and selectivity of alcohols over molybdenum carbide by supporting the carbide on high surface area supports. The investigations include evaluations of various support materials like active carbon (AC), carbon nanotubes (CNTs) and titanium dioxide, evaluations of the optimal loadings of both Mo_2C and the K_2CO_3 promoter on active carbon, as well as structural characterization by using BET surface area measurements, transmission electron microscopy (TEM) and X-ray diffraction (XRD).

9.3 Experimental

9.3.1 Catalyst preparation

AC, CNTs, and TiO_2 pellets were crushed and sieved to a size range of 0.6 to 1.4 mm. Additionally, CNTs were purified by refluxing 5 g in 500 ml of 37 wt % nitric acid at 110 °C for 5 h, followed by filtration, washing and drying before impregnation [209]. The precursor solution of $Mo_7O_{24}(NH_4)_6{\cdot}4H_2O$ was added to the individual supports in amounts corresponding to their pore volume (Table 9-1) and aged at room temperature for 1 h. The sample was then dried at 100 °C in air for 12-14 h and calcined at 450 °C in N_2 flow for 2 h with a heating rate of 5 °C min^{-1}, and subsequently carburized. Precursors used for preparation of all supported Mo_2C catalysts are shown in Table 9-1.

Table 9-1 Precursors used for preparation of all supported catalysts.

Precursors	Purity	Supplier	Pore volume [ml/g]
K_2CO_3	≥ 99%	Ridel de Haën	
$Mo_7O_{24}(NH_4)_6{\cdot}4H_2O$	≥ 99%	Sigma-Aldrich	
Active carbon	≥ 99%	Daihope	0.85
Carbon nanotubes[a)]	≥ 95%	Timesnano	3.5
TiO_2	≥ 99%	Saint-Gobain Norpro	0.75

a) Purity ≥ 98.2% after purification, detected by TEM-EDX.

Table 9-2 Composition of prepared catalysts.

Name	Catalysts [a)]	Loading of Mo [wt %]	Loading K_2CO_3 [wt %][c)]	K/Mo molar ratio
Bulk carbide[b)]	10%K_2CO_3/Mo_2C	100	10	0.14
AC_5_14K	0.5%K_2CO_3/5%Mo_2C/AC	5	0.5	0.14
CNT_5_14K	0.5%K_2CO_3/5%Mo_2C/CNT	5	0.5	0.14
TiO_2_5_14K	0.5%K_2CO_3/5%Mo_2C/TiO_2	5	0.5	0.14
AC_20_0K	20%Mo_2C/AC	20	0	0
AC_20_14K	2%K_2CO_3/20%Mo_2C/AC	20	2	0.14
AC_20_21K	3%K_2CO_3/20%Mo_2C/AC	20	3	0.21
AC_20_28K	4%K_2CO_3/20%Mo_2C/AC	20	4	0.28
AC_40_14K	4%K_2CO_3/40%Mo_2C/AC	40	4	0.14

a) The loading percentage of K_2CO_3 and Mo_2C are in weight percent (wt %).
b) The bulk carbide data was adapted from the work done by Christensen et al. [8].
c) Relative to total catalyst mass.

In a typical carburization process, the oxide/support precursors (6-8 g) were placed in a quartz holder, which was then placed in a quartz tube inside a tube furnace (Carbolite). The system was first purged with N_2 and then subjected to a flow of 20 vol % CH_4/H_2 (52 NmL min^{-1}) with a temperature programmed ramping (below 280 °C, ramp 5 °C min^{-1}, and above 280 °C, ramp 0.5 °C min^{-1}, up to 750 °C and kept at 750 °C for 2 h). Afterwards the sample was cooled down in the flow of 20 vol % CH_4/H_2 until the temperature was below 280 °C. Then N_2 was used to flush the system until room temperature was achieved. Before removing the sample from the furnace, it was exposed to a flow of 1 vol % O_2/N_2 for at least 2 h to passivate the sample [404-407]. For alkali-modified carbide samples, an incipient wetness impregnation step was applied using an aqueous

solution of K_2CO_3. The impregnated samples were then aged for 1 h, dried in N_2 at room temperature for 12-16 h and then calcined in flowing N_2 at 450 °C for 2 h with a heating rate of 5 °C min^{-1}. Table 9-2 shows the composition of the prepared catalysts with different supports and different loadings of Mo_2C and K_2CO_3 on AC. The catalysts can be divided in three groups: *a)* 5 wt % of Mo_2C on AC, CNT, and TiO_2 (all promoted by K_2CO_3 to yield a molar ratio of K/Mo = 0.14); *b)* 5, 20, 40 wt % of Mo_2C on AC (all promoted to K/Mo =0.14, mol/mol); *c)* 20 wt % Mo_2C/AC promoted to K/Mo = 0, 0.14, 0.21, 0.28, mol/mol. For the notation, for example AC_5_14K means that the support is activated carbon with a loading of 5 wt % Mo and promoted by K_2CO_3 to yield a K/Mo molar ratio of 0.14. The results for bulk carbides are taken from previous work in our lab [8].

9.3.2 Catalyst characterization

The specific surface area of supports, oxide precursors, carbides, and fresh catalysts were measured by nitrogen adsorption at liquid nitrogen temperature using a QuantaChrome Autosorb iQ_2 gas sorption analyzer. The samples were outgassed under vacuum at 250 °C for 4 h. The measurements of the specific surface areas were performed with a 7-point linear BET plot in the range p/p^0 = 0.05-0.3.

XRD was carried out on a PANalytical X'Pert PRO diffractometer operated at 45 kV and 40 mA with a 2θ range of 10° to 80° with a scanning rate of 0.00164 °/s on passivated samples; the total scan time was 45 min.

TEM was conducted on a FEI Titan 80–300 aberration corrected microscope operated at 300 kV, equipped with an Oxford Instruments INCA-EDX spectrometer for elemental analysis. The catalysts were dispersed in dry form on the TEM grids, which were Cu-grids coated with a holey carbon film.

9.3.3 Catalyst testing

The performance of the catalysts for CO hydrogenation has been evaluated in a fixed-bed continuous-flow reactor with a GC-FID/TCD detection system [6, 96]. The following species were quantified: C_1-C_4 alcohols: methanol, ethanol, 1-propanol, 1-butanol, 2-butanol, and iso-butanol; C_1-C_3 hydrocarbons: methane, ethene, ethane, and propane, as well as dimethyl ether (DME) and ethyl acetate. The gas flow rate was measured by a bubble flow meter. The mass balance for carbon was generally fulfilled to within 5%. Prior to the reaction, all catalysts were treated in situ with a flow of 20 vol % H_2 in N_2 (35 NmL min^{-1}) at 350 °C for 2 h with a heating rate of 3 °C min^{-1} to remove a possible passivation layer on the catalyst.

The conversion of CO (X_{CO}) is calculated from the molar flow rates of CO (F_{CO}) into and out of the reactor:

$$X_{CO} = \frac{F_{CO}^{in} - F_{CO}^{out}}{F_{CO}^{in}} \cdot 100\%$$

The CO_2-free selectivity to a given product (S_i) is based on the total number of carbon atoms in the products except CO_2:

$$S_i = (n_i y_i) / (\sum n_i y_i) \cdot 100\%$$

Where n_i ($n_i \geq 1$) is the number of carbon atoms in component *i*, and y_i is the mole fraction of component *i* in the product stream.

9.4 Results and discussion

9.4.1 Catalyst structure

The alkali promoted bulk Mo_2C suffers from a low specific surface area, because of the high carburization temperature (up to 750 °C) and high loading of K_2CO_3 promoter [8, 199]. The high carburization temperature also challenges the thermal stability of the support materials. It is therefore important to evaluate the surface areas of supports, oxide precursors, carbides, and fresh catalysts (carbides promoted by K_2CO_3). The results in Table 9-3 illustrate that the applied carburization conditions yield a bulk carbide with low surface area (11.5 m^2 g^{-1}), although the surface area is increased compared to its oxide precursor (3 m^2 g^{-1}) due to the generation of pores during the carburization process. However, the surface area decreases significantly to 2.4 m^2 g^{-1} after loading of K_2CO_3 (10 wt %), which occupies most of the pore structure. A similar tendency – that supported carbides show higher surface areas than their oxide precursors is observed for all samples except the titanium dioxide supported Mo_2C. Generally the surface areas of AC supported samples decrease both upon addition of K_2CO_3 and with increasing Mo_2C loadings. The surface area of the titanium dioxide supported MoO_3 decreases by a factor of 3.5 after carburization. This may be because titanium dioxide starts to transform from the higher surface area anatase phase to the low surface area rutile phase when the temperature is higher than 550 °C [408, 409]. We also observe rutile formation in the passivated TiO_2_5_14K sample, as shown in the supplementary material (Appendix E, Fig. S1). However, no specific Mo_2C reflection is observed, which is probably due to the small particles being formed and dispersed on the surface, which makes them difficult to analyze by XRD. Similar results are found for the other two 5 wt % loading of Mo_2C samples (on AC and CNT).

Table 9-3 BET surface area of supports, oxide precursors, carbides, and fresh catalysts.

Samples	Supports	MoO_3/Support	Mo_2C/Support	Fresh catalysts
		BET surface areas [m^2 g^{-1}]		
Bulk carbide	-	3	11.5	2.4
AC_5_14K	1270	963	1001	995
CNT_5_14K	291	144	163	155
TiO_2_5_14K	161	130	37	31
AC_20_0K	1270	674	730	730
AC_20_14K	1270	674	730	596
AC_20_21K	1270	674	730	626
AC_20_28K	1270	674	730	620
AC_40_14K	1270	313	463	356

Fig. 9-1 shows the X-ray diffractograms of bulk and AC supported molybdenum carbide samples. The observed reflections of bulk molybdenum carbide correspond well to Mo_2C in the Inorganic Crystal Structure Database (ICSD files of 618291 and 43322). There are two possible structures of molybdenum carbide: orthorhombic Mo_2C (often denoted as α-Mo_2C) and hexagonal Mo_2C (often denoted as β-Mo_2C) [410, 411]. It is very difficult to distinguish between hexagonal and orthorhombic Mo_2C by XRD patterns, since only reflections from the metal planes can be observed from XRD patterns and the placement of the metal atoms is essentially the same for the two structures [8, 412]. However, Page et al. [413] used a carburization procedure similar to the one

used in this study and found that the formed material had the orthorhombic structure according to the results of neutron diffraction.

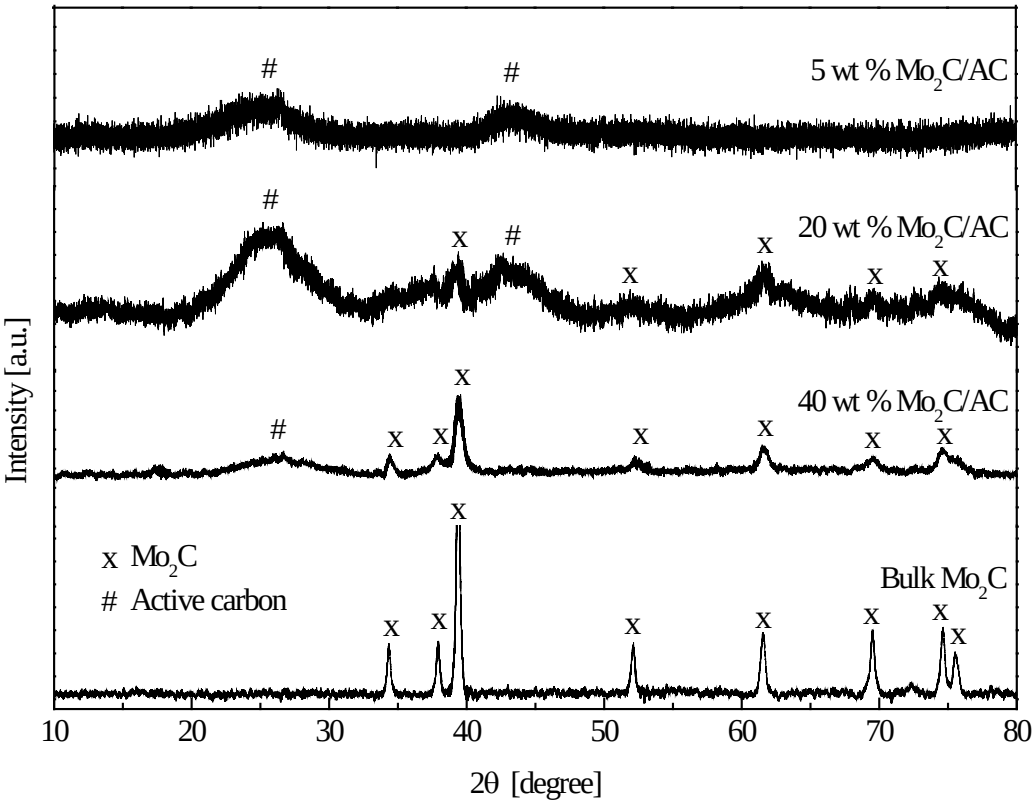

Fig. 9-1 XRD patterns of bulk and AC supported carbide samples (after passivation).

The XRD pattern of the 5 wt % Mo_2C/AC sample exhibits no specific Mo_2C reflections, but for the higher loadings of 20 wt % and 40 wt % Mo_2C on AC, Mo_2C reflections are visible. This is probably due to the higher concentration of Mo_2C on the support leading to larger particles and higher crystallinity of Mo_2C. The 40 wt % Mo_2C (AC_40_14K) shows much smaller BET surface area compared to those of lower loadings on Mo_2C (20 wt % and 5 wt %) on AC. Additionally, the TEM images of the 5 wt % of Mo_2C/CNT sample are shown in the Appendix E, Fig. S2. The Mo_2C particles are mainly located inside the carbon nanotubes.

9.4.2 Catalyst activity and selectivity

9.4.2.1 Time on stream catalytic behavior

Fig. 9-2 shows a typical activity vs. time on stream profile of a supported carbide catalysts, exemplified with the AC_20_21K catalyst. The activity is stable at 250 °C and 275 °C, while a slight decline in activity over time can be observed at 300 °C. The decline in activity could be due to carbon formation, which is a typical deactivation process for bulk Mo_2C and therefore most likely also for supported carbides [8, 198, 199]. Fig. 9-2 illustrates that the selectivity to methanol and higher alcohols gradually increases over time to a stable level, while the selectivity to hydrocarbons decreases over time at each tested temperature. This behavior could be due to

dispersion of K_2CO_3 taking place during the reaction, as it is known that K_2CO_3 is critical for alcohol synthesis over bulk molybdenum carbide [199].

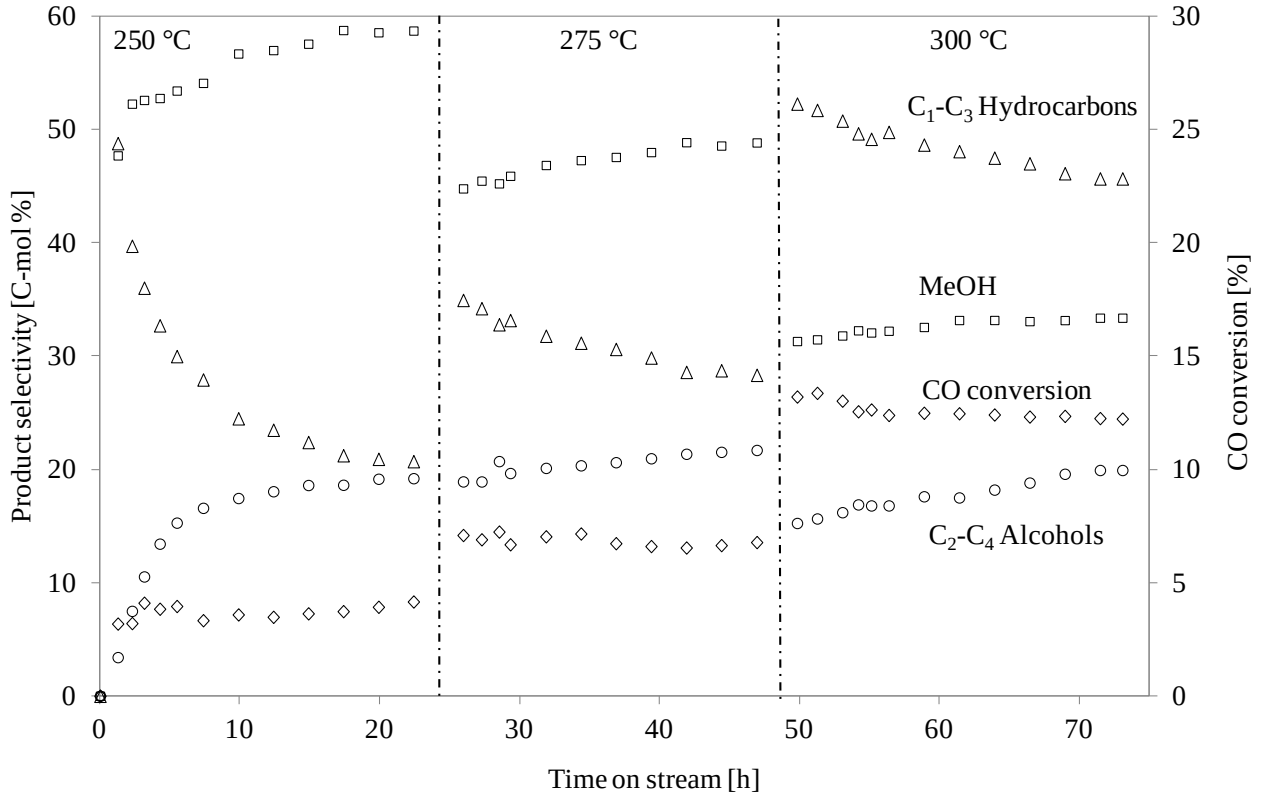

Fig. 9-2 The CO conversion and product selectivity as functions of the time on stream with stepwise changes in temperature for the AC_20_21K catalyst. The experimental conditions are: 100 bar, GSHV = 5000 h^{-1}, and H_2/CO = 1 (vol/vol).

9.4.2.2 Effect of support

Fig. 9-3 shows the CO conversion and the selectivity to different products at steady state over bulk and supported (5 wt % loading) Mo_2C catalysts at 250 °C. The CO conversion is at the same level for all supported carbides (2.4%, 3.6%, and 4.6% for AC_5_14K, CNT_5_14K, and TiO_2_5_14K, respectively), which is comparable to the bulk carbide (3.8%). However, the activity of the supported carbides based on Mo weight is 12 to 24 times higher than the bulk carbide. The TiO_2 supported catalyst shows the highest activity, although the catalyst has the lowest BET surface area. The higher activity of TiO_2 supported carbide compared to the other supported catalysts could be related to the special properties of TiO_2. It is known that TiO_2 can transfer electrons from Ti^{3+} to metals supported on it, which changes their catalytic properties [208, 414]. The product composition for the TiO_2 supported catalyst resembles the bulk carbide, and shows the highest selectivity to higher alcohols (34.3 C-mol %) and a high selectivity to hydrocarbons (46.2 C-mol %). The active carbon supported catalyst exhibits the highest total selectivity to alcohols (62 C-mol %) with methanol being the main alcohol, and consequently also produces the lowest amount of hydrocarbons. The CNT supported carbide produces mainly methanol and hydrocarbons.

As described above, TiO_2 is unstable during high temperature (750 °C) carburization, leading to loss of surface area. However, our recent in situ studies of the carburization process show that the required carburization temperature decreases with a decrease in the particle size of the precursors [374]. Therefore, TiO_2 could still be an interesting support for Mo_2C for higher alcohol synthesis, if

the carburization temperature could be decreased to below 550 °C to prevent the phase transition of TiO_2 from high surface area anatase to the low surface area rutile. The behavior of the CNT supported sample lies in between the AC and TiO_2 supported samples. However, the high cost of CNT makes it less attractive than the AC as a support. AC supported Mo_2C retains a large surface area after carburization, which is desirable, and it has the highest and alcohol selectivity and lowest hydrocarbon selectivity. Hence, this catalyst seems attractive for further development, where increasing the loading of Mo_2C on AC could be a potential way to increase the activity while keeping the selectivity high.

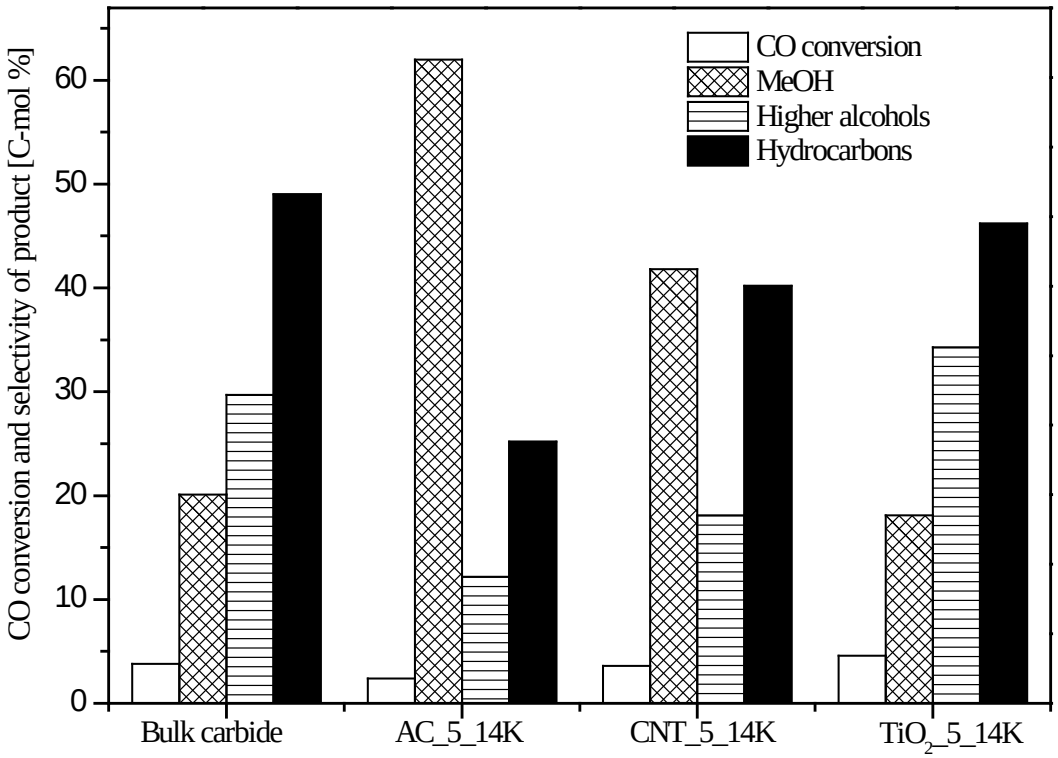

Fig. 9-3 CO conversion and selectivity of products at steady state over K_2CO_3 promoted bulk and supported (5 wt % loading, molar ratio K/Mo=0.14) Mo_2C catalysts at 100 bar, 250 °C, GSHV = 5000 h^{-1}, and H_2/CO = 1 (vol/vol).

9.4.2.3 Effect of temperature

Table 9-4 shows the catalytic performance of the AC_5_14K and TiO_2_5_14K catalysts in CO hydrogenation at various temperatures. For the AC_5_14K catalyst the selectivity to higher alcohols remains constant at about 12 C-mol % below 300 °C, but then decreases to about 6 C-mol % at 326 °C. From 250 to 326 °C the selectivity to hydrocarbons increases from 25.2 C-mol % to 71.6 C-mol %, while methanol and higher alcohols selectivities decrease.

Table 9-4 Effect of temperature on the catalytic performance of AC_5_14K and TiO_2_5_14K catalysts in CO hydrogenation at steady state, at 100 bar, GSHV = 5000 h^{-1}, and H_2/CO = 1 (vol/vol).

Catalyst	T [°C]	TOS[a)] [h]	CO conv. [%]	Carbon based, CO_2-free selectivity [C-mol %]		
				MeOH	$C_{2+}OH$	Hydrocarbons
AC_5_14K	250	29	2.4	62	12.2	25.2
	275	48	4.2	55.3	12.8	31.7
	300	53	8.6	43.2	12.3	44.2
	326	58	20.4	22.6	5.8	71.6
TiO_2_5_14K	250	24	4.6	18.1	34.3	46.2
	275	47	9.4	13.3	21.7	61.6
	300	51	85.1	0.3	0.4	99.3

a) TOS: time on stream.

Regarding the TiO_2_5_14K catalyst, both the CO conversion and the hydrocarbon selectivity increase steeply with increasing temperature. The higher alcohol selectivity is 34.3 C-mol % at 250 °C, but the selectivities to both methanol and higher alcohols decrease dramatically, when the temperature is increased.

9.4.2.4 Effect of the loading of active materials

Fig. 9-4 shows for AC supported catalysts the effect of the Mo_2C loading on the steady state CO conversion and the product selectivity at 275 °C. The bulk Mo_2C catalyst (100 wt % in Fig. 9-4) suffers from a low specific surface area, which leads to a low activity for CO hydrogenation [199]. The CO conversion and selectivity to different products vary with the Mo_2C loading. AC_20_14K exhibits the highest CO conversion, and a similar tendency can be observed at 250 °C and 300 °C as well (see Fig.S3 in the Appendix E). Decreasing the level of active material below 20 wt % leads to a loss of activity due to dilution from the support. The high selectivity to hydrocarbons might be caused by insufficient loading of the K_2CO_3 promoter. It has previously been found, that the selectivity to alcohols increases with increasing K_2CO_3 content up to 10 wt % over the bulk carbide (molar ratio of K/Mo=0.14) [199]. In this study, the added amount of K_2CO_3 for the catalysts in Fig. 9-4 corresponds to a molar ratio of K/Mo=0.14. However, K_2CO_3 may be partly deposited also on the support leading to less than optimal promoter levels on the active materials, particularly at low loading of Mo_2C.

The selectivity to higher alcohols increases with increasing Mo_2C loading on AC and reaches a maximum over bulk carbides, while the selectivity to methanol follows the opposite trend. According to our recent studies [374], involving in situ carburization and extended X-ray absorption of fine structure investigations, we found that the coordination numbers (CN) of Mo_C in molybdenum carbide structures are 3, 3.6, and 4.4 for bulk Mo_2C, 40 wt % Mo_2C/AC and 20 wt % Mo_2C/AC, respectively. Moreover, Shou and Davis [284] reported that MgO supported (5 wt %) Mo_2C showed higher CN of Mo-C/O (CN = 5.1) than bulk Mo_2C (CN = 3). These results indicate that the structure/composition of the supported carbide clusters differs from that of bulk carbide. The change of the structure/composition of the supported carbide clusters may change the electronic structure of catalytic surface, and consequently affect the catalytic properties. Our studies have also shown that the carbide particle size decreases with decreasing Mo loading on AC [374]. The variation in particle size with carbide loading may also affect the catalytic properties. One would expect smaller particles to have a larger amount of steps and defects that should bind carbon and oxygen more strongly. Smaller particles may therefore have a larger oxygen coverage at the reaction conditions. Density functional theory calculations by Medford et al. [415] showed that

oxygen is present in the carbide surface – even in syngas and that increasing oxygen coverage leads to a weakening of the carbon and oxygen binding energies on the surface. Such a weakening of the binding energies would also be expected to influence the catalytic properties. This could be one of the reasons why the catalytic properties of the supported carbides are different from the properties of the bulk carbide.

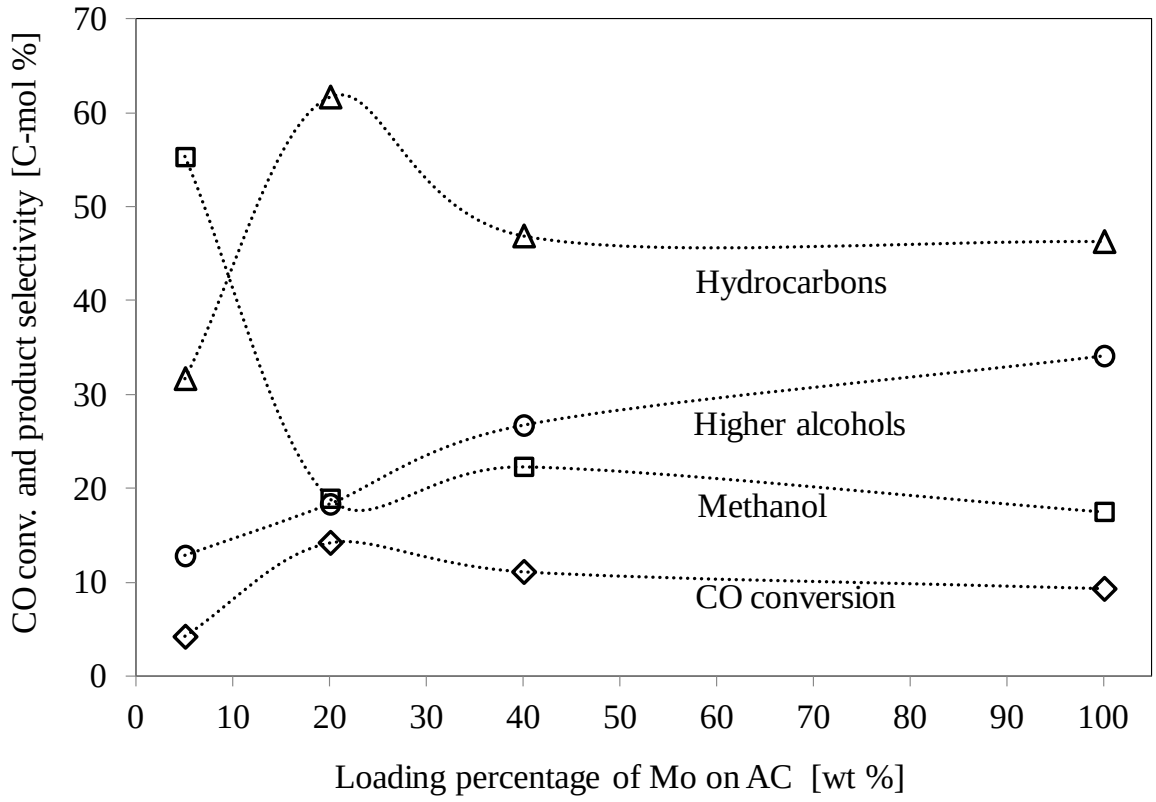

Fig. 9-4 CO conversion and selectivity of products at steady state over K_2CO_3 promoted catalysts with different loading of Mo on AC (molar ratio K/Mo=0.14) at 100 bar, 275 °C, GSHV = 5000 h^{-1}, and H_2/CO = 1 (vol/vol).

Fig. 9-5 shows the detailed distributions of alcohols and hydrocarbons that are obtained with varying loadings of Mo_2C on AC at steady state. The main alcohols are methanol and ethanol, and the dominant hydrocarbon is methane for both bulk and supported carbides. Bulk carbide typically produces a certain amount of alkenes as by products [8, 284, 401]. The trends in alkenes and alcohols are similar [284, 401]. The bulk carbide produces the most of ethanol and ethene, and the lower loading of Mo_2C on AC results in smaller amounts of ethanol and ethene, but higher amounts of methanol.

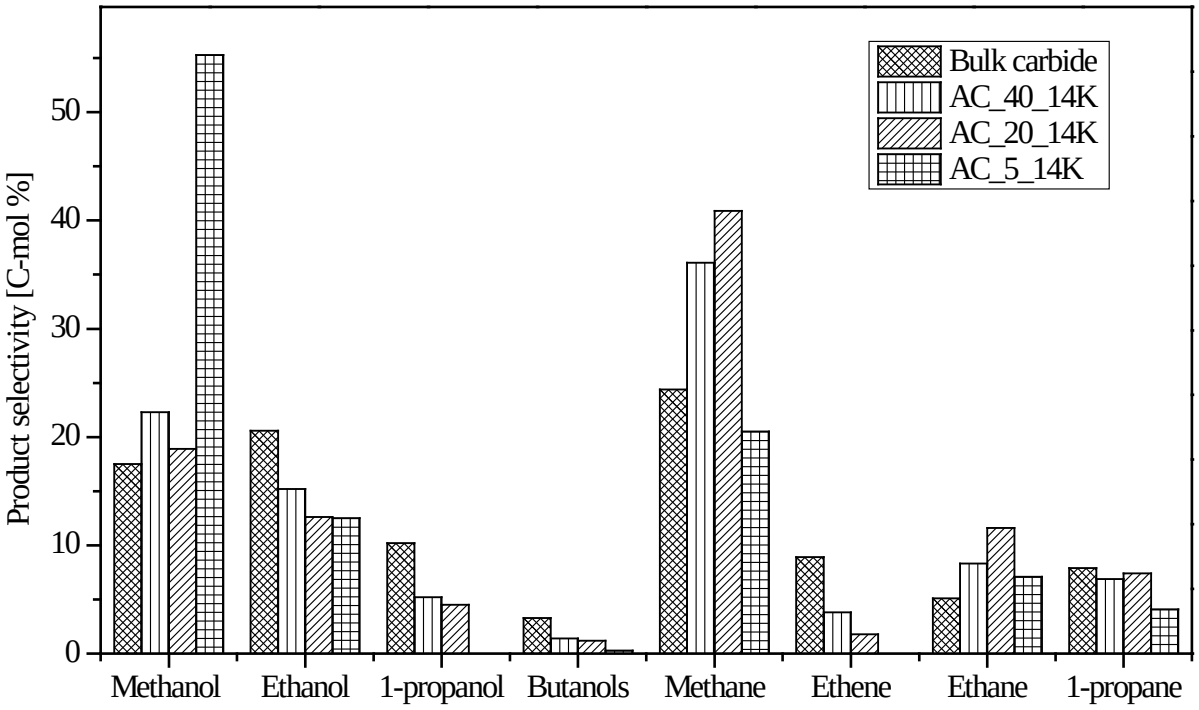

Fig. 9-5 Product distributions over K_2CO_3 promoted catalysts with different loading of Mo_2C on AC (molar ratio K/Mo=0.14) at steady state at 100 bar, 275 °C, 5000 h^{-1}, and H_2/CO = 1 (vol/vol).

9.4.2.5Effect of K_2CO_3 loading

The K_2CO_3 promoter plays an essential role for higher alcohol synthesis over bulk Mo_2C and it has been found that the selectivity to higher alcohols reaches a maximum at a molar ratio of K/Mo = 0.14 [199]. The amount of K_2CO_3 has a major influence on both activity and selectivity to different products [199]. Here, the molar ratios of K/Mo are kept constant (0.14) for all other catalysts. However, a dilution effect of the support should be considered. The 20 wt % Mo_2C/AC catalyst exhibits the highest activity, and therefore the effect of the K_2CO_3 loading on the 20 wt % Mo_2C/AC catalyst has been investigated further. As shown in Fig. 9-6, unpromoted Mo_2C/AC exhibits a high CO conversion with hydrocarbons as the dominant products (98.4 C-mol %). Upon addition of K_2CO_3 to Mo_2C/AC, the overall CO conversion is reduced, while the product distribution shifts from hydrocarbons to alcohols. The increase in alcohol selectivity continues until a molar ratio of K/Mo = 0.21, where both selectivities to higher alcohols and to alcohols in general reach a maximum. By addition of K_2CO_3 corresponding to K/Mo=0.28, the selectivity to alcohols increases from 1.6 C-mol % to 70.2 C-mol %, while the selectivity to hydrocarbons decreases from 98.4 C-mol % to 28.5 C-mol % and CO conversion declines from 47.2% to 3.5 % compared to the unpromoted carbide. This trend indicates that molybdenum carbides are active species for CO hydrogenation, and yet the presence of K_2CO_3 promoter is required for a high selectivity to alcohols, which is generally in agreement with the observations from K_2CO_3 promoted bulk carbide [199].

The effect of an alkali promoter on Mo_2C catalysts seems critical for producing alcohols. Lee et al. [401] have evaluated the role of different anions to potassium such as K_2CO_3, KOH, and CH_3COOK over Mo_2C. They suggested that the alkali promoter has a geometric effect by blocking the surface sites for adsorption of reactants and an electronic effect by changing the surface electron density [401]. Similarly, a site blocking effect of alkali on Mo_2C has been observed in other studies [8, 205, 284]. Thus the present observation of both decreasing CO conversion and shift in product selectivity with increasing alkali loading could be related both to surface blocking effects and electronic modifications.

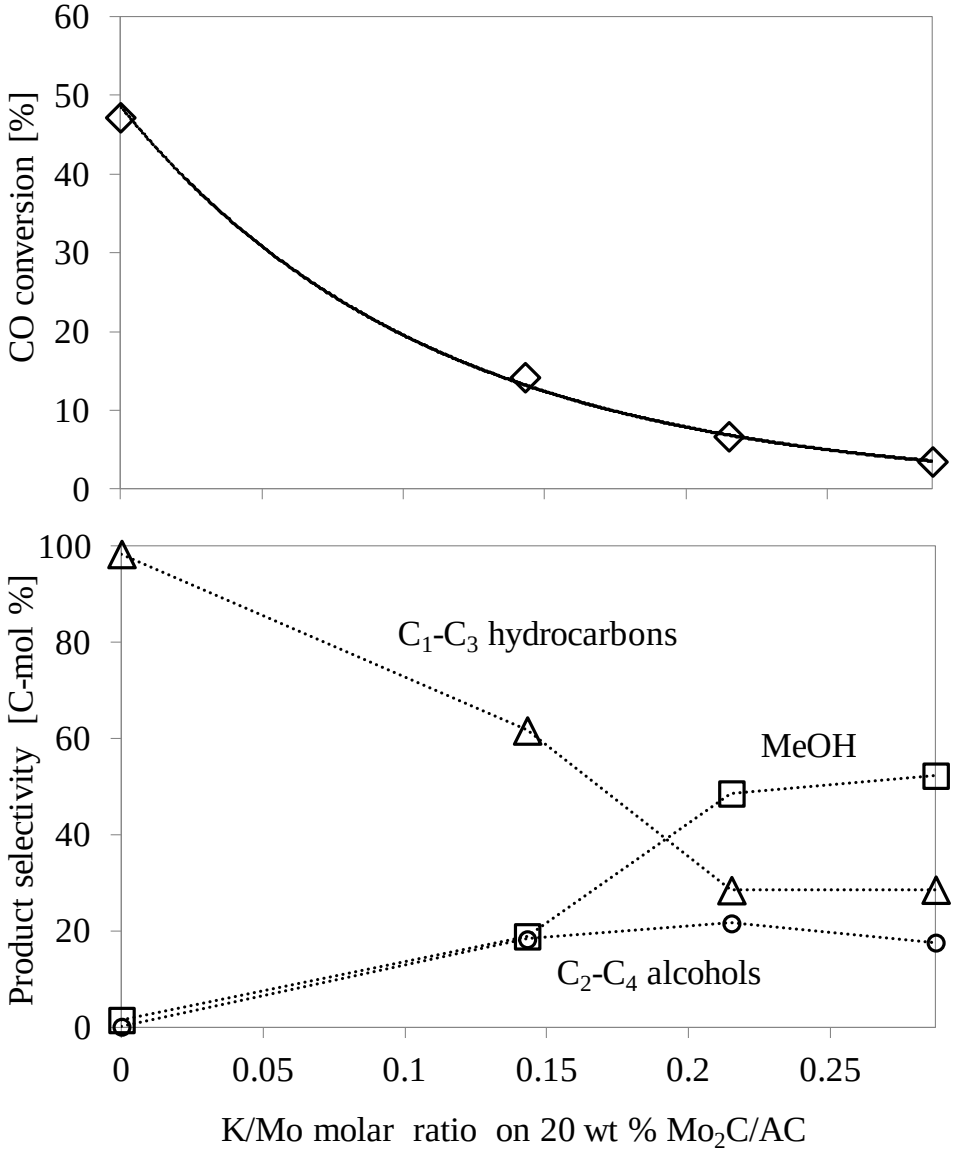

Fig. 9-6 The effect of K/Mo on CO conversion and the selectivity of products over the 20 wt % Mo_2C/AC at steady state at 100 bar, 275 °C, 5000 h^{-1}, and H_2/CO = 1 (vol/vol).

9.4.2.6 Productivity of alcohols

The space time yields (STY) of alcohols shown in Fig. 9-7 emphasize that the AC supported Mo_2C catalysts behave better than bulk carbides, although the majority of the increased alcohol production comes from methanol. At 275 °C the AC_20_14K (2 wt % K_2CO_3 promoted 20 wt % Mo_2C/AC), produces two times more higher alcohols and about 3 times more methanol compared

to bulk carbides. Hence, it is possible to raise the alcohol productivity through the use of the active carbon support.

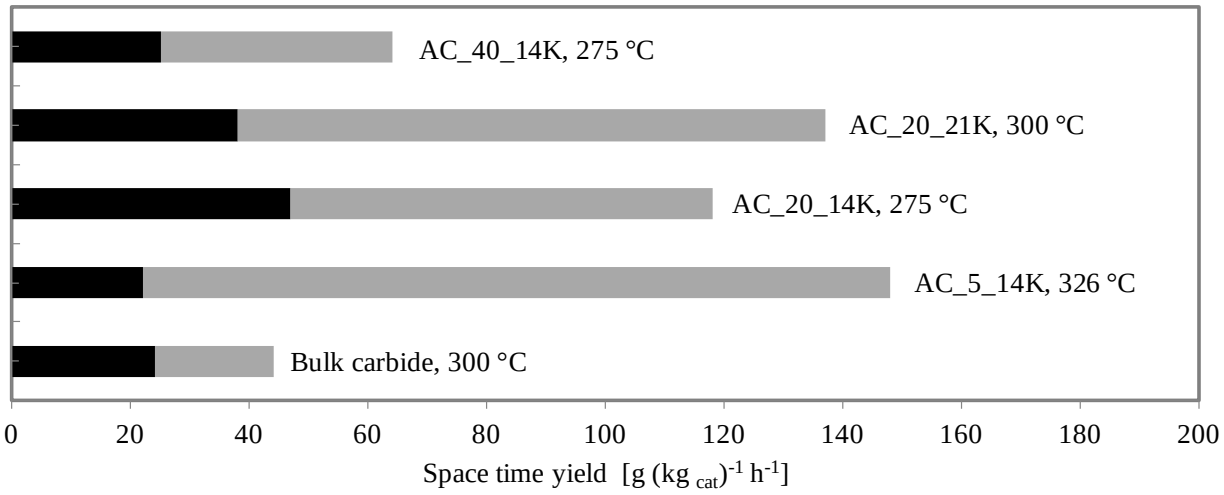

Fig. 9-7 The maximum space time yields of methanol (grey) and C_2-C_4 alcohols (black) over both bulk and AC supported carbides 100 bar, 5000 h^{-1}, and H_2/CO = 1 (vol/vol)

9.5 Conclusion

The catalytic activity of potassium promoted molybdenum carbide supported on different materials such as active carbon, carbon nanotubes, and titanium dioxide for higher alcohol synthesis from syngas is significantly affected by the nature of the support. Titanium dioxide seems to be a promising support due to its better selectivity to higher alcohols, however, the thermal stability of TiO_2 limits its application as a support for carbides due to high carburization temperature (750 °C). It would be interesting if the carburization temperature could be decreased to lower than 550 °C (the phase transition temperature for TiO_2 from high surface area anatase to the low surface area rutile) for example by decreasing the particle size of molybdenum oxide. Carbon nanotubes supported carbides produce mainly methanol and hydrocarbons. By supporting molybdenum carbide on a suitable carrier such as active carbon, can improve both the activity and selectivity to alcohols compared to bulk carbide. The potassium carbonate promoter plays an essential role in obtaining alcohols rather than hydrocarbons (unpromoted AC supported Mo_2C produces predominantly hydrocarbons). The optimum selectivity towards higher alcohols and to total alcohols was obtained at a K/Mo molar ratio of 0.21 over the 20 wt % Mo_2C on active carbon, which is higher than the bulk carbide (K/Mo=0.14). It is likely that the support material dilutes the promoter contents on the carbide. The selectivity to higher alcohols increases with increasing the Mo_2C loading on AC (at fixed K/Mo=0.14) and reaches a maximum over bulk carbides, while the selectivity to methanol follows the opposite trend. This effect of the Mo_2C loading on the selectivity could be related to the loadings of K_2CO_3 on the active Mo_2C phase and the size, structure and composition of the supported carbide clusters.

10 Simultaneous in situ XANES and XRD on formation of bulk and supported molybdenum carbides

10.1 Abstract

We have combined in situ X-ray absorption near edge spectroscopy with X-ray diffraction to follow directly the carburization process on formation of bulk and supported molybdenum carbide (20% and 40% Mo_2C on active carbon). We have identified that the bulk Mo_2C prepared by the temperature programmed reaction of molybdenum oxide in the flowing of 20 vol % CH_4/H_2 atmosphere is most likely to adopt an orthorhombic structure (α-Mo_2C). A two-step mechanism is discovered during the in situ carburization process, composed of the initial reduction of Mo(VI) oxide to Mo(IV) oxide and a succeeding conversion to carbide. The reduction and carburization temperatures are somewhat determined by crystal sizes. A decrease on particle size will initiate the onset of reduction and carburization at lower temperatures. In addition, the structures (coordination numbers of Mo_C and Mo_Mo) of bulk and supported molybdenum carbides are different. Finally, the catalytic performance of both bulk and active carbon supported carbides with respect to higher alcohols synthesis from syngas is reported in order to show the structure-performance relationships.

10.2 Introduction

Transition metal carbides have recently attracted a lot of attention in catalysis because they have been claimed to be comparable to noble metals in terms of their catalytic behaviors [416], for example Mo_2C with Ru [415, 417], and WC with Pt [418]. Meanwhile their resistance to poisons such as sulfur and to sintering is potentially better, and therefore, leading them to be potential candidates in substitution for the expensive noble metals [28, 419]. Previous studies demonstrated molybdenum carbide has excellent catalytic activity in a wide variety of reactions, such as higher alcohol synthesis [199, 203, 284, 401, 403, 420], hydrogenation of benzene [404], hydrogenolysis of alkanes [421], steam reforming [422, 423], water-gas shift [424, 425], and alkane isomerization [426]. However, the transition metallic carbides are rarely used in industrial applications, as more work is needed to improve the surface area of the bulk carbides [8, 401, 420] and to develop new methods to prepare supported carbide catalysts [427].

Apart from the catalytic performance also the synthesis of molybdenum carbides is crucial and therefore has attracted considerable attention over the last two decades [199, 427-430]. Mostly, temperature programmed reaction (TPR) of the molybdenum-based oxides with CH_4/H_2 mixture was used to transform it into the corresponding carbides [199, 428, 430, 431]. It seems that there are still needs for further understanding of molybdenum carbide regarding its preparation and structure, for instance, as it is stated in the following aspects.

i. Parameters such as CH_4/H_2 ratio, flow rate of gases, heating rate, final temperature, and isothermal time at the final temperature are important to the final properties of Mo_2C [417, 427, 430-432]. For instance, particle sizes of about 10 nm and 25 nm were observed by transmission electron microscopy when the final isothermal temperature was 700 °C and 800 °C, respectively [405]. There are no studies on

determination of the carburization temperatures for different particle sizes of molybdenum carbide. One would expect by loading less Mo_2C on a support would decrease the particle size of Mo_2C, which consequently would lower the temperature for carburization.

ii. The structure of molybdenum carbide can vary between MoC and Mo_2C, hence it is better describe at MoC_{1-x}. Apart from the cubic phase for MoC, both a hexagonal structure (P63/mmc, often donated as β-Mo_2C) [411, 412, 433] or an orthorhombic structure (Pbcn, often donated as α-Mo_2C) [411, 412, 434], can be formed for Mo_2C. Note that X-ray diffraction (XRD) can hardly distinguish those two phases, since only reflections from the metal planes can be observed from XRD patterns and the placement of the metal atoms is essentially be the same for the two structures [412]. This could be identified by the extended X-ray absorption fine structure (EXAFS) spectroscopy.

iii. In order to generate a protective oxygen layer on the surface, passivation with dilute O_2 is always necessary before exposing them to air, except that they are directly used in the reaction [205, 404-407]. Due to the at least the potential partial oxidation of the molybdenum carbide, it becomes very difficult to characterize ex situ the carbides samples without oxygen contamination.

These studies show that on the one hand that the influence of the support on the carburization temperature needs to be elucidated to prevent the molybdenum carbide to be too much sintered, on the other hand preferentially the carburization process should be performed in situ. In order to tackle both the amorphous and the crystalline structure of the catalysts, two complementary in situ techniques have been applied. In situ X-ray absorption near edge spectroscopy (XANES) together with EXAFS spectroscopy is capable in giving information both on the carburization degree and the local structure. On the other hand the combination with XRD can provide information on the long-range order. This combination has been found powerful in a number of previous studies [289, 371-373].

We have found the structure of catalysts that have been transformed into carbides and exposed to air after passivation in 1 vol % O_2/N_2 for 6 h, demonstrating the significant re-oxidation (more than 50% of Mo_2C has been re-oxidized, see the Appendix F) and the need for in situ studies. In the present work, we have combined in a next step in situ X-ray absorption spectroscopy (XAS) with XRD, following directly carburization process on formation of bulk and supported molybdenum carbide (20% and 40%, wt, Mo_2C on active carbon, AC). In addition, the crystal structure of bulk carbide is analyzed and the structures of bulk and supported molybdenum carbides are compared. Finally, the catalytic performance of both bulk and AC supported carbides with respect to higher alcohols synthesis is reported in order to conclude on structure-performance relationships.

10.3 Experimental section

10.3.1 In situ carburization

AC supported 20% and 40% (wt) molybdenum oxides were prepared by incipient wetness impregnation of AC with aqueous solution of $Mo_7O_{24}(NH_4)_6{\cdot}4H_2O$ and aged at room temperature for 1 h. Followed by drying at 100 °C in air for 12-14 h and calcination

at 450 °C in N_2 flow for 2 h with a heating rate of 5 °C min^{-1}. Bulk MoO_3 precursor was supplied by Sigma-Aldrich (3 m^2 g^{-1}). In a typical carburization process, 10-20 mg of bulk oxide or oxide/support precursors (sieve fraction of 100-200 µm) were loaded in a quartz capillary (OD = 0.5 mm for bulk MoO_3 and OD = 1 mm; wall thickness 0.02 mm) between quartz wool and the capillary was glued into a holder with epoxy resin. Heating was provided by a temperature-controlled hot-air furnace (Cyberstar). The system was purged with N_2 firstly and followed by passing a flow of 20 vol % CH_4/H_2 (30 ml min^{-1}) with a temperature programmed ramping (below 200 °C, ramp 5 °C min^{-1}, and above 200 °C, ramp 2 °C min^{-1}, up to 750 °C and maintain at 750 °C for 1 h). Afterwards the sample was cooled down to room temperature. Additionally, commercial bulk Mo_2C (Sigma-Aldrich) was used as a reference.

10.3.2 In situ XAS and XRD

The combined XAS/XRD measurements were carried out at the European Synchrotron Radiation Facility (ESRF, Grenoble, France) at the BM01B beamline (Swiss-Norwegian Beamlines). The storage ring was operated at electron energy of 6 GeV and injection currents of 200 mA. The beamline offers the possibility to rapidly switch between the XAS and XRD modes and hence carry out quasi-simultaneous measurements with the two techniques.

The in situ experiments were carried out using the quartz capillary micro-reactor originally developed by Clausen and Topsøe [375] for use with in situ XRD studies of catalysts, extended to combined XAS/XRD studies [376] and further developed by Grunwaldt and co-workers [287, 377] and stuff at the Swiss-Norwegian Beamlines [378] for use with in situ studies at synchrotron radiation sources. X-ray absorption spectra were acquired at the Mo K-edge in transmission mode using a continuously scanning Si(111) double-crystal monochromator and a gold-coated mirror for the rejection of higher harmonics. A Mo foil was always measured between the second and third ionization chamber for energy-calibration. XRD patterns were collected using a Si(111) channel-cut monochromator set to a wavelength of $\lambda = 0.503$ Å. The diffractometer with a high-resolution detector consisting of 6 individual channels equipped with Si(111) analyser crystals was scanned between 2θ values of 23° and 80°. Prior to the experiments, the diffractometer was calibrated using a crystalline powder Si standard. A repoducable procedure was run to exchange the dedicated monochromators after every XAS and XRD acquisition.

XAS data analysis was carried out using Athena and Artemis interfaces of the IFEFFIT software [288]. The spectra were energy-calibrated, normalised and background-subtracted. The k^2-weighted EXAFS spectra were Fourier-transformed on the k-range of 2-14 $Å^{-1}$ and fitted in R-space between 1.0-3.2 Å using single path standards generated by FEFF6 [288, 379].

10.3.3 Catalyst preparation and testing

For studies of the catalytic performance, the carbides were prepared similar to the in situ prepared carbides. We prepared bulk Mo_2C, 5%, 20%, and 40% Mo_2C/AC (all in wt %) samples. Before removing samples from the carburization furnace, a flow of 1 vol % O_2/N_2 was introduced for passivation about 6 h. Then all carbides were impregnated with an aqueous solution of K_2CO_3 with calculated molar amount (K/Mo = 0.14), the optimum

ratio for higher alcohol synthesis [8, 199]. The impregnated samples were then aged for 1 h and dried in N_2 at room temperature for 12-16 h and then calcined in flowing N_2 at 450 °C for 2 h with a heating rate of 5 °C min^{-1}. Higher alcohols synthesis has been evaluated in a fixed-bed continuous-flow reactor with a GC-FID/TCD detection system [6, 96, 197]. Methanol, ethanol, 1-propanol, 1-butanol, 2-butanol, and iso-butanol (C_1-C_4 alcohols), methane, ethane, ethane, and propane (C_1-C_3 hydrocarbons), as well as dimethyl ether (DME) and ethyl acetate were characterized. Prior to the reaction, the supported carbides was treated in situ with 20 vol % H_2 in N_2 flow (35 ml min^{-1}) at 350 °C with a heating rate of 3 °C min^{-1} for 2 h to remove a possible passivation layer formed after exposure in air. The gas flow rate was measured by a bubble flow meter. The mass balances for carbon is generally fulfilled to within 5 mol %.

10.4 Results and discussion

10.4.1 Investigation of samples during carburization

Fig. 10-1 shows the in situ XANES spectra and XRD record bulk MoO_3 sample upon heating to 750 °C in a flow of 20 vol % CH_4/H_2 is shown. Both the XANES and XRD data unravel that Mo(VI) oxide is first reduced to Mo(IV) oxide from 400 °C and then transformed into the carbide at around 550 °C.

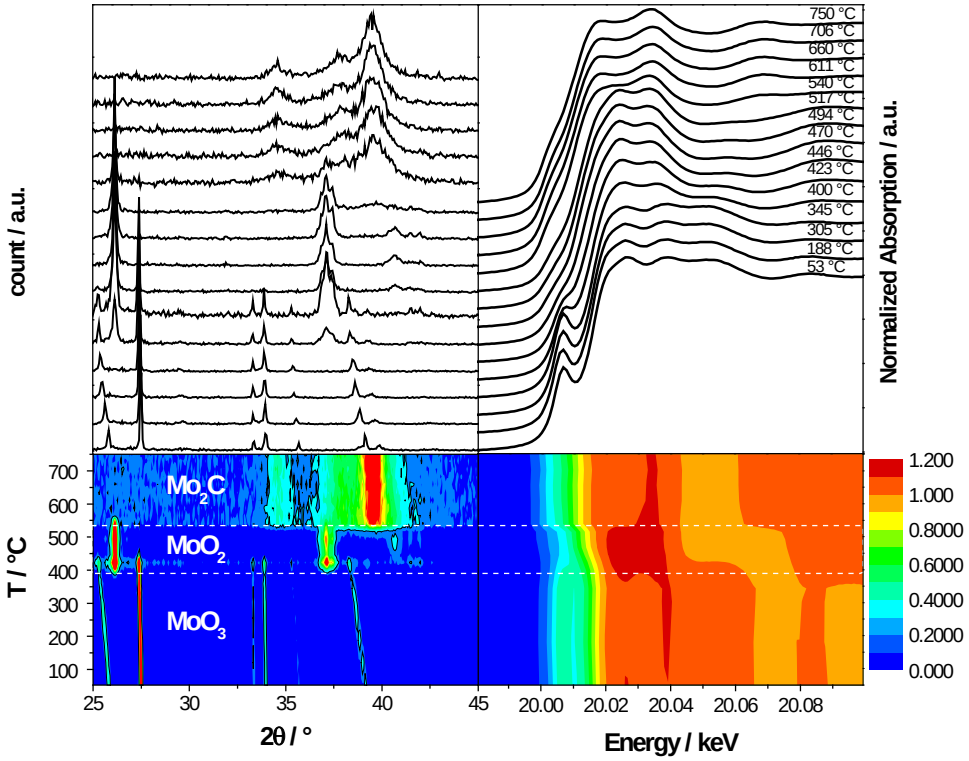

Fig. 10-1 Simultaneous in situ XANES and XRD on carburization process of bulk molybdenum carbides. For XANES: the colors from blue to red are the transition from no absorption to strong absorption refer to references; for XRD: the colors from blue to red are the transition from low intensity to high intensity.

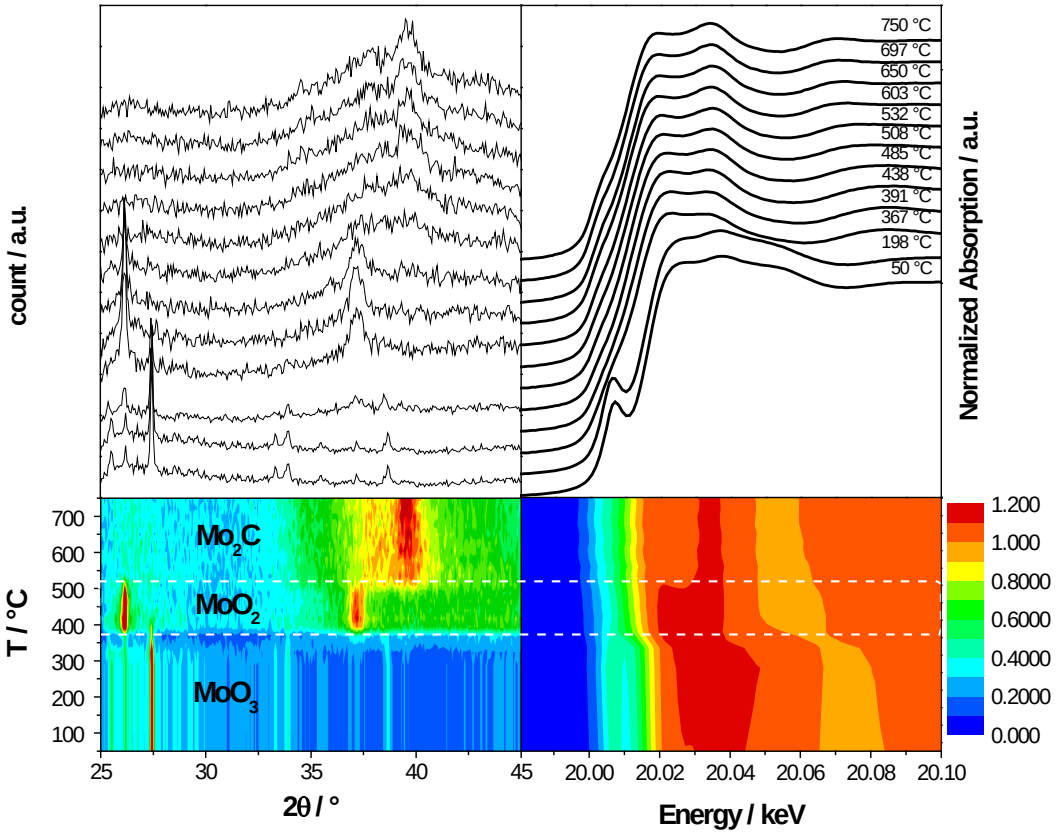

Fig. 10-2 Simultaneous in situ XANES and XRD on carburization process of 40% Mo_2C/AC. For XANES: the colors from blue to red are the transition from no absorption to strong absorption refer to references; for XRD: the colors from blue to red are the transition from low intensity to high intensity.

Regarding the 40% Mo_2C on AC sample, the in situ XRD and the linear combination analysis of XANES spectra exhibits a similar carburization process to the bulk carbide, but in lower temperatures for both reduction and carburization – Mo(VI) oxide is reduced to Mo(IV) oxide at 370 °C, which is 30 °C lower than in the case of bulk carbide samples. The final formation temperature of Mo_2C is at 500 °C (Fig. 10-2).

Table 10-1 Summary of carburization processes of bulk and supported carbides and XRD particles sizes of carbides.

Samples	Precusors	Transition temperature from MoO_3 to MoO_2 / °C	Carbide formation temperature / °C	XRD Particle sizes carbides / °C
Mo_2C	MoO_3	400	550	22
40 % Mo_2C/AC	MoO_3	370	500	9
20 % Mo_2C/AC	MoO_3	320	320	~2

For the 20% Mo_2C on AC sample, as it is shown in Fig. 10-3, the onset of Mo(VI) oxide reduction is around 320 °C, and the Mo_2C is formed simultaneously. Table 10-1 summarizes the parameters during carburization processes of bulk and supported carbides and XRD particles sizes of carbides. The bulk carbide has significant larger particles compared to these supported carbides, and the particle sizes of carbides also decrease

significantly with smaller loading of carbides on active carbon. The effect of the descending temperatures for Mo(VI) oxide reduction and the carburization is very likely due to the decrease of the particle sizes. The reduction and carburization temperatures are somewhat determined by crystal sizes.

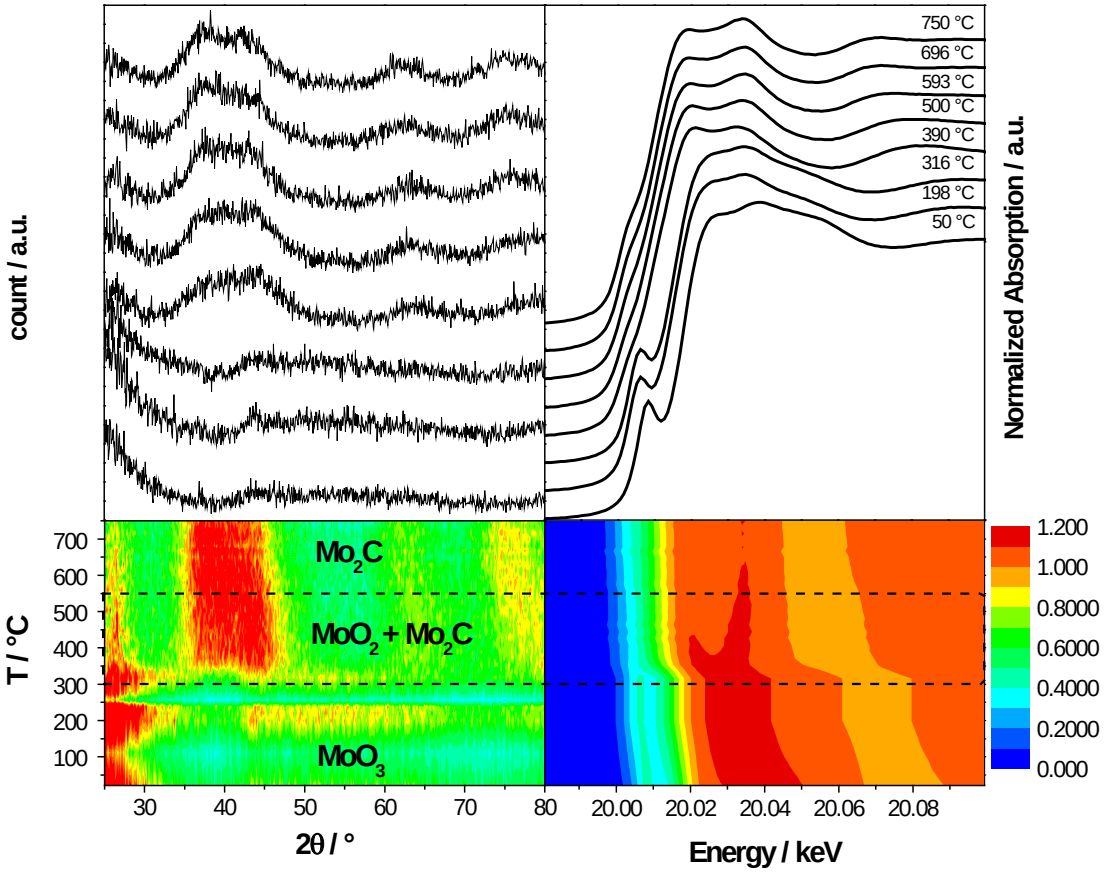

Fig. 10-3 Simultaneous in situ XANES and XRD on carburization process of 20% Mo_2C/AC. For XANES: the colors from blue to red are the transition from no absorption to strong absorption refer to references; for XRD: the colors from blue to red are the transition from low intensity to high intensity

The XRD patterns (Fig. 10-4) were recorded at room temperature after the carburization process. It shows that the bulk MoO_3 is transformed into Mo_2C presenting an orthorhombic or hexagonal structure. By contrast, the other two supported samples (40 wt % and 20 wt % Mo_2C on AC) show the presence of an additional MoC phase (in NaCl-type structure), whose amount increases with the decreasing Mo content (very likely by decreasing the crystal size).

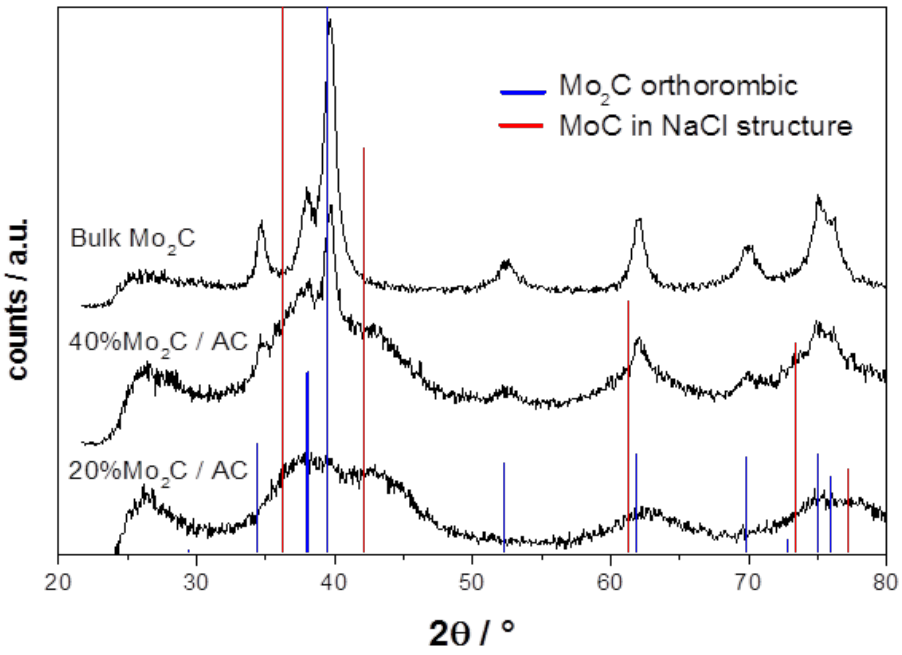

Fig. 10-4 XRD patterns of in situ formed bulk Mo_2C and active carbon supported Mo_2C at room temperature.

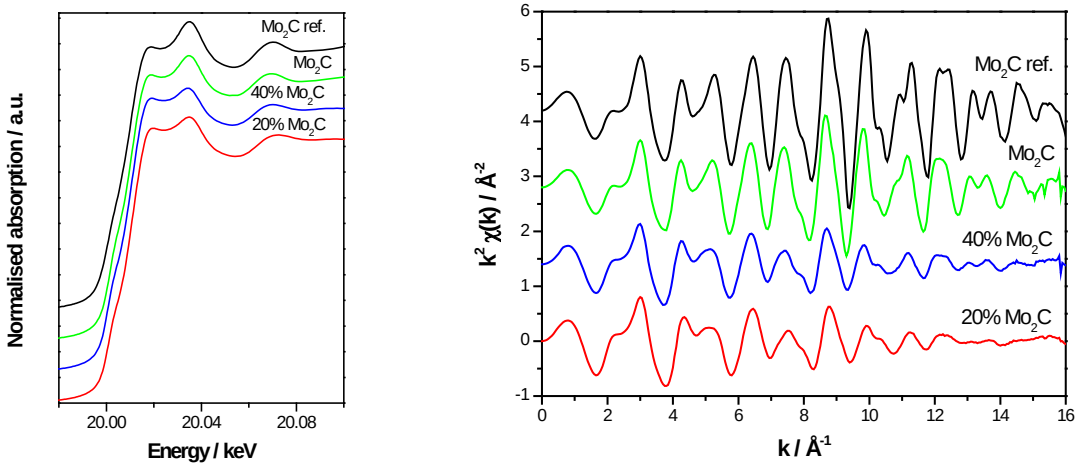

Fig. 10-5 XANES (left) and magnitude of the Fourier transform of the k^3-weighted at the Mo K edge (right) of: Mo_2C reference standards (black), in situ formed bulk Mo_2C (green), in situ formed AC supported 40% Mo_2C (blue) and 20% Mo_2C (red)

The two structural modifications of Mo_2C can be distinguished by the different coordination numbers (CN) of C (Mo_C) in the first shell according to the fitting results of the FT-EXAFS spectra for these three samples after carburization at RT (Fig. 10-5, right). Fig. 10-5 (left) shows XANES and magnitude of the Fourier transform of the k^3-weighted EXAFS function of the Mo K edge of Mo_2C reference standards, in situ formed bulk Mo_2C, 40% Mo_2C/AC and 20% Mo_2C/AC and Fig. 10-6 shows comparison of curve

fit (circle) to experimental Mo K edge extended X-ray absorption of fine structure (EXAFS) of the Mo_2C reference standards and all the samples.

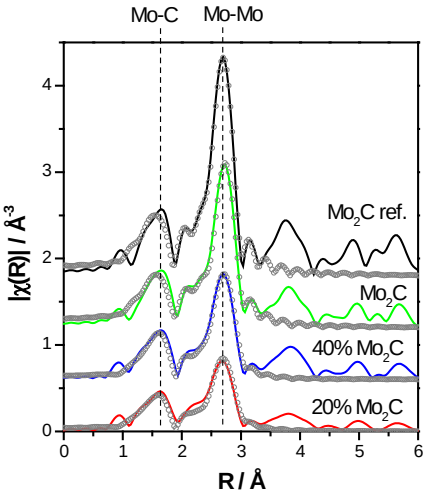

Fig. 10-6 Comparison of curve fit (circle) to experimental Mo K edge EXAFS of the: Mo_2C reference standards (black), in situ formed bulk Mo_2C (green), in situ formed AC supported 40% Mo_2C/AC (blue) and 20% Mo_2C/AC (red) .

Table 10-2 FT-EXAFS spectra fitting results at Mo K-edge of bulk Mo_2C and 40% and 20% Mo_2C (wt %) on active carbon

sample	shell	S_0^2 [a]	CN [b]	R [c] / Å	σ^2 (Å^2) [d]	ΔE_0 [e] / eV	R-factor
Mo_2C ref.	Mo-C	0.70	3.2 ± 0.7	2.16 ±0.01	0.003 ±0.002	4.6 ±0.67	0.016
	Mo-Mo		11.9 ± 1.2	2.88 ±0.004	0.006 ±0.001		
Mo_2C.	Mo-C	0.70	3.2 ± 0.7	2.14 ±0.01	0.004 ±0.003	5.3 ±0.72	0.021
	Mo-Mo		10.5 ± 1.2	2.86 ±0.004	0.006 ±0.001		
40%Mo_2C/AC	Mo-C	0.70	3.9 ± 0.7	2.13 ±0.01	0.007 ±0.003	6.6 ±0.90	0.039
	Mo-Mo		8.2 ± 1.4	2.87 ±0.01	0.010 ±0.001		
20%Mo_2C/AC	Mo-C	0.70	4.2 ± 0.9	2.13 ±0.02	0.007 ±0.003	5.7 ±1.12	0.053
	Mo-Mo		8.7 ± 1.8	2.89 ±0.01	0.011 ±0.001		

[a] S_0^2: amplitude reduction factor; [b] CN: coordination number; [c] R: interatomic distance; [d] σ^2: Debye Waller factor (mean square disorder); [e] ΔE_0: energy shift.

Indeed, the hexagonal one has 6 C-atoms surrounding Mo (Mo_C), whereas the orthorhombic has only 3. The fitting results in Table 10-2 shows that both the bulk commercial Mo_2C (reference) and the one obtained by in situ carburization of the bulk MoO_3 have a coordination number of the first shell of around 3, featuring the orthorhombic structure. On the other hand, the CN of Mo_C increases in the 40% and 20% Mo_2C/AC samples to 3.9 and 4.2 respectively. This latter result is in good agreement with the XRD data showing the appearance of the MoC in NaCl-type structure, which is characterized by a CN of Mo_C of 6. Meanwhile, the CNs of Mo (Mo_Mo) are 8.2 and 8.7 for the 40% and 20% Mo_2C/AC samples, respectively, which are lower than the bulk carbide (10.5). To some extent, the compositions of both 20% and 40% Mo_2C/AC are different from the bulk carbide. That is probably related to the decrease of crystal particle sizes. Additionally, it was reported recently that MgO supported (5%, wt) Mo_2C showed higher CN of Mo-C(O) (CN = 5.1±1.7) than bulk Mo_2C (CN = 3) [284]. It can be expected that the change of carbon contents in the metal lattice or structure of crystals would potentially change the d-electron density states of the solid, and consequently the catalytic properties. Therefore, it could be a potential method to tailor the catalytic properties of carbides by controlling the compositions of carbides by means of changing the crystal sizes such as using smaller molybdenum oxide precursors and loading different amount of oxide precursors on support for carburization.

10.4.2 Comparison of structure and catalytic performance

Here, as an example, we present the data of the bulk and AC supported carbides, 5%, 20%, and 40% (wt; promoted by K_2CO_3) for higher alcohols synthesis from syngas. The CO conversion and the selectivity at steady state conditions of these catalysts are shown in Fig. 10-7.

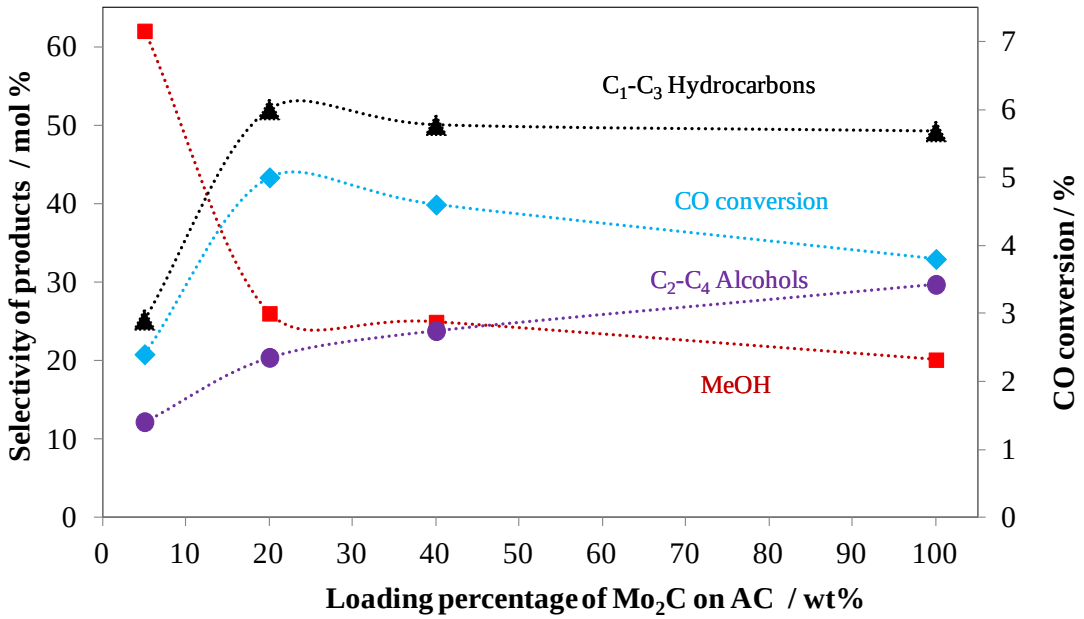

Fig. 10-7 CO conversion and selectivity of products at steady state over catalysts with different loadings of Mo_2C on AC at 100 bar, 250 °C, 5000 h^{-1}, and $H_2/CO = 1$.

As mentioned above the bulk Mo_2C (100 wt % one in Fig. 10-7) suffers from a low specific surface area, which results in low activity in CO hydrogenation [8]. However, the activity can be improved by loading carbides on active carbon, for example the 20% Mo_2C/AC exhibiting 32% higher CO conversion than bulk carbide, which even has 5 times higher weight of Mo. The selectivity of higher alcohols increases with increasing of Mo_2C loading on AC and reaches a maximum when using bulk molybdenum carbide, while selectivity of methanol and hydrocarbon decreases with increasing the Mo_2C load on AC. The effect of the Mo_2C loading on the selectivity could be related to the structure/composition of the supported carbide clusters, where the CNs of Mo_C and Mo_Mo are different from the CN's for the bulk carbide and this may be part of the explanations of the loading effect. It would therefore be of great interests to do theoretical and more experimental studies to further the fundamental understanding of the effect of structure/composition of carbides to their catalytic properties.

As mentioned above the preparation procedures of Mo_2C such as carburization temperature and final isotherm time are very important for the catalytic properties of carbides. The carburization temperatures for Mo_2C were reported sometimes in a relatively lower range from 590-750 °C [8, 425, 430, 432, 435-437] and sometimes at even higher temperatures 900-1100 °C [419, 438]. However, it seems that most of current literature-used temperatures for carburization are too high compared to what we observed for bulk Mo_2C (550 °C) with a relatively big particle, 22 nm. Higher carburization temperature would not only cause bigger particle size [405], but also the formation of carbon residue on the surface, which blocks the pores, covers the active sites and is difficult to remove [405, 430, 439]. For the Mo_2C with smaller particle size at around 9 nm and 2 nm the carburization temperatures decreases to about 500 °C and 320 °C, respectively. It would be expected that there would be a great benefit to lower the carburization temperature for preparing Mo_2C with smaller particles and lower carbon formation on the surface, which will potentially improve the catalytic activity for various reactions for example the higher alcohol synthesis, which activity is typically limited by the surface area of Mo_2C [8, 199]. Moreover, the decreasing of carburization temperature to less than 500 °C or even 400 °C would offer more possibilities for preparing Mo_2C directly in a plant reactor and to avoid an additional passivation process, which will potentially change the performance of catalysts. The passivated Mo_2C (in 1 vol % O_2/N_2) was reported recently with a decrease of activity about 40% compared a nonpassivated Mo_2C sample for Fischer-Tropsch synthesis [205]. These benefits would be applicable for the other reactions regarding the application of Mo_2C such as hydrogenation of benzene, hydrogenolysis of alkanes, steam reforming, water-gas shift, and alkane isomerization, which are very attractive processes for industries.

10.5 Conclusion

We have found the structure of catalysts that have been transformed into carbides and exposed to air after passivation in 1 vol % O_2/N_2 for 6 h, demonstrating the significant re-oxidation and the need for in situ studies. We have combined in situ XAS with XRD are shown to follow directly carburization process on formation of bulk and supported molybdenum carbide (20% and 40% Mo_2C on active carbon). We have identified that the bulk Mo_2C prepared by the way as previously described is most likely to adopt an orthorhombic structure (α-Mo_2C). A two-step mechanism is discovered during the in situ

carburization process, composed of the initial reduction of Mo(VI) oxide to Mo(IV) oxide and a succeeding conversion to carbide. The carburization temperature is somewhat determined by crystal sizes. A decrease on particle size can initiate the onset of carburization at a lower temperature. The catalytic behavior of bulk molybdenum carbide is different from what observed for support carbides, which could be due to the change of the structure/composition of molybdenum carbide clusters.

11 Conclusion

In this work, an experimental catalyst screening based on input from theoretical predictions has been applied to develop catalysts for methanol synthesis from syngas. Cu-Ni alloys of different composition have been identified as potential candidates for methanol synthesis. The Cu-Ni alloy catalysts have been synthesized and tested in a fixed-bed continuous-flow reactor for CO hydrogenation. The metal area based activity for a Cu-Ni/SiO_2 catalyst is at the same level as a Cu/ZnO/Al_2O_3 model catalyst. The high activity and selectivity of silica supported Cu-Ni alloy catalyst agrees with the fact that the DFT calculations identified Cu-Ni alloy catalyst as highly active and selective catalysts for the hydrogenation of CO to methanol.

This work has also provided a systematic study of Cu-Ni catalysts for methanol synthesis from syngas. We have studied the influence of 1) the support using carbon nanotubes, ZrO_2, SiO_2 and γ-Al_2O_3; 2) the pretreatment of catalysts; 3) the operating conditions, e.g. temperature and CO_2 co-feeding; 4) the Cu/Ni ratio; 5) catalyst preparation methods such as incipient wetness impregnation, co-precipitation or deposition-co-precipitation. In addition, various in situ characterization techniques such as XAS, XRD, TEM and FTIR together with DFT calculations have been applied for understanding the structure-activity relationships of Cu-Ni catalysts at simulated reaction conditions. The following conclusions can be drawn:

i. CO hydrogenation has been investigated over Cu-Ni supported on different carriers (SiO_2, CNT, ZrO_2 and γ-Al_2O_3). All supported Cu-Ni catalysts display major differences in product selectivity. However, the metal area based activities of all supported Cu-Ni catalysts are in the same level. It has been found that the SiO_2 and CNT supported catalysts show a very high selectivity to methanol – around 99 mol % and low selectivity to hydrocarbons (< 0.5 mol %) at all temperatures tested. The area-based activity of CO on the Cu-Ni/CNT and the Cu-Ni/SiO_2 catalysts is comparable to the model Cu/ZnO/Al_2O_3 catalyst. The other supports tested, γ-Al_2O_3 and ZrO_2, influenced the Cu-Ni alloy selectivity strongly by making more by-products (hydrocarbons and DME) than methanol. In particular, the γ-Al_2O_3 supported catalyst contains a significant amount of acid sites (333 μmol g^{-1}) and produces predominantly DME, which is probably due to the dehydration of methanol produced initially by the Cu-Ni alloys. The ZrO_2 supported catalyst also contains a high amount of acid sites (309 μmol g^{-1}), however, it produces largely hydrocarbons above 275 °C. It is likely that the support, ZrO_2, further converts the produced methanol and DME into hydrocarbons. The difference in selectivity is mainly related to subsequent reactions of methanol over the support.

ii. Cu-Ni/SiO_2 catalysts have been prepared with different calcination and reduction procedures and tested in the synthesis of methanol from H_2/CO. Calcination of the impregnated catalyst leads to a broader particle size distribution and bigger particles compared to that of direct reduced impregnated catalyst. By reducing impregnated Cu-Ni catalyst in a more dilute H_2 gas (2 mol % H_2/N_2, compared to the same catalyst reduced at 20 mol % H_2/N_2) the amount of Cu particles that segregate from the Cu-Ni particles could be decreased. In addition the Cu and Cu-

Ni particle sizes are smaller. Consequently, this increases the overall productivity of methanol.

iii. Addition of 3 mol % CO_2 to the H_2/CO leads to a significant loss of activity for the Cu-Ni/SiO_2 catalyst contrary to the case for the Cu/ZnO/Al_2O_3 catalyst. DFT calculations show in accordance with previous surface science studies that oxygen on the surface (one of the intermediates from water gas shift reaction) could lead to an enrichment of the Ni-content in the surface. Co-fed CO_2 in the syngas should result in an increased oxidative potential of the feed, and this could cause a change of the surface composition and hence the catalytic performance.

iv. Silica supported bimetallic Cu-Ni catalysts with different ratios of Cu to Ni have been prepared by impregnation. In situ reduction of Cu-Ni alloys with combined synchrotron XRD and XAS reveal a strong interaction between Cu and Ni, resulting in improved reducibility as compared to monometallic Ni. At high Ni concentrations, silica supported Cu-Ni alloys form a homogeneous solid solution of Cu and Ni, whereas at lower nickel contents copper and nickel are separately aggregated and form metallic Cu and Cu-Ni alloy phases. At the same reduction conditions, the particle sizes of reduced Cu-Ni alloys decrease with increasing in Ni content. The activity tests of Cu-Ni alloys for high pressure CO hydrogenation show that all Cu-Ni alloys produce mainly methanol regardless of the Cu/Ni ratio. The Cu-Ni alloy catalysts show similarities in the selectivity, which is mainly towards methanol (~99 mol %), while exhibiting differences in methanol productivity. The methanol productivity reaches a maximum in the molar ratio of around 1. One possibility is that the determining surface structure is similar for all Cu-Ni alloys, but the number of active sites varies with respect to the ratio of Cu to Ni.

v. Silica supported Cu-Ni alloy catalysts have been prepared via impregnation, co-precipitation, and deposition-co-precipitation methods and tested for methanol synthesis. It is found that co-precipitation and deposition-co-precipitation methods are more efficient than the impregnation method for preparation of small and homogeneous Cu-Ni alloy nanoparticles. The selectivity towards methanol is always higher than 99 mol %, and the area-based methanol formation rate over these catalysts are at the same level regardless of the preparation method. The methanol productivity increases in the order of impregnation < co-precipitation < deposition-co-precipitation. The increase in activity is caused predominantly by a decrease in particle size of the active metal alloy particles. A maximum methanol productivity of 0.66 kg kg_{cat}^{-1} h^{-1} with selectivity up to 99.2 mol % has been achieved for a Cu-Ni/SiO_2 catalyst prepared by the deposition-co-precipitation method.

vi. For all tested silica supported Cu-Ni catalysts, there is no apparent catalyst deactivation observed during the tested time on stream (40-100 h), contrary to the observation for the industrial Cu/ZnO/Al_2O_3 catalyst.

For higher alcohol synthesis, the main work has been done on CO hydrogenation over supported Mo_2C. The catalytic activity for higher alcohol synthesis of potassium promoted Mo_2C supported on different materials such as active carbon, carbon

nanotubes, and titanium dioxide is significantly affected by the nature of the support. TiO_2 seems to be a promising support due to its better selectivity to higher alcohols. However, the thermal stability of TiO_2 limited its application as a support for carbides due to high carburization temperature (750 °C) employed in these investigations. Carbon nanotubes supported carbides produce mainly methanol and hydrocarbons. Active carbon supported Mo_2C shows improvement in both the activity and selectivity to alcohols compared to the bulk carbide. The K_2CO_3 promoter plays an essential role in obtaining alcohols rather than hydrocarbons (unpromoted active carbon supported Mo_2C produces predominantly hydrocarbons). The optimum selectivity towards higher alcohols and to alcohols in general is obtained at a K/Mo molar ratio of 0.21 over the 20 wt % Mo_2C on active carbon. The optimum K level is higher than for the bulk carbide (K/Mo=0.14) which is likely because the support material dilutes the promoter contents on the carbide. The selectivity to higher alcohols increases with increasing the Mo_2C loading on active carbon (at fixed K/Mo=0.14) and reaches a maximum over bulk carbides, while the selectivity to methanol follows the opposite trend. This effect of the Mo_2C loading on the selectivity could be related to the loadings of K_2CO_3 on the active Mo_2C phase and the size, structure and composition of the supported carbide clusters.

Finally, combined in situ XAS and XRD have been used to follow directly the carburization process and formation of bulk and supported molybdenum carbides (20 wt % and 40 wt % Mo_2C on active carbon). The bulk Mo_2C prepared by temperature programmed carburization in flow of 20 mol % CH_4 in H_2 is most likely to adopt an orthorhombic structure (α-Mo_2C). A two-step mechanism is discovered during the in situ carburization process, composed of the initial reduction of Mo(VI) oxide to Mo(IV) oxide followed by a succeeding conversion to carbide. The necessary carburization temperature is to a significant extent determined by the crystal sizes. A decrease on particle size can initiate the onset of carburization at a lower temperature.

12 Future work

Regarding methanol synthesis, the stability of the industrial $Cu/ZnO/Al_2O_3$ methanol synthesis catalysts is still an important issue to tackle in future. In CO hydrogenation Cu-Ni alloy catalysts show similar activity and selectivity for methanol synthesis when compared to the industrial catalyst. From the preliminary in situ XRD studies on accelerated aging at high temperature (400 °C), it was observed that Cu-Ni alloy catalysts show a higher resistance towards sintering compared to the commercial $Cu/ZnO/Al_2O_3$ catalysts (see the appendix G). However, activity studies of the aged catalysts have not been carried out yet, and the stability of Cu-Ni catalysts needs to be further investigated under reaction conditions.

Ni and CO could form volatile $Ni(CO)_4$ carbonyl. However, its influence has neither been studied in the present work nor in the literature on CO hydrogenation over Cu-Ni catalysts and it remains unknown whether Ni may be removed with the effluent gas stream. Nevertheless, it would be important to determine in more detail, whether there is any Ni loss as the carbonyl, for example, by measuring the Ni contents in both fresh and spent catalysts.

Catalyst preparation methods have a significant influence on the activity of the catalysts. Cu-Ni catalysts prepared by deposition-co-precipitation, for example, exhibits about 3 times higher methanol productivity compared to similar catalysts prepared by the incipient wetness impregnation method. The studies on the effect of preparation conditions have all been carried out using SiO_2 as carrier, but the screening studies showed that carbon nanotubes lead to even more active catalysts, and this should be explored further in order to come even closer to the activity of the industrial catalyst. In addition, at this moment only 20 wt % loading of Cu+Ni was used, and the methanol productivity (0.66 kg L^{-1} h^{-1}) is close to the industrial required catalyst yield (1.0 kg L^{-1} h^{-1}). Therefore, increasing the loading of Cu-Ni (to 30-50 wt %) on the carbon nanotubes could be a potential way to increase the productivity of methanol.

Regarding higher alcohol synthesis, firstly, based on DFT calculations Cu-Ni has been proposed to be active for higher alcohol synthesis as well. Therefore, promoters such as K and Cs could be added to the Cu-Ni system (K and Cs to some extent can promote industrial $Cu/ZnO/Al_2O_3$ catalysts for higher alcohol synthesis). Secondly, alkali modified bulk molybdenum carbide was shown to produce ethanol as the main alcohol product. However, bulk Mo_2C suffers from a low specific surface area, partly due to the high carburization temperature (up to 750 °C). Based on in situ XAS and XRD analyses it was found that a decrease in the particle size of MoO_3 can initiate the onset of carburization at a lower temperature. It seems that most of current literature used temperatures for carburization (about 750 °C) that are too high compared to the required temperature for bulk Mo_2C (550 °C) from relatively large MoO_3 particles of 22 nm. From these new studies one can expect a great benefit from lowering the carburization temperature for preparing Mo_2C with smaller particles. This should potentially improve the catalytic activity for higher alcohol synthesis but also in other applications where carbides have been found beneficial, e.g., hydrogenation, hydrogenolysis, steam reforming or water gas shift reactions.

13 References

[1] M. Tsoskounoglou, G. Ayerides, E. Tritopoulou, Energy Policy 36 (2008) 3797.
[2] M. Asif, T. Muneer, Renew. Sustain. Energy Rev. 11 (2007) 1388.
[3] R. Quadrelli, S. Peterson, Energy Policy 35 (2007) 5938.
[4] G. Marland, T.A. Boden, R. Andres, Global, Regional, and National Fossil-Fuel CO_2 Emissions, Carbon Dioxide Information Analysis Center, Oak Ridge, 2010.
[5] CASE, http://www.case.dtu.dk/English/About%20CASE.aspx, 12/2012 (2012) .
[6] F. Studt, F. Abild-Pedersen, Q. Wu, A.D. Jensen, B. Temel, J.D. Grunwaldt, J.K. Nørskov, J. Catal. 293 (2012) 51.
[7] J.K. Nørskov, F. Abild-Pedersen, F. Studt, T. Bligaard, Proc. Natl. Acad. Sci. 108 (2011) 937.
[8] J.M. Christensen, L.D.L. Duchstein, J.B. Wagner, P.A. Jensen, B. Temel, A.D. Jensen, Ind. Eng. Chem. Res. 51 (2012) 4161.
[9] T.M.H. Arndal, L. Jensen, Synthesis of higher alcohols from syngas using carbon nanotube supported catalysts, Bachelor Thesis, Technical University of Denmark, (2011).
[10] D. Sutton, B. Kelleher, J.R.H. Ross, Fuel Process Technol. 73 (2001) 155.
[11] J. Rostrup-Nielsen, L.J. Christiansen, Concepts in syngas manufacture, World Scientific, London, UK, 2011.
[12] J.R. Rostrup-Nielsen, Catal. Rev., Sci. Eng. 46 (2004) 247.
[13] J.R. Rostrup-Nielsen, Catal. Today 71 (2002) 243.
[14] J.R. Rostrup-Nielsen, Catal. Today 63 (2000) 159.
[15] J.R. Rostrup-Nielsen, Catal.Today 18 (1993) 305.
[16] S. Velu, K. Suzuki, S. Hashimoto, N. Satoh, F. Ohashi, S. Tomura, J. Mater. Chem. 11 (2001) 2049.
[17] I. Wender, Fuel. Process. Technol. 48 (1996) 189.
[18] R.G. Herman, Stud. Surf. Sci. Catal.64 (1991) 265.
[19] R.G. Herman, Catal. Today 55 (2000) 233.
[20] M. Gupta, M. Smith, J.J. Spivey, ACS Catal. 1 (2011) 641.
[21] J.J. Spivey, A. Egbebi, Chem. Soc. Rev. 36 (2007) 1514.
[22] K. Waugh, Catal. Lett. 142 (2012) 1153.
[23] K. Waugh, Catal. Today 15 (1992) 51.
[24] J.B. Hansen, P.E.H. Nielsen, in: G. Ertl, H. Knözinger and F. Schüth (Eds.), Handbook of Heterogeneous Catalysis, Wiley-VCH, Weinheim, 2008, p. 2920.
[25] E. Supp, R. Quinkler, in: R. Meyers (Ed.), Handbook of Synfuels Technology, McGraw-Hill, New York, 1984, p. 2.
[26] Alcoholic fuels, CRC Taylor & Francis, NY, USA, 2006.
[27] V. Subramani, S.K. Gangwal, Energy Fuels 22 (2008) 814.
[28] K. Fang, D. Li, M. Lin, M. Xiang, W. Wei, Y. Sun, Catal. Today 147 (2009) 133.
[29] S. Zaman, K.J. Smith, Catal. Rev., Sci. Eng. 54 (2012) 41.
[30] P. Forzatti, E. Tronconi, I. Pasquon, Catal. Rev. , Sci. Eng. 33 (1991) 109.
[31] W.H. Chen, Methanol production and use, CRC, NY, USA, 1994.
[32] S. Lee, Methanol synthesis technology, CRC Press, 1989.
[33] J.P. Hindermann, G.J. Hutchings, A. Kiennemann, Catal. Rev., Sci. Eng. 35 (1993) 1.

[34] J.L.G. Fierro, Catal. Lett. 22 (1993) 67.
[35] L. Wang, D. Li, M. Koike, S. Koso, Y. Nakagawa, Y. Xu, K. Tomishige, Appl. Catal. A 392 (2011) 248.
[36] J.R. Rostrup-Nielsen, Science 308 (2005) 1421.
[37] K. Qin, W. Lin, P.A. Jensen, A.D. Jensen, Fuel 93 (2011) 589.
[38] H. Schmieder, J. Abeln, N. Boukis, E. Dinjus, A. Kruse, M. Kluth, G. Petrich, E. Sadri, M. Schacht, J. Supercritical Fluids 17 (2000) 145.
[39] S. Turn, C. Kinoshita, Z. Zhang, D. Ishimura, J. Zhou, Int. J. Hydrogen Energy 23 (1998) 641.
[40] A. Lapidus, A. Krylova, Y. Paushkin, J. Rathouský, A. Zukal, J. Stárek, Fuel 73 (1994) 583.
[41] K. Qin, P.A. Jensen, W. Lin, A.D. Jensen, Energy Fuels 26 (2012) 5992.
[42] N. Berkowitz, The chemistry of coal, Elsevier Science Pub. Inc., New York, 1985.
[43] H. Watanabe, M. Otaka, Fuel 85 (2006) 1935.
[44] L.D. Smoot, P.J. Smith, Coal combustion and gasification, Plenum Press, New York, 1985.
[45] A.W.J. Grupping, Patent US Patent 4,243,101 (1981).
[46] P.L. Spath, D.C. Dayton, A925634 (2003).
[47] G.A. Olah, Catal. Lett. 93 (2004) 1.
[48] J.H. Kim, M.J. Park, S.J. Kim, O.S. Joo, K.D. Jung, Appl. Catal. A 264 (2004) 37.
[49] I. Wender, Catal. Rev., Sci. Eng. 26 (1984) 303.
[50] G.A. Olah, A. Goeppert, G.K.S. Prakash, Beyond oil and gas: the methanol economy, Wiley-VCH, Weinheim, 2006.
[51] J.L. Keller, Alcohols as motor fuel?, Hydrocarbon Proc, 1979, p. 127.
[52] A. Blum, T. Duvdevani, M. Philosoph, N. Rudoy, E. Peled, J. Power Sources 117 (2003) 22.
[53] B. Emonts, J. Bøgild Hansen, S. Lœgsgaard Jørgensen, B. Höhlein, R. Peters, J. Power Sources 71 (1998) 288.
[54] G.K.S. Prakash, G.A. Olah, M.C. Smart, S.R. Narayanan, Q.J. Wang, S. Surumpudi, G. Halpert, US patent 6,444,343 B1 (2002).
[55] W. Wang, Y. Jiang, M. Hunger, Catal.Today 113 (2006) 102.
[56] W. Wang, A. Buchholz, M. Seiler, M. Hunger, J. Am. Chem. Soc. 125 (2003) 15260.
[57] G.A. Olah, Angew. Chem. Int. Ed. 44 (2005) 2636.
[58] C. Lormand, Ind. Eng. Chem. 17 (1925) 430.
[59] P.K. Frolich, M. Fenske, D. Quiggle, Ind. Eng. Chem. 20 (1928) 694.
[60] P. Frolich, D. Cryder, Ind. Eng. Chem. 22 (1930) 1051.
[61] P. Tijm, F. Waller, D. Brown, Appl. Catal. A 221 (2001) 275.
[62] A. Pinto, US patent 4238403 (1980).
[63] A.J. Connell, A. Pinto, US patent 3,940,428 (1976).
[64] H.H. Kung, Catal.Today 11 (1992) 443.
[65] G.W. Roberts, D.M. Brown, T.H. Hsiung, J.J. Lewnard, Ind. Eng. Chem. Res. 32 (1993) 1610.
[66] J.T. Sun, I.S. Metcalfe, M. Sahibzada, Ind. Eng. Chem. Res. 38 (1999) 3868.
[67] J. Nunan, K. Klier, C.W. Young, P.B. Himelfarb, R.G. Herman, J.Chem.Soc., Chem. Commun. (1986) 193.

[68] E.G. Baglin, G.B. Atkinson, L.J. Nicks, Ind. Eng. Chem. Prod. Res. Dev. 20 (1981) 87.
[69] Y. Amenomiya, Appl. Catal.30 (1987) 57.
[70] M. Shibata, Y. Ohbayashi, N. Kawata, T. Masumoto, K. Aoki, J. Catal. 96 (1985) 296.
[71] S.J. Bryan, J.R. Jennings, S.J. Kipling, G. Owen, R.M. Lambert, R.M. Nix, Appl. Catal. 40 (1988) 173.
[72] J. Li, W. Zhang, L. Gao, P. Gu, K. Sha, H. Wan, Appl. Catal. A 165 (1997) 411.
[73] A. Ota, E.L. Kunkes, I. Kasatkin, E. Groppo, D. Ferri, B. Poceiro, R.M. Navarro Yerga, M. Behrens, J. Catal. 293 (2012) 27.
[74] Y.A. Ryndin, R. Hicks, A. Bell, Y.I. Yermakov, J. Catal. 70 (1981) 287.
[75] F. Daly, J. Catal. 89 (1984) 131.
[76] G. Owen, C.M. Hawkes, D. Lloyd, J.R. Jennings, R.M. Lambert, R.M. Nix, Appl. Catal. 33 (1987) 405.
[77] B. Pommier, S.J. Teichner, in: Anonymous , SJ Teichner in MJ Phillips, M. Ternan, Proc. 9th Int. Congr. Catal, 1988, p. 610.
[78] M. Poutsma, L. Elek, P. Ibaria, A. Risch, J. Rabo, J. Catal. 52 (1978) 157.
[79] S. Ali, J. Goodwin, J. Catal. 176 (1998) 3.
[80] A. Gotti, R. Prins, J. Catal. 175 (1998) 302.
[81] J. Driessen, E. Poels, J. Hindermann, V. Ponec, J. Catal. 82 (1983) 26.
[82] Y. Kikuzono, S. Kagami, S. Naito, T. Onishi, K. Tamaru, Faraday Discuss. Chem. Soc. 72 (1981) 135.
[83] X. Li, L. Feng, Z. Liu, B. Zhong, D.B. Dadyburjor, E.L. Kugler, Ind. Eng. Chem. Res. 37 (1998) 3853.
[84] Z. Li, Y. Fu, J. Bao, M. Jiang, T. Hu, T. Liu, Y. Xie, Appl. Catal. A 220 (2001) 21.
[85] D. Li, C. Yang, W. Li, Y. Sun, B. Zhong, Top. Catal. 32 (2005) 233.
[86] H. Qi, D. Li, C. Yang, Y. Ma, W. Li, Y. Sun, B. Zhong, Catal. Commun. 4 (2003) 339.
[87] D. Li, N. Zhao, H. Qi, W. Li, Y. Sun, B. Zhong, Catal. Commun. 6 (2005) 674.
[88] S. Vukojević, O. Trapp, J.D. Grunwaldt, C. Kiener, F. Schüth, Angew. Chem. 117 (2005) 8192.
[89] M. Marchionna, L. Basini, A. Aragno, M. Lami, F. Ancillotti, J. Mol. Catal. 75 (1992) 147.
[90] J.S. Bradley, J. Am. Chem. Soc. 101 (1979) 7419.
[91] K. Li, D. Jiang, J. Mol. Catal. A 147 (1999) 125.
[92] H.H. Kung, Catal. Rev. Sci. Eng. 22 (1980) 235.
[93] J. Rathke, H.M. Feder, J. Am. Chem. Soc. 100 (1978) 3623.
[94] E.K. Poels, E.H. van Broekhoven, W.A.A. van Barneveld, V. Ponec, React. Kinet. Catal. Lett 18 (1981) 221.
[95] M. Saito, R. Anderson, J. Catal. 63 (1980) 438.
[96] J.M. Christensen, P.A. Jensen, A. Jensen, Ind. Eng. Chem. Res. 50 (2011) 7949.
[97] H. Chen, J. Lin, K. Tan, J. Li, Appl. Surf. Sci. 126 (1998) 323.
[98] Q. Wu, F. Studt, L.D.L. Duchstein, J.M. Christensen, J.B. Wagner, B. Temel, J.D. Grunwaldt, A.D. Jensen, in preparation.
[99] W.S. Epling, G. B Hoflund, D.M. Minahan, Appl. Catal. A 183 (1999) 335.
[100] M.C. Molstad, B.F. Dodge, Ind. Eng. Chem. 27 (1935) 134.

[101] D.S. Cryder, P.K. Frolich, Ind. Eng. Chem. 21 (1929) 867.
[102] M. Behrens, F. Studt, I. Kasatkin, S. Kuehl, M. Haevecker, F. Abild-Pedersen, S. Zander, F. Girgsdies, P. Kurr, B.L. Kniep, M. Tovar, R.W. Fischer, J.K. Nørskov, R. Schlögl, Science 336 (2012) 893.
[103] J. Nakamura, Y. Choi, T. Fujitani, Top. Catal. 22 (2003) 277.
[104] T. Fujitani, J. Nakamura, Appl. Catal. A 191 (2000) 111.
[105] J. Nakamura, I. Nakamura, T. Uchijima, Y. Kanai, T. Watanabe, M. Saito, T. Fujitani, J. Catal. 160 (1996) 65.
[106] J. Nakamura, T. Uchijima, Y. Kanai, T. Fujitani, Catal. Today 28 (1996) 223.
[107] I. Kasatkin, P. Kurr, B. Kniep, A. Trunschke, R. Schlögl, Angew. Chem. Int. Ed. 46 (2007) 7324.
[108] T. Askgaard, J. Nørskov, C. Ovesen, P. Stoltze, J. Catal. 156 (1995) 229.
[109] H. Topsøe, C. Ovesen, B. Clausen, N.Y. Topsøe, P. Højlund Nielsen, E. Törnqvist, J. Nørskov, Stud. Surf. Sci. Catal. 109 (1997) 121.
[110] C. Ovesen, B. Clausen, J. Schiøtz, P. Stoltze, H. Topsøe, J.K. Nørskov, J. Catal. 168 (1997) 133.
[111] R. Herman, K. Klier, G. Simmons, B. Finn, J.B. Bulko, T. Kobylinski, J. Catal. 56 (1979) 407.
[112] J. Frost, Nature 334 (1988) 577.
[113] W. Lewis, P.K. Frolich, Ind. Eng. Chem. 20 (1928) 285.
[114] M. Fenske, P.K. Frolich, Ind. Eng. Chem. 21 (1929) 1052.
[115] M. Behrens, J. Catal. 267 (2009) 24.
[116] J.S. Campbell, Ind. Eng. Chem. Process. Des. Dev 9 (1970) 588.
[117] M. Kurtz, H. Wilmer, T. Genger, O. Hinrichsen, M. Muhler, Catal. Lett. 86 (2003) 77.
[118] G.C. Chinchen, P.J. Denny, D.G. Parker, M.S. Spencer, D.A. Whan, Appl. Catal. 30 (1987) 333.
[119] K. Klier, V. Chatikavanij, R.G. Herman, G.W. Simmons, J. Catal. 74 (1982) 343.
[120] S. Lee, J.G. Speight, S.K. Loyalka, Handbook of alternative fuel technologies, CRC Tayler & Francis, NY, USA, 2007.
[121] Y.B. Kagan, G.I. Lin, A.Y. Rozovskii, Kinet. Catal. 17 (1976) 380.
[122] Y.B. Kagan, L. Liberov, E. Slivinskii, S. Loktev, G. Lin, A. Rozovskii, A. Bashkirov, Dokl. Akad. Nauk SSSR 221 (1975) 1093.
[123] Y.B. Kagan, A.Y. Rozovskii, G.I. Lin, E.V. Slivinskii, S.M. Loktev, L.G. Liberov, A.N. Bashkirov, Kinet. Catal. 16 (1975) 704.
[124] Y.B. Kagan, A.Y. Rozovskii, L. Liberov, S. Loktev, E. Slivinskii, in: Anonymous , G. 1. Lin, and AN Bashkirov, Dokl. Akad. Nauk SSSR, 1975, p. 1093.
[125] G.C. Chinchen, P.J. Denny, D.G. Parker, G.D. Short, M.S.W. Spencer K.C., D.A. Whan, Prepr. Am. Chem. Soc, Div. Fuel Chem. 29 (1984) 178.
[126] L. Grabow, M. Mavrikakis, ACS Catal. 1 (2011) 365.
[127] P. Rasmussen, P. Holmblad, T. Askgaard, C. Ovesen, P. Stoltze, J. Nørskov, I. Chorkendorff, Catal. Lett. 26 (1994) 373.
[128] P. Rasmussen, M. Kazuta, I. Chorkendorff, Surf. Sci. 318 (1994) 267.
[129] C. Ovesen, P. Stoltze, J. Nørskov, C. Campbell, J. Catal. 134 (1992) 445.
[130] J.B. Hansen, AlchE Spring National Meeting, Orlando, Fl, 1990.

[131] D.B. Rasmussen, T.V.W. Janssens, B. Temel, T. Bligaard, B. Hinnemann, S. Helveg, J. Sehested, J. Catal. (2012).
[132] G. Chinchen, P. Denny, J. Jennings, M. Spencer, K. Waugh, Appl. Catal. 36 (1988) 1.
[133] G. Chinchen, K. Mansfield, M. Spencer, Chem. Tech. 20 (1990) 692.
[134] J.D. Grunwaldt, A.M. Molenbroek, N.Y. Topsøe, H. Topsøe, B.S. Clausen, J. Catal. 194 (2000) 452.
[135] M.V. Twigg, M.S. Spencer, Topics Catal. 22 (2003) 191.
[136] B.J. Wood, W.E. Isakson, H. Wise, Ind. Eng. Chem. Prod. Res. Dev. 19 (1980) 197.
[137] K. Klier, R. Herman, Study of the deactivation of methanol synthesis catalysts. Final report EPRI-AF-694 (1978) .
[138] G. Roberts, D. Brown, T. Hsiung, J. Lewnard, Chem. Eng. Sci. 45 (1990) 2713.
[139] R.B. Anderson (Ed.), The Fischer-Tropsch synthesis, New York, 1984.
[140] H. Schulz, Appl. Catal. A 186 (1999) 3.
[141] M.E. Dry, J. Chem. Technol. Biotechnol. 77 (2002) 43.
[142] P. Forzatti, L. Lietti, Catal. Today 52 (1999) 165.
[143] J. Goldemberg, Science 315 (2007) 808.
[144] C.M. Fougret, W.F. Hölderich, Appl. Catal. A 207 (2001) 295.
[145] N. Kosaric, D. Ng, I. Russell, G. Stewart, Adv. Appl. Microbiol. 26 (1980) 147.
[146] M.A. Stadtherr, D.F. Rudd, Chem. Eng. Sci. 31 (1976) 1019.
[147] P.J. Crutzen, A.R. Mosier, K.A. Smith, W. Winiwarter, Atoms. Chem. Phys 389 (2008) 389.
[148] A. Sugier, E. Freund, Patent U.S.Patent 4,122,110 (1978).
[149] A. Sugier, E. Freund, Patent U.S. Patent 4,291,126 (1981).
[150] A. Sugier, E. Freund, J.F. Le Page, Patent U.S. Patent 4,346,179 (1982).
[151] P. Courty, D. Durand, A. Sugier, E. Freund, Patent U.S. Patent 4,659,742 (1987).
[152] P. Courty, D. Durand, A. Forestiere, P. Grandvallet, Patent U.S. Patent 4,675,343 (1987).
[153] P. Courty, P. Chaumette, D. Durand, C. Verdon, Patent U.S. Patent 4,780,481 (1988).
[154] P. Chaumette, P. Courty, D. Durand, P. Grandvallet, C. Travers, Patent U.S. Patent 4,791,141 (1988).
[155] P. Courty, P. Chaumette, C. Raimbault, P. Travers, Oil & Gas Sci.Tech. 45 (1990) 561.
[156] Institute of Coal Chemistry, Chinese Academy of Science, http://www.articlesnatch.com/Article/Mixed-Alcohol-Synthesis-Syngas-Successful-Pilot/1990561, access to 12/2012 (2011) .
[157] P.E.H. Nielsen, B. Temel, P. Beato, WO2012003901, (2012).
[158] A. Beretta, Q. Sun, R.G. Herman, K. Klier, J. Chem. Soc. , Chem. Commun. 1995 (1995) 2525.
[159] A. Beretta, Q. Sun, R.G. Herman, K. Klier, Ind. Eng. Chem. Res. 35 (1996) 1534.
[160] M.M. Burcham, R.G. Herman, K. Klier, Ind. Eng. Chem. Res. 37 (1998) 4657.
[161] G.B. Hoflund, W.S. Epling, D.M. Minahan, Catal. Lett. 45 (1997) 135.
[162] W.S. Epling, G.B. Hoflund, W.M. Hart, D.M. Minahan, J. Catal. 169 (1997) 438.
[163] D.M. Minahan, W.S. Epling, G.B. Hoflund, Catal. Lett. 50 (1998) 199.

[164] D.M. Minahan, W.S. Epling, G.B. Hoflund, J. Catal. 179 (1998) 241.
[165] W.S. Epling, G.B. Hoflund, D.M. Minahan, J. Catal. 175 (1998) 175.
[166] G.B. Hoflund, W.S. Epling, D.M. Minahan, Catal. Today 52 (1999) 99.
[167] G.B. Hoflund, W.S. Epling, D.M. Minahan, Catal. Lett. 62 (1999) 169.
[168] J.C. Slaa, J.G. Ommen, J.R.H. Ross, Catal. Today 15 (1992) 129.
[169] B.B. Breman, A. Beenackers, E. Oesterholt, Chem. Eng. Sci. 49 (1994) 4409.
[170] E.M. Calverley, K.T. Smith, J. Catal. 130 (1991) 616.
[171] J.G. Nunan, C.E. Bogdan, K. Klier, K.J. Smith, C.W. Young, R.G. Herman, J. Catal. 116 (1989) 195.
[172] K.J. Smith, R.B. Anderson, Can. J. Civ. Eng. 61 (1983) 40.
[173] L. Majocchi, L. Lietti, A. Beretta, P. Forzatti, E. Micheli, L. Tagliabue, Appl. Catal. A 166 (1998) 393.
[174] N.D. Subramanian, G. Balaji, C.S.S.R. Kumar, J.J. Spivey, Catal. Today 147 (2009) 100.
[175] A.D. de Aquino, A.J. Gomez Cobo, Catal. Today 65 (2001) 209.
[176] G.G. Volkova, T.M. Yurieva, L.M. Plyasova, M.I. Naumova, V.I. Zaikovskii, J. Mol. Catal. A 158 (2000) 389.
[177] G.G. Volkova, T.A. Krieger, L.M. Plyasova, V.A. Zaikovskii, T.M. Yurieva, in: Anonymous , Elsevier Science Ltd, 1997, p. 67.
[178] G.G. Volkova, T.M. Yur'eva, L.M. Plyasova, Kinet. Catal. 36 (1995) 810.
[179] N. Mouaddib, V. Perrichon, G.A. Martin, Appl. Catal. A 118 (1994) 63.
[180] J.A. Dalmon, P. Chaumette, C. Mirodatos, Catal. Today 15 (1992) 101.
[181] J.E. Baker, R. Burch, S.J. Hibble, P.K. Loader, Appl. Catal. 65 (1990) 281.
[182] J.E. Baker, R. Burch, S.E. Golunski, Appl. Catal. 53 (1989) 279.
[183] A. Kiennemann, C. Diagne, J.P. Hindermann, P. Chaumette, P. Courty, Appl. Catal. 53 (1989) 197.
[184] P. Courty, D. Durand, E. Freund, A. Sugier, J. Mol. Catal. 17 (1982) 241.
[185] D.K. Lee, J.H. Lee, S.K. Ihm, Appl. Catal. 36 (1988) 199.
[186] J. Llorca, N. Homs, O. Rossell, M. Seco, J.L.G. Fierro, Ramírez de la Piscina, P., J. Mol. Catal. A 149 (1999) 225.
[187] X.D. Xu, J.J.F. Scholten, D. Mausbeck, Appl. Catal. 82 (1992) 91.
[188] H.B. Zhang, X. Dong, G.D. Lin, X.L. Liang, H.Y. Li, Chem. Commun. 2005 (2005) 5094.
[189] X. Dong, X.L. Liang, H.Y. Li, G.D. Lin, P. Zhang, H.B. Zhang, Catal. Today 147 (2009) 158.
[190] H. Zhang, X. Yang, L. Zhou, Y. Su, Z. Liu, J. Nat. Gas Chem. 18 (2009) 337.
[191] M. Lin, K. Fang, D. Li, Y. Sun, Catal. Commun. 9 (2008) 1869.
[192] J.A. Sibilia, J.M. Dominguez, R.G. Herman, K. Klier, Prepr. Div. Fuel Chem., ACS 29 (1984) 261.
[193] X. Yang, Y. Wei, Y. Su, L. Zhou, Fuel Process. Tech. 91 (2010) 1168.
[194] Y. Lu, F. Yu, J. Hu, J. Liu, Appl. Catal. A 429 (2012) 48.
[195] M. Ding, M. Qiu, J. Liu, Y. Li, T. Wang, L. Ma, C. Wu, Fuel *In press* (2012) .
[196] J.M. Christensen, P.A. Jensen, N.C. Schiødt, A.D. Jensen, ChemCatChem 2 (2010) 523.
[197] J.M. Christensen, P.M. Mortensen, R. Trane, P.A. Jensen, A.D. Jensen, Appl. Catal. A 366 (2009) 29.

[198] H.G. Kim, K.H. Lee, J.S. Lee, Res. Chem. Intermediates 26 (2000) 427.
[199] H.C. Woo, K.Y. Park, Y.G. Kim, Appl. Catal. 75 (1991) 267.
[200] V.R. Surisetty, A. Tavasoli, A. Dalai, Appl. Catal. A 365 (2009) 243.
[201] S.F. Zaman, K.J. Smith, Catal. Today (2011) .
[202] S.F. Zaman, K.J. Smith, Catal. Commun. 10 (2009) 468.
[203] M. Xiang, D. Li, H. Xiao, J. Zhang, H. Qi, W. Li, B. Zhong, Y. Sun, Fuel 87 (2008) 599.
[204] M. Xiang, D. Li, W. Li, B. Zhong, Y. Sun, Catal. Commun. 8 (2007) 513.
[205] H. Shou, D. Ferrari, D.G. Barton, C.W. Jones, R.J. Davis, ACS Catal. 2 (2012) 1408.
[206] M.J. Menart, J.E. Hensley, K.E. Costelow, Appl. Catal. A 437 (2012) 36.
[207] M.A. Haider, M.R. Gogate, R.J. Davis, J. Catal. 261 (2009) 9.
[208] H. Ngo, Y. Liu, K. Murata, Reaction Kinetics, Mech. Catal. 02 (2011) 425.
[209] X. Pan, Z. Fan, W. Chen, Y. Ding, H. Luo, X. Bao, Nature Mater. 6 (2007) 507.
[210] M. Inoue, T. Miyake, T. Inui, Y. Takegami, J. Chem.Soc., Chem. Commun. (1983) 70.
[211] M. Inoue, T. Miyake, Y. Takegami, T. Inui, Appl. Catal. 11 (1984) 103.
[212] H. Hamada, Y. Kuwahara, Y. Kintaichi, T. Ito, K. Wakabayashi, H. Iijima, K.I. SANO, Chem. Lett. (1984) 1611.
[213] M. Komiyama, J. Sato, K. Yamamoto, Y. Ogino, Langmuir 3 (1987) 845.
[214] T. Tsunoda, H. Ogasawara, M. Komiyama, S. Ozawa, Y. Ogino, Chem. Lett. 10 (1981) 819.
[215] G. Lu, T. Hoffer, L. Guczi, Catal. Lett. 14 (1992) 207.
[216] B.K. Warren, B.D. Dombek, J. Catal. 79 (1983) 334.
[217] W. Keim, M. Berger, A. Eisenbeis, J. Kadelka, J. Schlupp, J. Mole. Catal. 13 (1981) 95.
[218] G.A. Mills, Fuel 73 (1994) 1243.
[219] L.E. Cratty Jr, W.W. Russell, J. Am. Chem. Soc. 80 (1958) 767.
[220] J. Nerlov, I. Chorkendorff, Catal. Lett. 54 (1998) 171.
[221] J. Nerlov, I. Chorkendorff, J. Catal. 181 (1999) 271.
[222] J. Nerlov, S. Sckerl, J. Wambach, I. Chorkendorff, Appl. Catal. A 191 (2000) 97.
[223] S. Uchiyama, Y. Obayashi, M. Shibata, T. Uchiyama, N. Kawata, T. Konishi, J. Chem. Soc. , Chem. Commun. 1985 (1985) 1071.
[224] S. Uchiyama, Y. Ohbayashi, T. Hayasaka, N. Kawata, Appl. Catal. 42 (1988) 143.
[225] E.B. Pereira, G.A. Martin, Appl. Catal. A 103 (1993) 291.
[226] P. Sermon, Y. Wang, Stud. Surf. Sci. Catal. 75 (1993) 2773.
[227] J. Llorca, Ramirez de la Piscina, P., N. Homs, E. Brum Pereira, P. Moral, G. Martin, Stud. Surf. Sci. Catal. 107 (1997) 9.
[228] M.A. Fraga, E. Jordão, React. Kinet. Catal. Lett. 64 (1998) 331.
[229] Y.Q. Wang, S.T. Qi, Y. Hou, React. Kinet. Catal. Lett. 70 (2000) 213.
[230] S. Uchiyama, Y. Ohbayashi, T. Hayasaka, N. Kawata, Appl. Catal. 42 (1988) 143.
[231] Y. Wang, S. Qi, Y. Hou, React. Kinet. Catal. Lett. 70 (2000) 213.
[232] C.L. Rasmussen, K.H. Wassard, K. Dam-Johansen, P. Glarborg, Int. J. Chem. Kinet. 40 (2008) 423.
[233] C.L. Rasmussen, A.E. Rasmussen, P. Glarborg, Combust. Flame 154 (2008) 529.
[234] C.L. Rasmussen, J.G. Jakobsen, P. Glarborg, Int. J. Chem. Kinet. 40 (2008) 778.

[235] J.M. Christensen, CHEC Report, Technical University of Denmark (2011).
[236] C.L. Rasmussen, K.H. Wassard, K. Dam-Johansen, P. Glarborg, CHEC Report No. R0604 (2006).
[237] J.M. Christensen, Katalytisk syntese af langkædede alkoholer fra syntesegas, Ph.D.Thesis, Technical University of Denmark, ISBN 9788792481603 (2011).
[238] J. Bart, R. Sneeden, Catal.Today 2 (1987) 1.
[239] R.A. Köppel, C. Stöcker, A. Baiker, J. Catal. 179 (1998) 515.
[240] T. Fujitani, M. Saito, Y. Kanai, M. Takeuchi, K. Moriya, T. Watanabe, M. Kawai, T. Kakumoto, Chem. Lett. 22 (1993) 1079.
[241] J. Wu, M. Saito, H. Mabuse, Catal. Lett. 68 (2000) 55.
[242] P.J. Berlowitz, D.W. Goodman, J. Catal. 108 (1987) 364.
[243] X. Youchang, B. Naasz, G. Somorjai, Appl. Catal. 27 (1986) 233.
[244] F. Abild-Pedersen, J.P. Greeley, F. Studt, J. Rossmeisl, T.R. Fronczek-Munter, P.G. Moses, E. Skulason, T. Bligaard, J.K. Nørskov, Phys. Rev. Lett. 99 (2007) .
[245] V. Pallassana, M. Neurock, J. Catal. 191 (2000) 301.
[246] J.K. Nørskov, T. Bligaard, A. Logadottir, S. Bahn, L.B. Hansen, M. Bollinger, H. Bengaard, B. Hammer, Z. Sljivancanin, M. Mavrikakis, J. Catal. 209 (2002) 275.
[247] A. Michaelides, Z. Liu, C. Zhang, A. Alavi, D.A. King, P. Hu, J. Am. Chem. Soc. 125 (2003) 3704.
[248] T. Bligaard, J.K. Nørskov, S. Dahl, J. Matthiesen, C.H. Christensen, J. Sehested, J. Catal. 224 (2004) 206.
[249] S. Wang, B. Temel, J. Shen, G. Jones, L.C. Grabow, F. Studt, T. Bligaard, F. Abild-Pedersen, C.H. Christensen, J.K. Nørskov, Catal. Lett. 141 (2011) 370.
[250] S. Wang, V. Petzold, V. Tripkovic, J. Kleis, J.G. Howalt, E. Skúlason, E.M. Fernández, B. Hvolbæk, G. Jones, A. Toftelund, Phys. Chem. Chem. Phys. 13 (2011) 20760.
[251] Z.M. Hu, K. Takahashi, H. Nakatsuji, Surf. Sci. 442 (1999) 90.
[252] Y. Yang, J. Evans, J.A. Rodriguez, M.G. White, P. Liu, Phys. Chem. Chem. Phys. 12 (2010) 9909.
[253] M.M. Günter, T. Ressler, B. Bems, C. Büscher, T. Genger, O. Hinrichsen, M. Muhler, R. Schlögl, Catal. Lett. 71 (2001) 37.
[254] W.J. Durand, A.A. Peterson, F. Studt, F. Abild-Pedersen, J.K. Nørskov, Surf. Sci. 605 (2011) 1354.
[255] E. Shustorovich, A.T. Bell, Surf. Sci. 205 (1988) 492.
[256] L.C. Grabow, F. Studt, F. Abild-Pedersen, V. Petzold, J. Kleis, T. Bligaard, J.K. Nørskov, Angew. Chem. Int. Ed. 50 (2011) 4601.
[257] G. Jones, J.G. Jakobsen, S.S. Shim, J. Kleis, M.P. Andersson, J. Rossmeisl, F. Abild-Pedersen, T. Bligaard, S. Helveg, B. Hinnemann, J. Catal. 259 (2008) 147.
[258] H. Falsig, B. Hvolbæk, I.S. Kristensen, T. Jiang, T. Bligaard, C.H. Christensen, J.K. Nørskov, Angew. Chem. Int. Ed. 47 (2008) 4835.
[259] F. Studt, F. Abild-Pedersen, T. Bligaard, R.Z. Sørensen, C.H. Christensen, J.K. Nørskov, Science 320 (2008) 1320.
[260] M.P. Andersson, T. Bligaard, A. Kustov, K.E. Larsen, J. Greeley, T. Johannessen, C.H. Christensen, J.K. Nørskov, J. Catal. 239 (2006) 501.
[261] J. Greeley, I. Stephens, A. Bondarenko, T.P. Johansson, H.A. Hansen, T. Jaramillo, J. Rossmeisl, I. Chorkendorff, J.K. Nørskov, Nature Chem. 1 (2009) 552.

[262] G. Jones, F. Studt, F. Abild-Pedersen, J.K. Nørskov, T. Bligaard, Chem. Eng. Sci. 66 (2011) 6318.
[263] L.C. Grabow, B. Hvolbæk, J.K. Nørskov, Top. Catal. 53 (2010) 298.
[264] A.R. Denton, N.W. Ashcroft, Phys. Rev. A 43 (1991) 3161.
[265] H. Okamoto, Desk handbook: phase diagrams for binary alloys, Asm Intl, 2000.
[266] M. Araki, V. Ponec, J. Catal. 44 (1976) 439.
[267] T. Van Herwijnen, W.A. De Jong, J. Catal. 34 (1974) 209.
[268] K.J. Andersson, F. Calle-Vallejo, J. Rossmeisl, I. Chorkendorff, J. Am. Chem. Soc. 131 (2009) 2404.
[269] The Dacapo plane wave/pseudopotential code is available as open source software at, 2012 (2010) .
[270] D. Vanderbilt, Phy. Rev. B 41 (1990) 7892.
[271] B. Hammer, L.B. Hansen, J.K. Nørskov, Phy. Rev. B 59 (1999) 7413.
[272] G. Kresse, J. Furthmüller, Comput. Mater. Sci. 6 (1996) 15.
[273] H.J. Monkhorst, J.D. Pack, Phy. Rev. B 13 (1976) 5188.
[274] C. Baltes, S. Vukojevic, F. Schuth, J. Catal. 258 (2008) 334.
[275] R. Matyi, L. Schwartz, J. Butt, Catal. Rev., Sci. Eng. 29 (1987) 41.
[276] T.W. Hansen, J.B. Wagner, P.L. Hansen, S. Dahl, H. Topsøe, C.J.H. Jacobsen, Science 294 (2001) 1508.
[277] P.L. Hansen, J.B. Wagner, S. Helveg, J.R. Rostrup-Nielsen, B.S. Clausen, H. Topsøe, Science 295 (2002) 2053.
[278] G.W. Huber, S. Iborra, A. Corma, Chem. Rev. 106 (2006) 4044.
[279] N.Y. Topsøe, H. Topsøe, Top. Catal. 8 (1999) 267.
[280] M. Kurtz, J. Strunk, O. Hinrichsen, M. Muhler, K. Fink, B. Meyer, C. Wöll, Angew. Chem. Int. Ed. 44 (2005) 2790.
[281] M. Schur, B. Bems, A. Dassenoy, I. Kassatkine, J. Urban, H. Wilmes, O. Hinrichsen, M. Muhler, R. Schlögl, Angew. Chem. Int. Ed. 42 (2003) 3815.
[282] G.X. Qi, X.M. Zheng, J.H. Fei, Z.Y. Hou, J. Mol. Catal. A 176 (2001) 195.
[283] M. Xu, J.H. Lunsford, D.W. Goodman, A. Bhattacharyya, Appl. Catal. A 149 (1997) 289.
[284] H. Shou, R.J. Davis, J. Catal. 282 (2011) 83.
[285] R.G. Herman, C.W. Young, K.J. Smith, K. Klier, Ind. Eng. Chem. Res. 30 (1991) 61.
[286] M.E. Dry, Appl. Catal. A 138 (1996) 319.
[287] J.D. Grunwaldt, M. Caravati, S. Hannemann, A. Baiker, Phys. Chem. Chem. Phys. 6 (2004) 3037.
[288] B. Ravel, M. Newville, J. Synchrotron Radiat. 12 (2005) 537.
[289] J.D. Grunwaldt, N. van Vegten, A. Baiker, Chem. Commun. (2007) 4635.
[290] T.W. Hansen, J.B. Wagner, R.E. Dunin-Borkowski, Mater. Sci. Tech. 26 (2010) 1338.
[291] F. Marino, E. Cerrella, S. Duhalde, M. Jobbagy, M. Laborde, Int. J. Hydrogen Energy 23 (1998) 1095.
[292] J. Stötzel, D. Lützenkirchen-Hecht, R. Frahm, B. Kimmerle, A. Baiker, M. Nachtegaal, M.J. Beier, J.D. Grunwaldt, J. Phy. Conf. Ser. 190 (2009) .
[293] A.I. Frenkel, C.W. Hills, R.G. Nuzzo, J. Phys. Chem. B 105 (2001) 12689.
[294] N. Schmahl, J. Barthel, G. Eikerling, Z. Anorg. Allgem. Chem. 332 (1964) 230.

[295] P. Scherrer, Nachr.Ges.Wiss.Göttingen 26 (1918) 98.
[296] P. Serp, E. Castillejos, ChemCatChem 2 (2010) 41.
[297] G. Tréglia, B. Legrand, P. Maugain, Surf. Sci. 225 (1990) 319.
[298] K. Wandelt, C.R. Brundle, Phys. Rev. Lett. 46 (1981) 1529.
[299] I. Sierra, J. Ereña, A.T. Aguayo, J.M. Arandes, J. Bilbao, Appl. Catal. B 94 (2010) 108.
[300] A. Gotti, R. Prins, J. Catal. 178 (1998) 511.
[301] K. Maruya, T. Komiya, T. Hayakawa, L. Lu, M. Yashima, J. Mol. Chem. A 159 (2000) 97.
[302] K. Maruya, A. Inaba, T. Maehashi, K. Domen, T. Onishi, J. Chem. Soc., Chem. Commun. (1985) 487.
[303] T. Maehashi, K.I. MARUYA, K. Domen, K.I. AIKA, T. Onishi, Chem. Lett. (1984) 747.
[304] S.C. Tseng, N.B. Jackson, J.G. Ekerdt, J. Catal. 109 (1988) 284.
[305] N.B. Jackson, J.G. Ekerdt, J. Catal. 126 (1990) 31.
[306] C.L. Su, D.H. He, J.R. Li, B.Q. Xu, Z.X. Cheng, Q.M. Zhu, Stud. Surf. Sci. Catal. 130 (2000) 3735.
[307] M. Momirlan, T. Veziroglu, Renew. Sustain. Energy Rev. 6 (2002) 141.
[308] X. Dong, H.B. Zhang, G.D. Lin, Y.Z. Yuan, K.R. Tsai, Catal. Lett. 3 (2003) 237.
[309] M. Kurtz, N. Bauer, C. Büscher, H. Wilmer, O. Hinrichsen, R. Becker, S. Rabe, K. Merz, M. Driess, R.A. Fischer, Catal. Lett. 92 (2004) 49.
[310] C. Higman, M. Van der Burgt, Gasification, Gulf Professional Publishing, 2008.
[311] C.H. Bartholomew, R.B. Pannell, J.L. Butler, J. Catal. 65 (1980) 335.
[312] M. Andersson, F. Abild-Pedersen, I. Remediakis, T. Bligaard, G. Jones, J. Engbæk, O. Lytken, S. Horch, J.H. Nielsen, J. Sehested, J. Catal. 255 (2008) 6.
[313] J. Sehested, S. Dahl, J. Jacobsen, J.R. Rostrup-Nielsen, J. Phys. Chem. B 109 (2005) 2432.
[314] Q. Wu, G.L. Chiarello, L.D.L. Duchstein, J.M. Christensen, J.B. Wagner, B. Temel, J.D. Grunwaldt, A.D. Jensen, in preparation.
[315] J.W. Geus, Catalyst preparation: science and engineering, Taylor and Francis/CRC Press, Boca Raton, FL, 2007.
[316] P. Munnik, M. Wolters, A. Gabrielsson, S. Pollington, G. Headdock, J. Bitter, P. de Jongh, K. de Jong, J. Phy. Chem. C 115 (2011) 14698.
[317] J.R.A. Sietsma, H. Friedrich, A. Broersma, M. Versluijs-Helder, A. Jos van Dillen, P.E. de Jongh, K.P. de Jong, J. Catal. 260 (2008) 227.
[318] J.R.A. Sietsma, J.D. Meeldijk, J.P. den Breejen, M. Versluijs-Helder, A.J. van Dillen, P.E. de Jongh, K.P. de Jong, Angew. Chem. Int. Ed. 119 (2007) 4631.
[319] W. Chu, L.N. Wang, P.A. Chernavskii, A.Y. Khodakov, Angew. Chem. Int. Ed. 47 (2008) 5052.
[320] T. Toupance, M. Kermarec, C. Louis, J. Phys. Chem. B 104 (2000) 965.
[321] C.H. Bartholomew, R.J. Farrauto, J. Catal. 45 (1976) 41.
[322] J.R.A. Sietsma, J.D. Meeldijk, M. Versluijs-Helder, A. Broersma, A.J. Dillen, P.E. de Jongh, K.P. de Jong, Chem. Mater. 20 (2008) 2921.
[323] J. Rossmeisl, A. Logadottir, J.K. Nørskov, Chem. Phys. 319 (2005) 178.
[324] S. Catillon-Mucherie, F. Ammari, J.M. Krafft, H. Lauron-Pernot, R. Touroude, C. Louis, J. Phy. Chem. C 111 (2007) 11619.

[325] S. Catillon-Mucherie, H. Lauron-Pernot, C. Louis, J. Phys. Chem. C 114 (2010) 11140.
[326] S. Yuvaraj, L. Fan-Yuan, C. Tsong-Huei, Y. Chuin-Tih, J. Phys. Chem. B 107 (2003) 1044.
[327] J.G. Jackson, R.W. Fonseca, J.A. Holcombe, Spectrochimica Acta Part B: Atomic Spectroscopy 50 (1995) 1449.
[328] J. Mu, D. Perlmutter, Thermochimica Acta 56 (1982) 253.
[329] H.E. Swift, F.E. Lutinski, W.L. Kehl, J. Phys. Chem. 69 (1965) 3268.
[330] J.H. Lin, P. Biswas, V.V. Guliants, S. Misture, Appl. Catal. A 387 (2010) 87.
[331] A. Ungureanu, B. Dragoi, A. Chirieac, S. Royer, D. Duprez, E. Dumitriu, J. Mater. Chem. 21 (2011) 12529.
[332] A. Naghash, T. Etsell, S. Xu, Chem. Mater. 18 (2006) 2480.
[333] L. Pauling, J. Am. Chem. Soc. 69 (1947) 542.
[334] T.J. Huang, T.C. Yu, S.Y. Jhao, Ind. Eng. Chem. Res. 45 (2006) 150.
[335] L.Y. Gan, R. Tian, X.B. Yang, D.H. Lu, Y. Zhao, J. Phy. Chem. C 116 (2012) 745.
[336] A.S. Moffat, Science 251 (1991).
[337] T.B. Reed, R. Lerner, Science 182 (1973) 1299.
[338] R.J. Nichols, J. Sci. Ind. Res. 62 (2003) 97.
[339] E. Guerreiro, O. Gorriz, G. Larsen, L. Arrúa, Appl. Catal. A 204 (2000) 33.
[340] J. Van de Loosdrecht, S. Barradas, E. Caricato, N. Ngwenya, P. Nkwanyana, M. Rawat, B. Sigwebela, P. Van Berge, J. Visagie, Top. Catal. 26 (2003) 121.
[341] A.J. Van Dillen, R.J.A.M. Terörde, D.J. Lensveld, J.W. Geus, K.P. De Jong, J. Catal. 216 (2003) 257.
[342] P. Porta, S. De Rossi, G. Ferraris, M. Lo Jacono, G. Minelli, G. Moretti, J.Catal. 109 (1988) 367.
[343] Z. Huang, F. Cui, H. Kang, J. Chen, X. Zhang, C. Xia, Chem. Mater. 20 (2008) 5090.
[344] V.R. Stamenkovic, B.S. Mun, M. Arenz, K.J.J. Mayrhofer, C.A. Lucas, G. Wang, P.N. Ross, N.M. Markovic, Nature Mater. 6 (2007) 241.
[345] M. Oezaslan, F. Hasché, P. Strasser, Chem. Mater. (2011) .
[346] M.J. Weber, A.J.M. Mackus, M.A. Verheijen, C. van der Marel, W.M.M. Kessels, Chem. Mater. 24 2973.
[347] M.L. Wu, D.H. Chen, T.C. Huang, Langmuir 17 (2001) 3877.
[348] H.H. Hwu, J. Eng Jr, J.G. Chen, J. Am. Chem. Soc. 124 (2002) 702.
[349] S. Zhou, K. McIlwrath, G. Jackson, B. Eichhorn, J. Am. Chem. Soc. 128 (2006) 1780.
[350] A. Kustov, A.M. Frey, K.E. Larsen, T. Johannessen, J.K. Nørskov, C.H. Christensen, Appl. Catal. A 320 (2007) 98.
[351] J. Sinfelt, J.L. Carter, D. Yates, J. Catal. 24 (1972) 283.
[352] J.H. Sinfelt, Science 195 (1977) 641.
[353] F. Wang, Y. Li, W. Cai, E. Zhan, X. Mu, W. Shen, Catal. Today 146 (2009) 31.
[354] L.C. Chen, S.D. Lin, Appl. Catal. B (2011) .
[355] J.H. Lin, V.V. Guliants, ChemCatChem 3 (2011) 1426.
[356] N. Schumacher, A. Boisen, S. Dahl, A.A. Gokhale, S. Kandoi, L.C. Grabow, J.A. Dumesic, M. Mavrikakis, I. Chorkendorff, J. Catal. 229 (2005) 265.

[357] J. Ahmed, K.V. Ramanujachary, S.E. Lofland, A. Furiato, G. Gupta, S. Shivaprasad, A.K. Ganguli, Colloids Surf. Physicochem. Eng. Aspects 331 (2008) 206.
[358] A. Kaiser, C. Görsmann, U. Schubert, J. Sol Gel Sci. Technol. 8 (1997) 795.
[359] J. Calles, A. Carrero, A. Vizcaíno, Microporous Mesoporous Mater. 119 (2009) 200.
[360] A. Vizcaíno, A. Carrero, J. Calles, Int. J. Hydrogen Energy 32 (2007) 1450.
[361] F. Mariño, G. Baronetti, M. Jobbagy, M. Laborde, Appl. Catal. A 238 (2003) 41.
[362] P. Li, J. Liu, N. Nag, P. Crozier, J. Catal. 262 (2009) 73.
[363] R. Pérez-Hernández, G. Mondragón Galicia, D. Mendoza Anaya, J. Palacios, C. Angeles-Chavez, J. Arenas-Alatorre, Int. J. Hydrogen Energy 33 (2008) 4569.
[364] V. Bergamaschi, F. Carvalho, Hydrogen production by ethanol steam reforming over Cu and Ni catalysts supported on ZrO_2 and Al_2O_3 microspheres, Materials Science Forum, Trans. Tech. Publ, 2008, p. 734.
[365] G. Ranga Rao, S.K. Meher, B.G. Mishra, P.H.K. Charan, Catal. Today (2012) .
[366] J. Bian, M. Xiao, S.J. Wang, Y.X. Lu, Y.Z. Meng, Appl. Surf. Sci. 255 (2009) 7188.
[367] I.N. Remediakis, F. Abild-Pedersen, J.K. Nørskov, J. Phys. Chem. B 108 (2004) 14535.
[368] C. Louis, Z.X. Cheng, M. Che, J. Phys. Chem. 97 (1993) 5703.
[369] C. Kittel, Introduction to solid state physics, Wiley New York, New York, 1996.
[370] C. Bernardo, I. Alstrup, J. Rostrup-Nielsen, J. Catal.96 (1985) 517.
[371] G. Sankar, P.A. Wright, S. Natarajan, J.M. Thomas, G.N. Greaves, A.J. Dent, B.R. Dobson, C.A. Ramsdale, R.H. Jones, J. Phys. Chem. 97 (1993) 9550.
[372] B.S. Clausen, H. Topsøe, R. Frahm, Adv. Catal. 42 (1998) 315.
[373] J.D. Grunwaldt, B.S. Clausen, Top. Catal. 18 (2002) 37.
[374] Q. Wu, G.L. Chiarello, A. Boubnov, J.M. Christensen, B. Temel, A.D. Jensen, J.D. Grunwaldt, in preparation (2012) .
[375] B. Clausen, G. Steffensen, B. Fabius, J. Villadsen, R. Feidenhans'l, H. Topsøe, J. Catal. 132 (1991) 524.
[376] B.S. Clausen, L. Gråbæk, G. Steffensen, P.L. Hansen, H. Topsøe, Catal. Lett. 20 (1993) 23.
[377] R. Kiebach, N. Pienack, W. Bensch, J.D. Grunwaldt, A. Michailovski, A. Baiker, T. Fox, Y. Zhou, G.R. Patzke, Chem. Mater. 20 (2008) 3022.
[378] H. Karaca, J. Hong, P. Fongarland, P. Roussel, A. Griboval-Constant, M. Lacroix, K. Hortmann, O.V. Safonova, A.Y. Khodakov, Chem. Commun. 46 (2010) 788.
[379] S. Zabinsky, J. Rehr, A. Ankudinov, R. Albers, M. Eller, Phy. Rev. B 52 (1995) 2995.
[380] J. Benard, J. Oudar, N. Barbouth, E. Margot, Y. Berthier, Surf. Sci. 88 (1979) L35.
[381] A. Roman, B. Delmon, J. Catal. 30 (1973) 333.
[382] H. Charcosset, R. Frety, A. Soldat, Y. Trambouze, J. Catal. 22 (1971) 204.
[383] T.B. Massalski, ASM International the Materials Information Society, 1990, p. 1442.
[384] W. Shen, J. Dumesic, C. Hill, J. Catal. 68 (1981) 152.
[385] K. Tsu, M. Boudart, Editions Technip (1961) 953.
[386] C.S. Chen, J.H. Lin, T.W. Lai, B.H. Li, J. Catal. 263 (2009) 155.

[387] M. Agnelli, H. Swaan, C. Marquez-Alvarez, G. Martin, C. Mirodatos, J. Catal. 175 (1998) 117.
[388] H.S. Taylor, Proc. R. Soc., London Series A 108 (1925) 105.
[389] T. Zambelli, J. Wintterlin, J. Trost, G. Ertl, Science 273 (1996) 1688.
[390] S. Dahl, A. Logadottir, R. Egeberg, J.H. Nielsen, I. Chorkendorff, E. Törnqvist, J.K. Nørskov, Phys. Rev. Lett. 83 (1999) 1814.
[391] Z.P. Liu, P. Hu, J. Am. Chem. Soc. 125 (2003) 1958.
[392] R.T. Vang, K. Honkala, S. Dahl, E.K. Vestergaard, J. Schnadt, E. Lægsgaard, B.S. Clausen, J.K. Nørskov, F. Besenbacher, Nature Mater. 4 (2005) 160.
[393] J. Engbæk, O. Lytken, J.H. Nielsen, I. Chorkendorff, Surf. Sci. 602 (2008) 733.
[394] H.S. Bengaard, J.K. Nørskov, J. Sehested, B. Clausen, L. Nielsen, A. Molenbroek, J. Rostrup-Nielsen, J. Catal. 209 (2002) 365.
[395] K. Yu, D. Ling, W. Spicer, J. Catal. 44 (1976) 373.
[396] P. Sabatier, Berichte der deutschen chemischen Gesellschaft 44 (1911) 1984.
[397] H.B. Zhang, X.L. Liang, X. Dong, H.Y. Li, G.D. Lin, Catal. Surv. Asia 13 (2009) 41.
[398] L.L. Newman, W.C. Schroeder, Patent US Patent 2,593,477 (1952) .
[399] M. Oertel, J. Schmitz, W. Weirich, D. Jendryssek-Neumann, R. Schulten, Chem. Eng. Technol. 10 (1987) 248.
[400] J. Hu, Y. Wang, C. Cao, D.C. Elliott, D.J. Stevens, J.F. White, Catal. Today 120 (2007) 90.
[401] J.S. Lee, S. Kim, Y.G. Kim, Topics Catal. 2 (1995) 127.
[402] M. Xiang, D. Li, W. Li, B. Zhong, Y. Sun, Catal. Commun. 8 (2007) 503.
[403] M. Xiang, D. Li, H. Qi, W. Li, B. Zhong, Y. Sun, Fuel 86 (2007) 1298.
[404] J.S. Lee, M.H. Yeom, K.Y. Park, I.S. Nam, J.S. Chung, Y.G. Kim, S.H. Moon, J. Catal. 128 (1991) 126.
[405] C. Liang, P. Ying, C. Li, Chem. Mater. 14 (2002) 3148.
[406] T. Miyao, I. Shishikura, M. Matsuoka, M. Nagai, S. Oyama, Appl. Catal. A., 165 (1997) 419.
[407] K.T. Jung, W.B. Kim, C.H. Rhee, J.S. Lee, Chem. Mater. 16 (2004) 307.
[408] R. Arroyo, G. Cordoba, J. Padilla, V. Lara, Mater. Lett. 54 (2002) 397.
[409] K. Okada, N. Yamamoto, Y. Kameshima, A. Yasumori, K.J.D. MacKenzie, J. Am. Ceram. Soc. 84 (2001) 1591.
[410] J. Dubois, T. Epicier, C. Esnouf, G. Fantozzi, P. Convert, Acta Metallurgica 36 (1988) 1891.
[411] T. Epicier, J. Dubois, C. Esnouf, G. Fantozzi, P. Convert, Acta Metallurgica 36 (1988) 1903.
[412] J.A. Nelson, M.J. Wagner, Chem. Mater. 14 (2002) 1639.
[413] K. Page, J. Li, R. Savinelli, H.N. Szumila, J. Zhang, J.K. Stalick, T. Proffen, S.L. Scott, R. Seshadri, Solid State Sci. 10 (2008) 1499.
[414] S. Tauster, S. Fung, R. Baker, J. Horsley, Science 211 (1981) 1121.
[415] A.J. Medford, A. Vojvodic, F. Studt, F. Abild-Pedersen, J.K. Nørskov, J. Catal. 290 (2012) 108.
[416] A.M. Alexander, J.S.J. Hargreaves, Chem. Soc. Rev. 39 (2010) 4388.
[417] S. Oyama, Catal.Today 15 (1992) 179.
[418] R. Levy, M. Boudart, Science 181 (1973) 547.

[419] A. Hanif, T. Xiao, P. Andrew, J. Sloan, M.L.H. Green, Chem. Mater. 14 (2002) 1009.
[420] Q. Wu, J.M. Christensen, G.L. Chiarello, B. Temel, J.D. Grunwaldt, A.D. Jensen, in preparation (2012) .
[421] J. Lee, S. Locatelli, S. Oyama, M. Boudart, J. Catal. 125 (1990) 157.
[422] R. Barthos, F. Solymosi, J. Catal. 249 (2007) 289.
[423] S.S.Y. Lin, W.J. Thomson, T.J. Hagensen, S.Y. Ha, Appl. Catal. A 318 (2007) 121.
[424] M. Nagai, K. Matsuda, J. Catal. 238 (2006) 489.
[425] J. Patt, D.J. Moon, C. Phillips, L. Thompson, Catal. Lett. 65 (2000) 193.
[426] M. Ledoux, C. Pham-Huu, H. Dunlop, S. Hantzer, S. Marin, M. Weibel, Catal. Today 15 (1992) 263.
[427] T. Xiao, A.P.E. York, K.S. Coleman, J.B. Claridge, J. Sloan, J. Charnock, M.L.H. Green, J. Mater. Chem. 11 (2001) 3094.
[428] L. Leclercq, A. Almazouari, M. Dufour, G. Leclercq, The chemistry of transition metal carbides and nitrides, Chapman & Hall, Glasgow,1996.
[429] T. Hyeon, M. Fang, K.S. Suslick, J. Am. Chem. Soc. 118 (1996) 5492.
[430] J.S. Choi, G. Bugli, G. Djéga-Mariadassou, J. Catal. 193 (2000) 238.
[431] J.G. Choi, J.R. Brenner, L.T. Thompson, J. Catal. 154 (1995) 33.
[432] J. Lee, S. Oyama, M. Boudart, J. Catal. 106 (1987) 125.
[433] K. Kuo, G. Hägg, Nature 170 (1952) 245.
[434] E. Parthe, V. Sadogopan, Acta Crystallogr. 16 (1963) 202.
[435] L.T. Thompson, J. Patt, D.J. Moon, C. Phillips, US patent 6.623.720, (2003).
[436] N.M. Schweitzer, J.A. Schaidle, O.K. Ezekoye, X. Pan, S. Linic, L.T. Thompson, J. Am. Chem. Soc. 133 (2011) 2378.
[437] X.H. Wang, H.L. Hao, M.H. Zhang, W. Li, K.Y. Tao, J. Solid State Chem. 179 (2006) 538.
[438] A.P.E. York, J.B. Claridge, A.J. Brungs, S.C. Tsang, M.L.H. Green, Chem. Commun. (1997) 39.
[439] I. Barin, Frontmatter, Wiley Online Library, Weinheim, 2008.

Appendix A: Supplementary materials for Chapter 4

Microkinetic model:

(1) CO + * → CO*
(2) H_2 +2*→2H*
(3) CO* + H* → HCO* + * Rate determining step
(4) HCO* + H* → H_2CO* + *
(5) H_2CO* + H* → H_3CO* + *
(6) H_3CO* + H* → H_3COH + 2*Rate determining step

Treating reaction (3) and (6) as being rate determining and everything else being in equilibrium leads to:

$$k_1 p_{CO} \theta_* = k_{-1} \theta_{CO}$$

$$k_2 p_{H_2} \theta_*^2 = k_{-2} \theta_H^2$$

$$R_3 = k_3 \theta_{CO} \theta_H - k_{-3} \theta_{HCO} \theta_*$$

$$k_4 \theta_{HCO} \theta_H = k_{-4} \theta_{H_2CO} \theta_*$$

$$k_5 \theta_{H_2CO} \theta_H = k_{-5} \theta_{H_3CO} \theta_*$$

$$R_6 = k_6 \theta_{H_3CO} \theta_H - k_{-6} p_{MeOH} \theta_*^2$$

the coverages are hence:

$$\theta_{CO} = K_1 p_{CO} \theta_* = C_{CO} \theta_* \qquad \text{with } K_1 = \frac{k_1}{k_{-1}}$$

$$\theta_H = \sqrt{K_2 p_{H_2}} \theta_* = C_H \theta_* \qquad \text{with } K_2 = \frac{k_2}{k_{-2}}$$

$$\theta_{H_2CO} = K_4 \theta_{HCO} C_H \qquad \text{with } K_4 = \frac{k_4}{k_{-4}}$$

$$\theta_{H_3CO} = K_5 \theta_{H_2CO} C_H = K_5 K_4 \theta_{HCO} C_H^2 \text{with } K_5 = \frac{k_5}{k_{-5}}$$

under steady state $R_3 = R_6$ and hence:

$$k_3\theta_{CO}\theta_H - k_{-3}\theta_{HCO}\theta_* = k_6\theta_{H_3CO}\theta_H - k_{-6}p_{MeOH}\theta_*^2$$

substitution yields

$$k_3 C_{CO} C_H \theta_*^2 - k_{-3}\theta_{HCO}\theta_* = k_6 K_5 K_4 \theta_{HCO} C_H^3 \theta_* - k_{-6}p_{MeOH}\theta_*^2$$

$$\theta_{HCO} = \frac{k_3 C_{CO} C_H + k_{-6}p_{MeOH}}{k_6 K_5 K_4 C_H^3 + k_{-3}}\theta_* = C_{HCO}\theta_*$$

and

$$\theta_{H_2CO} = K_4 C_{HCO} C_H \theta_* = C_{H_2CO}\theta_*$$

$$\theta_{H_3CO} = K_5 K_4 C_{HCO} C_H^2 \theta_* = C_{H_3CO}\theta_*$$

Since the sum of all coverages equals 1:

$$\theta_* = \frac{1}{1 + C_{CO} + C_H + C_{HCO} + C_{H_2CO} + C_{H_3CO}}$$

The total rate can now be expressed via R_3.
This an also be written as:

$$R_3 = k_3\theta_{CO}\theta_H(1 - \gamma_3)$$

where

$$\gamma_3 = \frac{\theta_{HCO}\theta_*}{K_3\theta_{CO}\theta_H}$$

with $K_3 = \frac{k_3}{k_{-3}}$

Scaling parameters from Fig.4-2

Surface	ΔE_C	ΔE_{CO}
Ag	3.86	0.20
Cu	2.33	-0.40
Pd	0.29	-1.45
Pt	0.89	-1.57
Rh	0.17	-1.60
Au	3.56	-0.10
Ni	0.3	-1.42
Ir	0.36	-2.01
Ru	0.08	-1.70
Re	-0.77	-1.93
Co	0.45	-1.27

Surface	ΔE_C	ΔE_{HCO}
Ag	3.86	0.26
Cu	2.33	-0.20
Pd	0.29	-1.11
Pt	0.89	-1.17
Rh	0.17	-1.13

Surface	$0.25\Delta E_C + 0.5\Delta E_O$	ΔE_{H2CO}
Ag	0.57	-0.58
Cu	-0.26	-0.60
Pd	-0.52	-1.04
Pt	-0.49	-1.19
Rh	-1.22	-1.52

Surface	ΔE_O	ΔE_{H3CO}
Ag	-0.80	-1.06
Cu	-1.69	-1.61
Pd	-1.18	-1.24
Pt	-1.42	-1.42
Rh	-2.52	-1.92

Transition state scaling parameters from Fig.4-3

Surface	$\Delta E_H + \Delta E_{CO}$	$\Delta E_{H\text{-}CO}$
Ag	0.26	0.74
Cu	-0.77	0.15
Pd	-2.05	-0.99
Pt	-2.36	-1.11
Rh	-2.29	-1.13
Au	-0.24	0.34

Surface	$\Delta E_H + \Delta E_{HCO}$	$\Delta E_{H\text{-}HCO}$
Ag	0.57	0.78
Cu	-0.33	0.24
Pd	-1.46	-0.48
Pt	-1.71	-0.83
Rh	-1.57	-1.11

Surface	$\Delta E_H + \Delta E_{H2CO}$	$\Delta E_{H\text{-}H2CO}$
Ag	-0.24	0.12
Cu	-0.73	-0.40
Pd	-1.38	-0.56
Pt	-1.73	-0.81
Rh	-1.96	-1.24

Surface	$\Delta E_H + \Delta E_{H3CO}$	$\Delta E_{H3CO\text{-}H}$
Ag	-0.75	0.03
Cu	-1.74	-0.40
Pd	-1.59	-0.54
Pt	-1.96	-0.83
Rh	-2.36	-1.11

Surface coverages of Cu and CuNi[a]

	θ_{H3CO}	θ_{H2CO}	θ_{HCO}	θ_{CO}	θ_H	θ_*
Cu	$2.3\text{x}10^{-14}$	$1.5\text{x}10^{-15}$	$1.2\text{x}10^{-16}$	$5.6\text{x}10^{-7}$	0.03	0.97
$^{AA}Cu_3Ni$	$7.0\text{x}10^{-7}$	$7.4\text{x}10^{-7}$	$1.3\text{x}10^{-9}$	$1.1\text{x}10^{-4}$	0.21	0.79

[a] Reaction conditions are 523 K, 45 bar H_2, 45 bar CO, 5 bar CH_4, 5 bar H_2O.

X-ray diffraction pattern of the $Cu/ZnO/Al_2O_3$ catalyst

The $Cu/ZnO/Al_2O_3$ catalyst was firstly reduced at 220 °C for 1 h and then it was cooled down to room temperature. Afterwards, a long scan of XRD was run at this temperature. The XRD pattern of $Cu/ZnO/Al_2O_3$ catalyst is shown below. The XRD shows distinguished Cu and ZnO peaks with the average particle size of metallic Cu being about 6 nm, and about 3 nm for ZnO according to Scherrer equation. There was no specific Al_2O_3 peak in the pattern, which means Al_2O_3 was either amorphous or finely dispersed in the catalysts.

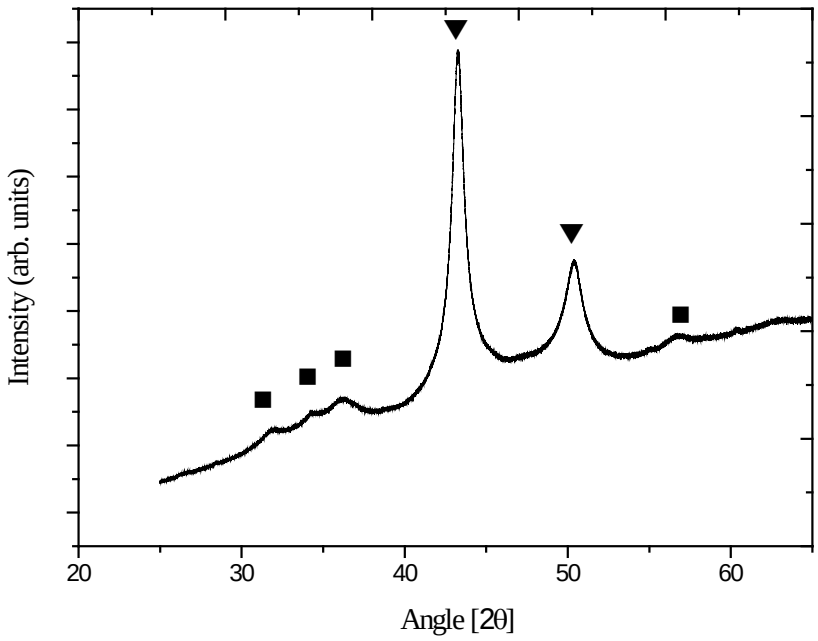

The XRD pattern of reduced $CuZnO/Al_2O_3$ catalyst; ▼ - metalic Cu, ■ - ZnO.

Appendix B: Supplementary materials for Chapter 5

This electronic supplementary information gives further details, background information and results to support the main paper, in particular with respect to in situ XAS, EXAFS data analysis, and testing.

Table S1
The amount of catalyst and the flow rate of syngas for activity testing (the gas flow rate is referring to 298.15 K and 1 atm).

Catalysts	Weight [g]	Gas flow rate [Nml min^{-1}]
Cu-Ni/SiO_2	1.80	115
Cu-Ni/CNTs	0.80	174
Cu-Ni/Al_2O_3	2.96	152
Cu-Ni/ZrO_2	5.15	113
Cu/ZnO/Al_2O_3	0.41	115

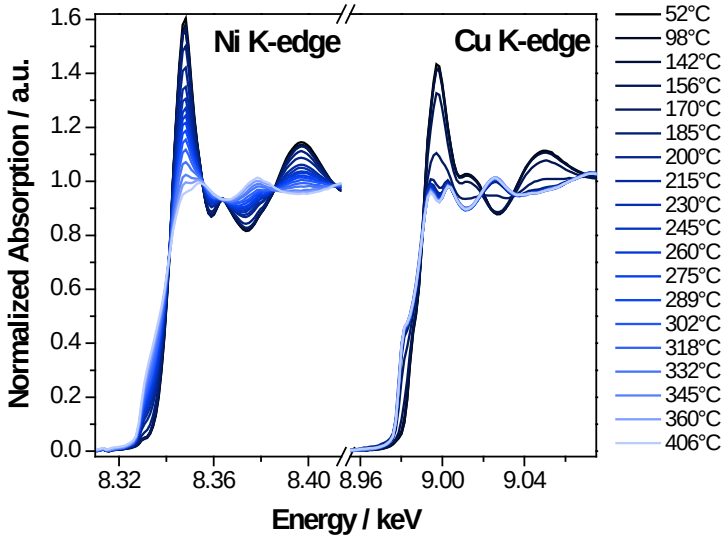

Fig. S1. Typical XANES spectra at the Ni K-edge and the Cu K-edge recorded at different temperature during reduction of Cu-Ni/CNT: 5 mol % H_2/He (40 ml min^{-1}); temperature increase from 50 to 406 °C using a heating ramp of 5 °C min^{-1}; spectra recorded every 15 °C, corresponds to the 3D-plot of Figure 1.

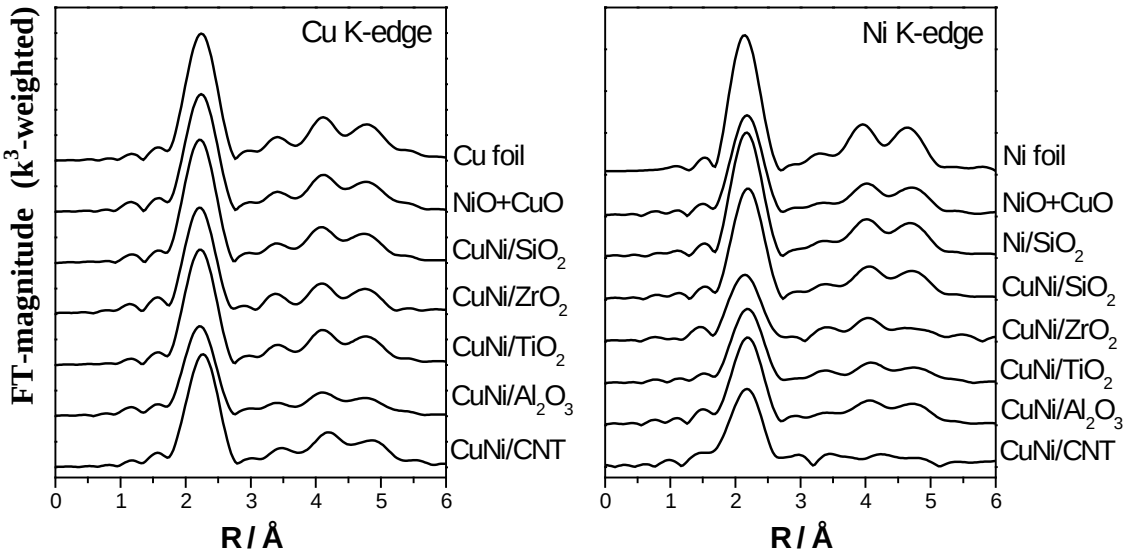

Fig. S2. Typical Fourier transformed k^3-weighted EXAFS spectra at both the Ni K- (left panel) and Cu K- (right panel) edges of the investigate CuNi-supported samples recorded at RT after reduction in 5% H_2/He at 410 °C (except for the one on Al_2O_3 which was reduced up to 600 °C).

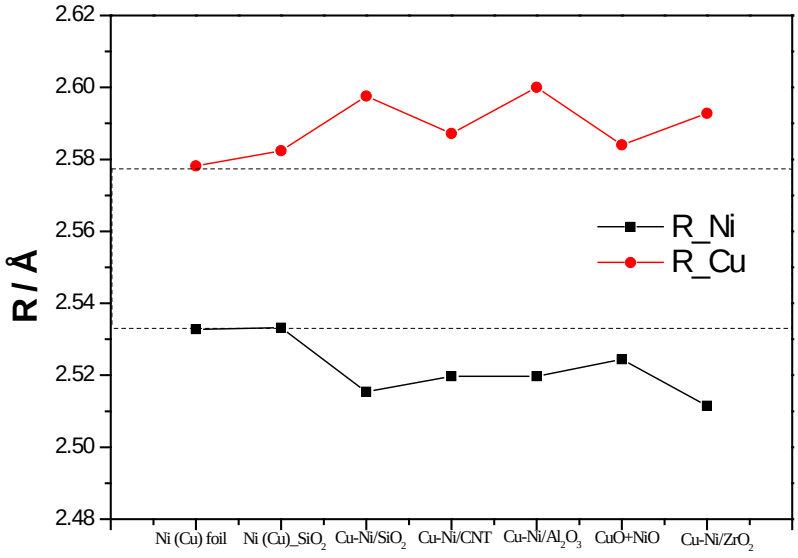

Fig. S3. Comparison of the interatomic distance R, obtained from the fitting of the Fourier Transformed k^3-weighted spectra of Fig. S2 (see Table S2), of single (Ni or Cu) metal samples (Ni foil, Cu foil, Ni/SiO_2 and Cu/SiO_2) with the bimetallic samples (CuNi supported samples).

Table S2

Fit results at Ni K- and Cu K-edges: S02 Amplitude reduction factor; CN: coordination number; R: interatomic distance; σ^2: Debye Waller factor (mean square disorder); ΔE_0: energy shift.

sample	**shell**	S_0^2	**CN**	**R / Å**	**σ^2 (Å^2)**	**ΔE_0 / eV**	**R-factor**
Ni foil	Ni-Ni	0.70±0.04	12*	2.533 ±0.002	0.0055 ±0.0004	5.85 ±0.39	0.0020
Ni/SiO_2	Ni-Ni	0.70	11.4 ± 0.4	2.533 ±0.002	0.0061 ±0.0003	5.17 ±0.29	0.0008
NiO + CuO mix	Ni-Ni	0.70	10.8 ± 1.1	2.524 ±0.005	0.0072 ±0.0007	6.14 ±0.82	0.0098
1Ni1Cu/SiO_2	Ni-Ni(Cu)	0.70	11.1 ± 0.6	2.515 ±0.002	0.0067 ±0.0004	6.59 ±0.39	0.0020
1Ni1Cu/CNT	Ni-Ni(Cu)	0.70	9.6 ± 1.0	2.520 ±0.006	0.0069 ±0.0012	6.06 ±0.66	0.0059
1Ni1Cu/Al_2O_3	Ni-Ni(Cu)	0.70	9.4 ± 1.9	2.520 ±0.013	0.0071 ±0.0017	6.18 ±1.8	0.0340
1Ni1Cu/ZrO_2	Ni-Ni(Cu)	0.70	9.4 ± 1.8	2.511 ±0.016	0.0088 ±0.0014	1.37 ±2.40	0.0392
Cu foil	Cu-Cu	0.76±0.05	12*	2.582 ±0.002	0.0081 ±0.0005	3.66 ±0.42	0.0030
Cu/SiO_2	Cu-Cu	0.76	6.8 ± 1.3	2.582 ±0.011	0.0075 ±0.0015	3.35 ±1.82	0.0134
NiO + CuO mix	Cu-Cu	0.76	11.1 ± 0.7	2.584 ±0.002	0.0081 ±0.0006	3.88 ±0.44	0.0025
1Ni1Cu/SiO_2	Cu-Cu(Ni)	0.76	11.2 ± 0.8	2.598 ±0.003	0.0079 ±0.0006	3.46 ±0.52	0.0052
1Ni1Cu/CNT	Cu-Cu(Ni)	0.76	11.2 ± 0.7	2.587 ±0.002	0.0087 ±0.0006	3.76 ±0.41	0.0024
1Ni1Cu/Al_2O_3	Cu-Cu(Ni)	0.76	9.5 ± 0.7	2.600 ±0.003	0.0091 ±0.0007	3.53 ±0.47	0.0026
1Ni1Cu/ZrO_2	Cu-Cu(Ni)	0.76	10.5 ± 0.9	2.593 ±0.004	0.0087 ±0.0007	3.13 ±0.67	0.0029

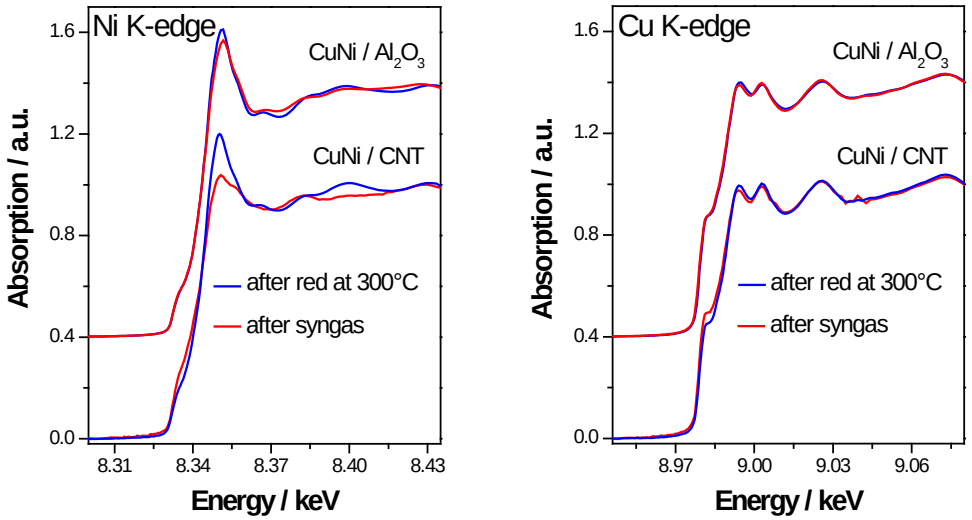

Fig. S4. In situ XANES spectra at the Ni K- (left panel) and Cu K- (right panel) recorded on CuNi/CNT (lower curves in the figures) and CuNi/Al_2O_3 (upper curves in the figures) after reduction in 5% H_2/He at 300 °C (blue curves) and preceeding exposure to syngas (2.5 mol % H_2/2.5 mol % CO/He) for 100min at 300 °C (red curves).

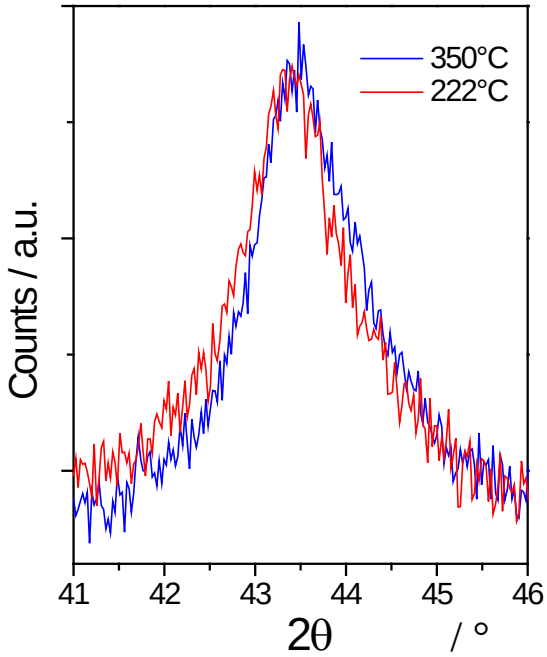

Fig. S5. Comparison 2θ of the in situ XRD patterns recorded during reduction of the CuNi/CNT sample at 222 °C (red curve) and 350°C (blue curve) in the 41°-46° region.

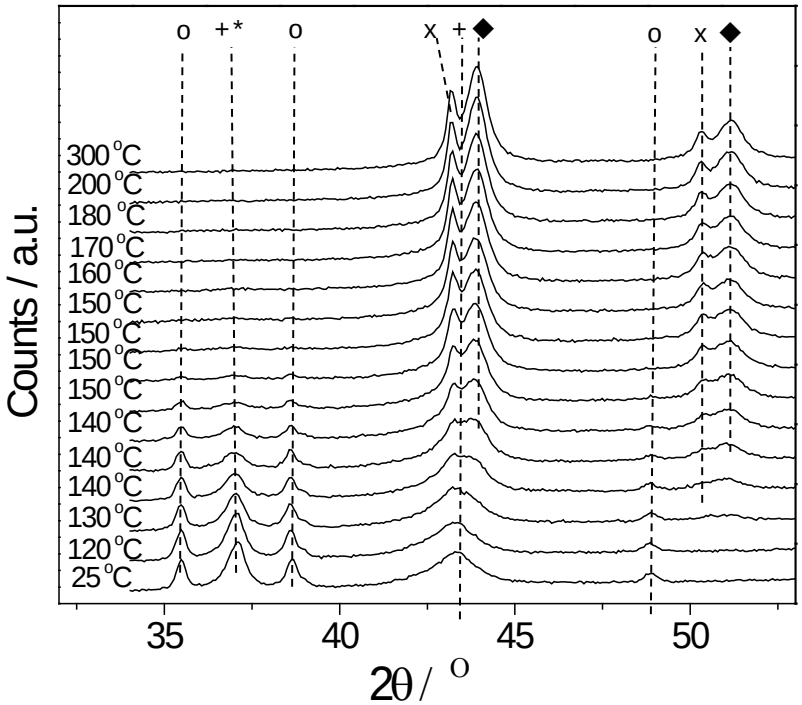

Fig. S6. In situ XRD at selected temperature during reduction of Cu-Ni/SiO_2. The symbols indicate the main reflections of: (o) CuO; (+) NiO; (*) $Cu_xNi_{1-x}O$; (x) metallic Cu; (◆) Cu-Ni alloy. For each XRD scan, it takes 10 mins, during the scanning processes, the temperatures are maintained.

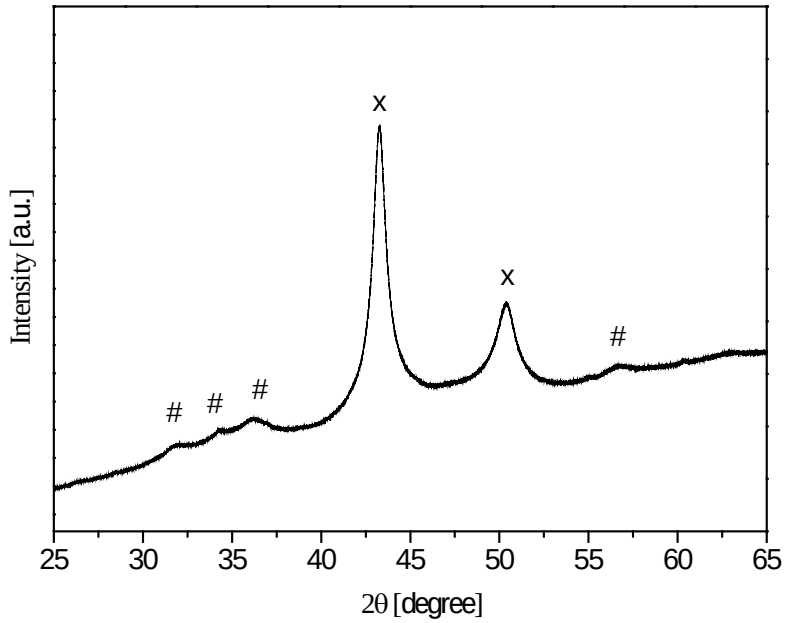

Fig. S7. The XRD pattern of reduced Cu/ZnO/Al_2O_3 catalyst; (x) metallic Cu; (#) ZnO.

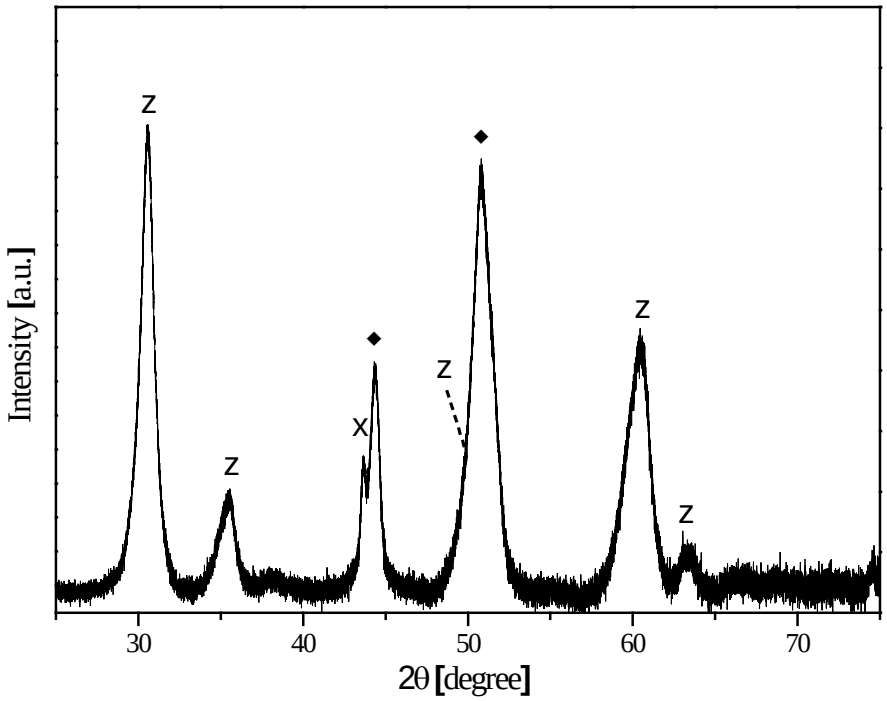

Fig. S8. The XRD pattern of reduced Cu-Ni/ZrO_2 catalyst; (x) metalic Cu; (◆) Cu-Ni alloy; (z) ZrO_2.

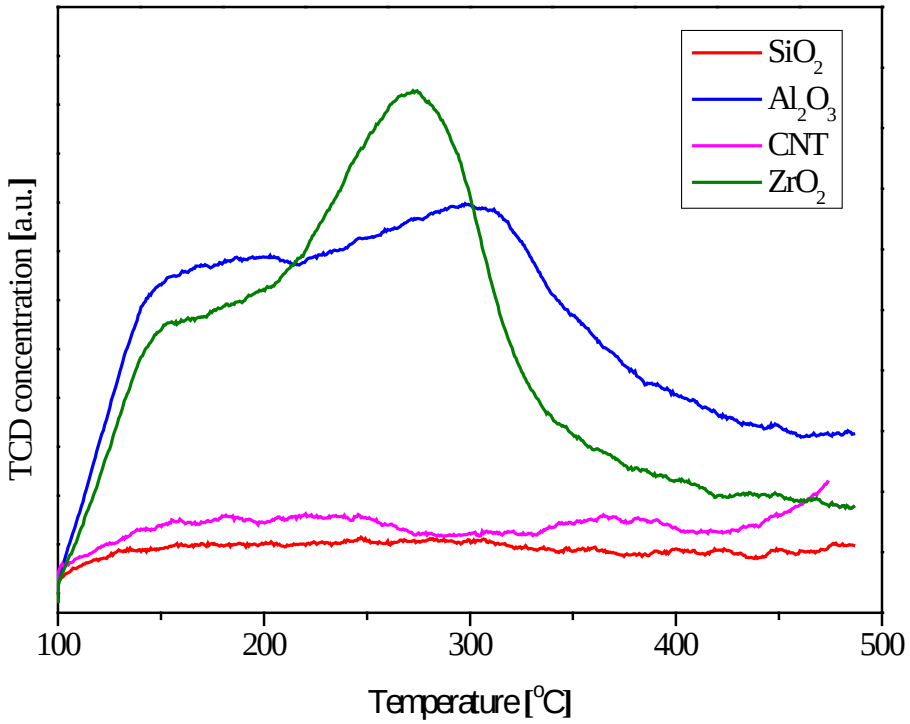

Fig. S9. The NH_3-TPD plots of supported Cu-Ni catalysts.

Table S3 Shift of the two main reflections, corresponding to the crystal planes [111] and [002], in CuNi alloy as a function of the Cu:Ni molar ratio.

ICSD _code	**Composition**	**2θ_[111] / °**	**2θ_[002] / °**
53758	Cu	43.17	50.27
628549	$Cu_{1.9}Ni_{0.1}$	43.47	50.64
628547	$Cu_{1.2}Ni_{0.8}$	44.00	51.26
628543	$Cu_{1.0}Ni_{1.0}$	43.96	51.21
628545	$Cu_{0.16}$ $Ni_{1.84}$	44.47	51.82
52265	Ni	44.50	51.85

Appendix C: Supplementary materials for Chapter 6

Table S1 The amount of catalyst and the flow rate of syngas for activity testing (the gas flow rate is referring to 298.15 K and 1 atm)

Catalysts	Test condictions	Weight [g]	Gas flow rate [Nml min^{-1}]		
			250 °C	275 °C	300 °C
Cu-Ni/SiO_2-calc-20H2	100 bar, H_2/CO =1	1.78	115	115	240
Cu-Ni/SiO_2-dried-20H2	100 bar, H_2/CO =1	2.21	152	-	-
Cu-Ni/SiO_2-dried-2H2	100 bar, H_2/CO =1	0.89	115	115	115
Cu/ZnO/Al_2O_3	100 bar, H_2/CO =1	0.41	115	115	230
Cu-Ni/SiO_2-calc-20H2	65 bar, H_2/CO =62/38	2.64	178	178	178
Cu-Ni/SiO_2-calc-20H2	65 bar, H_2/CO/CO_2 =62/35/3	2.18	143	143	280[a)]
Cu/ZnO/Al_2O_3	65 bar, H_2/CO/CO_2 =66/31/3	0.51	280	-	-

[a)] Test conditions: 65 bar, H_2/CO/CO_2 =66/31/3

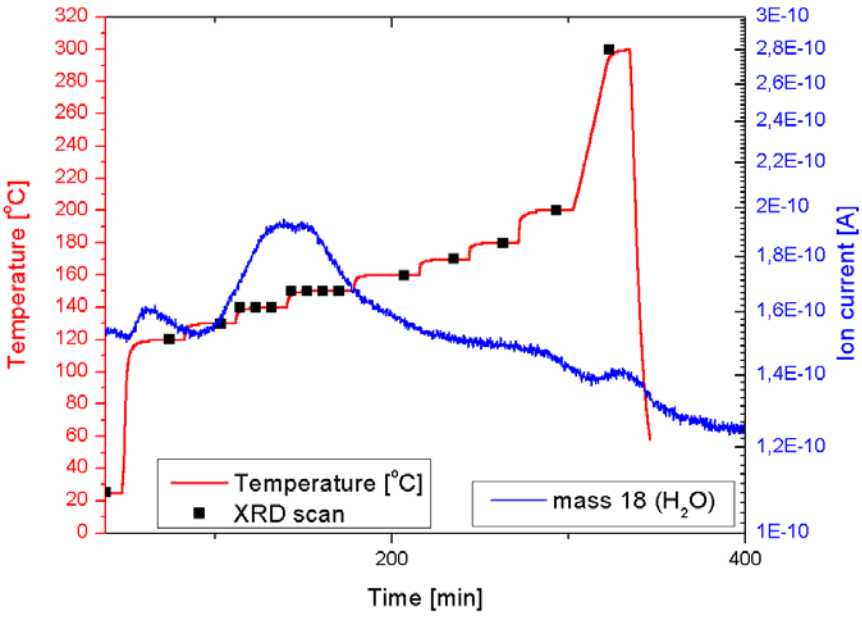

Fig. S1. In situ XRD scanning record and the mass of water that detected by mass spectrometry of Cu-Ni/SiO_2-calc catalyst.

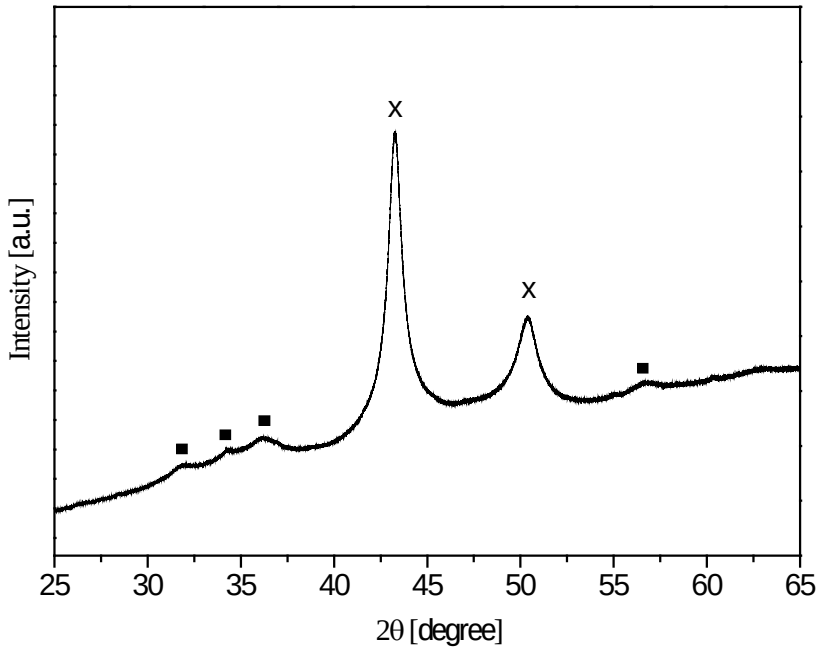

Fig. S2. The XRD pattern of reduced Cu/ZnO/Al_2O_3 catalyst; (x) metallic Cu; (■) ZnO.

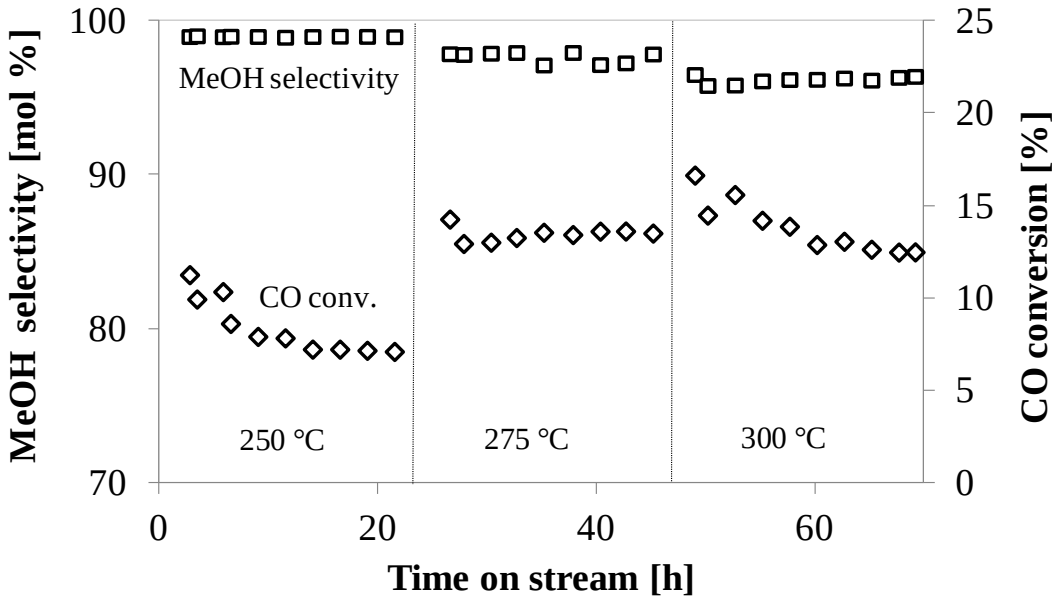

Fig. S3. Time on stream of CO conversion and selectivity of products over CuZnO/Al_2O_3 catalysts at 100 bar, GSHV=16000 h^{-1}, and H_2/CO=1.

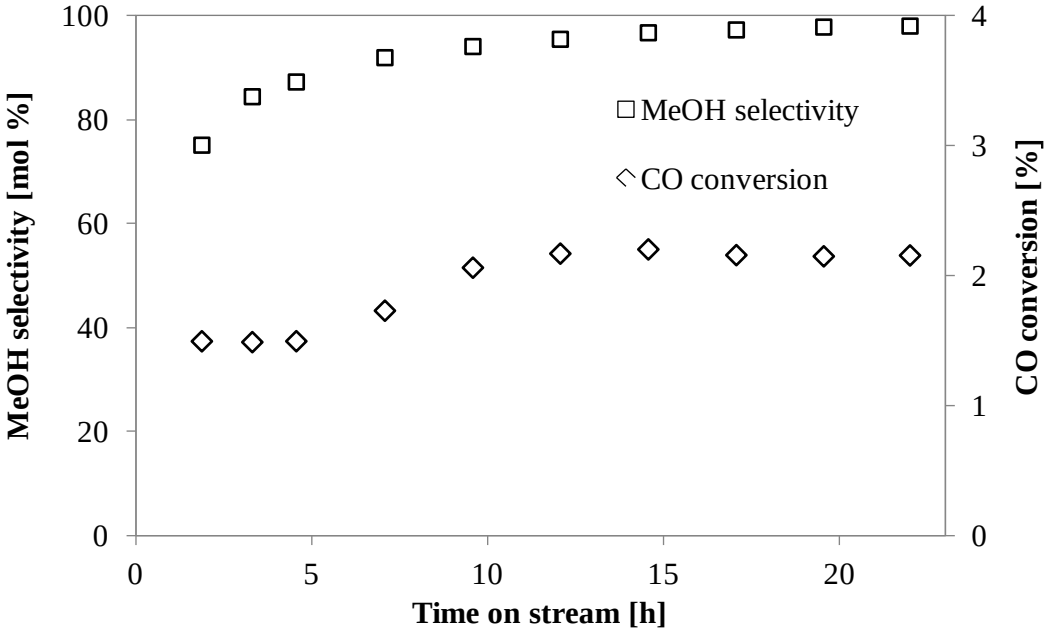

Fig. S4. Time on stream of CO conversion and product selectivity over CuNi/SiO_2-oxide catalyst at 100 bar, 250°C, GSHV=2000 h^{-1}, and $H_2/CO/CO_2$=62/35/3.

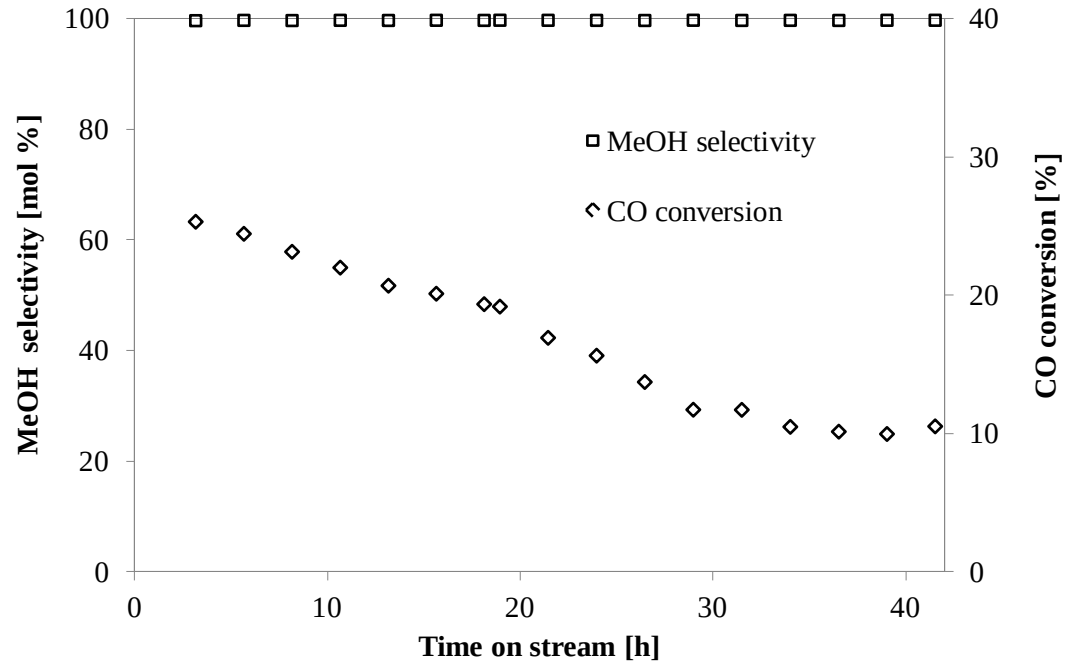

Fig S5. Time on stream of CO conversion and selectivity of products over CuZnO/Al_2O_3 catalysts at 65 bar, 250°C, GSHV=31000 h^{-1}, and $H_2/CO/CO_2$=66/31/3.

Appendix D: Supplementary materials for Chapter 8

This electronic supplementary information gives further details, background information and results to support the main paper, in particular with respect to in situ XAS, EXAFS data analysis, and testing.

CO hydrogenation

The performances of all Cu-Ni samples for CO hydrogenation were evaluated in a fixed-bed continuous-flow reactor with an online GC-FID/TCD detection system (6890N from Agilent Technologies). A bubble flow meter was used for determination of the volumetric flow rate of the reactor effluent. Methanol, ethanol, 1-propanol, 1-butanol, 2-butanol, iso-butanol, methane, ethane, ethane, propane, dimethyl ether (DME), and ethyl acetate were analyzed by GC. The alcohols were separated using a DB1 column whereas CO, H_2, CO_2, N_2 and hydrocarbons were analysed using a Parapak N column and followed by a 13 x Molesieve column. Prior to the reaction, all samples were pre-reduced in situ in a flow of 1.4 mol % H_2 in N_2 gaseous mixture for 12 h by heating to 280 °C with a heating rate of 1-1.5 °C min^{-1}. The carbon mass balance was generally fulfilled to within 5 mol %.

The conversion of CO (X_{CO}) is calculated from the molar flow rates of CO_2 (F_{CO}) into and out of the reactor:

$$X_{CO} = \frac{F_{CO}^{in} - F_{CO}^{out}}{F_{CO}^{in}} \cdot 100\% \ [\%]$$

The selectivity to a given product (S_i) is based on the total number of carbon atoms in the products:

$$S_i = (n_i y_i) / (\sum n_i y_i) \cdot 100\% \ [mol\ \%]$$

Where n_i ($n_i \geq 1$) is the number of carbon atoms in components *i*, and y_i is the fraction of component *i* in the product.

The space time yield (*STY*) of methanol is the production rate of methanol per mass of catalyst:

$$STY_{MeOH} = \frac{M_{MeOH} F_{MeOH}}{m_{cat}} \ \left[kg\ kg_{cat}^{-1}\ h^{-1} \right]$$

where, M_{MeOH} is the molar mass of methanol in the product and F_{MeOH} is the molar flow rate of methanol out of the reactor. Here, we report the *STY* in the units of mass of methanol produced per hour and per mass of catalyst (m_{cat}), which includes both active metals and support.

The metal area based activity of methanol is the production rate of methanol per metal surface area of catalyst:

$$Area\,based\,activity = \frac{STY_{MeOH}}{M_{MeOH} \times S_{active\ metal} \times 3600 \frac{s}{h}} \left[mol\ m^{-2}\ s^{-1} \right]$$

where, M_{MeOH} is the molar mass of methanol in the product, $S_{active\ metal}$ is the metal surface area of catalyst determined from the sulfur chemisorption.

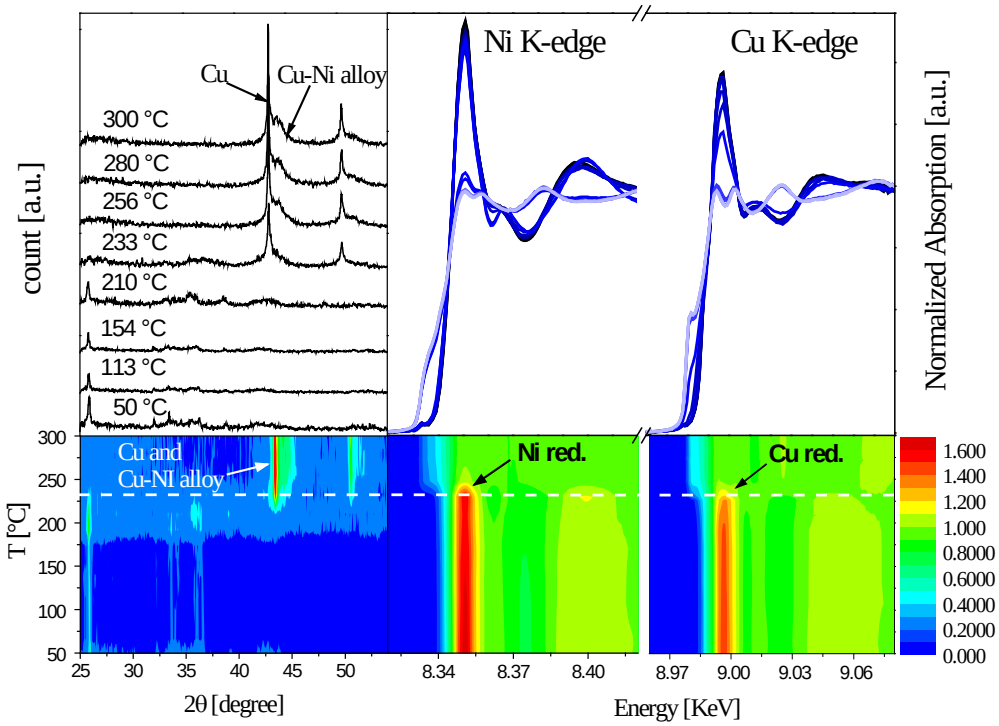

Fig. S1. Simultaneous in situ XANES and XRD for reduction of Cu_1Ni_1/SiO_2 catalysts. For XANES: the colors from blue to red are the transition from no absorption to stronger absorption refer to references; for XRD: the colors from blue to red are the transition from low intensity to high intensity.

Table. S1. Fitting results at Ni K-edge: S02 amplitude reduction factor; CN: coordination number; R: interatomic distance; σ^2: Debye Waller factor (mean square disorder); ΔE_0: energy shift; χ^2_ν Reduced Chi-square

sample	shell	S02	CN	R / Å	σ^2 (Å^2)	ΔE_0 / eV	R-factor	χ^2_ν
Ni foil	Ni-Ni	0.70±0.04	12*	2.533 ±0.002	0.0055 ±0.0004	5.85 ±0.39	0.0020	1712
Ni/SiO_2	Ni-Ni	0.70	11.4 ± 0.4	2.533 ±0.002	0.0061 ±0.0003	5.17 ±0.29	0.0008	350
Cu_1Ni_3/SiO_2	Ni-Ni(Cu) Ni-O	0.70	8.5 ± 1.8 2.6 ± 1.4	2.517 ±0.011 2.158 ±0.039	0.0079 ±0.0017 0.010 ±0.013	5.68 ±1.53	0.0149	12750
Cu_1Ni_1/SiO_2	Ni-Ni(Cu)	0.70	10.4 ± 1.0	2.517 ±0.005	0.007 ±0.0008	5.69 ±0.75	0.0089	2444
Cu_3Ni_1/SiO_2	Ni-Ni(Cu)	0.70	10.0 ± 0.8	2.509 ±0.004	0.0080 ±0.0007	5.59 ±0.63	0.0021	1041

Table. S2. Fitting results at Cu K-edge: S02 amplitude reduction factor; CN: coordination number; R: interatomic distance; σ^2: Debye Waller factor (mean square disorder); ΔE_0: energy shift; χ^2_ν Reduced Chi-square

sample	shell	S02	CN	R / Å	σ^2 (Å^2)	ΔE_0 / eV	R-factor	χ^2_ν
Cu foil	Cu-Cu	0.76±0.05	12*	2.578 ±0.002	0.0081 ±0.0005	3.66 ±0.42	0.0030	1329
Cu/SiO_2	Cu-Cu	0.76	6.8 ± 1.3	2.582 ±0.011	0.0075 ±0.0015	3.35 ±1.82	0.0134	247
Cu_1Ni_3/SiO_2	Cu-Cu(Ni)	0.76	10.0 ± 0.9	2.604 ±0.004	0.0085 ±0.0007	2.68 ±0.64	0.0036	739
Cu_1Ni_1/SiO_2	Cu-Cu(Ni)	0.76	11.6 ± 0.7	2.584 ±0.002	0.0087 ±0.0005	3.15 ±0.42	0.0027	535
Cu_3Ni_1/SiO_2	Cu-Cu(Ni)	0.76	11.2 ± 0.7	2.579 ±0.002	0.0088 ±0.0005	3.33 ±0.43	0.0027	581

Appendix E: Supplementary materials for Chapter 9

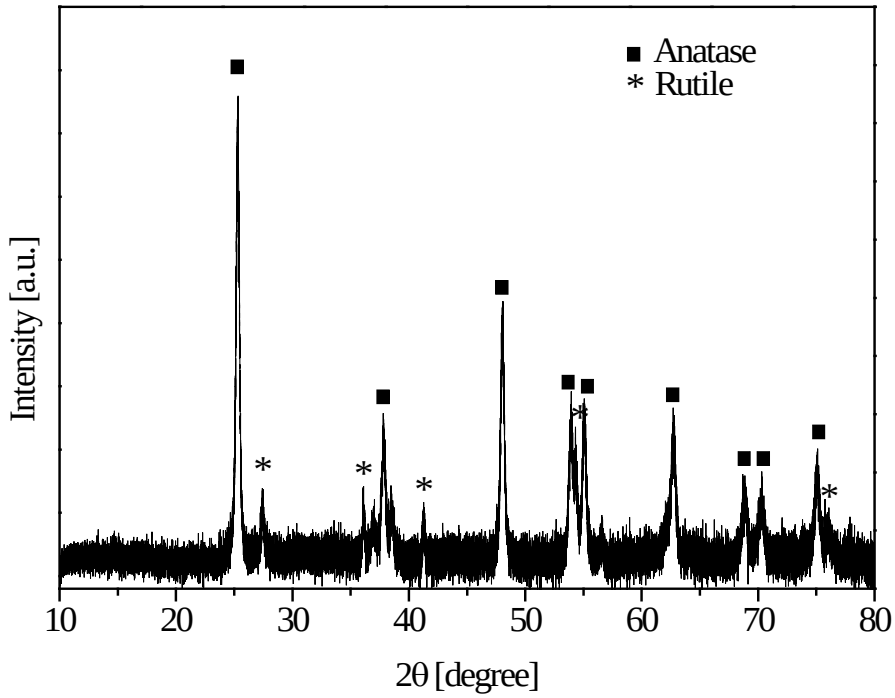

Fig. S1. XRD patterns of TiO_2_5_14K sample (after passivation).

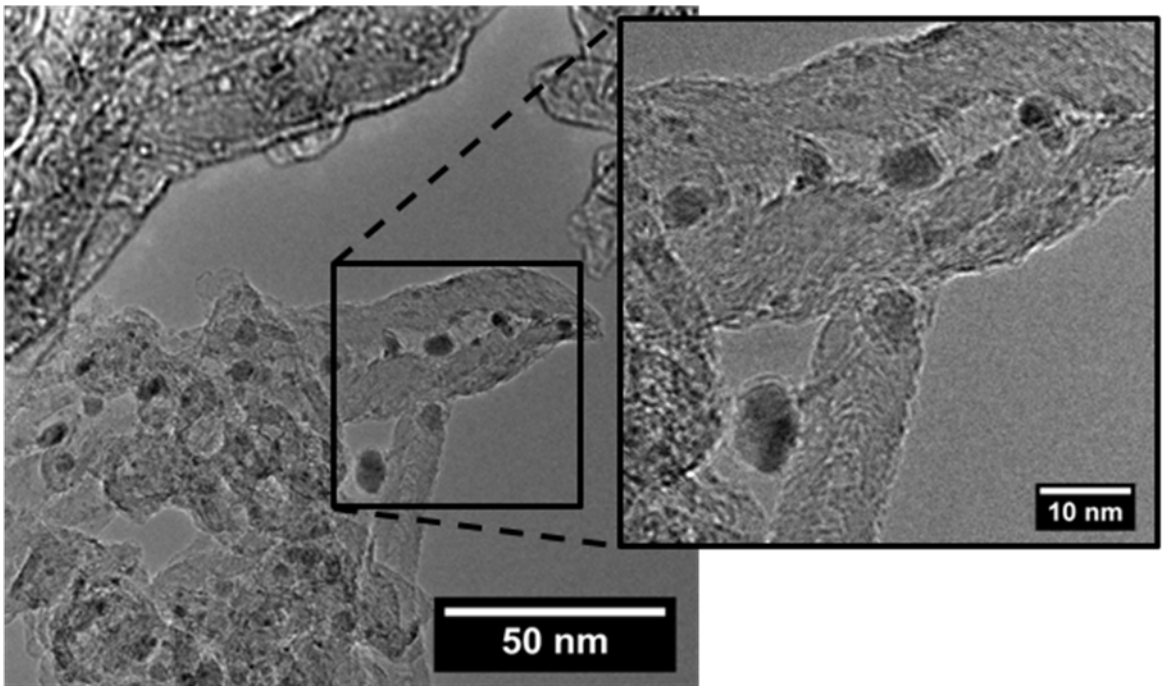

Fig. S2. TEM images of 5 wt % Mo_2C /CNT sample (after passivation).

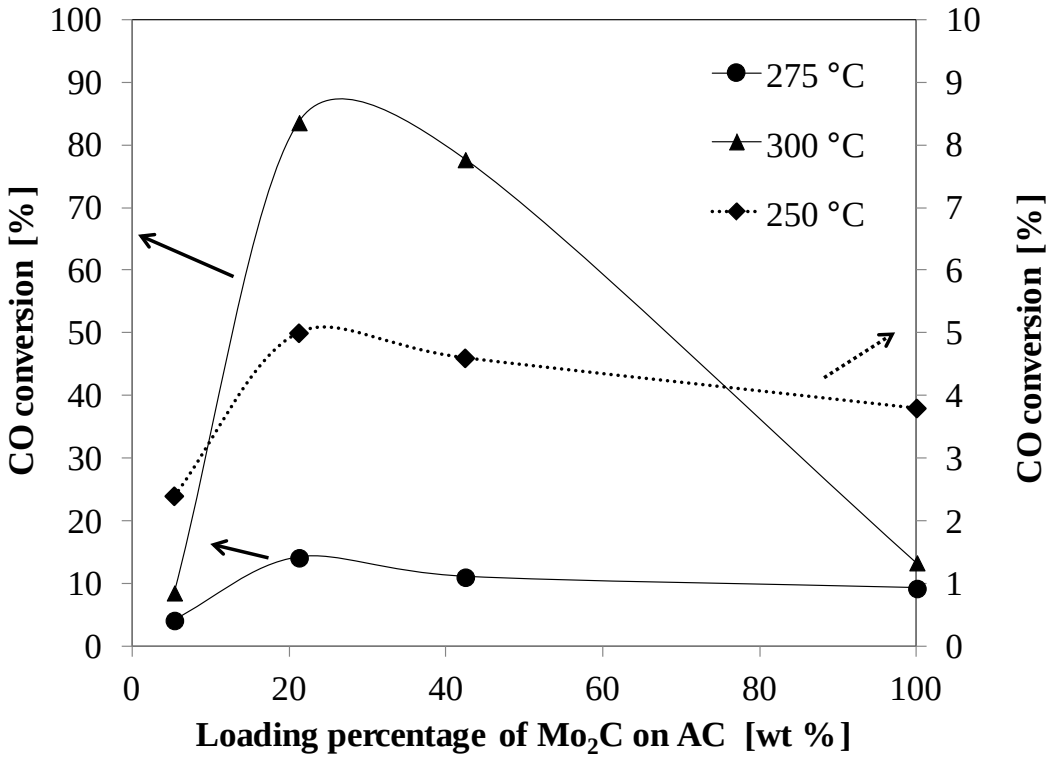

Fig. S3. The effect of the Mo_2C loading on AC on the steady state CO conversion at different temperatures.

Appendix F: Supplementary materials for Chapter 10

This electronic supplementary information gives further details, background information and results to support the main paper, in particular with respect to the sample preparation and EXAFS data analysis.

Molybdenum carbide (5.3 wt %) supported on: active carbon (AC), carbon nanotubes (CNT), and titanium oxide were prepared from supported molybdenum oxide by temperature programmed reaction (TPR) flowing in 20 mol % CH_4/H_2 (Air Liquide) Firstly, AC, CNTs, and TiO_2 pellets were crushed and sieved to a size range of 0.6 to 1.4 mm. Additionally, CNTs were purified by refluxing 5 g commercial CNT in 500 ml 37 wt % nitric acid at 110 °C for 5 h, followed by filtration, washing and drying before impregnation. The precursor solution of $Mo_7O_{24}(NH_4)_6 \cdot 4H_2O$ in volume of pores of each supports were added to the supports individually and aged at room temperature with continuous stirring for 1 h. The sample was then dried at 100 °C in air for 12-14 h and calcined at 450 °C in N_2 flow for 2 h with a heating rate of 5 °C min^{-1}.

In a typical carburization process, the oxide/support precursors (6-8 g) were placed in a quartz holder, which was then placed in a quartz tube inside a Carbolite tube furnace. The system was first purged with N_2 and then subjected to a flow of 20 mol % CH_4/H_2 (52 NmL min^{-1}) with a temperature programmed ramping (below 280 °C, ramp 5 °C min^{-1}, and above 280 °C, ramp 0.5 °C min^{-1}, up to 750 °C and maintain at 750 °C for 2 h). Afterwards the sample was cooled down in the flow of 20 mol % CH_4/H_2 until the temperature was lower than 280 °C. Then N_2 was used to flush the system until room temperature was achieved. Before sample being removed from the furnace, the carbide samples were exposed to a flow of 1 vol % O_2/N_2 for more than 6 h for passivating.

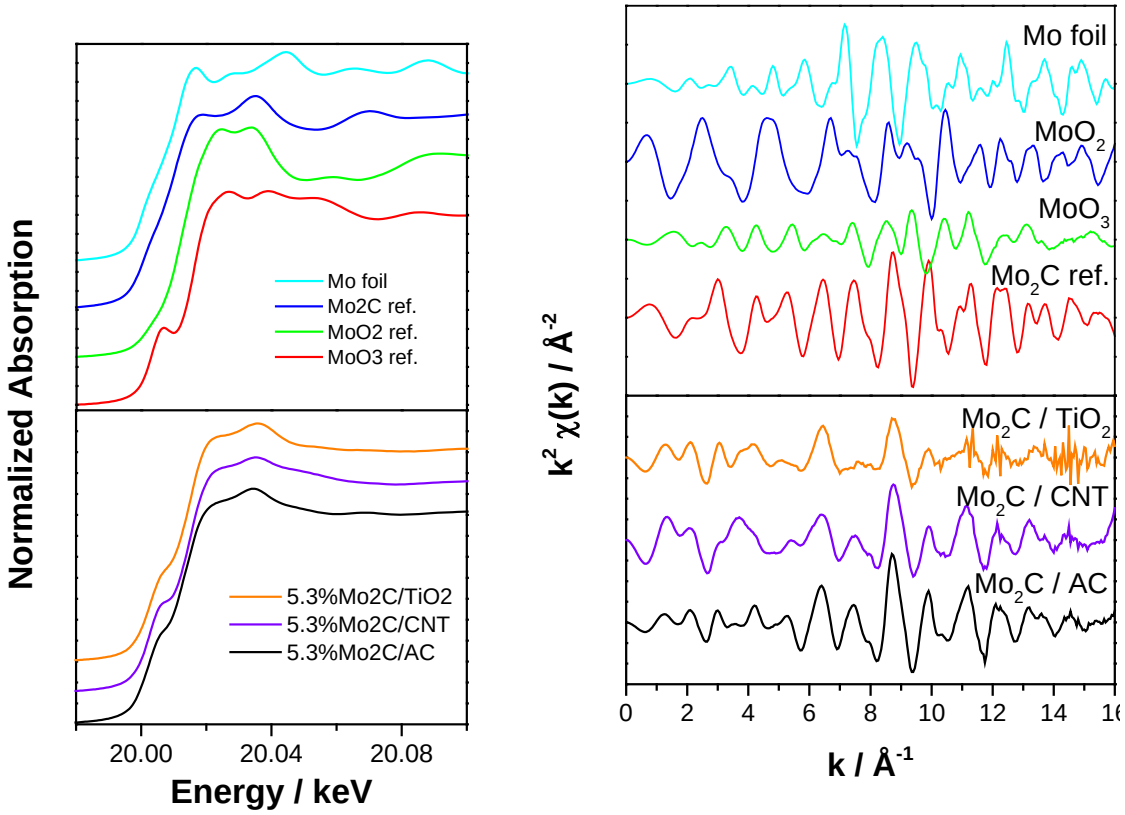

Fig. S1. XANES at the Mo K-edge of: (a) Mo reference standards; (b) Passivated 5.3%Mo_2C on TiO_2, CNT and AC, and magnitude of the Fourier transform (not corrected for phase shifts) of the k^3-weighted Mo K-edge EXAFS of (c) Mo standards; (d) Passivated 5.3%Mo_2C on TiO_2, CNT.

Table S1. Linear combination fitting results of passivated 5.3%Mo_2C on TiO_2, CNT and AC samples

Samples	**% MoO_2**	**% MoO_3**	**% Mo_2C**
5.3% Mo_2C/TiO_2	12.4	54.3	33.3
5.3% Mo_2C/CNT	2.2	67.2	30.6
5.3% Mo_2C/AC	7.6	45.1	47.3

Appendix G: In situ XRD aging studies of Cu-Ni and commercial catalysts

Preliminary XRD studies of sintering of Cu-Ni/SiO_2 (30 wt % Cu+Ni) and model Cu/ZnO/Al_2O_3 catalysts under accelerated aging conditions

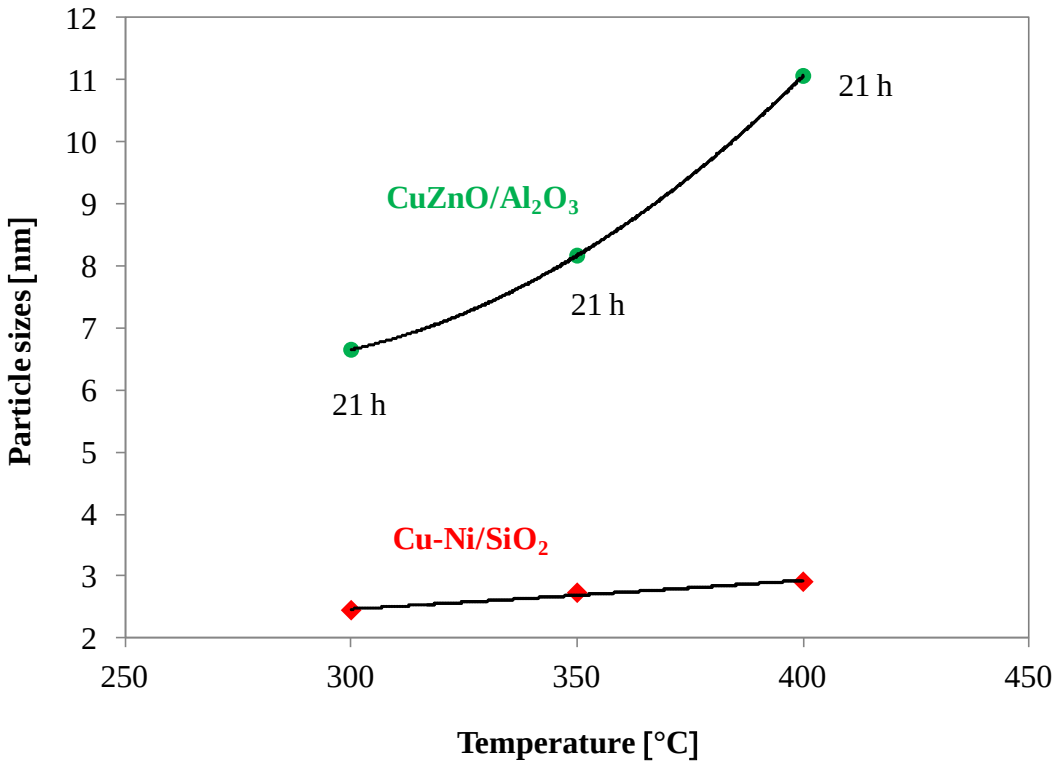

Fig.1. Estimated particle sizes of Cu and Cu-Ni alloys from in situ XRD patterns, both catalysts have been aged in 2% H_2/CO gas mixture at 300, 350, and 400 °C for 21 h, respectively.

Appendix H: Abstracts for conferences

1. Abstract 1: '*Novel highly active and selective Cu-Ni based methanol synthesis catalyst*' The 15th International Congress on Catalysis (ICC), 01.07.2012-06.07.2012, Munich, Germany (Poster presentation).
2. Abstract 2: '*Higher alcohols synthesis from syngas over carbon-nanotube supported iron-chromium catalysts*'; The 15th International Congress on Catalysis (ICC), 01.07.2012-06.07.2012, Munich, Germany (Poster presentation).
3. Abstract 3: '*Active carbon supported molybdenum carbides for higher alcohols synthesis from syngas*'; SynFuel 2012, 29.06.2012-30.06.2012, Munich, Germany (Poster presentation).
4. Abstract 4: '*Supported molybdenum carbides for higher alcohols synthesis from syngas*'; The 242nd ACS National Meeting: Chemistry of Air, Space, and Water, 28.8.2011-2.9.2011, Denver, USA (Oral presentation).
5. Abstract 5: '*Supported Cu/Group VIII metal alloys for synthesis of alcoholic fuels from syngas*'; The 22nd North American Catalysis Society Meeting (NAM), 5.6.2011-10.5.2011, Detroit, USA (Oral presentation).

Abstract 1: Novel highly active and selective Cu-Ni based methanol synthesis catalyst

Qiongxiao Wu[1], Jakob M. Christensen[1], Anker D. Jensen[1]*, *[1]Department of Chemical and Biochemical Engineering, Technical University of Denmark, Lyngby, Denmark;* Felix Studt[2], Frank Abild-Pedersen[2], Jens K. Nørskov[2,3], *[2]SUNCAT, Center for interface Science and Catalysis, SLAC, Menlo Park and [3]Department of Chemical Engineering, Standford University, Stanford, the USA;* Burcin Temel[4], *[4]Haldor Topsøe A/S, Kgs. Lyngby, Denmark;* Gian Luca Chiarello[5],Jan-Dierk Grunwaldt[1,5], *[5]Institute of Chemical Technology and Polymer Chemistry, Karlsruhe Institute of Technology, Karlsruhe, Germany*

Introduction

Methanol is an efficient fuel in an internal combustion engine or in a fuel cell, and it has therefore been suggested as an alternative energy carrier [1]. Despite the significant methanol production nowadays, the replacement of gasoline would however require more than a hundredfold increase in methanol production [2]. Moreover, deactivation of the commercial Cu/ZnO methanol synthesis catalyst poses one of the biggest problems. More than one third of the activity is lost after the first 1000 h of operation, something that often determines the economic lifetime of the catalyst [3]. It would therefore be of great value, if methanol synthesis catalysts with greater activity and stability could be developed. Based on a screening of a large number of bimetallic alloys using a newly developed microkinetic model, we have constructed volcano plots for methanol synthesis. The theoretical turnover frequency (TOF) is plotted as a function of two descriptors, namely the carbon and oxygen binding energies and Cu/Ni alloys are suggested as active methanol synthesis catalysts [4]. Herein, we present catalytic test results, characterization and extensive density functional theory (DFT) calculations for the CO hydrogenation over Cu/Ni bimetallic alloys [5].

Experimental

Cu/Ni based catalysts were prepared by the incipient wetness impregnation method. The catalyst precursors were dried at 100 °C and directly reduced in the reactor with 1% H_2 in N_2 flow at 280°C for 12 h. Performances of catalysts for high-pressure CO hydrogenation have been evaluated in a fixed-bed, continuous-flow reactor with a GC-FID/TCD detection system [6]. Typical reaction conditions were: P=100 bar; T=250-300°C. Reduction processes and phase compositions were investigated using in-situ XRD. The activity based on the amount of active materials was compared to a $Cu/ZnO/Al_2O_3$ model catalyst similar to the systems used in industry. Additionally, *in-situ* X-ray diffraction (XRD), *in-situ* X-ray adsorption spectroscopy (XAS) and *in-situ* transmission electron microscopy (TEM) have been used to clarify the structure of the Cu/Ni catalysts.

Results and Discussion

Figure 1 shows the theoretical activity volcano for the production of methanol from CO and H_2. Cu is observed to be closest to the top of the volcano among the transition metals, and there are several bimetallic alloys within the same region. An interesting alloy found in the screening procedure is Cu_3Ni. Figure 1 shows that one of the possible step sites of this alloy, denoted $^{AA}Cu_3Ni$, is predicted to possess a higher methanol synthesis activity than the step site of pure Cu metal. Table 1 shows that the methanol space time yields (STY) for a $CuNi/SiO_2$ catalyst indeed were at the same level as the STY's for the $Cu/ZnO/Al_2O_3$ model catalyst.

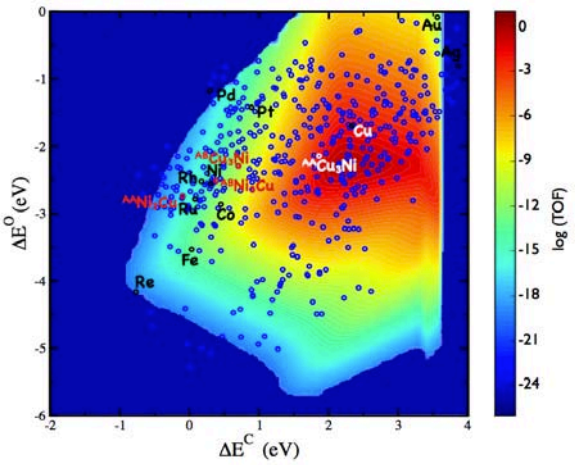

Figure 1. Theoretical activity volcano for the production of methanol from CO and H_2. The turnover frequency is plotted as a function of carbon and oxygen binding energies for a range of binary alloys. Two different steps for either of Cu_3Ni and $CuNi_3$ alloys are depicted in red; the Cu step of Cu_3Ni is depicted in white. Reaction conditions are 523 K, 45 bar H_2, 45 bar CO, and 10 bar methanol.

Table 1. Behavior of $CuNi/SiO_2$ and $Cu/ZnO/Al_2O_3$ catalysts in CO hydrogenation at steady state at 100 bar, and H_2/CO = 1.0 vol/vol.

Catalysts	**T** [°C]	**GHSV** [h^{-1}]	**CO conv.** [%]	**Carbon based, CO_2-free selectivity** [mol%]			**$MeOH_{STY}$** [b] $g/(g_{active\ materials} \cdot h)$
				MeOH	**C_{2+} oxygenates**	**HC**[a]	
$CuNi/SiO_2$	275	5200	5.2	98.2	1.4	0.4	1.6
$CuNi/SiO_2$	300	5200	8.2	98	1.4	0.6	3.3
$Cu/ZnO/Al_2O_3$	275	16000	13.5	97.6	2.1	0.3	1.7
$Cu/ZnO/Al_2O_3$	300	32000	12.7	96.3	2.8	0.9	3.7

[a] HC: hydrocarbons. [b] STY: space time yield of methanol based on the amount of active materials (0.175 g metallic Cu + Ni for $CuNi/SiO_2$ catalyst, 0.71 g Cu + ZnO for $Cu/ZnO/Al_2O_3$ catalyst according to elemental analysis according to elemental analysis) in 1 g catalyst precursor.

Conclusions

In-situ XRD shows that only the CuNi alloy is present in the reduced catalyst. It seems likely that the surface after reduction is enriched in Cu and that CO can pull Ni out onto the surface. In-situ XAS shows that Cu and Ni can be reduced simultaneously. The high activity of silica supported CuNi alloy catalyst agreed with the fact that the DFT calculations identified Cu rich CuNi alloy catalysts as highly active catalysts for the hydrogenation of CO to form methanol.

References

(1) G.A. Olah, *Angew. Chem. Int. Ed.* **2005**, 44, 2636.
(2) G.A. Olah, *Catal. Lett.* **2004**, 93,1.
(3) J.B. Hansen, AlChE Spring National Meeting, Orlando, Fl, **1990**.
(4) J.K. Nørskov, F. Abild-Pedersen, F. Studt, T. Bligaard, *PNAS*. **2011**, 108, 937.
(5) F. Studt, F. Abild-Pedersen, Q. Wu, A.D. Jensen, J. Grunwaldt, B. Temel, J.K. Nørskov, submitted to *J. Catal.*, **2011**
(6) J.M. Christensen, P.A. Jensen, A.D. Jensen, *Ind. Eng. Chem. Res.* **2011**, 50, 7949.

Abstract 2: Higher alcohols synthesis from syngas over carbon-nanotube supported Fe-Cr catalysts

Qiongxiao Wu[1], Trine M. H. Arndal[1], Lars L. Jensen[1], Jakob M. Christensen[1]; Anker D. Jensen[1* 1*]Department of Chemical and Biochemical Engineering, Technical University of Denmark, Lyngby, Denmark; Linus D. L. Duchstein[2], [2]Center for Electron Nanoscopy, Technical University of Denmark, Lyngby, Denmark; Burcin Temel[3], [3]Haldor Topsøe A/S, Lyngby, Denmark; Jan-Dierk Grunwaldt[1,4], [4]Institute of Chemical Technology and Polymer Chemistry, Karlsruhe Institute of Technology, Karlsruhe, Germany

Introduction

Higher alcohols synthesis (HAS) from syngas has recently drawn considerable attention for its application in the field of biofuel and bioadditive production [1-3]. Higher alcohols may be produced directly from syngas, which may be obtained by gasification of renewable sources such as biomass and waste. In the 1980s van der Riet et al. [4] studied the HAS with a $K/Fe/Cr_2O_3$ catalyst and achieved a high total selectivity to C_{2+} oxygenates of 83.4 wt% at 5 mol% CO conversion, but after these very promising, initial results there have been no subsequent reports on HAS with the K-Fe-Cr system. Recently, carbon-nanotubes (CNTs) have been reported as a novel interesting carrier for catalysts due to the unique chemical and physical properties of the nanotubes [5]. Here, CNT-supported K-Fe-Cr catalysts have been investigated. The investigations include high pressure (100 bar) activity evaluations, BET surface area measurements, X-ray diffraction (XRD) studies, and transmission electron microscopy (TEM) evaluations.

Experimental

Fe-Cr supported on CNTs or silica were prepared by co impregnating the supports with a precursor solution containing the metal salts. Additionally, CNTs were purified by refluxing CNTs in 37 wt% nitric acid at 110 °C for 5 h, followed by filtering, washing and drying. Performance of catalysts for HAS from syngas has been evaluated in a fixed-bed continuous-flow reactor with a GC-FID/TCD detection system [6]. Prior to the reaction the catalysts precursor were in-situ subjected to a reducing treatment in a flow of 20% H_2 in N_2 for 12-14 h at 400 °C. Typical operating conditions are: P = 100 bar; T = 250-400 °C; GHSV = 5000 h^{-1}; Feed: $H_2/CO=1$ (v/v).

Results and Discussion

Table 1 shows the catalytic properties of $K_2CO_3/Fe_1Cr_2/CNTs$ catalyst in CO hydrogenation at steady state. From 300˚C to 400 ˚C the selectivity to alcohols decreased from 83.7 % to 68.9 %, while the hydrocarbon (HC) selectivity increased from 13.4 % to 30.3 %. The selectivity to C_{2+}-oxygenates reached 42.8 mol% at 300˚C. The alcohol space time yield reached 87 $g \cdot kg_{cat} h^{-1}$. The production of alcohols or hydrocarbons followed Anderson-Schulz-Flory (ASF) distributions. The chain growth probabilities for both alcohols and hydrocarbons are different, which may indicate that the intermediates for the alcohols and hydrocarbons are different. Figure 1 shows that the catalytic particles mainly are spread inside the CNTs. In the calcined catalyst, Fe_3O_4 particles were identified by XRD. No chromium-related reflections were observed in the XRD patterns indicating that Cr compounds in the catalyst were amorphous or finely dispersed. The particle sizes are in the range of 3-10 nm. Additionally,

the opened/impregnated CNTs did not seem to have agglomerated compared to the raw CNTs.

Table 1. Behavior of K_2CO_3/Fe_1Cr_2/CNTs catalyst in CO hydrogenation at steady state at P = 100 bar, H_2/CO = 1.0 vol/vol, and GHSV = 5000 h^{-1}.

T [°C]	CO conv. [mol%]	Space time yield [g/ kg_{cat} h^{-1}]	Carbon based, CO_2-free selectivity [mol%]				Chain growth probability (α)	
		alcohol	Overal alcohols	Hydro-carbons	C_{2+}-oxygenates	MeOH	α_{Alc}	α_{HC}
300	3.6	11	83.7	13.4	42.8	43.8	0.32	0.42
325	4.4	26	85.0	13.2	31.8	55.0	0.26	0.41
350	4.7	32	81.9	17.7	26.0	56.3	0.26	0.29
400	8.2	87	68.9	30.3	22.5	47.2	0.29	0.30

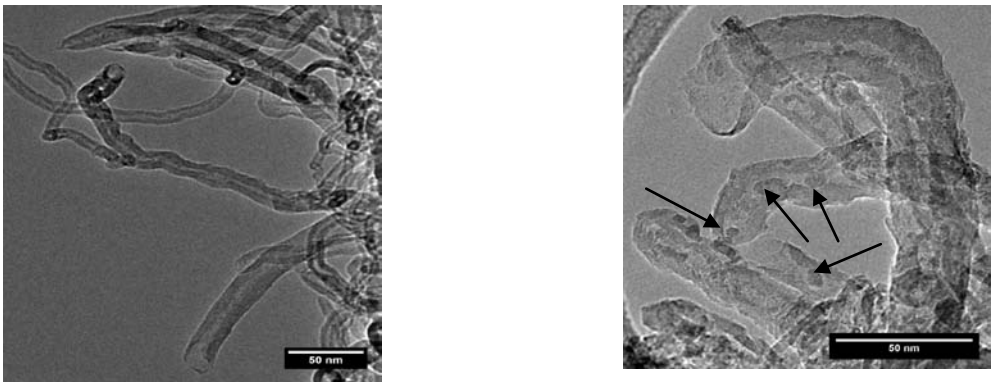

Figure 1. TEM images of the raw CNTs (left) and the fresh K_2CO_3/Fe_1Cr_2/CNTs (right, the individual catalytic particles highlighted with black arrows).

Conclusions

A carbon-nanotube supported iron-chromium alcohol synthesis catalyst was synthesized, tested and characterized. At 300 °C it showed up to 43.8 mol% and 39.9 mol% selectivity to methanol and higher alcohols, respectively (3.6 mol % CO conversion). The production of alcohols or hydrocarbons followed ASF distributions. Chromium compounds in the catalyst were in the form of either amorphous or finely dispersed particles. Fe_3O_4 particles are mainly spread inside of the CNTs.

References

(1)Subramani, V., and Gangwal, S.K. *Energy Fuels,* **2008**, 22(2), 814.

(2) Spivey, J.J., and Egbebi, A., *Chem. Soc. Rev.*, **2007**, 36(9), 1514.

(3) Christensen, J. M., Mortensen, P. M., Trane, R.; Jensen, P. A., Jensen, A.D. Appl. Catal. A, **2009**, 366, 29.

(4) van der Riet, M., Copperthwaite, R.G., Demarger, S.F.,Hutchings, G.J. *J. Chem. Soc. Chem. Commun.*, **1988**, 10, 687.

(5) Serp, P., Castillejos, E. *ChemCatChem*, **2010**, 2, 41

(6) Christensen, J.M., Jensen, P.A., Jensen, A.D. *Ind. Eng. Chem. Res.* **2011**, 50, 7949.

Abstract 3: Active carbon supported molybdenum carbides for higher alcohols synthesis from syngas

Qiongxiao Wu[a], Gian Luca Chiarello[b], Jakob M. Christensen[a], Burcin Temel[c], Jan-Dierk Grunwaldt[a,b], Anker D. Jensen[*a]

[a] *Department of Chemical and Biochemical Engineering, Technical University of Denmark, Søltofts Plads, Building 229, 2800 Kgs. Lyngby, Denmark*
[b] *Institute of Chemical Technology and Polymer Chemistry, Karlsruhe Institute of Technology, Engesserstr. 20, 76131 Karlsruhe, Germany*
[c] *Haldor Topsøe A/S, Nymoellevej 55, 2800 Kgs. Lyngby, Denmark*

Summary : This work provides an investigation of the high pressure CO hydrogenation to higher alcohols on K_2CO_3 promoted active carbon supported molybdenum carbide. Both activity and selectivity to alcohols over supported molybdenum carbides increased significantly compared to bulk carbides in literatures. The optimal loadings of both molybdenum carbide and the K_2CO_3 promoter on active carbon have been investigated. The catalysts were characterized using BET surface area measurements, transmission electron microscopy and X-ray diffraction. Additionally, *in-situ* X-ray diffraction and *in-situ* X-ray absorption spectroscopy were applied for determining the carburization temperature and evaluating the composition of the carbide clusters of different samples through determinations of the Mo-C and Mo-Mo coordination numbers.

Keywords : active carbon; molybdenum carbides; higher alcohols; syngas;

Introduction

The synthesis of liquid fuels such as methanol, and higher alcohols from syngas have received a renewed attention for the production of fuels and fuel additives especially with syngas produced by gasification of biomass or coal [1-2]. Higher alcohols are more attractive as a fuels or fuel additive due to their better miscibility with hydrocarbon components, improved water tolerances and higher overall heating value compared to methanol [3]. Additionally, higher alcohols can be used as liquid carriers of hydrogen and dehydrated to olefin feedstocks used in the production of polymers. Alkali modified bulk molybdenum carbide has previously been shown to produce ethanol as the main alcohol product [4-5]. However, the bulk molybdenum carbide suffers from a low specific surface area, which results in low activity for CO hydrogenation [6]. It would therefore be interesting to identify a suitable support material for molybdenum carbide that can accommodate a larger specific surface area of the active material.

This work provides an investigation of the high pressure CO hydrogenation to higher alcohols on active carbon supported molybdenum carbide. The optimal loadings of both molybdenum carbide and the K_2CO_3 promoter on active carbon have been investigated. The catalysts are characterized using BET surface area, transmission electron microscopy (TEM), *in-situ* X-ray diffraction (XRD) and *in-situ* X-ray absorption spectroscopy (XAS).

Experimental

Molybdenum carbides supported on active carbon (AC) were prepared by temperature programmed reaction of supported molybdenum oxide precursors in a flow of 20 vol% CH_4 in H_2. These supported carbides were impregnated with an aqueous solution of K_2CO_3 with calculated amount. The performance of catalysts for the higher alcohol synthesis from syngas has been evaluated in a fixed-bed continuous-flow reactor with a GC-FID/TCD detection system (6890N from Agilent Technologies) [2,6]. A bubble flow meter was used for determination of the volumetric flow rate of the reaction effluent. Prior to the reaction, the supported carbides were *in-situ* treated with a 20% H_2 in N_2 flow (52 ml/min) at 350 °C for 2 h to remove a possible oxide passivation layer formed during air exposure. Typical reaction conditions were: P=100 bar; T=250-300°C; GHSV=5000 h^{-1}; Feed: H_2/CO=1 (v/v). To understand the carburization process *in-situ* XAS and XRD measurements at the Mo K-edge were performed at the HASYLAB/DESY and ESRF. The specific surface areas of both fresh and used catalysts were determined by N_2 adsorption at 77 K.

Results

Fig.1 shows the effect of the Mo_2C loading on the CO conversion and the CO_2-free selectivities at steady-state conditions. As mentioned above the bulk Mo_2C (100 wt% point in Figure 1) suffers from a low specific surface area, which results in low activity for CO hydrogenation [6]. The CO conversion and selectivities to different products varied with the Mo_2C loading on AC. 5.3 wt% Mo_2C/AC showed the highest methanol selectivity - up to 55.3 mol%. 21.2 wt% Mo_2C/AC exhibited the highest hydrocarbon (HC) selectivity. The selectivity

*** Corrresponding author**
E-mail : AJ@kt.dtu.dk
Phone/fax : +45 45252841/45882285

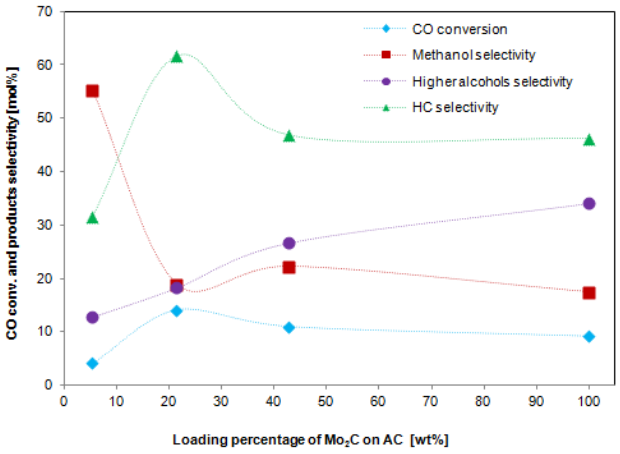

Fig. 1. The effect of Mo_2C loading (the molar ratio: K/Mo = 0.14) on CO conversion and the CO_2-free selectivity at steady state. P=100 bar; T=275°C; GHSV=5000 h^{-1}; Feed: H_2/CO=1 (v/v).

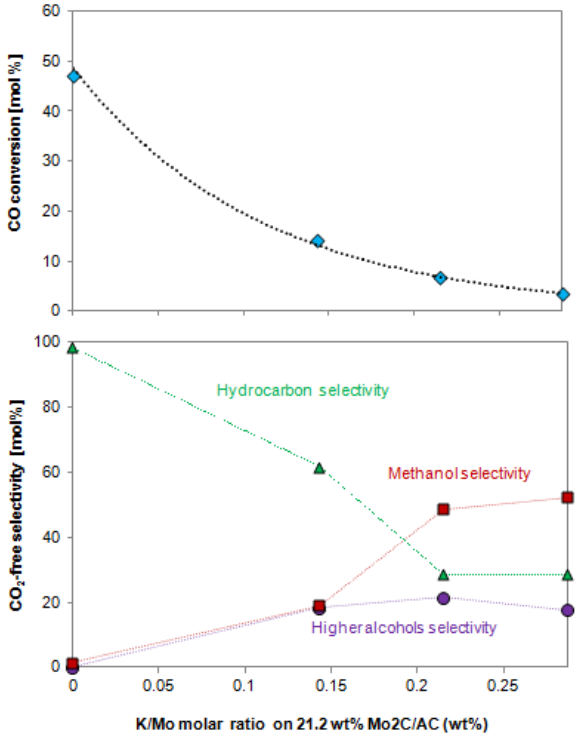

Fig. 2. The effect of K_2CO_3 loading on CO conversion and the CO_2-free selectivity at steady state, P=100 bar; T=275°C; GHSV=5000 h^{-1}; Feed: H_2/CO=1 (v/v).

to higher alcohols increased with increasing the Mo_2C loading on AC and reached a maximum with bulk carbides. The effect of the Mo_2C loading on the selectivity could be related to the composition of the supported carbide clusters. It was reported that MgO supported (5 wt%) Mo_2C showed higher coordination number (CN) of Mo-C(O) (CN = 5.1±1.7) than bulk Mo_2C (CN = 3) according to the results of *in-situ* extended X-ray absorption fine structure measurements [7]. The coordination numbers for active carbon supported clusters could thus be different from the CN's for the bulk carbide and this may be part of the explaination of the loading effect. The CO conversion showed a maximum, when 21.2 wt% Mo_2C was loaded on active carbon. This indicated that this catalyst has the largest active surface area.

Additionally, for bulk Mo_2C it was observed that the selectivity to alcohols increased with increasing the K_2CO_3 content up to 10 wt% (the molar ratio: K/Mo = 0.14) and then stagnated [4]. Here, the molar ratios of K/Mo were kept as a constant 0.14 for all catalysts, but a dilution effect of the support should be considered. The amount of K_2CO_3 has a dramatic influence on the selectivity to different products, and the 21.2 wt% Mo_2C/AC catalyst exhibited the highest activity. Hence, the effect of the K_2CO_3 loading on the 21.2 wt% Mo_2C/AC catalyst as well. This is shown in Fig.2. Unpromoted Mo_2C/AC exhibited a high activity for CO conversion with HCs as the dominant products (>99 mol%). Upon addition of K_2CO_3 the overall CO conversion was reduced, while the product distribution shifted dramatically from HCs to alcohols. The increase in alcohol selectivity at the expense of HCs continued until the molar ratio of K/Mo = 0.22, where both the selectivity to higher alcohols and to alcohols in general reached a maximum.

Conclusions

The active carbon supported molybdenum carbide catalysts showed improved activity and alcohol selectivity compared to bulk carbides. Unpromoted Mo_2C/AC exhibited a high activity for CO conversion to Hydrocarbons as the dominant products with a trace amount of alcohols. The potassium carbonate promoter plays an essential role in obtaining alcohols rather than hydrocarbons. The optimum selective towards higher alcohols and to alcohols at a K/Mo molar ratio of 0.22. The effect of the molybdenum carbide loading on the selectivity could be related to the composition of the supported carbide clusters. The current work focuses on evaluating the composition of the carbide clusters of different samples by determining the Mo-C and Mo-Mo coordination numbers using *in-situ* XAS and XRD investigations.

Acknowledgements

The experimental work is financed by the Technical University of Denmark, Haldor Topsøe A/S, and the Danish Ministry for Science, Technology and Development under the "Catalysis for Sustainable Energy" initiative.

References

[1]J.J. Spivey, A. Egbebi. *Chem. Soc. Rev.* 36 (2007) 1514.
[2]J. M. Christensen, P. M. Mortensen, R. Trane, P. A. Jensen, A.D. Jensen. Appl. Catal. A. 366 (2009) 29.
[3]Spath, P. L.; Dayton, D. C. *A925634*. 2003.
[4]I. Wender. *Fuel. Proc. Technol.* 48 (1996)189.
[5]H.C. Woo, K.Y. Park, Y.G. Kim, I.S. Nam, J.S. Chung, J.S. Lee, *Appl. Catal.* 75 (1991) 267.
[6]J. M. Christensen, L.D.L. Duchstein, J.B. Wagner, B. Temel, P. A. Jensen, A.D. Jensen. *Submitted to Ind. Eng. Chem. Res.* 2011.
[7]H. Shou, Davis, R.J. *J. Catal.* 282 (2011) 83.

Abstract 4: Supported molybdenum carbides for higher alcohols synthesis from syngas

Qiongxiao Wu[1], Jakob M. Christensen[1], Gian Luca Chiarello[2], Burcin Temel[3], Jan-Dierk Grunwaldt[2] and Anker D. Jensen[1]*

[1] *Department of Chemical and Biochemical Engineering, Technical University of Denmark, Søltofts Plads, Building 229, 2800 Kgs. Lyngby (Denmark)*

[2] *Institute of Chemical Technology and Polymer Chemistry, Karlsruhe Institute of Technology, Engesserstr. 20, 76131 Karlsruhe*

[3]*Haldor Topsøe A/S, Nymoellevej 55, 2800 Kgs. Lyngby (Denmark)*

[*] *Corresponding author email address: AJ@kt.dtu.dk*

Introduction

The synthesis of higher alcohols (C_{2+} alcohols) has received a renewed attention lately for their application as alternative fuels and additives especially with syngas produced by biomass or coal gasification [1-4]. Previously, alkali modified bulk molybdenum carbide (β-Mo_2C) was shown to produce ethanol as the main alcohol product [5, 6]. However, the bulk β-Mo_2C suffers from a low specific surface area, which results in low activity for CO hydrogenation [6]. Therefore, it would be interesting to determine a suitable support material for molybdenum carbide. This work provides an investigation of the high pressure CO hydrogenation to higher alcohols on molybdenum carbide based catalysts supported on various materials, *i.e.* active carbon, carbon nanotubes and titanium dioxide. The investigation includes also a comprehensive characterization of the catalysts by BET, X-ray diffraction (XRD), *in-situ* transmission electron microscopy (TEM) and X-ray absorption spectroscopy (XAS) investigations.

Experimental

Molybdenum carbides supported on active carbon (AC), carbon nanotubes (CNTs), and titanium dioxide were prepared by temperature programmed reaction (TPR) of supported molybdenum oxide precursors in a flow of 20 vol% CH_4/H_2. These carbides were impregnated with an aqueous solution of K_2CO_3 with calculated amounts. The performance of catalysts for higher alcohols synthesis (HAS) from syngas has been evaluated in a fixed-bed continuous-flow reactor with a GC-FID/TCD detection system. Prior to the reaction, the supported carbides were treated *in-situ* with 20% H_2 in N_2 flow (35 ml/min) at 350 °C for 2 h to remove a possible passivation layer formed after exposure in air. Typical operating conditions were: P=100 bar; T=250-300 °C; GHSV=5000 h^{-1}; Feed: H_2/CO=1 (v/v). Particle sizes and phase compositions were investigated using XRD. The specific surface areas of both fresh and used catalysts were determined by N_2 adsorption at 77 K. *In-situ* TEM was used to study the catalyst morphology in H_2 gas flow from 25 to 600 °C. *In-situ* XAS, the Mo K-edge measurements were performed at the synchrotron of Hamburg HASYLAB-X beamline.

Results and Discussion

Table 1 shows the catalytic performance of $K_2CO_3/Mo_2C/TiO_2$ catalyst in CO hydrogenation at steady state. The CO conversion and selectivity to hydrocarbons were enhanced by increasing temperature, while the selectivity of methanol and higher alcohols decreased. The higher alcohols selectivity reached 34.3 mol% at 250 °C, however, the selectivity to both methanol and higher alcohols decreased dramatically when the temperature was increased. This may be caused by insufficient loading of the K_2CO_3 promoter. Indeed, it has been observed for bulk Mo_2C that the selectivity to alcohols increases with increasing the K_2CO_3 content up to 10 wt% and then stagnates [5]. Here 10 wt% K_2CO_3 based on active materials (Mo_2C) were added for all catalysts and the dilution effect of support might be considered.

Table 1. Effect of temperature on the catalytic performance of $K_2CO_3/Mo_2C/TiO_2$ in CO hydrogenation at steady state.

Catalyst	T	CO conv.	Carbon based, CO_2-free selectivity [mol%]		
	[°C]	[mol%]	MeOH	C_{2+}OH	HC
$K_2CO_3/Mo_2C/TiO_2$	250	4.6	18.1	34.3	46.2
$K_2CO_3/Mo_2C/TiO_2$	275	9.4	13.3	21.7	61.6
$K_2CO_3/Mo_2C/TiO_2$	300	85.1	0.3	0.43	99.3

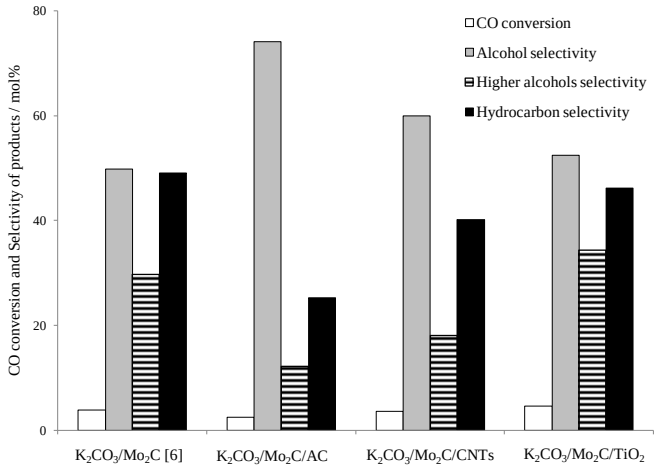

Figure 1. CO conversion and product selectivity (at 250 °C) at steady state over the investigated catalysts (5.3 wt% Mo_2C for all supported catalysts).

Figure 1 shows the CO conversion and the selectivity to different products at steady state. The active carbon supported catalyst exhibited the highest alcohols selectivity with methanol being the dominant alcohol. On the other hand, TiO_2 supported catalyst showed the highest selectivity to higher alcohols.

Conclusions

The catalytic activity of molybdenum carbides supported on different materials such as active carbon, carbon nanotubes, and titanium dioxide in higher alcohol synthesis from syngas is significantly affected by the support nature. In particular TiO_2 seems to be a promising support due to its better selectivity to higher alcohols. The future work is focused on improving both the selectivity of the catalysts towards higher alcohols by modifying the K_2CO_3 loading of the catalysts and the activity by increasing the loading of the Mo_2C.

Acknowledgement

This work is financed by Technical University of Denmark, Haldor Topsøe A/S, and the Danish Ministry for Science, Technology and Development under the "Catalysis for Sustainable Energy" initiative.

References

(1)Subramani, V., and Gangwal, S.K. *Energy Fuels*, **2008**, 22(2), 814.

(2) Spivey, J.J., and Egbebi, A., *Chem. Soc. Rev.*, **2007**, 36(9), 1514.

(3) Christensen, J. M., Mortensen, P. M., Trane, R.; Jensen, P. A., Jensen, A.D. Appl. Catal. A: General **2009**, 366, 29.

(4) Wender, I. *Fuel. Proc. Technol*, **1996**, 48,189

(5) Woo, H.C., Park, K.Y., Kim, Y.G., Nam, I.S., Chung, J.S., Lee, J.S., *Appl. Catal.* **1991**, 75, 267.

(6) Christensen, J. M., Duchstein, L.D.L., Wagner, J.B. Temel, B., Jensen, P. A., Jensen, A.D. *submitted to Ind. Eng. Chem. Res.* **2011.**

Abstract 5: Supported Cu/Group VIII metal alloys for synthesis of alcoholic fuels from syngas

Qiongxiao Wu[1], Jakob M. Christensen[1], Burcin Temel[2], Jan-Dierk Grunwaldt[3] and Anker D. Jensen[1]*

[1]*Department of Chemical and Biochemical Engineering, Technical University of Denmark, Søltofts Plads, Building 229, 2800 Kgs. Lyngby (Denmark)*

[2] *Haldor Topsøe A/S, Nymoellevej 55, 2800 Kgs. Lyngby (Denmark)*

[3] *Institute of Chemical Technology and Polymer Chemistry, Karlsruhe Institute of Technologye, Engesserstr. 20, 76131 Karlsruhe (Germany)*

[*] *Tel.: +45 45252841. Fax: +45 4588 2258, E-mail address: aj@kt.dtu.dk*

Introduction

Alternatives to petroleum-derived fuels and chemicals are being sought in an effort to enhance energy security and the air quality through development of novel technologies for the production of synthetic fuels and chemicals using renewable energy sources such as biomass [1,2]. Higher alcohols (C_{2+} alcohols) are being considered as potential alternative synthetic fuels, as they can be produced by syngas derived from biomass [2,3]. There are two processes involved in this technique: First, syngas (CO and H_2) is thermo-chemically formed by the gasification of biomass, and then the syngas is converted into higher alcohols [3].

Catalyst systems of copper combined with group VIII metals such as Co [4] and Ni [5] have shown interesting results for higher alcohols synthesis (HAS) with respect to selectivity and activity. Recently it was reported that nano-particles outside/inside carbon nanotubes (CNTs) showed better performances than nano-particles on conventional supports [6]. It might thus be envisioned that Cu-Ni/Co supported on CNTs could have a better performances for HAS as well. This work provided a systematic study of Cu-Ni or Cu-Co catalysts for HAS from syngas. Different Cu/Ni (or Co) ratios, supports and operating conditions were employed. The work included activity evaluations and spectroscopic investigations.

Materials and Methods

Cu/Group VIII metal based catalysts were prepared by impregnation (with ultrasonic treatment). Nitrate salts of Cu, Co, and Ni as well as CNTs (Sigma-Aldrich) and Al_2O_3 were used for preparation of catalysts. All catalyst precursors were dried at 120 °C overnight and calcined in air or N_2 (CNT based cats.) at 400 °C for 4 h. Performance of catalysts for HAS from syngas has been evaluated in a fixed-bed continuous-flow reactor with a GC-FID/TCD detection system. Prior to the reaction, samples of the oxide precursor of catalysts were pre-reduced in situ by a 10% H_2 in N_2 gaseous mixture for 12 h at 300 °C with a heating rate of 1°C/min. Typical operating conditions are: P = 60-100 bar; T = 250-325 °C; GHSV = 2000 h^{-1}; Feed: H_2/CO=1 (v/v). TPR was carried out for identifying the reduction temperatures of catalysts and complementary in-situ XAS experiments are conducted. Particle sizes and phase composition were investigated using in-situ XRD. The specific surface areas of both fresh and used catalysts were determined by N_2 adsorption at 77 K. In-situ TEM was used to study the catalyst morphology in H_2 gas flow from 25 to 600 °C.

Results and Discussion

The CO conversion and productivity of alcohols are enhanced by increasing pressure and temperature. However, the selectivity to alcohols is decreased by increasing temperature, while the selectivity to hydrocarbons is increased. The TPR revealed that a strong interaction occurs between copper and nickel in the mixed oxide catalysts since they were more easily reduced than the pure CuO and NiO oxides.

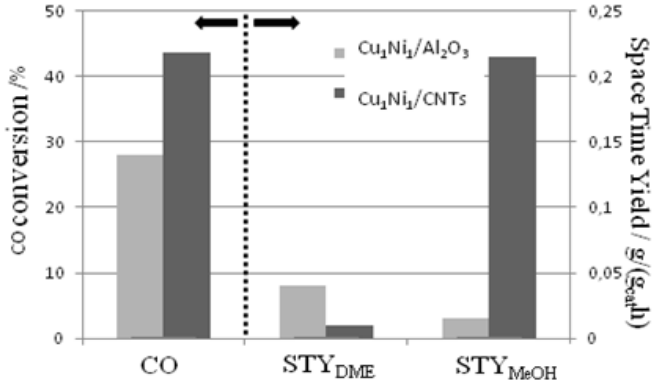

Figure 1. CO conversion, space time yield (STY, g/(g_{cat}h)) of methanol (MeOH) and dimethyl ether (DME) at 100 bar, 300 °C, GHSV 2000 h^{-1} and V(H_2)/V(CO)=1 over Cu_1Ni_1 /CNTs and Cu_1Ni_1 /Al_2O_3 catalysts (20 wt% Cu and Ni for both catalysts). Time on stream +50 h.

Figure 1 shows that Cu-Ni catalysts supported on Al_2O_3 and CNTs exhibited different catalytic behaviors for CO hydrogenation. The CNTs supported catalyst showed much higher activity than the Al_2O_3 supported one. The former one mainly produced methanol, while the latter one produced DME. This is due to the lewis acidic sites of γ-Al_2O_3 that can dehydrate methanol to DME. The current work is focused on changing the catalytic selectivity of the catalysts towards higher alcohols by modifying the basicity of the catalysts with alkali and other promoters.

Significance

This work is significant for an industrial utilization for alcoholic fuels production. The nature of catalysts and reaction mechanism may be inferred from the presented results.

References

1. Subramani, V., and Gangwal, S.K. *Energy Fuels*, 22(2), 814 (2008).
2. Spivey, J.J., and Egbebi, A., *Chem. Soc. Rev.*, 36(9), 1514 (2007).
3. Christensen, J. M., Mortensen, P. M., Trane, R.; Jensen, P. A., Jensen, A.D. *Appl. Catal. A* 366, 29 (2009).
4. Courty, P., Durand, D., Freund, E., Sugier, A. *J. Mol. Catal.* 17, 241 (1982).
5. Fraga, M. A., and Jordão, E. React. *Kinet. Catal. Lett.* 64, 331 (1998)
6. Serp, P., and Castillejos, E. *ChemCatChem*, 2, 41 (2010)